Development of a Small Scale CHP Biomass System for the Luxembourgish Market

Sacha Oberweis

Faculty of Computing, Engineering and Technology

Staffordshire University

A thesis submitted in partial fulfilment of the requirement of Staffordshire University for the degree of

Doctor of Philosophy

February 2011

aides à la formation recherche

Fonds National de la Recherche Luxembourg

Any sufficiently advanced
technology is indistinguishable from magic
Arthur C. Clark

Abstract

Global climate change is one of the greatest challenges of the 21^{st} century. Rising ambient temperatures and deterioration of weather patterns are anticipated to result from increased atmospheric concentrations of greenhouse gases caused in part by the use of fossil fuels for electricity generation and domestic heating purposes.

The possibility of a global temperature rise of between 1° and 4.5° Celsius has led to considerable research efforts into the effects of changes in temperature and other climatic variables. The increasing use of private capital in the energy industry has altered the focus from the provision of a service to the need to make profits from the production and sale of a commodity. Additionally, with respect to Luxembourg, the dependency on imported energy is an important risk factor.

This thesis presents biomass as an essential alternative to substitute for some of the fossil fuels in the domain of heat, cooling and power generation. The results presented show an increase in energy utilisation and thus energy efficiency and reduction in emissions when used in combined generation modes as opposed to single generation. These results are gathered through meticulous analytical models, computational fluid dynamics (CFD), and laboratory testing of real life biomass systems. The technologies and analysis investigated here are targeted at those involved in climate change research, providing them with valuable data on the energy analysis of biomass and its associated emissions, highlighting the potential for reduction in pollutions when biomass is used instead of fossil fuels; in energy policy making; investors; engineers; and all others involved in the biomass design and operation of combined generation of biomass applications.

***

De globale Klimawandel as eng vun de gréissten Erausfuederunge vum 21^{ten} *Jorhonnert. Et gëtt domat gerechent, dass déi ëmmer méi héich Konzentratiounen vun Zäregas, erbäigefouert vum benotzen vun fossillen Energieträger fier d'Produktioun vun Elektresch an Waarmwaser, schold si un den ëmmer méi héigen Temperaturen a Klimaverännerungen.*

D'Wahrscheinlechkeet vun enger globaler Erhéijung vun $1°$ *a* $4.5°$ *Celsius hued dobäi zougedroen, dass ëmmer mei Ustrengungen an der Entwécklung vun de Grënn vun Temperaturverännerungen an aner Klimawandelerscheinungen gemaach ginn. D'Méiglechkeet vun enger krasser Verännerung vun eisem Liewenswandel huet bis elo nach ni bekannten Auswierkungen op International Agencen gemaach fier eng Äntwert a Léisung op déi sougenannten 'Karbon' – Problemer ze fannen. De Kyoto Protokoll an d'EU2020 Zieler zwéngen dei meescht industrialiséiert Länner fir hir Karbonausstéis drastesch bis 2020 an doriwwer eraus, ze reduzéieren. D'Benotzen vu Biomass als Brennstoff as esou eng Léisung, mat Ofstand ee vun den eelsten Energieträger, ass onëmstridden eng vun de Méigleschkeeten déi vun engem Klimawandel kéint beaflosst gin. D'Privatiséierung vum Energieberäich ass onëmstridden Schold dorun dass d'Energieindustrien hire Fokus vun engem 'Service Provider' op de Profit vum Verkaaf vun engem Produit oder Service verluecht hun.*

Dës Studie mécht en Effort fir Biomass als en alternativen Brennstoff am Beräich vun Hëtzen, Kielen an der elektresch Produktioun ze presentéieren. Donieft soll ënnerstrach ginn, dass d'Benotzen vun Kleng-Kraaft-Wierker (BHKW) eng drastesch Verbesserung vun der Energie-Effizienz erméiglecht. Ech erhoffen mer, dass des Technologien, vun deene Leit déi am Beräich vum Klimawandel, den relevanten Fuerschungszenter, Verwaltungen, Investoren, Ingenieuren an all anneren Leit déi sech dofier interesséieren appreciéiert a verstanne ginn.

Contents

Abstract ii
Table of Contents iv
List of Figures ix
List of Tables xiv
Foreword xvi
Acknowledgments xviii
Nomenclature xx

1 Introduction **1**
1.1 Thesis Background 1
1.2 Project Objectives and Scope 2
1.3 Thesis and Contribution to Knowledge 3
1.4 Thesis Outline 5

2 Biomass Tri-generation Technology **7**
2.1 Biomass as a Renewable Energy Source 7
2.1.1 World Energy Consumption 7
2.1.2 Energy Situation, Present and Future Outlook for Luxembourg 11
2.2 Biomass Conversion Processes 16
2.2.1 Indirect Conversion Processes 19
2.2.2 Direct Conversion Processes 25
2.2.3 Biomass Combustion Products 29
2.2.4 Biomass Combustion Modelling 32
2.3 Biomass Power Generation 34
2.3.1 Large Scale Systems 35

2.3.2 Small Scale Systems 36
2.3.3 Stirling Engine Modelling 41
2.4 Biomass Refrigeration 42
2.4.1 Absorption Refrigeration Cycles 42
2.4.2 Working Fluids for Absorption Refrigeration Systems . . . 46
2.4.3 Absorption Cooling Modelling 47
2.5 Biomass Applications 49
2.5.1 Single Generation Applications 49
2.5.2 Combined Dual Systems (CHP/CCH) 51
2.5.3 Tri-generation Systems 53
2.5.4 Future Trends 54
2.6 Conclusion 55

3 Theory of Biomass Combined Generation Technologies 57
3.1 Introduction 57
3.2 Theory of the Combustion of Solid Biomass 58
3.2.1 Adiabatic Flame Temperature 61
3.2.2 Dissociation of Biomass Combustion Products 62
3.3 Theory of Heat Transfer in a Shell and Tube Heat Exchanger . . . 64
3.3.1 Heat Transfer and Overall Heat Transfer Coefficient 64
3.3.2 Analysis of a Shell and Tube Heat Exchanger 67
3.3.3 Determination of Pressure and Friction Losses 69
3.4 Theory of the Stirling Engine 71
3.4.1 Stirling Engine Cycle Analysis 73
3.4.2 Third Order Design Method for Stirling Engines 77
3.4.3 Performance Evaluation of a Stirling Engine 79
3.5 Theory of Absorption Cooling 84
3.5.1 Energy Transfer of Heat Exchangers and Vapour in a TCA Unit 86
3.5.2 Reactor Mass and Temperature Calculations 89
3.5.3 Condenser Mass and Temperature Calculations 91
3.5.4 COP of a TCA Absorption Heat Pump 92
3.6 Theory of Combined Generation Systems 93

3.6.1 Comparison of Combined Cooling and Heating with the Conventional Generation of Cooling and Heating 95
3.6.2 Comparison of Tri-generation System with the Separate Generation System of Power, Heat and Cooling and the Combined Systems of CCH and CHP 96
3.7 Conclusion 97

4 Computational Fluid Dynamics and Analytical Modelling 99
4.1 Introduction 99
4.2 Modelling of the Biomass Combustion 100
4.2.1 Analytical Model of Biomass Combustion 100
4.2.2 Verification of the Analytical Model of Biomass Combustion 103
4.2.3 Verification of the General CFD Flow Analysis Applied to a Thermal Situation 108
4.2.4 Computational Fluid Dynamics of the Biomass Combustion System 110
4.3 Modelling of Heat Exchangers for Biomass Applications 115
4.3.1 Analytical Model of Shell and Tube Heat Exchangers . . . 115
4.3.2 Verification of the Analytical Model of Heat Exchangers . 116
4.3.3 Verification of the CFD Heat Transfer Model Applied to a Plate Fin 119
4.3.4 Computational Fluid Dynamics of the Shell and Tube Heat Exchanger 126
4.4 Modelling of a γ-type Stirling Engine for Biomass Applications . . 129
4.4.1 Analytical Model of a γ-type Stirling Engine 130
4.4.2 Verification of the Analytical Model of a γ-type Stirling Engine 142
4.4.3 CFD Analysis of the γ-type Stirling Engine 146
4.5 Modelling of the Absorption Cooling Process for Biomass Applications 157
4.5.1 Analytical Model of the Thermo Chemical Accumulator Absorption Cooling Process 157
4.5.2 Verification of the Analytical TCA Model 162

4.6 Modelling of the Combined Generation Systems 165
4.7 Conclusion 167

5 Experimental Setup and Plan 169
5.1 Introduction 169
5.2 Experimental Setup 170
5.2.1 Carborobot Farmer F40 170
5.2.2 γ-type Stirling Engine 174
5.2.3 Shell and Tube Heat Exchanger 177
5.2.4 ClimateWell TCA Absorption Unit 179
5.3 Data Acquisition and Instrumentation 180
5.3.1 Data Acquisition System and Software 181
5.3.2 Temperature Measurements 182
5.3.3 Air Pressure Measurement 182
5.3.4 Air Flow Measurement 183
5.3.5 Exhaust Gas Flow Measurement 184
5.3.6 Water Flow Measurements 185
5.3.7 Emission Measurements 185
5.3.8 Solid Biofuels Properties 188
5.4 Test Plan and Procedure 190
5.4.1 Experimental Plan for Boiler Performance 190
5.4.2 Experimental Plan for Stirling Engine Performance 191
5.4.3 Experimental Plan for Absorption Cooling Performance . . 193
5.4.4 Experimental Plan for Solid Biofuels Properties 194
5.4.5 Experimental Plan for CCH Performance 196
5.4.6 Test Procedure 196
5.5 Calibration 198
5.5.1 Calibration of Gas Analysers 198
5.5.2 Calibration of Thermocouples 199
5.5.3 Data Logging System Configuration 200
5.5.4 Calibration of Bomb Calorimeter 200
5.5.5 Calibration of Double Pass Particulate Monitor 201
5.6 Error Analysis 202

5.6.1 Temperature Measurement Uncertainty 204
5.6.2 Air Flow Measurement Uncertainty 205
5.6.3 The Other Measurements Uncertainties 208
5.7 Conclusion 210

6 Results and Discussion **212**
6.1 Introduction 212
6.2 Biomass Combustion Performance and Products 213
6.2.1 Biomass Fuel Properties 213
6.2.2 Performance Evaluation of the Biomass Boiler 224
6.2.3 Emissions for Single Generation of DHW 230
6.3 Stirling Engine Performance Analysis 236
6.3.1 The Effect of Changing Gas and the Pressure 236
6.3.2 The Stirling Engine as a Cooler 241
6.4 Absorption Cooling Performance Analysis 246
6.4.1 Comparison of COP for Different Operating Conditions . . 246
6.4.2 Single Generation of Cooling 255
6.4.3 Combined Cooling and Heating 258
6.4.4 Emissions for Cooling Only and CCH 261
6.5 Comparative Savings for Combined and Single Generation 267
6.6 General Discussion 271

7 Conclusions and Recommendations **273**
7.1 Conclusions 273
7.2 Recommendations 275

A Chemical Properties of Substances **277**

B Specifications of Apparatuses and Instruments **279**

References **297**

List of Figures

2.1 World fossil fuel consumption from 1800 to 2050 (raw data published by IEA) 9
2.2 EU2020 targets for renewable percentage of total primary energy consumption (current and target) 10
2.3 The potential of wood based biomass in Luxembourg 15
2.4 The potential of straw based biomass in Luxembourg, (RUBIN, 2008) 17
2.5 SIDEROS pellet stove, Sideros (2011) 49
2.6 Tiled stove from Austria 50

3.1 Combustion pot for wood pellet combustion 59
3.2 Cross sectional view of a 3D representation of the heat exchanger 65
3.3 Cross-sectional view of a tube 65
3.4 Correction factor plot for a shell and tube heat exchanger with one shell pass 69
3.5 γ-type Stirling engine (cross-sectional cut) 72
3.6 Diagram for the convention of crank angle and piston movement . 73
3.7 Five engine cells with separating walls 75
3.8 Regenerator temperature profile 81
3.9 Schematic of a single TCA unit 85
3.10 Sankey diagram for CCH 93

4.1 Flow diagram for the biomass combustion model 102
4.2 Side view of the wind-tunnel experiment to validate CFD flow results 108

4.3 Side view of the velocity distribution on the three horizontal levels across the wind-tunnel 109
4.4 Cross-sectional view of the Carborot F40 with annotations 111
4.5 Cross-sectional view of the air flow inside the Carborot F40 112
4.6 Carborot F40 boiler tubes with ash removal fins 113
4.7 Velocity vectors of the water flow inside the boiler of the Carborobot F40 114
4.8 Elecro shell and tube heat exchanger 115
4.9 Plate fin with thermocouple locations 120
4.10 Ansys result plot of nodal temperatures across a plate fin 124
4.11 Comparison between experimental, numerical, Ansys and Solidworks results 125
4.12 Velocity profile inside the shell 127
4.13 Velocity profile inside the tubes 127
4.14 Temperature distribution across the shell 128
4.15 Temperature distribution across the tubes 128
4.16 Flow diagram for the Stirling model 131
4.17 Volume variations with crank angle for the γ-type Stirling engine 134
4.18 Schmidt P-V diagram for a γ-type Stirling engine 144
4.19 P-V diagram for a γ-type Stirling engine from the 3^{rd} order analysis 145
4.20 Temperature profile for the heater at 10bar air 147
4.21 Velocity distribution for the heater at 10bar air 148
4.22 Gas temperature profile for the cooler and its connecting tubes . . 149
4.23 Gas velocity vectors across the cooler and its connecting tubes . . 150
4.24 Water temperature profile for the cooler and its connecting tubes 151
4.25 Water velocity vectors across the cooler and its connecting tubes . 152
4.26 Gas velocity distribution in the compression space and its header 153
4.27 Water temperature variations in the cooling jacket of the compression space 154
4.28 Water velocity vectors in the cooling jacket of the compression space (bottom view) 155
4.29 Water velocity vectors in the cooling jacket of the compression space (side view) 156

4.30 Flow diagram for the TCA model 161
4.31 Salt concentration of the TCA unit with indicated 'swap' periods 162
4.32 Outlet temperatures for condenser and reactor 163

5.1 Schematic diagram of the experimental test setup 171
5.2 Test rig assembly and data acquisition equipment 172
5.3 Carborobot Farmer F40 173
5.4 Heater assembly 174
5.5 Crankcase assembly 175
5.6 Compression cylinder lining 176
5.7 Displacer piston mounted on the displacer base 176
5.8 Leroy-Somer LSRPM90SC generator 177
5.9 Elecro heat exchangers installed with their respective connections and pumps 178
5.10 ClimateWell TCA unit 179
5.11 H.E.A.T. Technology Division Data Logger 182
5.12 Barometer used in the present study 183
5.13 Orifice plate mounted at the air inlet to the combustor 184
5.14 Digital flow meter to measure flow rate ($MW1$) 186
5.15 Spring based flow meter to measure flow rates ($MW3$), ($MW4$) and ($MW5$) 186
5.16 Magneto-dynamic oxygen analyser 187
5.17 Infra-red NO_x gas analyser 187
5.18 Dynoptic opacity particulate monitor 188
5.19 PARR bomb calorimeter 189

6.1 Shredded Miscanthus 214
6.2 Straw pellets dia: $\pm$ 6 mm 214
6.3 Miscanthus logs 60 $mm \times$ 60 mm 214
6.4 Moisture content for the different fuel samples 215
6.5 Bulk densities for the different fuel samples 216
6.6 Ash content for the different fuel samples 217
6.7 Volatile matter content for the different fuel samples 218
6.8 Fixed carbon content for the different fuel samples 219

6.9 Energy content for the different fuel samples 220
6.10 Ash content vs. higher heating value for the different fuel samples 221
6.11 Volatile matter and fixed carbon vs. HHV for the different fuel samples 222
6.12 Accuracy of measured and correlated HHV 223
6.13 Comparison of inlet and outlet heat 225
6.14 Comparison of specific fuel consumption 226
6.15 Comparison of fuel consumption 227
6.16 Comparison of thermal efficiency for single generation of DHW . 228
6.17 Comparison of net heat output 229
6.18 Emissions of CO_2 for different fuels against net energy output . . 231
6.19 Emissions of CO for different fuels against net energy output . . . 232
6.20 Emissions of NO_x for different fuels against net energy output . . 233
6.21 Emissions of C_6H_{14} for different fuels against net energy output . 234
6.22 Particulate emissions for different fuels against net energy output 235
6.23 Temperature variations as a function of crank angle 237
6.24 P–V diagram at 10 *bar* charge pressure 238
6.25 Pressure drop in the heat exchangers at 10 *bar* 239
6.26 Total mass of working gas in the engine 240
6.27 Actual work output for air at 10 *bar* 241
6.28 Comparison of thermal efficiency for all gases 242
6.29 Torque and power calibration graph 243
6.30 Apparent and true power at 0 *bar* pressure 244
6.31 Oscilloscope screen shot for the ampere-meter 244
6.32 Variation of cooling temperature output of the Stirling engine . . 245
6.33 COP against heat source temperature for 18°C cooling temperature247
6.34 COP against heat source temperature for 20°C cooling temperature248
6.35 COP against heat source temperature for 22°C cooling temperature249
6.36 COP against heat source temperature for 24°C cooling temperature250
6.37 COP against heat source temperature for 26°C cooling temperature251
6.38 COP against cooling temperature for 20°C heat sink temperature 252
6.39 COP against heat source temperature for 25°C heat sink temp. . 253
6.40 COP against heat source temperature for 30°C heat sink temp. . 254

6.41 Cooling COP for different Reynolds numbers 255
6.42 COP and cooling temperature against time 256
6.43 COP and heat source temperature against time 257
6.44 Heating COP and heat sink temperature against time 258
6.45 Heat pump COP and heat sink temperature against time 259
6.46 Comparison of all COP's 260
6.47 Emissions of CO_2 for cooling only and CCH 262
6.48 Emissions of CO for cooling only and CCH 263
6.49 Emissions of NO_x for cooling only and CCH 264
6.50 Emissions of C_6H_{14} for cooling only and CCH 265
6.51 Emissions of particulate matter for cooling only and CCH 266
6.52 Performance utilisation for cooling, heating and combined cooling and heating 268
6.53 Comparison of CO_2 emission for combined and single generation schemes 269
6.54 Comparative difference in energy utilisation 270

List of Tables

3.1 System connections dependent on status 92

4.1 Model output for different iterations and calculated value for the final iteration 108
4.2 Dimensions of the shell and tube heat exchanger 117
4.3 Geometrical data for the shell and tubes 117
4.4 Correlated and published data for density, specific heat capacity, thermal conductivity and viscosity 119
4.5 Fluid properties for the tube and shell side of the heat exchanger 119
4.6 Output from the heat exchanger evaluation model in comparison with calculated values 120
4.7 Stirling engine specifications 129
4.8 Input parameter/specifications used for the analytical model of the Stirling engine 133
4.9 Gas properties for the Stirling engine model 133
4.10 Geometrical parameters for the heater, regenerator and cooler . . 135
4.11 Temperature and error results for the different iterations 139
4.12 Output from the Schmidt analysis 142
4.13 Output from the third order analysis 143
4.14 Input parameter/specifications used for the analytical model of the TCA unit 159
4.15 Input data used for the analytical model of the TCA unit 160
4.16 Comparison of COP results 164
4.17 Input data for the performance evaluation model 165
4.18 Comparison between computed and calculated values 167

5.1 Carborobot Farmer F40 test series 191
5.2 Carborobot test parameters 192
5.3 γ-type Stirling engine test series 192
5.4 γ-type Stirling engine test parameters 193
5.5 Absorption performance test series for cooling only 194
5.6 Absorption cooling unit test parameters 195
5.7 Absorption performance test series for CCH 196
5.8 Absorption cooling unit test parameters for CCH 197
5.9 Data logging interface configuration and calibration 200
5.10 Technical specifications of K type thermocouple 204
5.11 Uncertainty of thermocouples used in the present study 205
5.12 Measurement Uncertainties 208
5.12 Measurement Uncertainties 209
5.12 Measurement Uncertainties 210

6.1 Type of fuels used in the test series 214

A.1 Chemical specifications of the substances used in this study 277
A.2 K_p equilibrium values of the substances used in this study 278

B.1 Carborobot boiler specifications 279
B.2 Generator specifications 280
B.3 Heat exchanger specifications 280
B.4 ClimateWell TCA absorption unit specifications 281
B.5 Mercury barometer specification 282
B.6 Manometer specifications 282
B.7 Magneto-dynamic oxygen analyser specifications 282
B.8 Gas analysers specifications for CO, CO_2, Hexane and NO_x . . . 283
B.9 Double pass particulate monitor specifications 283
B.10 Oxygen bomb calorimeter thermometer specifications 284
B.11 Relative random uncertainties for the flow meters 289

Foreword

Occasionally in life a passion develops that consumes one with intense excitement and clarity that almost all life's trials and tribulations descent into passing triviality. I have been blessed with three such passions; my family, my love for engineering and a desire to make a contribution to humanity and the environment, however small. In enabling the latter to prosper throughout the course of my MSc and PhD, I am most grateful to Prof Tarik Al-Shemmeri. I feel that his patience and understanding has gone far beyond the call of duty and has turned into a friendship.

My philosophy behind this study has been emphasized on renewable energy. That the supply of fossil fuels is finite, is now beyond contention. That there is damage to the environment from the use of such fuels is arguably in extent. Thus, whether the motivation is profit, convenience, necessity or of higher form, there is a common purpose; renewable and sustainable power must be developed and applied at a cost that guarantees its implementation. It is my firm believe that there is no right solution but merely a combination of solutions adopted in the best way possible to their respective application and use. Two parts of this solution, I believe to be, are energy efficiency and biomass.

The idea to investigate high efficient combined energy and heating systems for Luxembourg evolved from the idea to reduce fuel import dependency and energy shortage. Here, a combination of biomass combustion, Stirling engine and absorption cooling technology is used. A mathematical and computational model are developed to gather preliminary data and then compare the models to real-life systems.

It is my firm believe that occasionally research is difficult to be accepted and it is thus necessary to provide proof of its working principles to the general public and policy makers. Hence, this study should hopefully provide a deeper insight into the use of biomass as a renewable fuel for small scale combined heat and power systems for Luxembourg.

Sacha Oberweis

Acknowledgements

Firstly, I must thank Professor Tarik Al-Shemmeri for his support and advice as well as access to his wisdom and large database of amusing anecdotes. Also, to Professor Peter Ogrodnik for his understanding and support in particular during the draft stages of this thesis.

My thanks to my colleagues and students in the Faculty of Computing, Engineering and Technology for their camaraderie and support. Of particular note are Mr Ian Pinks for his invaluable help in setting up the test rig, Mr Haydn Richardson for his expertise in machining and tea breaks, Mr Abbas Daragheh for his support in F12, Mr Paul Bentley and Mr Dave Martin for their support in all electrical questions and problems.

Thanks also to my parents, sister and friends, who have offered advice, willing ears and distractions as well as motivational and financial support. I would particularly like to thank my girlfriend who, no doubt, wishes never again to hear the words 'biomass' or 'energy efficiency'. I fully understand the sentiment.

Advice from discussions with staff in other university departments, external research institutes and companies has been invaluable. Your assistance was most appreciated. The financial support by the FNR ('Fonds national de la recherche') from Luxembourg in the form of an AFR and several accompanying measures to cover the participation fee at conferences is gratefully acknowledged.

Finally, I would like to dedicate this work to my grandparents and the sacrifices, small and large, they had to endure for my right and freedom to live in a free world as well as my parents for being an inspiration.

I declare that this thesis has been completed by myself and that, expect where indicated to the contrary, the research documented is entirely my own.

Stafford, March 31, 2011
Sacha Oberweis

Nomenclature

Roman Symbols

A	area (m^2)
$\left(\frac{A}{F}\right)$	air to fuel ratio
cp	specific heat capacity at constant pressure (J/kgK^{-1})
cv	specific heat capacity at constant volume (J/kgK^{-1})
d	diameter (m)
d_H	hydraulic diameter (m)
E	energy (J)
E_K	kinetic energy (J)
E_P	potential energy (J)
f	frequency (Hz)
FC	fixed carbon $(wt\%)$
F_{LMTD}	LMTD correction factor
G	Gibb's free energy (J)
H	enthalpy (J)
h	heat transfer coefficient (W/m^2K^{-1})
${H_f}^0$	enthalpy of formation (J)
HHV	higher heating value (MJ/kg)
H_{sol}	heat of dissolution (kJ/kg)
H_{vap}	specific heat capacity of vaporisation (kJ/kg)

k	thermal conductivity (W/mK^{-1})
K_p	dissociation equilibrium constant
L	length (m)
LHV	lower heating value (MJ/kg)
m	mass (kg)
$\dot{m}$	mass flow (kg/s)
M	molar mass
MC	moisture content $(wt\%)$
n	number of moles
Nu	Nusselt number
P	pressure (Pa)
Pr	Prandtl number
P_x	perimeter (m)
Q	heat (J)
$\dot{Q}$	heat flow (W)
r	radius (m)
R	gas constant $(J/kgmol^{-1})$
Re	Reynold's number
R_f	fouling factor
S	entropy (J)
St	Stanton number
T	temperature (K)
U	overall heat transfer coefficient (W/m^2K^{-1})
UA	heat loss factor (kJ/hrK^{-1})
V	volume (m^3)
$\dot{V}$	volume flow rate (m^3/s)

$\bar{V}$	velocity (m/s)
VM	volatile matter $(wt\%)$
W	work (J)
$\dot{W}$	power (W)
$wt\%$	weight percentage $(\%)$
x	concentrations in TCA

Greek Symbols

β	phase advance angle (rad)
Δ	difference
δ	derivative / elemental
ΔT_m	logarithic mean tempeature difference (K)
ε	effectiveness / performance
η	efficiency
η_{cc}	combustion efficiency
θ	crank angle (deg)
μ	dynamic viscosity (kg/ms^{-1})
ρ	density (kg/m^3)
Σ	sum
ν	fraction of moles
Φ	equivalence ratio
ω	rotational speed (rad/s)

Subscripts

0	reference state
1	state 1
2	state 2
ac	air-conditioning

act	actual
air	air
amb	ambient
ar	as received
c	cold / compression
cb	condenser bottom tank
cf	condenser fluid
ch	charging
cs	cross-sectional
ct	condenser top tank
cx	condenser
d	dry
dis	discharging
e	expansion
el	electrical
f	fluid
$fill$	fill
$fuel$	fuel
g	gas
h	hot / heater
hs	heat sink
i	inner / inside
k	cooler
mc	monohydrate crystals
o	outer / outside
P	product

pr	primary
R	reactant
r	regenerator
rb	reactor bottom tank
rf	reactor film
rt	reactor top tank
rx	reactor
s	heat source
sg	single–generation
ss	salt solution
$stoi$	stoichiometric
th	thermal
ste	steam
tot	total
tri	tri-generation
vap	vapour
w	wall
ws	water solution

Other Symbols

D	dead
g	$g = 9.81 m/s^2$
π	$\pi = 3.1415$
S	swept
T_{suth}	Sutherland constant for gases

Acronyms

AEL	Energy Agency in Luxembourg

CCH combined cooling and heating

CFD computational fluid dynamics

CHP combined heat and power

COP coefficient of performance

$CRTE$ Resource Centre for Environmental Technologies

DHW domestic hot water

EU European Union

IEA International Energy Agency

LCA life-cycle assessment

NTU number of transfer units

RES renewable energy source

TCA thermo-chemical accumulator

UN United Nations

WHO World Health Organisation

Chapter 1

Introduction

1.1 Thesis Background

Global climate change is one of the most serious threats to the Earth and the greatest challenge facing human society in the twenty-first century. Rising temperature and changes in precipitation patterns are expected to be the result of an advanced greenhouse effect caused by excess atmospheric concentrations of carbon dioxide and other greenhouse gases. The enhancement has been caused by anthropogenic emissions since the industrial revolution and currently around one third of emissions are attributed to fossil-fuelled electricity generation. With the accelerating industrial and economic development of many countries, electricity demand is expected to increase rapidly. If this demand is covered using conventional fossil fuel technologies, the consequences for greenhouse gas levels may be significant.

The possibility of a global temperature rise of between 1° and 4.5° Celsius has led to considerable research effort into the effects of changes in temperature and other climatic variables. Studies suggest a wide range of detrimental impacts from rising sea levels, spread of vector borne diseases, increased storm activity and damage, and changes in availability of water (IEA, 2011). The potential for significant disruption and losses to human activities has prompted unprecedented levels of activity from international agencies in order to find solutions to and agreement on the carbon problems. The landmark agreements, the Kyoto protocol and the EU2020 targets committed most industrial nations to cuts on

their carbon emission levels and form the basis for reducing emissions by 2020 and beyond. The increased use of renewable energy sources and enhanced energy efficiency are two of the key options available to mitigate climate change. Biomass is one such resource that has been widely used for energy purposes since the existence of mankind, that would inevitably be influenced by any climate change. The increasing use of private capital in the energy industry has altered the focus from the provision of a service to the need to make profits from the production and sale of a commodity. Additionally, with respect to Luxembourg, the dependency on imported energy is an important risk factor.

1.2 Project Objectives and Scope

The project has several distinct objectives:

- To contribute towards the understanding of biomass as a renewable energy.
- To develop and verify computer models of the biomass combustion, Stirling engine and absorption cooling process.
- To use computational fluid dynamics as a design tool.
- To test the components modelled for various conditions.
- To demonstrate the increased performance of combined generation schemes over single generation.

The project is developed in three key stages, that look firstly at the current and potential Biomass market for energy purposes and its compliance to current national, European and world legislations and protocols; secondly, a computer model will be developed and verified to estimate the performance of the biomass combustion, power generation through a Stirling engine and absorption cooling technology; and thirdly, a performance evaluation of the components analysed and modified with the computer model will be carried out. The investigation of the current and potential biomass market will be conducted through a vigorous literature review into the key elements of the topic: biomass combustion, power generation, absorption, and combined generation schemes. The conclusion of

this literature review will be used to propose and develop a computer model and computational fluid dynamics model of the system. The final design will then be tested under various conditions in the laboratory. The knowledge obtained from the analytical models as well as computational fluid dynamics will contribute towards the testing of the final design. An accordance between all three sets of results will then validate the models developed. These models can then be used in future work as models to get preliminary results without extensive testing.

1.3 Thesis and Contribution to Knowledge

Overall the aim for this project is:

> *To develop and test a suitable small-scale biomass unit adopted to the Luxembourgish market*

While considerable attention has been paid to biomass as a renewable fuel, there is no corresponding investigation of biomass fuelled small scale combined application specifically for Luxembourg. Additionally, absorption cooling driven by biomass is not well understood and this thesis goes some way towards addressing that. The continuous combustion of small scale biomass application is not efficient at all (Welfring & Weidenhaupt, 2003), but this project aims to prove the contrary by implementing a suitable combined system to improve the overall efficiency. It is anticipated that the technologies and analysis presented here will be understood and welcomed by those involved in climate change research, in energy policy making, investors, engineers and others involved in the biomass design and operation of combined generation of biomass applications.

The scientific interest of the project and its importance are based on preliminary findings of a literature review. The proposed biomass unit will contribute towards R&D work in the area of renewable energy, increase in efficient energy systems and reduction in global GHG emissions. Of particular interest to Luxembourg, a more efficient utilisation of its wood resources as a fuel can contribute towards the reduction of energy dependency, highly criticised by the International Energy Agency (IEA, 2011). The following is a list of papers and a book that have been published or are currently under review based on the work presented in this

thesis. Next to the overall BFR/AFR grant scheme awarded by the FNR, several accompanying measures were awarded towards the expenses occured during the conference participations in France and Spain.

- Book
  - Oberweis, S. and Al-Shemmeri, T.T. 2009. Design of a 20kW Biomass Heat Generator: CFD Modelling and Dissociation. *VDM Verlag*. ISBN 978-3639159226
- Conferences
  - Oberweis, S., Al-Shemmeri, T.T. and Packer, N. 2007. The Impact of Dissociation on the Flame Temperature in Biomass Combustion. *Proceedings of the Heat-SET conference*. 18-20 April 2007. Chambéry, France. funded through the Accompanying Measures of the FNR (Luxembourgish Research Council)
  - Oberweis, S. and Al-Shemmeri, T.T. 2010. Effect of Biodiesel Blending on Emissions and Efficiency in a Stationary Diesel Engine. *Proceedings of ICREPQ'10 conference*. ISSN 2172-038X. 23-25 March 2010. Granda (E). funded through the Accompanying Measures of the FNR (Luxembourgish Research Council)
  - Oberweis, S. 2010. The Potential of Electricity, Heat and Refrigeration from Biomass. *Woody-Biomass Symposium in Luxembourg "Privatbësch Besetzer"*. 17^{th} November 2010
  - Oberweis, S. and Al-Shemmeri, T.T. 2011. γ-Stirling engine – The effect of different working gases and pressures. *Proceedings of ICREPQ'11 conference*. ISSN 2172-038X. 13-15 April 2011. Las Palmas (Gran Canaria, E). *full paper accepted for presentation*. funded through the Accompanying Measures of the FNR (Luxembourgish Research Council)
- Journal papers

- Al-Shemmeri, T.T.and Oberweis, S. 2011. Correlation of NO_x Emissions with Flame Temperature in Biodiesel Combustion. *Applied Thermal Engineering*, *in press*
- Oberweis, S. and Al-Shemmeri, T.T. 2011 Emissions and performance of a stationary diesel engine run on Biodiesel blends. *International Journal of Oil, Gas and Coal Technology*, *in press*
- Oberweis, S. and Al-Shemmeri, T.T. 2011 Design considerations of a a γ-type Stirling Engine. *Proceedings of the IMechE Journal A: Power and Energy*, *under review*
- Oberweis, S. and Al-Shemmeri, T.T. 2011 Performance Evaluation of a Lithium-Chloride Absorption Refrigeration Unit Driven by a Biomass Heat Source. *Proceedings of the IMechE Journal A: Power and Energy*, *under review*

1.4 Thesis Outline

The thesis consists of seven chapters, together with their relevant appendices. Chapter two introduces the combustion of biomass, Stirling engine technology and absorption cooling and their advantages and deficiencies by means of a literature review to highlight current and past research to lay a basic forming knowledge for the work in this thesis.

Chapter three presents the theory involved with the technology encountered in this thesis. A mathematical model is presented here to estimate the products from biomass combustion, simulate the performance of a γ-type Stirling engine, as well as the simulation of a thermo-chemical accumulator absorption cooling unit.

Chapter four includes a mathematical verification of the models developed in chapter three by fastidious hand calculations. Additionally, the computational fluid dynamics model results are shown with verification for heat transfer and fluid flow simulations. These results provide a good insight into the results to be expected from the actual testing.

Chapter five introduces the test procedure and methods as well as all the relevant equipment used for the data acquisition. Calibration of the data recording equipment and a detailed uncertainty analysis is carried out to reduce potential errors in the results. Test plans are presented to show how the data is gathered.

Chapter six presents and discusses the results gathered in the laboratory testing and their comparison with the simulation results obtained from the models developed in chapter three. The major results presented are the variation of performance between single and combined generation modes as well as the impact of emissions for the different systems.

Finally, chapter seven will present general conclusions drawn from the work presented and some suggestions for further work in this area of renewable energies.

Chapter 2

Biomass Tri-generation Technology

This chapter presents a historical overview of Biomass to energy related technologies as well as a state of the art review of the different technologies encountered in the course of this thesis. Additionally a focus on the energy situation in Luxembourg as well as the future outlook for the Luxembourgish energy sector in respect to current legislations is presented.

2.1 Biomass as a Renewable Energy Source

2.1.1 World Energy Consumption

Since the early stages of human evolution, energy played an important role. Over the years this importance grew bigger and bigger as humans evolved and the civilisations started to appear. In the early stages of their existence, energy however was only used for cooking and heating by means of open fires. Biomass is the first known source of energy used by humans for cooking and keeping warm. The continued increase in population and the associated expansion in industry and the discovery of coal allowed the industrial revolution to emerge in the United Kingdom in the later part of the 18^{th} century. The first known uses of coal date back to 1000 BC in China, and it was only brought to Europe by Marco Polo in 1275 AD. The first time coal was extracted from underground and used was in

parts of Europe now known as the Netherlands in the 1600's. The importance of coal is still today extensive in the energy production sector, whereas petrol has become the predominant energy medium in the transport sector. In 1769, James Watt patents his first improved steam engine, which is still regarded as one of the most important breakthroughs of the industrial revolution. However, it took almost 100 years until Charles A. Parsons builds the first modern steam turbine in 1884. The vast increase in energy consumption to generate the necessary steam, resulted in coal replacing wood as the main energy supply in 1890. Reciprocating steam engines powered the first electric generators in the 1880's. Because these plants were inefficient, a large amount of waste steam was available for process use or building heat. Early electrical developers provided electricity to customers and sent the waste heat through steam pipes for space heating. This concept of Combined Heat and Power was first implemented in 1884 to provide energy for the Del Coronado Hotel in San Diego, USA (Cleveland, 2009).

The advances of technology and the economic boom since WWII (apart from a few recessions), have led to our modern civilised world that is highly dependent on energy consumption. Ranging from air-conditioning to Z10 (BMW), there is a constant influx of new energy intensive devices aiming to facilitate or enhance our lifestyle. Unfortunately, the reserves of fossil fuels are limited due to the fact that they are consumed faster than nature can reproduce them. The fossil fuels being used today were produced between 50 million and 350 million years ago. Obviously, the reserves are not long-lasting and estimates are that they will probably run out by the end of the century. Figure 2.1 shows the evolution of the world's energy consumption of fossil fuels from 1800 to present (IEA, 2011). The projections to 2030 are estimates published by the Internal Energy Agency based on current consumption data and world population growth. The dotted projections are estimates based on the '450 scenario'. This scenario is based on the required reduction of CO_2 to prevent a global temperature rise of $2°C$. As can be seen, there is a drastic reduction of fossil fuel consumption required in the coming years. Additionally the graph clearly shows the exponential rise of the consumption in the last 50 years (IEA, 2009). From 1997 until 2007 the consumption of oil alone has risen by as much as 15% (IEA & OECD, 2008). This will cause major political problems to the world in the fight for the remaining reserves. Inventions

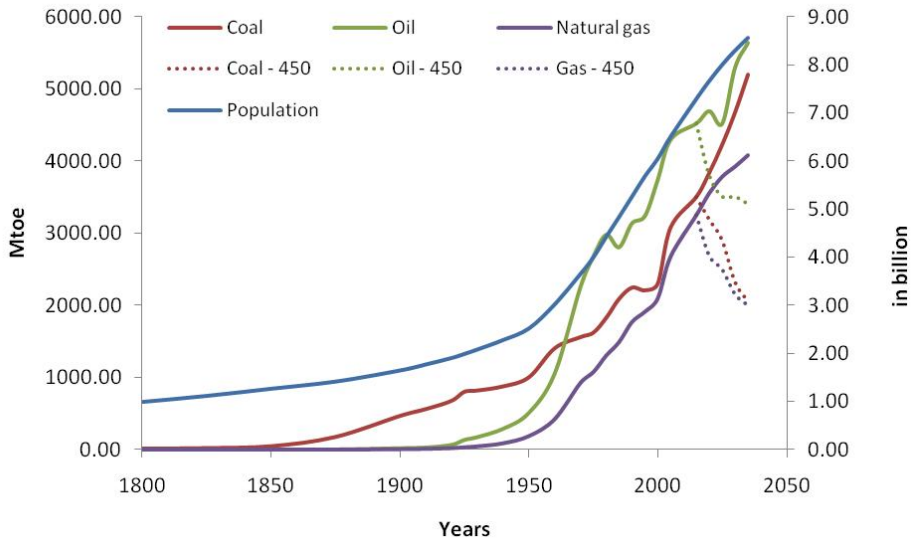

Figure 2.1: World fossil fuel consumption from 1800 to 2050 (raw data published by IEA)

and the massive use of oil and coal to gain energy, however, have bad influences on nature. During the combustion process of fossil fuels harmful emissions and particulates are released to the atmosphere. They undoubtedly cause short and long term harm to nature and mankind, e.g. cancer and ozone layer damage due to the Greenhouse effect (Geelen *et al.*, 2009). Fossil fuels accounted for 85% of worlds primary energy supply and over 94% of energy for transportation. The production of use of fossil fuels contributes to 80% of anthropogenic GHG emissions worldwide and fossil fuel power generation currently accounts for over one third of global annual carbon dioxide emissions (Quadrelli & Petersen, 2007). In 2006, the EU had reached a 7% share (of gross inland consumption) and the latest progress report indicates that the EU is unlikely to reach either the electricity or transport target for 2010. More recently, the Community has agreed targets for 2020. The 2005 share (measured in terms of gross final energy consumption) was 8.5% (9.2% in 2006), and the EU2020 target is 20%, as shown on Fig. 2.2 for all EU27 countries. Although the EU2020 targets have outlined the reduction of energy use by increasing energy efficiency, energy efficient strategies have been on the rise for several years. In December 2009, the climate conference took place

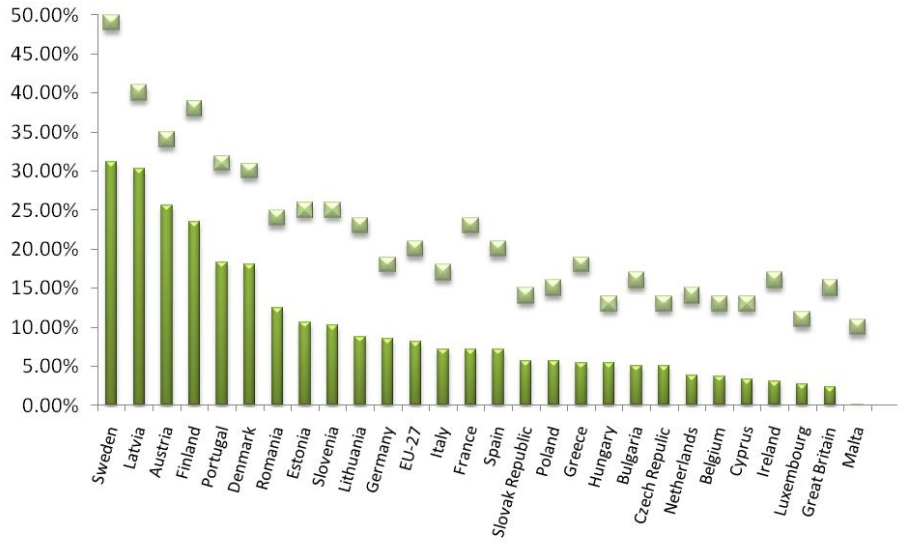

Figure 2.2: EU2020 targets for renewable percentage of total primary energy consumption (current and target)

in Copenhagen, Denmark. The signing countries have agreed to a twelve point accord that can be summarised as follows (UN, 2009a):

- The challenge imposed by climate change and a strong political will to urgently combat climate change.
- Agreement that global emission cuts are required with a view to reduce them so as to hold the increase in global temperature below $2°C$.
- Developed countries shall provide adequate, predictable and sustainable financial resources, technology to support developing countries.
- Kyoto signing countries agree to implement quantified economy-wide emission targets for 2020.
- Non-Kyoto signing countries will implement mitigation actions in the context of sustainable development.
- Reducing emissions from deforestation and forest degradation and the need to enhance removals of greenhouse gas emission by forests.

- Pursue opportunities and other approaches to use markets to enhance cost-effective mitigation actions.
- Additional and predictable funding to developing countries to enhance the action resulting from this accord.
- A panel to study the contribution of the potential source of revenue towards the above goal.
- The Copenhagen Green Climate Fund shall be established as an operating entity of the financial mechanism of the Convention to support projects, etc.
- A technology mechanism to accelerate technology development and transfer in support of action on adaption and mitigation.
- An assessment of the implementation of this accord by 2015.

2.1.2 Energy Situation, Present and Future Outlook for Luxembourg

Luxembourg is situated in the heart of the European Union, sharing borders with Belgium, France and Germany. With 2586 km^2, Luxembourg is one of the smallest countries of the EU and has a population close to half a million. In terms of landscapes, the country is divided into two distinct regions. Luxembourg is divided into 3 districts (Luxembourg, Diekirch and Grevenmacher), 12 "cantons", approximately 120 local communities and 4 electoral territories. The economic performance from 1950 to 1970 seemed to be related to the economic structure at the time, which was dominated by the iron and the steel industry until the first oil crisis and the simultaneous world crisis in the market for steel. This led to the implementation of an eminently successful industrial diversification policy from the end of the 1950's. As a matter of fact, the early 1970's was the first period during which the average growth of the Luxembourg economy exceeded that of neighbouring countries. Since the end of the 1970's, on the other hand, the rapid development of financial services began to stimulate the growth in

Luxembourg. The economic cycle in Luxembourg tends to mirror what happens in other European countries. However, the extent of variations in GDP is more marked, which is characteristic of a small-scale economy that is very open to the exterior and, therefore, more vulnerable to external crises. Consideration of GDP aggregates makes it easier to understand the reasons underlying the exceptional growth of GDP in Luxembourg from the early 1980's (Anon., 2011c).

Luxembourg is a unique country with respect to energy in Europe. It is completely landlocked, it has few indigenous energy resources, and it is almost entirely dependent on imports of both fossil fuels and electricity to meet its energy needs. Luxembourg is one of the smallest member states of the European Union and is hugely dependent on imported power, 92% of the electricity is produced in Belgium and Germany. Domestic energy production in Luxembourg accounted for approximately 2% of total energy supplies in 2007. Currently oil, which is 100% imported, is the largest source of primary energy in Luxembourg, representing nearly 64% of primary energy consumption. Gas, which supplies 18% of primary energy demands, is also 100% imported. In respects to total primary energy supply per capita, Luxembourg lies ahead in the European Union with more than double the amount than the average. This is largely due to the consumption of transport fuel by its neighbouring countries supplied in Luxembourg due to severe differences in tax compared to France, Belgium and Germany. Although this contributes negatively to the energy balance and has a bad impact on the CO_2 emissions, the tax gained plays a major role in the receipts of the government's budget. Renewable energy contributed 2% of Luxembourg's total energy supply in 2007 compared to EU averages of 8%. The share of TPES from renewable energy sources has remained more or less static for the last 10 years. Wood and waste, mainly used for electricity generation, provide the vast majority of Luxembourg's renewable energy supply, although small amounts of solar heat are also used. In addition, small-scale hydropower generated 60 GWh in 1996 (12% of domestic electricity generation). In 1996, municipal waste accounted for 46% of total renewable TPES and hydropower to 13%, providing 55% and 13% of renewable electricity generation respectively. Using renewable energy sources contributes to diversification and thus helps to increase security of energy supply. The share of renewable energy sources in gross inland energy consumption is very

small. Renewable energy sources account for about 16% of gross electricity production. In particular in the area of biomass, small amounts (15 $ktoe$) of wood are reported as being used in the residential sector, and 1 GWh was also generated in 2005 from biogas. Biomass is the second most important renewable source with a share of 5% of total gross electricity production. Wood and municipal wastes are the most important biomass resources in Luxembourg. Small amounts of wood are used in the residential sector to provide heating and power and primary heat production from wood (wastes) amounted to 744 GWh. Wastes, including animal products and gases from biomass, are important for the production of both electricity and heat.

In 1985, the Vienna convention was signed for the protection of the ozone layer which made initial arrangements for the Montreal Protocol, signed in 1989 on substances that deplete the ozone layer (UN, 2009b). In 1999, Luxembourg signed a protocol to abate acidification, eutrophication and ground-level ozone in Gothenburg (UN, 1999). This protocol was ratified in 2001. The protocol sets emission ceilings for 2010 for four pollutants: sulphur, NO_x, VOC's and ammonia. These ceilings were negotiated on the basis of scientific assessments of pollution effects and abatement options. Parties whose emissions have a more severe environmental or health impact and whose emissions are relatively cheap to reduce will have to make the biggest cuts. Once the Protocol is fully implemented, Europe's sulphur emissions should be cut by at least 63%, its NO_x emissions by 41%, its VOC emissions by 40% and its ammonia emissions by 17% compared to 1990. The protocol also sets tight limit values for specific emission sources (e.g. combustion plants, electricity production, dry cleaning, cars and lorries) and requires best available techniques to be used to keep emissions down. Hence, the emissions of sulphur and NO_x from biomass combustion need to be investigated, in order to adapt the design concept to meet the targets set in this protocol. In 1997 the Kyoto agreement was signed to reduce emissions of greenhouse gases by 5.2% compared to the year 1990. Its goal is to lower overall emissions of six greenhouse gases - carbon dioxide, methane, nitrous oxide, sulphur hexafluoride, hydrofluorocarbons, and perfluorocarbons, averaged over 2008 to 2012 (UN, 2008). Currently there are different laws and regulations to be considered regarding biomass as an energy resource in Luxembourg. The law

from the 14^{th} October 2005 shows the changes to the old law, governing cogeneration in general, to account for the impacts of renewable energies in cogeneration in Luxembourg (Mémorial, 2005). The law from 20^{th} April 2009 governs the subsidiaries for users and producers regarding the efficient energy consumption and generation of electricity from renewable energy sources (Mémorial, 2009). Other subsidiaries can be obtained from local councils, subject to availability. A study by the AEL and the CRTE determined that between 2.5% and 4.2% of the energy required for heating in Luxembourg can be based on biomass. Furthermore, they propose to initialise a Center for Wood energy (Holzenergiezentrum) which should govern the demand and the availability of biomass, assure its quality (e.g. DIN 51731), guarantee the selling price for biomass and hence promote the market of biomass in Luxembourg (Welfring & Weidenhaupt, 2003). In 2006, the department of environment published the national plan of proposed actions regarding the reduction of CO_2 emissions. Concerning the potential in the domain of renewable energies, the report proposes the following main actions to be taken: increase the percentage of renewable energies in the electricity generation; blending of the natural gas with biogas; the increased installations of cogeneration units to increase energy efficiency; an increased use of biomass/biogas and promoting the research in these areas to increase their efficiencies (Emwelt.lu, 2006). In 2007, the department of environment and the department of economy and commerce published a study carried out by the Fraunhofer institute about the potential and the development of strategies for an increased utilisation of renewable energies in Luxembourg. The very extensive report regroups the current status quo and historical development of the different renewable energies used in Luxembourg; the current policies and laws in place; the theoretical, the technical and practical potential for renewable energies in Luxembourg. In the domain of short rotation coppice this is a practical potential of 71 GWh by 2010 and 284 GWh by 2020. This is based on 5% and 20% of the total available surface for SRC for 2010 and 2020 respectively (Emwelt.lu, 2007). Similar results are published by the EEA and OPOCE in an article about the European guidelines regarding Biomass. Next to 69 $Mtoe$ currently used biomass they claim that another 189 $Mtoe$ can be added until 2010 and another 239 $Mtoe$ until 2020.

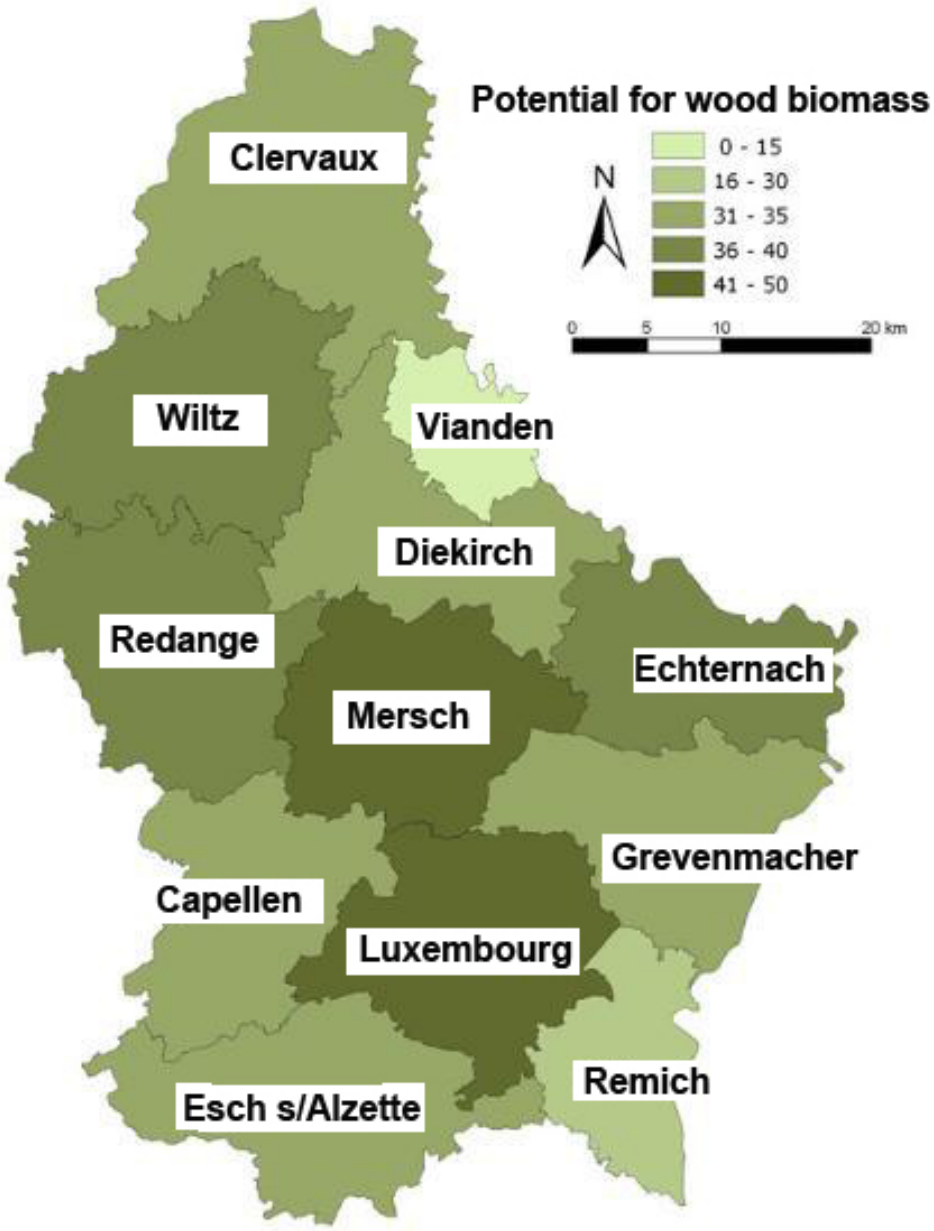

Figure 2.3: The potential of wood based biomass in Luxembourg

This is especially important in the domain of electricity generation (Wiesenthal & Mourelatou, 2006).

The International Energy Agency gives recommendations about Luxembourg's energy situation in their review in 2004 (IEA & OECD, 2004). These recommendations include reducing GHG emissions in a cost effective manner. Furthermore, they consider cost-effective ways of supporting highly efficient cogeneration, and assess renewable energy policies in the broader portfolio of energy policy. In 2009, the IEA published a new review of the energy situation in Luxembourg. Their major critic is aimed at the huge energy dependency on imported fossil fuels and the high subsidies for high cost renewable energy systems. They propose the investment in cost-effective EU-wide solutions, reducing the high risk of fossil fuel dependency, increase energy efficiency, and explore all possibilities to develop domestic RES for the 2020 targets. In the study by the AEL and CRTE, several recommendations were given regarding the wood as an energy resource in Luxembourg. Amongst them are a more efficient utilisation of wood as an energy source, public awareness and training of involved organisations, introduction of an efficient wood and wood-waste inventory program and quality control, and an increased efficiency of wood conversion into energy. Only recently has the European council decided to commit itself to increasing the percentage of renewable energies of the total primary energy consumption to 20% by 2020 inside the EU. For Luxembourg, this amounts to 13% of its total primary energy supply. In 2008, the end report of the RUBIN project, an INTERREG III(A) project, presented several maps showing the potential for biomass in Luxembourg. Figure 2.3 shows the potential for wood based biomass, whereas Fig. 2.4 shows the potential for straw. Additionally, the Rubin project identified the potential of economic and ecologic influence on the region investigated. The estimates presented for the potential of biomass account for the requirements of food and other limitations imposed by nature protection laws, etc. (RUBIN, 2008).

2.2 Biomass Conversion Processes

Biomass is an organic/plant based biofuel. The fact that biomass can be planted, grown, harvested and used as a fuel in a relatively short time span from 2–3

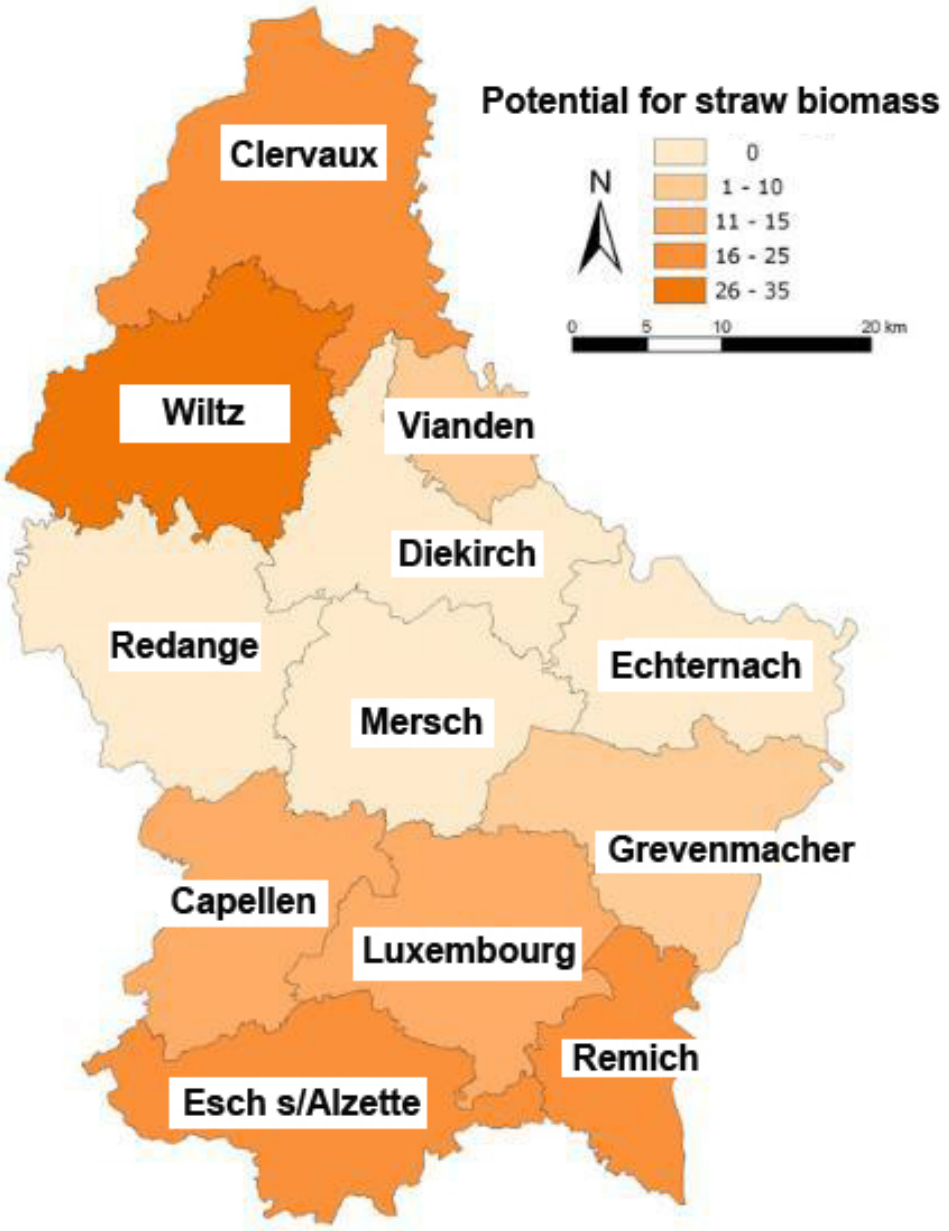

Figure 2.4: The potential of straw based biomass in Luxembourg, (RUBIN, 2008)

years up to 25 years, in comparison to fossil fuels, makes biomass a renewable option as a fuel. Also, the carbon released during the combustion of the biomass will be absorbed again during the growing period of the plant material through photosynthesis. This makes biomass a carbon neutral fuel, although an extensive life-cycle analysis (LCA) is required to determine the degree of carbon neutrality of the fuel. The classification and standards regulating the terminology and test methods regarding solid biofuels from the ISO standard is used in this study. The majority of these standards are currently still in draft form in particular DD CEN/TS 15357:2006 regulating the terminology, definitions and descriptions of solid recovered biofuels. Often biofuels are classified as primary and secondary biofuels. Whereas primary biofuels includes firewood, wood chips, pellets, animal wastes, forest and crop residues and landfill gas, secondary biofuels are usually subdivided into 1^{st}, 2^{nd} and 3^{rd} generation fuels as follows (Nigam & Singh, 2010):

- 1^{st} generation: Bioethanol through fermentation of starch or sugars; and biodiesel through transesterification of plant oils.
- 2^{nd} generation: Bioethanol through enzymatic hydrolysis; biodiesel through thermo-chemical processes; and biomethane through anaerobic digestion.
- 3^{rd} generation: biodiesel from algae; bioethanol from algae and sea weeds; and hydrogen from green algae and microbes.

Virgin wood consists of wood and other products which have not been subjected to chemical treatments (e.g. paint). Most of the harvested virgin wood is used in the paper or timber processing industry. The non usable parts e.g. distorted wood, branches and stumps can be used for energy purposes. Virgin wood often requires pre-processing in the forest (e.g. cutting to length) prior to transportation to a processing plant as well as sorting and cleaning to get rid of mud, stones, ice, etc (Anon., 2011d). Energy crops denote all biomass that is grown for energy purposes only. Although some governments provide subsidies for growing energy crops, this is not the case in all countries. Among energy crops are willow and poplar (woody biomass), as well as straw and Miscanthus (grasses), aquatics, and oil and starch based crops to produce Biomethanol and Bioethanol (Biomass, 2011). The latter have been extensively grown in Brazil and the US. The choice

of the crop is usually influenced by the type of biofuels desired, e.g. liquid, solid, as well as the soil properties and the adaption of the crop to the climate where it is grown (Goor *et al.*, 2000). Agricultural residue varies widely and often requires very diverse energy conversion processes. They vary from dry (straw) to wet (animal slurry). Straw can be regarded either as a waste or an energy crop depending on whether it is grown for energy purposes only, or if the leftovers are used in the biofuels production. Often these types can be used in numerous other markets, and decisions whether to use them for energy or alternative purposes need to be assessed carefully. There are residues and waste at all points in the food supply chain. Industrial waste and co-products can be divided into woody and non-woody materials and are often converted into energy on site to comply with energy reduction regulations imposed on industry. Energy from waste is the process of burning waste to generate energy. Waste can be obtained from the food processing industry, domestic green waste or industrial co-products (DEFRA, 2011b).

2.2.1 Indirect Conversion Processes

The production of Biofuels is sometimes referred to as indirect conversion processes as opposed to direct conversion process. There are three major indirect conversion processes, namely physical, thermal and biochemical. Quite often harvested, forest derived biomass tends to be of various lengths and size, as well as bulk density. Bulk density is not an intrinsic property of a material; it can change depending on how the material is handled (ISO, 2009b). Physical pre-processing can consist of cutting, chipping, grinding or shredding as well as moisture content reduction. Obviously, entire trees cannot be burnt in conventional domestic wood stoves, nor stored in a cellar. Hence, size reduction techniques are used to produce standard log sizes, pellets, briquettes or wood chips. In order to estimate the size of fuel storage, the number of deliveries and total annual fuel consumption; the energy density of a particular fuel is often used. This density is obtained by multiplying the calorific value of a particular fuel by its bulk density. Since the bulk density, unlike volumetric density, is intrinsic to a material, the same type of biomass can have different energy densities depending on whether it is being

used as pellets or logs for example (CarbonTrust, 2011). As the bulk density is often changed during conversion processes, the energy density is changed as well. This inclines that the same volume (m^3) of logs has a lower energy content than the same volume of pellets (Vinterbäck, 2004). Also, to facilitate transport and commercialisation these processes are often used during, or on site, where the harvesting of the biomass feedstock takes place.

Typically size reduction is applied by grinding, cutting or impact mechanisms. For pellet production, in some countries, sizes, as well as quality, are regulated by standards and have an impact on the potential of added drying time. In the European Union, initially only Austria (ÖNorm M7135), Sweden (SS187120) and Germany (DIN plus 51731) have a set standard (Fiedler, 2004). Since 2005, the TC335 technical committee has published a series of European technical standards amongst which is the EN14961:2010 (ISO, 2010) outlining the fuel specifications and classes for solid biofuels. The most common mechanism is wood chipping. Although it is an energy intensive process, there are several operational improvements to the life cycle of the biomass, namely bulk density, handling, preparation for drying and transportation costs. The original use of pellets was livestock feed or compressed grasses. Forestry residues and sawdust leftovers, otherwise lost, can be pelletised for simplified storage and transport. The increased bulk and hence energy density and facilitation of fuel feed increases efficiencies of the biomass system. General hardware used are presses of various types, e.g. impact, extrusion, hydraulic and briquetting.

Dewatering refers to the removal of all or part of the contained moisture from the biomass as a liquid (Mursito *et al.*, 2010). The difference to drying processes is that here the moisture is removed as a vapour. Open air solar or wind drying is often used in case of a too moist biomass prior to the energy conversion process. A good example is the recommended storage of log wood for a period of one year in a dry cool place prior to combustion in a wood stove. This prevents a smoky combustion and increases the combustion efficiency as less energy is required to burn off excess water content. The current DIN 51731 (ISO, 2009a) regulation limits the moisture content for pellets to less than 10 wt%, whereas the European standard sets limits to either 10, 15 or 20 wt% for M10, M15 or M20 designated pellets respectively.

For most types of biomass it is important to weigh off cost versus efficiency improvement as sometimes the moisture content cannot be reduced significantly without major cost involvement as well as energy input (Stahl *et al.*, 2004). Domestic and agricultural bio-waste and aquatic type biomass often have moisture contents in the region of 80 wt% and above. As flame temperature and combustion efficiency are directly dependent on moisture content, wet biomass needs to undergo this process prior to direct conversion processes. The method of dewatering or drying biomass should be as energy efficient as possible and should not have a major impact on the total efficiency of the cycle (Wahlund *et al.*, 2002). Obviously an additional use of energy to dry the biomass reduces the effective energy output of the total conversion process. Most commonly, centrifuges, hydro-cyclones, expressions presses, thickening or flotation hardware is used for dewatering biomass. Solar drying or wind methods have been in place for hundreds of years and are still used today. The final moisture content of air-dried biomass is usually around 35 wt% less. The biggest advantage is the low cost, whereas the process can be rather lengthy (up to a year) and space consuming as adequate stocking is required to allow for venting and to prevent fouling. Whenever it is necessary to reduce the moisture content from any type of biomass feedstock, air drying, mechanical dewatering, and drying with waste heat or stack gases should be considered first as these process have the least or even no impact on the overall efficiency of the biomass life cycle.

Biomass gasification processes are generally designed to produce low to medium energy fuel gases, synthesis gases for the manufacture of chemicals, or hydrogen. The chemistry of biomass gasification is very similar to that of coal gasification. This allows for an easy substitution or blending of biomass with coal systems. This similarity of the two fuels is, however, limited to the gases they generate during combustion. Biomass is much more reactive, as it contains more volatile matter (70% to 90%) than coal (30% to 45%) and hence gasification occurs under much less severe operating conditions. Adding steam or oxygen as co-reactants to the biomass can result in large changes in reaction rates and yields. Different factors can be used to classify the design, e.g. heat transfer (internal or external), reactant contact (fixed or fluidised bed), reactant flow (co- or counter-current), gasyfying medium (steam with oxygen, air with oxygen, hydrogen with oxygen),

or by the way of removing residue (dry ash or slagging). Over the years several process variations have been identified; pyrolytic gasification, partial oxidation, steam gasification, gasification in liquid water, and hydro-gasification. Biomass gasifiers can be categorized in three major categories, i.e. up-draft (counter-current) fixed bed; down-draft (co-current) fixed bed; and circulating fluidised bed systems, though other designs are also available. One of the more innovative pyrolytic gasification processes is an indirectly heated, fluid bed system. In two fluid bed reactors, using sand as a heat transfer medium, the combustion of char formed takes place with air within the combustion reactor. The heat released is sufficient for the pyrolysis of the combustible fraction in the pyrolysis reactor. Keeping the two reactors separated keeps the nitrogen away from the pyrolysis gas. Hence the yield gas is of high quality and can be upgraded to a high-energy gas to substitute natural gas. Projected gas yields are about 670 m^3 of pyrolysis gas or about 200 m^3 of methane per dry ton of feed (Murakami *et al.*, 2007).

All thermal conversion processes, using less than stoechiometric amount of oxygen needed for complete combustion can be considered partial oxidation. If the oxygen is supplied by air then low energy gases are formed compared to high energy gases, where pure oxygen, or oxygen enriched air is used. Quite often multi zone combustion chambers are used to maximise the yields. In vertical shafts the feed is introduced at the bottom allowing it to dry in a first zone with the ascending hot gases. The dried feed descends to the actual pyrolysis zone with the gases ascending and the ash and char descending further into the lowest zone in the shaft. Steam gasification involves two stages (Anthal, 1978). Volatile compounds are formed at temperatures in the range of $300°C$ – $500°C$. Above $600°C$ gases are formed (Higman & van der Burgt, 2003). Waste gasification has gained popularity over the years as an alternative to incineration. This gives the possibility of using gas turbines for power generation instead of the steam cycle used in current incineration plants. Biomass gasification is being used to improve the efficiency and to reduce the investment costs of biomass electricity generation through the use of gas turbine technology. They can be as economical as conventional coal fired plants (Badin & Kirschner, 1998). In another gasification process, water is kept in the liquid phase at elevated temperature (above $374°C$) and hydrostatic pressure. Increasing the temperature even further, an

increase in H_2 concentration can be observed. The medium energy product gas is produced directly in contrast to medium energy gas-phase processes, that require either oxygen in place of air; or the dual reactor system to keep the nitrogen in air separated from the product. Methane can be produced by adding hydrogen to the gasification process. One method involves methanisation of the carbon monoxide with hydrogen. Another features a direct reaction of the feed with hydrogen. The feedstock is converted with hydrogen containing relatively high methane concentrations in the first stage reactor. This char is gasified in a second reactor to generate hydrogen-rich synthesis gas for the first stage (Misirlioglu *et al.*, 2007). Kruse (2009) reviews the challenges and technical solutions required before large-scale production facilities for hydrothermal biomass gasification can be built. Depending on the reaction processes it is possible to produce either methane or hydrogen. The author identified the size of the plant to be one of the most important questions. Different processes should be regarded depending on what plant size is required. The higher the process temperature is, the larger the plant should be. This is due to the fact that the relative energy loss expected increases with temperature, but decreases with volume.

Pyrolysis is the thermal decomposition of biomass in the absence of oxygen. During pyrolysis several chemical processes take place, notably dehydration, cracking, coking and aromatisation, producing water, carbon oxides, other gases, charcoal, organic compounds, tars and polymers (ETSU, 1976). Many products are being formed during any type of pyrolysis, fast (Wiggers *et al.*, 2009) or conventional slow (Ratte *et al.*, 2009), but there are often additional separation techniques required to obtain the final desired products. There are different forms of fast pyrolysis. Ablative fast pyrolysis rapidly converts larger sized biomass particles on the heated wall of a vortex reactor tube. During rapid thermal processing, wood particles are rapidly pyrolysed during a residence of only 400 – 500 milliseconds (Ratte, 2003). The biomass feedstock is mixed with a solid heat transfer agent to achieve the required fast heating rates (Karle & Shaligram, 2009). In vacuum pyrolysis wood chips are processed under vacuum in a multiple hearth reactor. Condensation of individual streams from the hearth allows primary separation of the liquid products. Although slow by nature, this process is considered a fast pyrolysis process, since the system is operated under

vacuum and the vapours are extracted as soon as they are released (Kaltschmitt & Bridgwater, 1997). Probably the greatest attribute for pyrolysis is the multitude of possible products, depending on the conditions involved. The majority of woody-type biomass is celluloses and the two major accepted pathways occurring during the pyrolysis of celluloses are dehydration (char, tar, CO_2, CO, H_2O) and depolymerisation (char and combustible volatiles). There are four basic types of biomass pyrolysis and all of them involve formation of large amounts of water vapour (Shen & Gu, 2009). The process of pyrolysis can be endothermic or exothermic depending on the temperature of the products. Usually below $400°C$, the reaction is endothermic, requiring heat input to take place. Above $400°C$ there is enough energy present for the pyrolysis to sustain itself and hence not requiring much additional heat input.

Partial oxidation process is the pyrolysis of biomass with an oxygen lean air mixture. This leaves the products of combustion only partially oxidised. This form of gasification was well used in WWII, particularly in Sweden, to power automobiles, trucks and buses with little modifications to the engine required. During partial oxidation, low energy gases are formed that contain higher concentrations of hydrogen, carbon monoxide and carbon dioxide than medium energy gases. Fisher *et al.* (1976) proposed a system of a three stage vertical shaft furnace. Shredded feedstock is inserted into the furnace from the top. In the first zone, the feed is dried by the rising hot gases. In zone two, pyrolysis takes place as described above. In the third zone the remaining char is then partially oxidised. Although reforming was initially used in petroleum conversion processes, it can be used for biomass too (Wang *et al.*, 2009). Retort furnaces allow for the production of char on a commercial scale in industrialised countries. Compared to more primitive systems (e.g. kilns) they recover by-products during the carbonisation process. Various configurations of retort furnaces are available (Soltes *et al.*, 1981):

- Stafford and Seaman batch process
- Badger-Stafford process is a continuous version of the Stafford and Seaman process

- Reichert process is a continuous process
- Lambiotte process is a 3-stage continuous process

Modern installations recover all the by-products, ultimately becoming a bio-refinery.

2.2.2 Direct Conversion Processes

There are a number of technologies available to make use of a wide variety of biomass types as renewable energy resources. Whereas in indirect conversion processes the feedstock is converted into a usable fuel, in direct conversion processes either the raw feedstock or the pre-processed biofuels can be used to release the stored energy. While for some types of biomass there may be a number of usage options, for others there may be only one appropriate technology. Generally, three different direct conversion technologies are considered: direct firing, co-firing and gasification. Gasification has been described in the preceding section (2.2.1 Indirect conversion processes). During the direct conversion process of biomass feedstock, the gasified biofuels is directly incinerated to convert into usable energy (e.g. steam production to drive a turbine).

Biomass is not only the oldest form of combustion, but is also one of the most complex combustion systems to manage since it involves the use of solid fuels in a multi-phase reaction system with thermal and mass fluxes. Any wood fire will present several processes going on simultaneously. At the top of the fire fresh wood will still be visible and quite often it is steaming and possibly hissing as the water content evaporates from the wood. The part of the fire directly underneath this part will be black, with reduced size, with the flames some distance of its surface drying the fresh wood. The black part is pyrolysis taking place, where the organic material is being converted into liquids, char and gases. Removing some of this blackened wood from the fire can present the liquids on the surface as being pungent smoky smelling tar–like materials. Further combustion will see these liquids evaporate and mix with air and burn in yellow and blue flames. The majority of the heat released is produced in this stage. The radiating heat from the flames feeds back to the body of the fire to evaporate the tar like liquids

to maintain the flames. The layer beneath the pyrolysis layer is made of char where all the volatiles have been removed. During this stage the remainder of the wood is consumed and only white ash remains. The complexity of estimating an accurate heat release from wood combustion is the fact that only these gases burn and release heat. The liquids and the solids do not burn but actually consume heat in the drying and volatilisation processes needed for them to be chemically converted into fuel gases. This means that the key to good combustion is the rate at which fuel gases are evolved from the solid biomass and char. This rate depends on the temperature and the intensity of the heat flux supplied to the solid surface and the pyrolysis liquids. During the char combustion phase, this rate is influenced by the velocity with which oxygen, carbon dioxide and water vapour can reach the hot char surface to produce the fuel gases, hydrogen and carbon monoxide. This can be observed by forcing air into a fire and having the char colour change from red-orange (camp fires) to an almost incandescent appearance (temperatures in excess of $1500°C$). Biomass combustion is used for several applications: heat for daily living use; community applications including district heating; industrial use for both process heat and electricity production; and the transportation of fuels. They range from air starting to metered fuel delivery with excess air control methods, available for pellets, chips or entire logs. The air starving control methods is often achieved with CO and lambda controls for high efficiency and minimum emissions (Dornburg & Faaij, 2001).

The most common types of combustor configuration currently in use are grate burners and fluidized bed burners. Less common are the suspension fired burners and pile burners. They are very simplistic with a low efficiency although they provide a good control over the combustion. They were one of the first types to be used and have since evolved into underfed burners, where the fuel is added from underneath to allow for drying. Suspension fired boilers are not widely common in biomass combustion. Here air is introduced into the dust particles to keep them suspended in the air for combustion. Initially developed for coal, they are limited to particle sizes of 1mm, and research has been carried out for sawdust and straw. The problem with sawdust emerges from the often uncertainty of impurities resulting from colours or adhesives and there have been problems with severe deposit build ups and resulting high costs in maintenance (Tobiasen

et al., 2007). Facing the stricter emission regulations, a new technology emerged in wood combustion. In fluidized bed combustion (FBC), steam of gas moves upwards through a bed of free-flowing granular materials (e.g. sand, limestone), in which gas velocity is large enough to allow free circulation (Splinthoff, 2000). The combustion takes place at a lower temperature than the above mentioned combustion processes and hence present a reduction in NO_x and SO_2 emissions. However, this process requires a post combustion separation system to extract the granular material from the flue gases. In circulating fluid beds (CFB) and their predecessor bubbling fluidized bed (BFB), are both a continued development from FBC systems. Here the air velocity is increased to cause voids in the granular material. CFB system can have issues with high alkaline fuels; however, they have increased efficiency in sulphur reduction compared to their predecessors (Koornneef *et al.*, 2007). Fluidized beds are very suitable for high-moisture fuels (e.g. wastes and sludge), high-ash fuels (e.g. some types of municipal solid waste and refuse-derived fuel) and low volatile fuels (including anthracite and petroleum coke) (Minchener *et al.*, 2000).

Grate burners have an inclined platform where the combustion takes place. The grates are mainly classified into stationary sloping grates (Griselin & Bai, 2000), travelling grates (Subramaniam & Marwaha, 2006), reciprocating grates (Hermansson *et al.*, 2006), and vibrating grates (Yang *et al.*, 2007). Vibrating grates may have the longest life and highest availability. The grate assembly can be optimised significantly by allowing a better under-grate primary air distribution, by enhancing the mixing of biomass fuels on the grate, and by improving fabric seals of the system to lower air leakage (Zhou *et al.*, 2005). Grate burners show great competence in biomass combustion due to their great fuel flexibility and can adapt to a wide range of fuels of varying moisture and ash contents. The grate assembly plays an important role in the gas-fuel mixing in the fuel bed as well as the control of overall excess air in the boiler. Therefore, advanced secondary air systems are widely used in to order to enhance the mixing and lower the pollutant emissions as well as deposition and corrosion (Yin *et al.*, 2008). Lora & Andrade (2009) discuss the maturity level of different biomass conversion technologies. They make a clear distinction between the technologies used according to the size (kW) of the plant. In the range of 5–200 kW, they class

the combustion/steam cycle as well as the combustion/Stirling engine at a level of high maturity, yet with a medium commercial feasibility. At the time of publication they only classified the combustion/steam cycle technology above 1000 kW output at high commercial feasibility. The major problems for these small scale technology, at the moment, is often the low current market impact and the relatively high investment cost compared to proven technologies.

Co-firing is the process of replacing part of the fossil fuel supplied to a system with a carbon neutral fuel. Generally it is referred to as the adding of biomass to the combustion of coal, however, co-firing of vegetable oils to substitute heavy fuel oil is also undertaken. The blending of biodiesel with petro–diesel is another good example. Currently all sixteen major UK power plants are co-firing biomass, at an average level of 3% making use of fuels including wood, olive cake, palm kernel expeller, sewage sludge and energy crops to meet eligibility targets for ROC's (Renewable Obligation Certificates). These ROC's have an added market value and also reduce carbon emission allowance costs. In order to qualify for ROC's according to the current legislation in the UK, from 1^{st} April 2010 until 21^{st} March 2011, the percentage of fuel derived from energy crops for co-firing will increase to 50%. When co-firing biomass with coal there are two general approaches for mixing the fuels. Co-milling consists of blending the biomass component with the coal and pulverising the blend together in the existing coal mill. Direct injection, however, involves a completely separate feed system for the biomass fuel and involves additional implementation costs due to the requirements of additional handling, drying, milling and burners. The benefit of direct injection is the advanced flexibility of handling and processing the biomass with less potential of affecting the primary coal feeding system. Since biomass has different milling properties from coal and also considerable greater volatile matter content, separate feeding systems can allow co-firing with strict limits on the volatile content of fuels used.

Most biomass combustion designs these days have four major key elements: a fuel feeding system, a grate assembly, a secondary air system and an automatic ash removal system to reduce shut of-times. The fuel is added at the highest point of the grate and the moving motion spreads the fuel evenly with the primary air provided through holes in the stairs. As the biomass descends on the grate it goes

through various stages. Firstly the freshly added biomass will be dried and/or preheated. In a second stage pyrolysis takes place and even further down there is a stage of char burning. At the very bottom of the grate the ash cools down and can be extracted with a stationary screw system (Alstom, 2004). Capacities of grate-fired boilers range from 4 to 300 MW_e in biomass fired combined heat and power plants. The heat release rate per grate area may be up to about 4 MW_{th}/m^2 as a result of high volatile and low ash characteristics of typical biomass fuels (EPA, 2007). Heating boilers for solid fuels with an output up to $300kW$ are regulated by EN303-5:1999 (ISO, 1999). The purpose of this standard is to specify the necessary terminology for solid fuel heating boilers, the design requirements, the technical heating requirements and testing, as well as the marking requirements. The standard gives clear indication of the minimum required boiler efficiency in respect to net nominal heat output of the boiler. All testing requirements are described in order to guarantee a common method of testing for different boiler types.

2.2.3 Biomass Combustion Products

Biomass combustion is a source of undesirable particulate matter smaller than 10 μm (PM_{10}) in the ambient air. Since PM_{10} is regarded as one of the most relevant parameters in air pollution (Donaldon *et al.*, 2002), the PM emissions from biomass combustion can hinder the further propagation of bioenergy. Particulate matter (PM) describes the sum of airborne solid particles and droplets. Particle pollution is a complex mixture of airborne particles and liquid droplets composed of acids, water, black carbon, metals, etc. The particle size is the most important when describing the behaviour of particles. For example PM_{10} summarises all particles and droplets with an aerodynamic diameter smaller than 10 μm. The environmental protection agency (EPA) groups particle pollution into two categories (EPA, 2011c):

- Coarse particles ($PM_{10-2.5}$) are those found near roadways and dusty industries and have a diameter range between 2.5 to 10 μm.
- Fine particles ($PM_{2.5}$) are those found in smoke and haze and have a diameter less than 2.5 μm.

Beside coarse and fine particles, ultrafine particles are those smaller than 0.1 μm (Hinds, 1999). The size and density governs the retention period and travel in the atmosphere. Coarse particles tend to settle to the ground by gravity within hours, while fine particles can remain in the atmosphere for several weeks. Particulate matter in the ambient air is a mixture of directly emitted primary aerosols and secondary aerosols formed in the atmosphere. PM is partially of natural origin, while anthropogenic emissions lead to additional PM in the ambient air caused by primary and secondary aerosols. Coarse particles from primary aerosols originate mainly from mechanical processes (construction activities, road dust, resuspension, wind etc.) whereas fine particles are particularly produced through combustion (WHO, 2006). Main sources of fine particulate matter are Diesel engines and biomass combustion. Additional aerosols are formed in the atmosphere through conversion of gaseous precursors such as sulphur oxides (SO_2, SO_3), nitrogen oxides (NO, NO_2), ammonia (NH_3) and Non-Methane Volatile Organic Compounds ($NMVOC$). Reaction products are ammonium sulphates and ammonium nitrate, aldehydes and ketones as an oxidation product of $NMVOC$. Greatest producer of secondary aerosols are stationary combustion processes (energy, industry, domestic fuel: SO_2, SO_3 and NO, NO_2), agriculture (NH_3), Diesel engines (NO_x), use of solvent, chemical industry and petro chemistry ($NMVOC$) (Umweltbundesamt, 2005). Long exposures to particulate matter can cause serious health problems such as higher morbidity, affection of lungs and a shorter life expectancy, mainly in subjects with pre-existing heart and lung diseases. The particle size is a main determinant of health effects. Coarse particles are generally filtered in the nose and throat where as particulate matter smaller than PM_{10} can settle in the lungs and may reach the alveolar region. The size PM10 cant be seen as a strict edge between respirable and non-respirable particles, but has been agreed upon for monitoring by most regulatory agencies so far. The World Health Organisation (WHO) though has published 2006 its latest Air Quality Guideline (AQGs) based on health effects with limiting values for PM_{10} and $PM_{2.5}$, both for short-term and long- exposures. The European Community has set in directives 1999/30/EC and 96/62/EC limits for PM_{10} in the air. In the first phase, started on 1^{st} January 2005, the limit of the yearly average is 40 $\mu g/m^3$ and for daily average (24 hour mean) 50 $\mu g/m^3$. The daily

average is not allowed to be exceeded more than 35 times per year. In the second phase starting 1^{st} June 2010, the yearly average standard will be 20 $\mu g/m^3$ and the daily average limit 50 $\mu g/m^3$ whereas the allowed number of daily excess will be reduced to 7 days per year.

Investigations on particle emissions showed that wood combustion plants can achieve a high combustion quality if well designed and properly operated, thus resulting in low emissions of unburned hydrocarbons and soot (Nussbaumer, 2005). However, automatic wood boilers exhibit fairly high mass concentrations of particulate emissions in the raw gas, i.e. typically in the order of magnitude of 100 mg/m^3 at 13 vol.% O_2 for natural wood chips and up to several 100 mg/m^3 for other fuels such as bark. Particles from well designed and operated automatic wood combustion consist mainly of inorganic matter such as salts, while particles from wood stoves operated under poor conditions consist mainly of soot and organic substances. Combustion particles are a mixture of solid particles and condensables, both containing organic and inorganic fractions. Especially the organic emission is strongly influenced by the combustion conditions. High organic emissions are correlated with low combustion efficiency and high potential for toxic organic substances, e.g. benzo(a)pyrene (BaP) or fluorene and can be avoided by high combustion temperature, sufficient oxygen availability in the flame enhanced by good mixing and sufficiently long residence time in the combustion zone. The emission of inorganic particles can be slightly influenced by the combustion conditions, however, it depends on different formation mechanisms. High temperature typically enhances the conversion of ash material to the gas phase and consequently the emission of inorganic particles. Under typical conditions, organic particles are most relevant in poorly operated manual wood combustion devices, while inorganic particles are most dominant in automatic wood combustion plants operated at high temperatures. Depending on the aim of the measurement, different sampling strategies are commonly used e.g. for product testing and health studies. Pellet combustion and log wood boilers with forced draft achieve relatively low particle emissions not only under ideal operation conditions, but also under operation conditions which are assumed to be typical and should reflect the emissions under practical conditions of most installed heating devices of the respective categories (Nussbaumer *et al.*, n.D.).

Messerer *et al.* (2007) investigate the feasibility of particulate reduction with heat reclaim in small-scale biomass application through added heat exchangers to the flue gases. The observed deposition efficiencies up to 95% depending on the temperature, velocity and retention time of the flue gases in the heat exchanger. Since they investigate different deposition technologies, they concluded that diffusion was the most efficient for particle diameters $< 50\ nm$, and thermophoresis for particles with diameters $> 100\ nm$. The heat recovery of the heat exchanger was established between 75% and 90% depending on operating conditions.

2.2.4 Biomass Combustion Modelling

A large proportion of the work carried out in this project is based on numerical and computational modelling. This section will review the advances of biomass combustion modelling and its related technologies, through numerical approaches and computational fluid dynamics (CFD).

Pericleous (2008) made a parametric study to determine the variation of fuel nitrogen conversion with changes in the input variables including the inlet fuel nitrogen concentration. The fuel nitrogen conversion predicted is similar to those reported in experimental studies on gaseous fuels. The conversion decreased with increasing fuel nitrogen inputs as shown in experimental data. Huang *et al.* (1996) made a numerical study of three dimensional fluid flow and heat transfer in a shell and tube heat exchanger. They used combustion gases on the shell side and cooling water in the tubes. Computations for Reynolds numbers up to 10,000 were performed. The flow and heat transfer characteristics in this heat exchanger were studied and the effect of different baffle size and position investigated. The velocity and temperature distributions as well as the total heat transfer rate were calculated. The flow field predictions were compared with experimental data. Recommendations were made for suitable baffle size and position . Wardeneier & van de Bulck (1997) made a computational model of a steady-state waste combustion and air flow optimization in a field scale rotary kiln. The focus of the model is on the gas phase fluid dynamics. The goal of the study was to screen various air inlet designs for their mixing characteristics and

residence time distribution. The actual air inlet configuration in an existing full-scale incinerator was chosen as a reference for comparison. The methodology and usefulness of the approach was fully demonstrated and typical design results were reported. Prasad & Shiva (2004) show that it is not just sufficient to debate about validation, but that it is becoming increasingly necessary to at least start debating about establishing standards for development, distribution and use of CFD codes. The paper discusses the problems in application of CFD for industrial flows and suggests possible solutions and the need for unified action by the CFD community including the concept of Global Benchmarking. Computer programs for modelling fluid flow in or around various objects have met with varying degrees of success in the past. Hadjsophocleus (n.D.) gives guidelines for the use of CFD simulations for fire and smoke modelling. The paper aims at providing a better understanding of fundamental fire dynamics concepts and their limitations and impact on model predictions. The fires described are all happening in compartments. The results were then compared to real life systems.

Cooper & Coronella (2005) describes CFD simulations of particle mixing in a binary fluidized bed. From these simulations it is possible to identify the solids wake trailing a rising gas bubble by looking at the vertical solids flux. The simulations predict a well-mixed fluidized bed with modest localised segregation. Kaer (2006) describes the CFD software FLUENT^{TM}as a mechanistic deposit formation model for straw-fired boilers. The paper gives a description of the concept used to model fuel conversion on the grate and the coupling to the CFD code. In the remainder of the paper, the development and implementation of a CFD based deposition model is presented. The model used was applied to the straw-fired Masnedo boilers and the results obtained were in good quantitative agreement with both measurements and observations at the plants.

Stopford (2002) describes the recent advances of CFD modelling in the power generation and combustion industries. The paper focuses on coal-fired furnaces and laminar combustion which are typical of CFD models involving complex multi-phase flows and reacting systems. Also, the article discusses the advances in software packages and their relative ease of use and hence accelerating the time for development of new products. Gomez-Barea & Lechner (2010) review the current modelling of biomass gasification in fluidized beds. They identified that

de-volatilization and conversion of tar and char are not yet accurately modelled. This is primarily because the chemical process of tar generation and conversion has yet to be fully understood. They outline the lack of CFD models to the many models of other classes. This could be due to the fact that there is to date no proof of CFD leading to more precise results than fluidization models (regarding the combustion of biomass). Rostami *et al.* (2004) present a biomass pyrolysis model for CFD applications. The authors generate a more efficient way of incorporating the distributed activation energy model (DAEM) by using the integrals in a closed mathematical form. The obtained results are compared with experimental data. The findings do generally agree with these findings and the authors do recommend some changes for further work regarding the kinetic parameters. The input data for the program however relies on the accuracy of the experiments used in the model. Gerber *et al.* (2010) present an Eulerian multiphase approach for modelling the gasification of wood in fluidized beds. The difference to other methods using the Eulerian method is that the results are based on the assumption that the bed material is composed of wood and char only. The paper describes the importance of bed temperature compared to the initial bed height and the throughput regarding the product gas concentrations. They determine the importance of operating conditions on the tar content in the product gas.

Nikoo & Mahinpey (2008) present a simulation of biomass gasification in fluidized bed reactor using ASPEN Plus. They include hydrodynamic parameters as well as kinetic modelling in their simulations. A lab-scale pine gasifier is used to validate their proposed model. They determine an increased production of hydrogen and enhanced carbon conversion efficiency by raising the temperature. A direct correlation between the equivalence ratio and the carbon dioxide production and carbon conversion efficiency was established.

2.3 Biomass Power Generation

There are several ways to classify prime mover technologies, based on fuel used, technical maturity, market shares or capacity range. Traditional systems like reciprocating internal combustion engines, steam turbines and combustion turbines

are the most common movers installed. However, there are some new technologies at various stages of maturity that are emerging or re-emerging (Cogen, 2011). Amongst those are fuel cells, Stirling engines and micro-turbines, and organic ranking cycle (ORC) systems.

2.3.1 Large Scale Systems

Steam engines are the most common technology used in power plants and industries as a prime mover. In theory, steam turbines equipped with a suitable boiler can be run on any fuel. As a well developed technology they have a long life and with proper handling and maintenance are very reliable. Their limits include low electrical efficiency, slow-start-up time, and poor partial load performance. Hence, they are more favourable for large central plant utilities or industrial co-generations than in distributed energy or even small scale applications. Steam turbines are used in large scale power plants with MW's output (EPA, 2011b).

Reciprocating internal combustion engines are usually classified in two categories: spark ignition engines, which are operated mainly with natural gas (or biogas); and compression ignition engines, which can be driven by diesel fuel as well as other heavy fuel oil. Similar to steam turbines, reciprocating engines are a well developed technology and were among the first prime movers to be used in combined heat and power applications. In addition to fast start-up time and good operating reliability, a high efficiency at partial loads give consumers a flexible power source. This makes them especially attractive for emergency or standby power supplies. They are probably the most widely used prime movers for applications below 1 MW. One of the drawbacks of reciprocating engines is the vibrations and hence the noise they generate. This increases cost due to noise insulation as well as maintenance costs due to material ware (Alanne & Saari, 2004). From an environmental aspect, reciprocating engines, if fuelled by fossil fuels, have high emissions. Partial or entire substitution by renewable fuels has proven reliable and useful (Oberweis & Al-Shemmeri, 2010).

Combustion turbines, similar to steam turbines have been primarily used in large scale co-generation plants as prime movers. Units with less than 1 MW

output are usually not considered due to their low electrical efficiency and consequent higher cost per W_e output. The advantage against steam turbines is their lower footprint and straight forward installation with lower cost involvement. In comparison with reciprocating engines they have usually lower emissions. Quite often additional fuels are used to raise the exhaust temperature to $1000°C$ in a process called supplementary firing. This increases the amount of high pressure steam produced and results in a higher net electrical efficiency for combined-cycle gas turbines. Unfortunately, combustion turbines require the input of fossil fuels, primarily natural gas. Also, the high temperatures require extensive maintenance and material costs. High ambient temperatures or high altitude regions can have a negative effect on the performance of combustion turbines (EPA, 2011a).

2.3.2 Small Scale Systems

Micro turbines extend combustion turbine technology to smaller scales. They can be used with a multitude of fuels as hot gases and either direct exhaust or heat transferred to air is used to drive the turbine. Although they have extremely high rotational speed, as much as $120,000\ rpm$, there is no need for lubricating oil. They also have lower emissions and less noise pollution than other engines with similar output. Their disadvantages to more mature technologies are their relative novelty and hence lack of track record as well as having high initial costs involved with them. As normal combustion turbines they are subject to ambient conditions. However, they can be easily used in combined heat/cooling and power units. Talbotts Heating (Pritchard, 2005) tested a biomass fuelled indirect micro turbine in a partner project with the Department of Trade and Industry (dti). Although a working prototype was run for almost $5,000$ hours, they identified low efficiencies on the heat exchanger used as well as micro-turbine availability having been reduced dramatically due to a weak market and a lack in demand. Jurado *et al.* (2004) showed that the introduction of mirco-gas turbines into an already existing grid can provide grid stability, by reducing the power demand from the main grid feeder. However, they state that the system is still to premature to be used as grid security, as biomass based mirco-turbines are not an uninterruptible power supply.

The main advantage of using fuel cells as a prime mover is their quietness. Since the principle is based on chemical processes and involves zero moving parts, the noise level is reduced drastically compared to other technologies. The basic principle involves the use of hydrogen and oxygen to generate electricity with high efficiency. Although this technology has been primarily used in the transport sector, it also shows a potential for combined heat and power applications due to the waste heat generation. This technology is, however, in its footsteps and only 40 MW of phosphoric acid fuel cells ($PAFC$), one of the technologies, are installed worldwide (Wu & Wang, 2006).

Based on the steam process, the organic Rankine cycle (ORC) has been developed for an efficient use of solar, geothermal and biomass energy for decentralised units. Instead of water, an organic working fluid is used (e.g. silicon oil, Toluol) with better steam characteristics at lower temperatures and pressures. The fluid choice depends on the fuel used and silicon oil is of particular interest for biomass applications (BIOS, 2011). Dong *et al.* (2009) present a review on the development of small-scale and micro-scale biomass-fuelled CHP systems with concentration on ORC technology. The authors highlight one of the major advantages of ORC for biomass-fuelled applications as the ability of the organic working fluids to lead to high turbine efficiency in both full and partial loads. They discuss the high investment costs of ORC, however they claim that the operating costs are considerably lower, compared to conventional steam, due to its good controllability, high degree of automation, and low maintenance costs.

In 1816, the Reverend Dr Robert Stirling patented a new design for a hot air engine with an "economiser", as he called his regenerator. There are two main differences to standard hot air engines, namely the closed loop of the working gas and the regenerator. There was, however, a disadvantage to his new design as the working gas, being used continuously, needed to be cooled down at the end of each cycle. The regenerator is an addition to counteract these added losses due to cooling by acting as intermediary storage for the heat. This means that the overall efficiency of this design can reach higher values as standard steam turbines. The first real working model of this type of air engine was developed by Robert Stirling's brother. It was a β-type engine, containing compression and expansion pistons in the same cylinder used for pumping water. In 1824, James

Stirling then tried increasing the pressure of the working gas above atmospheric pressure which resulted in an increased efficiency of the engine due to a higher pressure differential between expansion and compression spaces. In 1827, both Stirling brothers submitted a new patent which described the use of different gases, other than air, as the working medium. Lowering the density of the gas will lower the work required to "push" the gas around the engine (Steimle *et al.*, 2007). In 1828, the first machine reaching 15 kW was built by a Glaswegian company called Girdwood. Important in all this work is the notion that the theoretical scientific knowledge regarding Thermodynamics was unknown at the time. Carnot first published his work in 1824, which led to the dismantling of the idea that heat was a constant substance called caloricum. In 1842, Julius Robert von Mayer published his theories about the principles of mechanical equivalent of heat. The third patent of the Stirling brothers describes the importance of the high temperature differential as well as the importance of heat rejection. This led to a new machine which achieved an efficiency of 18%, compared to a general 2% efficiency of steam engines at that time. At the end of the 19^{th} century, several machines were being designed and were operational although they never achieved the high efficiency ratings of the Stirling brothers. Notably, though is the machine developed by Alexander Kirk in 1862, which produced cold air for the purpose of cooling. The inventions by Rudolph Diesel and Nicolaus Otto (based on the work of Alphonse Beau de Rochas) led to a decrease in the interest of Stirling engines. The only notable research carried out was by the company N.V. Philips' Gloeilampenfabriken in Eindhoven (NL). This research was driven by the fact that Philips intended to conquer the American market for radios. As radios back then required enormous amounts of energy to run (compared to today) combined with the then scarce availability of electrical power, Philips needed to source an alternative energy generator to battery power. The actual idea was given to Philips design engineers at the IFA (International Radio Exhibition Berlin, D) in 1938. The first engine that evolved from this new area of Philips' research was an α-type engine running at 1,500 rpm, which made it the first high speed Stirling engine generating 16 kW. Philips developed numerous similar engines in the years before WWII; however, none managed to pass beyond development status (Darlington & Strong, 2005). In 1940, a β-type engine that generated 500 W at

1,500 rpm when run on air was developed. The same engine managed to generate 1.1 kW with 16% efficiency if the working gas was hydrogen. This engine, much close to the original design of the Stirling brothers, led to the development of the type 10-engine which was later used in the development of heat pumps and cooling engines. In 1942, Philips went back to the α-type configuration, which led to the application of a patent in 1943. This engine generated 8 kW at 3,000 rpm with the working gas pressure (air) set to 1 MPa. This development was interesting in respect to its number of four cylinders.

After WWII, Philips realised the huge potential of Stirling engines and started looking for research partners to work together on the design of newer engines. This led to the first commercialisation of Philips based Stirling engines in 1948. This first attempt was an engine with a V arrangement of its cylinders, generating 294 kW. However, due to the volume of 3,016 cm^3 per cylinder there were problems reaching the designed speed of 1,500 rpm as well as the heaters underperforming due to the appearance of cracks or melting of the heater tubes. In 1953, Philips decided to cancel further research in Stirling engines. Reasons were the financial allocations to the newly created division of televisions as well as the uncertainty of a successful commercialisation of the Stirling engine due to operating problems. However, these designs of the Stirling engine did not get scrapped due to the invention of the rhombic drive which led to the possibility to keep the crankcase at atmospheric pressure (reducing the weight of the engine), as well as a more linear motion of the pistons (reducing friction and vibration). This led to the presentation of a first attempt in 1956, generating 22.06 kW. This was remarkable as it was the first time an engine delivered what is was designed to, as well as an efficiency of 38%. Numerous engines were developed with this new rhombic drive. In 1958, first trials were carried out regarding the design of a Stirling engine capable of driving a boat. In the following years, numerous engines designed for cooling were developed generating roughly 20 kW at 70°C. This led to systems to be used in the production of liquid helium in 1965. In 1968 the first engine using a swash plate to convert the linear motion of the pistons into a rotary motion was used. At the end of the sixties, Philips entered a joint venture with USS (United Stirling Sweden), to develop an engine capable of being an alternative to diesel engines for buses, boats as well as stand-alone electricity

generators. The first one year trial took place in 1971, however it was determined that the success was limited by the efficiency of 25% (35% were estimated too competitive), the reliability needed to be improved as a reduction in maintenance requirements. The major down side, however, were the massive production costs compared to standard diesel engines. Similar results were obtained in testing a Stirling engine in the 1976 Ford Torino. During 1970 and 1978, the Advenco project was aimed to design low cost engines. This was primarily aimed at reducing the high cost of some exotic materials, e.g. cobalt. In 1978, the Ford company stopped all developments regarding Stirling engines. Philips followed this initiative by the end of 1979; however, they continued their developments in the area of cooling cycle engines. During the years of research at Philips several joint ventures were concluded with other organisations and although they all made some contributions toward Stirling engine design, none of them really led to major commercialisations. The major problems usually were the high costs compared to cheap diesel and petrol engines as well as maintenance issues and shut-down requirements (Walker, 1980).

However, not only Philips carried out research in the post WWII years. Notably, USS and MTI (Mechanical Technology Incorporated) started developing a Stirling engine in 1978 co-financed by NASA and the DOE (US department of energy). This resulted in an engine with reduced maintenance requirements and generating 63 kW with 39% efficiency in 1983. Sunpower worked on the design of a 10 kW solar driven Stirling engine in 1984. Still in operation, they produce free piston engines ranging from 35 W to 7.5 kW designed by the company founder William Beale. In 1982, Lane & Beale (1982) presented a 4 kW biomass driven Stirling engine in Bangladesh with an efficiency of 10%. Instead of converting the linear motion of the free piston into a rotary motion to drive a generator, a linear generator type is used. This reduces the weight of the engine considerably (Organ, 1997). Since 1995, WhisperTech produces Stirling engines for their CHP systems, generating either 800 W DC or 1.2 kW AC electricity. They use a 4 cylinder engine with a wobble yoke drive to convert the 4 axis linear motion into a single rotary motion (de Paepe *et al.*, 2006; Onowwioma & Ugursal, 2006). The Stirling Systems AG (StirlingAG, 2011) developed a 1 kW free piston engine which was used in a $20,000$ hours field test finished in 2007. Although they

announced a market introduction in 2008 no news has been given by the company. Numerous individuals contributed to the development of Stirling engines. Notably here are Dr Kammerich and D. Viebach who both managed to develop a working prototype of 1 kW and 0.5 kW respectively without any financial contributions from major companies. A modified version of the engine designed by D. Viebach is used as the basis for calculations and laboratory experiments in the coming chapters.

2.3.3 Stirling Engine Modelling

Several evaluations have been presented over the years in order to predict and facilitate the design of engines. The first analysis was carried out by Schmidt almost 50 years after the actual invention of the engine. Schmidt assumed that the compression and expansion spaces are kept constant and at the same temperature throughout the cycles. His major contribution was to link the pressure in the engine to the volume which he assumed to behave in a sinusoidal fashion. An analysis of non-isothermal assumptions was first carried out by Finkelstein (1994) in 1960. He was the first to introduce the concept of conditional temperatures depending on the direction of the working gas flow, by assuming that the heat transfer within the working space takes place due to forced convection. He divides the engine into different cells (expansion, cooler regenerator, heater and compression) and represents them by control volumes using the equation of state as well as energy and mass conversation laws. This principle is further developed by adding the losses due to pumping friction in the heat exchangers by Urieli & Berchowitz (1984). As their simulation is based on an alpha type engine, the simulation in this report has been adapted to accommodate the gamma type engine. Additionally, a different configuration for the heater, cooler and regenerator are used. The layout of the evaluation is described in the following chapters. The approach developed by Urieli is also used by Scollo *et al.* (2008) to design and construct a Stirling engine prototype. They use the program to estimate results and improve their design and show the usefulness of this method to get preliminary indicative information of the engine behaviour. Investigations on Stirling engine analysis shows that almost all literature deals with ideal regeneration and

zero dead volume (Formosa & Despesse, 2010), alpha (Puech & Tishkova, 2011) or beta-type engines (Cheng & Yu, 2010). The imperfect regeneration and losses due to pumping friction and dead volumes has been attributed little attention (Kongtragool & Wongwises, 2003). Martini (1983) describes the various approaches and limitations of first, second and third order methods to stimulate Stirling engines. Whereas first order design methods are usually used to give an initial idea at the beginning of the design stage, they are limited in the way that neither the working gas properties nor the engine layout are considered in the calculations. One notable first order design method is the power estimation describe by Beale (West, 1981, see), who determined that most Stirling engines conformed to a simple equation. The simulation used in this paper is of the third order form. The third order is an amelioration of the second order by means of modelling the interaction between the different processes, assumed to be going on simultaneously and independently. The advantage of these methods is the capability to compute flows and temperatures inside the engine which cannot be measured in practice (Organ & Finkelstein, 2010; Kongtragool & Wongwises, 2006; Yuan & Spradley, 1992). Mahkomov (2006) investigated some design changes to a biomass driven Stirling engine based on a numerical analysis and CFD simulations. The basis for this investigation was that the designed engine was not performing according to its specifications. He determined that high hydraulic losses in the regenerator as well as large dead volume of the engine were major factors reducing the power of the engine. Furthermore, he determined that changing the engine from a γ to α configuration whilst keeping the maximum pressure and temperature of the heater unchanged would increase the efficiency.

2.4 Biomass Refrigeration

2.4.1 Absorption Refrigeration Cycles

The vapour-compression refrigeration/cooling cycle was described by Oliver Evans in 1805 but it was Jacob Perkins who in 1835 registered the first patent (IIR, 2007). The machine ran on ethyl ether. Vapour-compression refrigeration/cooling is by far the most widely used system. Refrigerant vapour is compressed by a

mechanical compressor. It is passed to a condenser where it changes state by evolving heat to the surroundings. Liquid refrigerant then passes through a regulator (expansion valve) and vaporises in an evaporator, producing useful cooling. The principle of absorption cooling was first described by the French scientist Ferdinand Carré in 1858. The original design used water and sulphuric acid and in 1926 Albert Einstein proposed an alternative design, the Einstein refrigerator. This machine is a single-pressure absorption refrigerator using ammonia as a pressure-equalizing fluid, butane as a refrigerant, and water as an absorbing fluid, it has no moving parts, and it does not require electricity to operate, needing only a heat source, e.g. a small gas burner or an electric heating element. Commercial production of absorption refrigeration units began in 1923 by AB Arctic, which was bought by Electrolux in 1925. The first compression machines that proved to be successful on an industrial scale were developed by James Harrison in Australia. Thermal refrigeration describes a process in which refrigerant vapour is generated from a binary solution by the application of heat, cooled and liquefied by giving up heat to the surroundings, and then allowed to evaporate producing cooling. The resultant vapour is reabsorbed into the solution due to its affinity with the absorbent. The binary solution is then returned to the generator to complete the cycle. An isobaric diffusion absorption cooler was first patented by the Swedes Baltzer von Platen and Carl Munters in 1922 (Herold *et al.*, 1996). It used a bubble pump to circulate the solution and, in consequence, had no moving parts. Water-lithium bromide absorption systems were developed in the US in the 1940's. They were based on a modified Carré cycle with water as refrigerant. They are primarily used in air-conditioning since they cannot function at sub-zero temperatures due to the freezing point of water. Small capacity powered diffusion absorption refrigerators have been commercially produced by Electrolux since 1928 (Jacob *et al.*, 2003). Designed as domestic refrigerators, for small portable applications and for hotel rooms, they have cooling capacities of a few tens of watts and COP's generally between 0.1 and 0.3. The performance of the devices has been assessed during the last half century by various researchers such as Watts & Gulland (1985), Stierlin *et al.* (1992), Backström & Emblik (1965) and Chen *et al.* (1996). The University of Stuttgart obtained grants from the Joule Craft programme to develop a single stage ammonia-water diffusion

absorption cooling machine with a capacity of 2.5 kW (Jacob & Eicker, 2006; Jacob *et al.*, 2007). The first two machines failed to reach their design capacity and lost performance in operation. The best COP was found to be between 0.05 and 0.15 with a cooling capacity of 0.5 to 1.5 kW in continuous operation. The third prototype developed and subsequently modified in 2006 eventually gave a cooling capacity of 2.0–2.4 kW at $18/15°C$ respectively, with an average COP of 0.3 corresponding to a source temperature of $125°C$. Although there is extensive research done on solar thermal cooling, there is currently very little work done on micro-scale cooling from biomass combustion. Large scale is having a good market introduction in some countries (Seyboth *et al.*, 2008).

The process of vapour absorption cooling is described in detail by various authors (ASHRAE, 2009; Dossat & Horan, 2001; Althouse *et al.*, 2000). Single effect absorption refrigeration systems consist of four main components: generator, condenser, evaporator and absorber. Simplistically high temperature heat supplied to a generator is used to preferentially evaporate refrigerant from the binary solution. It changes state and is cooled in the condenser by rejecting medium level heat to the surroundings. Refrigerant from the condenser passes to the evaporator through a reduction valve where it evaporates at low pressure thereby producing the cooling effect. The vapour continues to the absorber where it is absorbed by cooled solution from the generator and condensed absorbent which are collectively termed weak flow. The resulting strong flow is then returned to the generator to complete the cycle. Heat exchangers can be used to increase the efficiency of the process. The addition of a solution heat exchanger to the system (which transfers heat from the weak to the strong solution) in particular has been shown to significantly increase the efficiency of the system (Aphornratana, 1995). Multi effect absorption refrigeration cycles have been developed to enhance COP's of single effect devices which are typically of the order of 0.50–0.70 in developed systems (Srikhirin *et al.*, 2001). Multi effect systems use level heat rejected by the condenser to generate additional cooling in multiple stages. In a double effect cycle vapour refrigerant is condensed at high pressure in the generator of the second stage (Vliet *et al.*, 1982). Double effect systems produce COP's approaching 1.0. If the refrigerant pair is water ammonia, the pressure in the first stage can be very high. However, in contrast to LiBr/water it

can be considered to be a combination of two separate single effect cycles. Thus, by integrating the evaporators and condensers of both stages the maximum pressure can be reduced to acceptable levels. These machines have only two pressure levels. Adding further stages, triple or quadruple effect machines simply increase complexity at diminishing improvements in COP (Grossman *et al.*, 1995).

Theoretical studies of an absorption refrigeration cycle with heat recovery from the absorber have shown a 10% increase in COP (Kaushik & Kumar, 1987). Half-effect absorption systems combine two single-effect cycles operating at different pressures which reduces the generating temperature significantly below that required for a single effect machine albeit operating at a much reduced COP (Groll, 1997). Combined vapour absorption-compression machines are hybrid devices, in which the condenser and evaporator of a vapour compression machine are replaced by a generator and absorber. This reduces the pressure differential across the compressor and potentially increases the COP. Double effect machines have also been developed in which heat rejected from the first stage is supplied to the generator of the second (Rane *et al.*, 1993). Dual-cycle absorption refrigeration cycles are similar to double effect systems, but use two pairs of working fluids. Typically, a single effect water/ammonia system is heated by waste heat and rejects heat to a single effect LiBr/water system. Cooling is obtained from both cycles (Hanna *et al.*, 1984). Absorption refrigeration cycles have been modified in various configurations by incorporating ejectors. Chung *et al.* (1984) and Chen (1988) use ejectors to maintain higher pressures in the absorber than the evaporator. The ejectors are driven by a high pressure solution from the generator and entraining vapour from the evaporator. This increases pressure by around 20% thereby elevating the COP. In contrast, Aphornratana & Eames (1998) use water vapour from the generator as the driving fluid. It is similar in principle and produces a COP close to unity. Its drawback is that the generator requires a high temperature heat source of $190°C$ to $210°C$. LiBr/water absorption systems have a higher refrigeration capacity at heat source temperatures below $90°C$ (Gupta *et al.*, 1997).

2.4.2 Working Fluids for Absorption Refrigeration Systems

Various refrigerants have been used for vapour compression systems. Ammonia was first investigated by Tellier in 1862 and exploited by David Boyle (1837-1891) in America, and Carl von Linde (1842-1934) in Germany. Fluorocarbon refrigerants were developed as safe (non-toxic and non-flammable) refrigerants; following research conducted by Swarts, (in 1893-1907) in Ghent. The Frigidaire Corporation, headed by Thomas Midgley, developed the first three fluorocarbon refrigerants, in 1930. Subsequently, the Montreal Protocol banned CFC's and HCFC's due to their effects on the ozone layer. Srikhirin *et al.* (2001) provided an exhaustive list of the thermodynamic and physical properties required by sorption systems. The best and most common refrigerant/absorption pairs are water/ammonia and LiBr/water. Ammonia and water are stable for a wide range of operating temperatures and pressure. Ammonia has a suitably high latent heat of vaporization and a freezing point of $-77°C$ which makes it suitable for low temperature applications. Since both ammonia and water are volatile, the cycle requires a rectifier to purge water that normally evaporates with ammonia. Other disadvantages include: high pressure, toxicity, and corrosive action to copper and copper alloy. However, water and ammonia are environmentally friendly and of low cost. LiBr/water is limited to applications above $0°C$ due to the freezing point of water. They do not need a rectifier. The system must be operated under vacuum conditions, and at high concentrations. Further research has suggested that other working pairs may be of interest. R22 and R21 have been widely suggested due to their solubility with a number of organic solvents. Among the latter are Dimethyl Ether of Tetraethylene Glycol (DMETEG) and Dimethyl Formamide (DMF) (Bhaduri & Verma, 1986b,a). Binary mixtures using inorganic salt absorbent such as LiBr/water or NaOH/water may eventually prove to be the most successful working pairs for absorption refrigeration systems (Best & Holland, 1990). However, the solution is prone to crystallization at high concentrations. Gommed & Grossman (2007) designed and tested an absorption cooling prototype based on liquid dessicant system. They use a lithium chloride salt and water mixture as the working fluid and obtained a lot of realistic data

regarding the operation of the main components dehumidifier and regenerator as well quantitative data about their performance. They observed an overall COP of 0.8 with average 16 kW dehumidification capability. Bales *et al.* (2008) showed that the thermal storage of TCA is sufficient for small scale solar cooling applications that do not have large night cooling loads. Sanjuan *et al.* (2010) investigated the advantages of salt desiccants (LiCl) versus liquid absorption systems. Their major finding is that the absorption process and the energy storage is combined in one so that the production of cooling energy can be decoupled from the solar gains without external storage tank. They show that these units are able to substitute big absorption systems due to the small size. They also show good adaptability and many possibilities of operation for medium and small scale systems. The lithium chloride / water pair has been tested by Climatwell (2011) and is currently used in their solar absorption cooling technology. They have shown that this pair is not suitable for seasonal storage due to its high cost of the salt. However the system can deliver either cooling or heating and the problem of crystallisation has been overcome and that enables the enhancement of the storage density and COP with a so-called "closed three phase absorption".

2.4.3 Absorption Cooling Modelling

To facilitate optimisation, effective modelling is an important tool. Misra *et al.* (2006) showed that for an ammonia/water vapour absorption refrigeration system, optimization produced a significant improvement in the system performance without any additional investment. Combining thermodynamic and mass flow equations with the equations for the thermodynamic properties of ammonia-water, in particular, has allowed optimisation for ammonia/water systems. da Costa *et al.* (2005) developed a sophisticated model for diffusion-absorption refrigeration cycle using ammonia-water helium as working fluids. It produced a COP of 1.0 at a generator temperature of $195°C$ and evaporator temperature of $-5°C$ while working at $25\,bar$. Each sub-component of a system must be optimised if the system as a whole is to be optimised. The work done by Gommed & Grossman (2007) is based on the previous work conducted by Grossman & Michelson

(1986), a modular computer simulation of absorption systems. The advantage of the simulation is the capability of modelling various systems and working fluids.

Bales & Nordlander (2005) investigated the characteristics of the thermo chemical accumulator developed by ClimateWell. The TCA is a three-phase absorption heat pump that stores energy in the form of crystallised salt ($LiCl$) with water being the other substance. They estimated the thermal COP to be 0.7 but could not verify this in the laboratory testing. Conde (2004) presents a complete collection of interpolating equations for the most important properties of aqueous solutions of lithium chloride. The equations are based on old and new literature based on the available technology of measurement at the time of their respective publication. The data included in this research was based on accuracy levels of the original publications. All the equations were programmed in MathCad calculation sheets and can be obtained from the author for use. Zohar *et al.* (2005) developed a thermodynamic model for an ammonia-water diffusion absorption refrigerator which demonstrated that a system operating with helium as auxiliary gas produced a coefficient of performance up to 40% higher than a system working with hydrogen. Similarly, Mayia (2003) demonstrated in a computer simulation that helium was superior to hydrogen as an auxiliary fluid. Its greater viscosity, however, required a larger head. In a series of experiments at the Stuttgart University of Applied Sciences, Jacob *et al.* (2008) was able to reduce the generator heating temperatures in an ammonia/water diffusion absorption cooler from 150–170°C down to 110–155°C primarily by increasing the concentration of ammonia within the system. A recent generation of storage materials, called selective water sorbents and presenting intermediate behaviours between solid adsorbents, salts hydrate and liquid absorbents. These sorbents are two component materials based on a porous host matrix with an inorganic salt inside its pores, such as lithium chloride (Frenzi *et al.*, 2007). The important advantage of such a composite is the possibility to controllably modify its water sorption properties in a wide range by changing some variables (Aristov, 2007).

2.5 Biomass Applications

2.5.1 Single Generation Applications

The combustion of biomass in direct conversion processes has heat as its primary output. This heat can then be used for either: power generation, heating, refrigeration, or a combination thereof. Heating is usually separated further, depending on whether there is need for space heating, domestic hot water or a combination of the two. These systems are very similar to standard conventional fossil fuel domestic central heating systems. Depending on the amount of heat required they can vary from one room pellet stoves ($< 10\ kW$) to family sized housing central heating systems of up to 30 kW. Figure 2.5 shows a typical pellet stove from Sideros (2011), Italy, that can be used for added heating in a single room or can be integrated into the central heating system. These stoves are usually based on pellets and need to be filled regularly, some even on a daily basis depending on the rate of use. Tiled stoves are more aesthetic than stoves and are

Figure 2.5: SIDEROS pellet stove, Sideros (2011)

based on the principle of radiating heat storage. They usually have a combustion period during which they burn off the fuel in the system and store the heat of

combustion in the tiles. This radiating heat is then used to heat the room(s) that share a wall with the tiled stove. Contrary to the pellet stoves above, these tiled stoves involve a high capital cost and are rarely added during a renovation (due to even further increased costs). Figure 2.6 shows a tiled stove, as they can be typically found in the Alp region of Europe. Larger systems incorporate domestic

Figure 2.6: Tiled stove from Austria

hot water preparation. They are rated up to 30 kW and require as little maintenance as conventional heating systems, depending on the unit. Fully automated systems have automatic ash removal systems integrated and the fuel is provided through feed screws (if pellet or chip type). Some countries like Germany and Luxembourg have stringent policies on fuel storage for domestic houses and require separate fuel storage rooms, to be separate from the room where the unit is installed. During new builds, balloon shaped tanks are dug in next to the house to limit space usage. These systems generally consist of a combustion chamber, a heat exchanger, a fuel storage and an exhaust. Additionally, there can be an ash removal screw, a heat exchanger cleaning system, sensors to regulate an optimal combustion etc. Different combustion chamber layouts can be used here, depending on the size of the unit and type of fuel. The general three different

firing methods are feeding from the top, from either side, or from the bottom. Additionally, side and top feeds can include a moving or stationary grate and even have a water cold screw feed to prevent back-burning (Anon., 2011a). Single generation for power as well as for refrigeration is not recommended for small scale purposes. Although it is technically possible to only generate either power or cooling from the combustion of biomass, the idea does not favour the idea of high energy efficiency, which should be a vital aspect of today's technologies. This is due to the fact that the conversion efficiencies for power generation and cooling are usually very low and in order to maximise the overall system performance it is advisable to generate power and refrigeration in either combined heat and power systems or tri-generation systems.

2.5.2 Combined Dual Systems (CHP/CCH)

The concept of combining heat with power (CHP) is nothing new; however, the market share is still limited. Large scale systems are currently installed throughout the world as part of district heating systems. Small scale systems have long been difficult to manufacture on a cost-effective basis, as the major problems tended to be reliability and high production costs. Microgen, as part of the British Gas Group, offers the Sunpower (Beale & Chen, 1992, see) systems in the UK as part of a CHP system. Sunpower worked on a small Stirling free-piston engine for cogeneration using solar energy as the heat source. The Infinia Corporation is the leading manufacturer in free piston Stirling engines. Infinia produce numerous engines for military and space programs as well as a CHP system together with Enatec (2011) and Rinnai. Their engines range from 55 W to 3 kW similar as Sunpower. Together with Enatec their main focus is to increase the efficiency of generating electricity and heat from natural gas. Sunmachine have developed a Stirling engine driven by a biomass gasifier. Recently, Baxi (2011) and Whispergen (2011) have introduced a CHP system based on Stirling engine technology (with the fuel input being natural gas). These systems generate around 1 kW_{el} and a further 7.5–15 kW heat. Similar, the Dachs is a CHP unit by Senertec (2011) providing different modules running either on natural

gas, heating oil, biodiesel or rapeseed oil to produce 5.5 kW_{el} and between 10–15 kW_{th} depending on the unit.

Hawkes & Leach (2007) investigated cost-effective operating strategies for residential micro-combined heat and power. The author determines that, compared to standard practice in large scale system, heat-led strategy is not cost-effective, however, a combined approach of heat load and electricity load during winter months. In summertime it varies depending on the prime mover technology used. Thiers *et al.* (2010) studied a wood pellet Stirling engine micro-CHP unit (Sunmachine) in order to characterize its annual performance when integrated to a building. First, through a test bench experiment, both transient and steady state behaviours of the micro-CHP unit have been characterized and modelled. Then a more complete model representing a hot water and heating system including the micro-CHP unit and a stratified storage tank has been carried out. This model has been coupled to a building model. A sensitivity analysis by simulation shows that the dimensioning of different elements of the system strongly influences its global energy performance. Several other manufacturers are involved in the development of Stirling engines for small scale cogeneration applications, notably Enatec and BG have a 1 kW system; SOLO is working on gas fired units with an output ranging between 2–9 kW and Baxi in the UK are now commercialising a 1 kW_{el} unit for domestic applications. Field tests of the Enatec system have shown it to be a reliable machine, which can operate unattended in a micro cogeneration system providing a home with up to 1 kW of power at 10% efficiency. They are currently working on improving this efficiency and reducing manufacturing costs (van der Woude *et al.*, 2004). Stirling engines have limited demonstration projects because they are still considered an emerging technology, the investment cost for the unit is still about twice as high as an internal combustion engine driven cogeneration unit of the same capacity. Thomas (2008) did some comparative testing on four different micro-CHP units; the SenerTec "Dachs" (natural gas, heating oil or biodiesel), the SOLO Stirling 161 (natural gas and LPG), the PowerPlus Technologies ecopower unit (natural gas and LPG); and the Micro-CHP SM5A by Stirling Denmark (biogas and natural gas). Although, different operation procedures would lead to non-comparable results, the author claims that SenerTec "Dachs" provides the highest electric efficiency (27.7%), the SOLO Stirling unit

reaches highest overall efficiencies (98.5%) and the ecopower unit offers lowest emissions ($CO = 0.1\ mg/m^3$; $NO_x = 8.4\ mg/m^3$). Hence, it is impossible to declare an overall ranking. From an economic point of view the cost of the units is approximately 3,000 € per kW_{el} and does not allow low beneficial operation in single-family houses. This is primarily due to highly fluctual heat demand and hence prevents a sufficient yearly time of operation. The author further discusses that an operational use of approximately 5,000 hr/a should be feasible to meet a good payback period.

2.5.3 Tri-generation Systems

Combined cooling, heating and power (CCHP) is usually made up by a prime mover and a thermally activated technology. The prime mover in most cases generates electricity and the waste heat is used for heating and/or cooling purposes. Combined heat cooling and power systems have been in commercial production for decades. Typically, the chillers have capacities of 30 $kW+$ and are fed by waste heat from industrial processes. They can offer significant advantages over single powered systems since waste heat is, by definition, free and the cost of using it small. In recent years combined heat and power technology has been applied to smaller units. Sun (2008) used the waste heat from a gas engine driving a vapour compression chiller to power an absorption chiller. The coefficient of performance for the system was 1.84 under optimal conditions. Lin *et al.* (1996) demonstrated that a small domestic diffusion absorption refrigerator could be powered by waste heat from a diesel engine albeit with a low COP of 0.016 to 0.031. At such a low COP it is questionable whether the additional expense in utilizing waste heat in this way could be justified. Another study by Najjar (1996) used a proportion of gas turbine exhaust heat to drive an aqua-ammonia absorption system with an evaporator connected to an air pre-cooler inlet supply to the GT compressor, and found an enhancement of about 21% and 28% in overall increase in efficiency and specific fuel consumption. Trigen Energy Corporation started a tri-generation project at Kansas City in USA in spring of 1997. This tri-generation plant supplies over 8,000 tons (28,135 kW) of cooling to eleven buildings in the downtown business district, on a base of cogeneration. Later, more than 10 similar systems

were built in the USA. Currently a system installed in Augsburg (D) produces 7.6 MW_{el} and 15 MW_{th} with an overall performance of 81.2%. In Pfaffenhofen (D) the installed plant is based on steam power technology and generates 40 GWh_{el}/a with an additional heat production of 120 GWh_{th}/a and a 18 GWh/a of refrigeration (Oberweis, 2010, see).

2.5.4 Future Trends

Recent developments in third generation biofuels have made use of tri-generation units to process the fuels. Additionally, hydrogen can be produced from left over heat in tri-generation systems. The general idea here is to use renewable energy sources to produce third generation biofuels. Contrary to other biofuels conversion processes, the energy input during the production stage of the biofuels life cycle is entirely renewable and contributes toward the carbon neutral of the fuel. Scott *et al.* (2010) describe the challenges of producing biodiesel from algae, especially the early stages of the research. In large scale systems the carbon dioxide and nitrous oxides can be reclaimed by green algae, for their photosynthesis, to produce cleaner combustion products. Since flue gases from power plants account for almost 7% of total carbon dioxide emissions, flue gases are envisioned to have a great potential to diminish CO_2 and to provide a very promising alternative to current GHG emissions mitigation strategies (Teresa *et al.*, 2010). The laboratory studies carried out by Zeiler *et al.* (1995) using a green algae, demonstrated that this algae can efficiently utilize simulated flue gas containing high levels of carbon dioxide, as well as sulphur and nitrogen oxides, as a feedstock to produce substantial biomass. In this study several important parameters for productivity have been identified including nutrient levels. When analysing the performance of systems, it is often assumed that roughly 89% of the heat generated during the combustion can be used by the system. This is usually referred to as sensible heat, whereas the latent heat represents the heat stored in the water vapour discharged through the flue. Capturing this heat can improve the efficiency of heating boilers from roughly 82% to close to 97%, depending on the model investigated. Unfortunately, capturing this heat comes at a cost: the boiler needs to be condensing. Condensation only takes place when the flue gases within the boiler

are at their dew point of $57°C$. This entails that, in order to achieve continuous condensing operation, the heat exchanger surfaces and therefore the return water must be at this temperature. This can be achieved by using an underfloor heating system, or alternatively by running the boiler flow temperature so that it runs as low as possible for the longest time. Some companies therefore have started to install weather compensation technologies to their boilers that automatically vary the operating flow temperature in accordance with the outside temperature (Viesmann, 2011).

2.6 Conclusion

This conclusion will present added value to the thesis outline presented in the previous chapter. The world's energy consumption with an emphasis on the huge increase since WWII is presented in light of the current efforts to prevent a global increase of temperature. In order to achieve this, measures have been put into place, Copenhagen accord, 450 scenario and EU2020 targets, via increased energy efficiency along with a decrease of fossil fuels as a primary energy source. The impacts resulting from these measures are discussed in particular for the Government of Luxembourg, which is highly dependent on the import of fossil fuels.

The conversion processes for biomass show that 1^{st} generation biofuels are often involved with indirect conversion processes and transport issues. These need to be reduced to a minimum in order to be competitive financially and environmentally with other fuel technologies. This is in particular interesting for Luxembourg due to its relatively small size in relation to other countries in Europe. The products released during the combustion of biomass are discussed according to their health risk and the regulations put in place to reduce their impact. The introduction of 3^{rd} generation biofuels show further potential to reduce emission, however, this has not yet been tested on small scale systems.

Power generation for small scale biomass applications are limited to field trials or have very little market introduction, although there has been a huge increase in biomass boilers in the last decade. Although being the oldest technology encountered, the Stirling engine has yet again become popular with research

teams and designers. This is reflected in this thesis by using a γ–type Stirling engine for power generation.

The impact of CFC's and HFC's etc. has renewed the interest in absorption cooling in small scale applications over the last few years when driven by solar energy. Thermo-chemical accumulators however, should show a viable use in biomass applications. In particular due to the aspect of requiring a heat sink, there is a potential for using waste heat from Biomass to drive the absorption process in combined systems.

The literature has shown that reducing the energy used can be achieved by increased energy efficiency. This can be accomplished by converting the maximum possible amount of available energy released during the combustion of biomass into useful outputs. Hence, combined generation systems or better still trigeneration will be investigated during the course of this study. Quad-generation does show a viable option for large scale units at the moment, however the amount of increased capital cost does not yet seem feasible for small scale units, which is the concern of this thesis as it focuses on the domestic market in Luxembourg. In this thesis the following unique and new tasks will be conducted to satisfy the use of biomass for the Luxembourgish market:

- Extended analytical modelling of the Stirling engine. A 500 W engine will be built and tested.
- Extensive tests on the different biomass fuels suitable for the Luxembourgish market will be tested in view of thermal efficiency, emissions, and suitability for the Luxembourgish market.
- CFD tests will be conducted in order to optimise the combustion process
- Extended analytical modelling of the thermo-chemical accumulator absorption. A 7 kW unit will be driven with waste heat from biomass combustion and the results will be compared to the analytical model.
- An analytical model of a combination of the technologies encountered will be compared to the empirical data gathered during the test stages.

Chapter 3

Theory of Biomass Combined Generation Technologies

3.1 Introduction

This chapter presents the theory necessary for the development of numerical and computational models to predict the performance of biomass combined generation schemes. All the symbols used are defined in the nomenclature, unless otherwise stated. The first and second law of Thermodynamics as well as the energy conservation, equation of mass and the Van der Waal's equation of state will be briefly highlighted as they will be used as the foundations for the models developed. Equations (3.1)–(3.4) have been adopted from Cengel & Boles (1997). The three major components, the biomass combustor, the Stirling engine as well as the refrigeration unit will be investigated separately to outline a working model. A combination of all the components will then result in a combined generation unit. The 1^{st} law of Thermodynamics, or the conservation of energy principle, can be applied to open systems and is written mathematically as follows:

$$Q - W = \Delta H + \Delta E_K + \Delta E_P \tag{3.1}$$

Assuming there is no displacement ($W = 0$) and no change in kinetic nor potential energy of the working substance, equation (3.1) reduces to:

$$Q = \Delta H \tag{3.2}$$

This means that the heat released during open system combustion is equal to the change in enthalpies. The change in enthalpy during combustion is made up from two components: the enthalpy of formation, which is constant; and the change in sensible enthalpy during the rise in temperature.

$$H_{tot} = {H_f}^0 + (H - H_0) \tag{3.3}$$

Next to the conservation of mass and energy principles, the Van der Waals equation of state (3.4) will be used to derive the model of the Stirling engine.

$$\left(P + \frac{a}{V^2}\right)(V - b) = R\,T \tag{3.4}$$

where a and b are Van der Waal's constants

3.2 Theory of the Combustion of Solid Biomass

Combustion is a sequence of exothermic chemical reactions between a fuel and an oxidant and is a convenient way of converting the stored solar energy in a biomass into a useful form such as heat. However, the amount of useful heat available depends on several factors, for example the type of biomass, the moisture content, the amount of air available to the combustion, and the combustion environment as shown in Fig. 3.1. There are usually two types of enthalpy associated with the complete combustion process:

- the enthalpy of formation
- the enthalpy of combustion

The enthalpy of formation, described in equation (3.3), of a compound is the change of enthalpy due to the formation of 1 mole of a substance, at a specified

Figure 3.1: Combustion pot for wood pellet combustion

state due to its chemical composition. This is based on the state of its constituent elements in their standard states. The enthalpy of combustion is the amount of energy released as a combustible compound is burned during a steady-flow process at a specified state (298 K and 1 atm). These enthalpy values can be found in textbooks in tabulated form (Keating, 2007). A more convenient way of presenting the energy content and comparing fuels accordingly are heating values, also known as calorific values. They represent the energy released when a combustible compound is burnt completely in a steady-flow process and the products are returned to the state of the reactants. They are usually referred to as the higher heating value (HHV) and the lower heating value (LHV). The difference between the two is that the higher heating value includes the loss of energy during combustion due to the presence of water. New condensing boilers have the capability to recover this heat, present as water vapour in the flue gases, and by doing so, increase the efficiency of the boiler. The calorific values can be determined in a bomb calorimeter and are presented in MJ/kg. In the

absence of a bomb calorimeter, there are published correlations to determine the heating values. However, these formulas usually take into account the chemical composition of the fuel and this is often not known at priori. All fuels in this study have been analysed in a bomb calorimeter and for the purpose of this project only complete combustion will be investigated. Consider the following general hydrocarbon fuel combustion:

$$Fuel + Air \rightarrow Products\ of\ combustion + Energy \tag{3.5}$$

$$\begin{aligned} &[C_{R1} + H_{R2} + O_{R3} + N_{R4} + S_{R5}] + R_6[O_2 + 3.76N_2] \\ &\rightarrow P_1\, CO_2 + P_2\, H_2O + P_3\, NO_2 + P_4\, SO_2 + P_5\, N_2 + P_6\, O_2 \end{aligned} \tag{3.6}$$

Note that the composition of air is simplified to $O_2 + 3.76\, N_2$. The stoichiometric air to fuel ratio $\left(\frac{A}{F}\right)_{stoi}$ in which P_6 is zero can be derived from the equation of complete combustion:

$$\begin{aligned} \left(\frac{A}{F}\right)_{stoi} &= \frac{(M_{O_2} + 3.76 \times M_{N_2})\, R_6}{M_C R_1 + M_H R_2 + M_O R_3 + M_N R_4 + M_S R_5} \\ &= \frac{137.28\, R_6}{12R_1 + R_2 + 16R_3 + 14R_4 + 32R_5} \end{aligned} \tag{3.7}$$

The equivalence ratio is commonly used to quantitatively indicate whether a fuel-oxidiser mixture is rich, lean or stoichiometric. It is the ratio of stoichiometric air to fuel ratio to that actually used:

$$\Phi = \frac{\left(\frac{A}{F}\right)_{stoi}}{\left(\frac{A}{F}\right)_{act}} \tag{3.8}$$

In the presence of excess air, additional oxygen will be present in the products of the combustion.

3.2.1 Adiabatic Flame Temperature

The energy released during the combustion process in open systems can be determined by the following equation,

$$Q = \dot{m}_{fuel}\, LHV\, \eta_{cc} \tag{3.9}$$

The useful net heat released during the combustion is proportional to the LHV, rather than the HHV, of a fuel as some of the heat liberated is consumed in converting the hydrogen reaction into water vapour. This water is subsequently evaporated and possibly superheated to the final mixture temperature. And the heat released during the combustion according to equation (3.5), therefore becomes:

$$Q = (\dot{m}\, cp)_{air}\, \Delta T \tag{3.10}$$

Assuming that the open combustion takes place at constant pressure, the heat capacity for constant pressure is used rather than constant volume. The temperature difference denotes the difference between the temperature of the flue gas leaving the combustion chamber and the temperature of the air introduced into the combustion chamber. This inlet temperature is often at ambient temperature but can be raised by means of heat recuperation or introduction of excess heat from the flue gases or other process streams. It is often required to know the temperatures in the combustion chamber. If within the combustion chamber there is no work transfer and if any changes in kinetic and potential energies are negligible, equation (3.2), then the chemical energy released during the combustion is transferred internally to raise the temperature of the combustion products. Not all the energy released is utilised and it is known that this happens through radiation and conduction losses to the surroundings. The smaller the heat loss, the larger the temperature rise will be. Hence, the maximum possible temperature is reached when the heat transfer is reduced to zero. This condition is very significant and this temperature is known as the adiabatic flame temperature (of an adiabatic process, $Q = 0$). Since the enthalpies of reactants and products are functions of temperatures which is unknown at priori, an iterative technique is required with an initial guess temperature until equation (3.2) converges.

3.2.2 Dissociation of Biomass Combustion Products

The adiabatic flame temperature, discussed in the previous section, is however only a theoretical temperature. Some of the heat will be unaccounted for by means of losses; and additional heat will be lost due to the presence of chemical equations other than equation (3.6). As a matter of fact several chemical reactions take place depending on the amount of oxygen available and the product's temperature. Take for instance the burning of pure carbon, which is released during the initial stages of the combustion of a biomass, combined with oxygen to form carbon dioxide:

$$C + O_2 \leftrightarrow CO_2 + E \tag{3.11}$$

The energy released E during this exothermic reaction, will contribute towards raising the temperature inside the combustion chamber. Under certain conditions, there may be enough energy present for the carbon dioxide to undergo a reverse reaction. This reverse reaction is endothermic and will lower the temperature of the combustion products. Dissociation of individual species of fuels implies that the combustion process of some of the reactions is reversible. Hence, some of the energy indicated in equation (3.11) will be lost. The reaction equations below, will adjust themselves to an equilibrium state. This phenomenon is known as dissociation and it is responsible for lowering the combustion temperature. At some temperature T, a fraction of ν moles of any species among the products dissociate. For the C-H-O-N system, the complete chemical equilibrium proposed by Way (1976) is used. The following reverse reactions need to be included in

the stoichiometric equation of combustion.

$$\begin{aligned} CO + 0.5\,O_2 &\rightleftharpoons (1-\nu)\,CO_2 \\ H + H &\rightleftharpoons (1-\nu)\,H_2 \\ O + O &\rightleftharpoons (1-\nu)\,O_2 \\ N + N &\rightleftharpoons (1-\nu)\,N_2 \\ 0.5\,O_2 + 0.5\,N_2 &\rightleftharpoons (1-\nu)\,NO \\ 0.5\,H_2 + OH &\rightleftharpoons (1-\nu)\,H_2O \\ H_2 + 0.5\,O_2 &\rightleftharpoons (1-\nu)\,H_2O \end{aligned} \tag{3.12}$$

Generally a dissociated reaction takes the form,

$$\nu_{R1}\,R_1 + \nu_{R2}\,R_2 \rightleftharpoons \nu_{P1}\,P_1 + \nu_{P2}\,P_2 \tag{3.13}$$

A general equilibrium constant for any reverse reaction is given by:

$$K_p = \frac{n_{P1}\,\nu_{P1}\,n_{P2}\,\nu_{P2}}{n_{R1}\,\nu_{R1}\,n_{R2}\,\nu_{R2}} \tag{3.14}$$

In order to determine K_p, the Gibbs function, adopted from Cengel & Boles (1997), is commonly used:

$$\Delta G = V\Delta P - S\Delta T \tag{3.15}$$

Assuming equilibrium, the temperature is constant ($\Delta T = 0$) and applying the ideal gas law, then the above equation becomes:

$$\Delta G = n\,R\,T\,\frac{\Delta P}{P} \tag{3.16}$$

Integrating between state 1 and 2, (assuming n, R and T being constant):

$$G_2 - G_1 = n\,R\,T\,\ln\left(\frac{P_2}{P_1}\right) \tag{3.17}$$

For a reversible reaction with two reactants and two products the above equation becomes:

$$G_P - G_R = n\,R\,T\,\ln\left(\frac{P_{R1}\,P_{R2}}{P_{P1}\,P_{P2}}\right) \tag{3.18}$$

The bracket on the right hand side of the above equation is known as the equilibrium constant K_p; values for $\ln(K_p)$ are published in tables as shown in Appendix A. Now, equation (3.14) can be solved for ν for each individual constituent to determine the dissociated form of the combustion equation.

3.3 Theory of Heat Transfer in a Shell and Tube Heat Exchanger

Heat exchangers are devices especially designed to enhance the exchange of heat transfer between two media. Shell and tube heat exchangers are generally bigger in size than the double-pipe category and less complex than cross-flow heat exchangers. They have an outer shell with flow passages, which may consist of one, or more passes of fluid, flowing past a number of tubes running in parallel to each other carrying the second fluid. The shell may have baffles, and the tubes may have fins on the external and even internal surfaces to improve the heat transfer between the two fluids. Figure 3.2 shows a cross-sectional view of a single pass with numerous tubes shell and tube heat exchanger. This heat exchanger is modelled in a 3D software package and will later be used in the testing.

3.3.1 Heat Transfer and Overall Heat Transfer Coefficient

There are two aspects associated with heat transfer in heat exchangers: the heat loss from the hot fluid or the heat loss gain by the cold fluid,

$$Q = \dot{m}\,cp\,\Delta T \tag{3.19}$$

and the heat exchange from one fluid (hot) to the other (cold):

$$Q = A\,U\,\Delta T \tag{3.20}$$

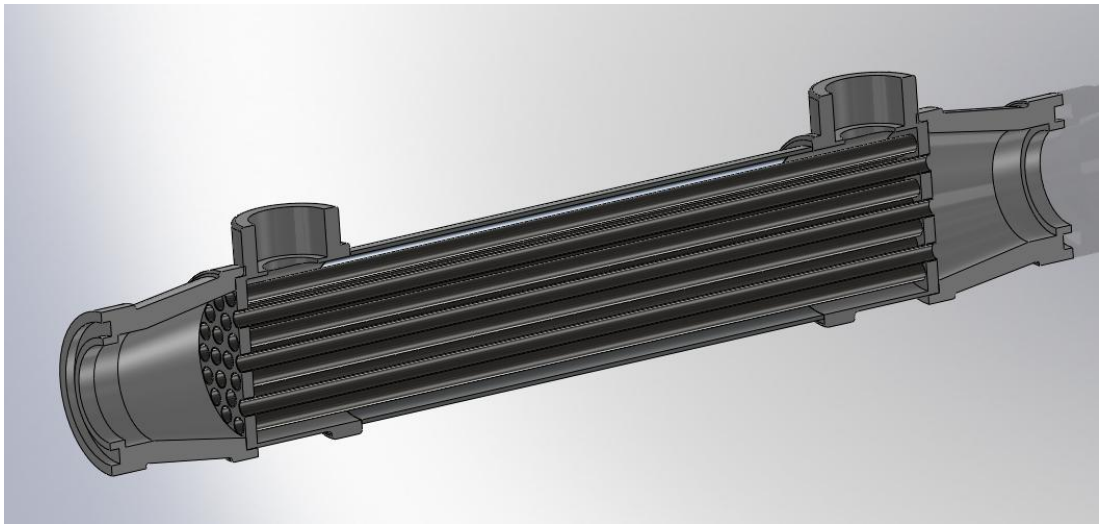

Figure 3.2: Cross sectional view of a 3D representation of the heat exchanger

The analysis and design of heat exchangers in this project is based on the works

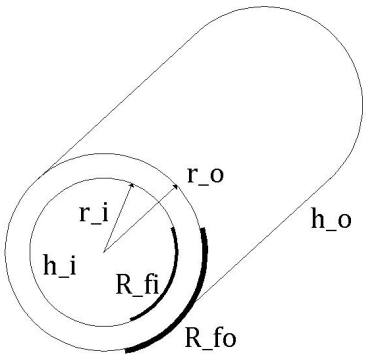

Figure 3.3: Cross-sectional view of a tube

of Kays & London (1984) on compact heat exchangers. The overall heat transfer coefficient for a heat exchanger of tubular configuration is dependent on the reference side of the tube. Figure 3.3 is a sketch of a tube of material conductivity k and of length L. With reference to the tube inner radius and outer radius

respectively, the overall heat transfer coefficient can be written as follows:

$$U_i = \frac{1}{\frac{1}{h_i} + R_{fi} + \frac{r_i}{k}\ln\left(\frac{r_o}{r_i}\right) + \frac{r_i}{r_o}R_{fo} + \frac{r_i}{r_o h_o}} \tag{3.21}$$

$$U_o = \frac{1}{\frac{r_o}{r_i h_i} + \frac{r_o}{r_i}R_{fi} + \frac{r_o}{k}\ln\left(\frac{r_o}{r_i}\right) + R_{fo} + \frac{1}{h_o}} \tag{3.22}$$

The convection heat transfer coefficient h can be determined through the scaling parameter approach described by Kays & London. All parameters are usually dependent on the type of heat exchanger used. The parameters below are based on the shell and tube heat exchanger shown in Fig. 3.2. The hydraulic diameter d_H represents the ratio of the two important size parameters of a heat exchanger, namely the wetted area and the perimeter.

$$d_H = \frac{4A}{P_x} \tag{3.23}$$

The factor 4 is included for convenience. For flow in a circular pipe the hydraulic diameter thus becomes equal to the pipe internal diameter. The Reynolds number is the ratio of the inertial forces to the viscous forces. The value of Re determines the flow regime, whether laminar or turbulent. Both friction and the heat transfer coefficient are strongly dependent on the type of flow, thus Re is used as the independent variable in the presentation of flow, friction and heat transfer data.

$$Re = \frac{\rho\,\bar{V}\,d}{\mu} \tag{3.24}$$

There are two methods of presenting the convective heat transfer coefficient h, either using the Stanton (St) or Nusselt (Nu) number. The physical significance of St is that it can be related to the ratio of the convection heat transfer to the thermal capacity of the flowing fluid.

$$St = \frac{A_{cs}}{A} \times \frac{T_o - T_i}{T_w - T_f} \tag{3.25}$$

Thus the value of St can be obtained directly from the heat exchanger dimensions and temperature measurements. The Nusselt number is the other standard method for the presentation of heat transfer data and is usually presented in graphical or empirical form in terms of the Prandtl and Reynolds number or in the following equation.

$$Nu = \frac{h\,d}{k} \tag{3.26}$$

The Nusselt number on the inside of a tube, in case of forced convection (presence of a pump or fan), can be determined as follows Kays & London:

- laminar flow $Re < 2500$ then $Nu = 4.1$
- turbulent flow $Re > 10000$ then $Nu = 0.023\,Re^{0.8}\,Pr^{n}$

where $n = 0.3$ if fluid is being cooled and $n = 0.4$ if fluid is being heated.

The Prandtl number is defined as the ratio of kinematic viscosity to the thermal diffusivity and thus represents the ratio of the viscous to the thermal boundary layers.

$$Pr = \frac{cp\,\mu}{k} \tag{3.27}$$

3.3.2 Analysis of a Shell and Tube Heat Exchanger

The temperature difference is not constant over the length of a heat exchanger; therefore this temperature distribution must be taken into account in any evaluation. The logarithmic mean temperature method is used to achieve this. It is assumed that the shell fluid is fluid B, whereas the tube fluid is represented by fluid A. The temperature profile is not as straight forward as for a double-pipe heat exchanger, for which the logarithmic mean temperature difference is given below. The heat transfer δQ across any hot section δx for a small section of area δA.

$$\delta Q = U\,\delta A\,\Delta T \tag{3.28}$$

Defining the temperature difference at any section, by the overall temperature difference,

$$\frac{\delta \Delta T}{\Delta} = \frac{\delta T_A - \delta T_B}{\frac{Q}{U}\,\delta A} \tag{3.29}$$

Equation (3.29) needs to be integrated with respects to the inlet and outlet fluid temperatures. It can then be rewritten in the case of a concentric heat exchanger as follows:

$$\Delta T_m = \frac{\Delta T_o - \Delta T_i}{\ln\left(\frac{T_o}{T_i}\right)} \tag{3.30}$$

Shell and tube heat exchangers usually have a more complicated temperature profile: for example due to the presence of baffles resulting in multi-directional fluid flow on the shell-side. These baffles are introduced to increase shell side fluid velocities, turbulences and mixing. The LMTD has to be corrected to account for the true or effective temperature for cross flow and multi-pass flow arrangements. The correction factor uses two dimensionless terms; which are related to all four temperatures.

$$X = \frac{T_{co} - T_{ci}}{T_{hi} - T_{ci}} \tag{3.31}$$

$$Z = \frac{T_{hi} - T_{ho}}{T_{co} - T_{ci}} \tag{3.32}$$

And the heat transfer term therefore changes to

$$Q = U\ A\ F_{LMTD}\ \Delta T_m \tag{3.33}$$

where F_{LMTD} is a correction factor as defined by Bowman *et al.* (1940):

$$F_{LMTD} = \frac{\frac{\sqrt{Z^2+1}}{Z-1}\ln\left(\frac{1-\Psi}{1-Z\Psi}\right)}{\ln\left(\frac{\frac{2}{\Psi}-1-Z+\sqrt{Z^2+1}}{\frac{2}{\Psi}-1-Z-\sqrt{Z^2+1}}\right)} \tag{3.34}$$

where:

$$\Psi = \frac{1-\frac{XZ-1}{X-1}}{Z-\frac{XZ-1}{X-1}} \tag{3.35}$$

For the purpose of this study, the Bowman equation (3.34) was plotted in Fig. 3.4.

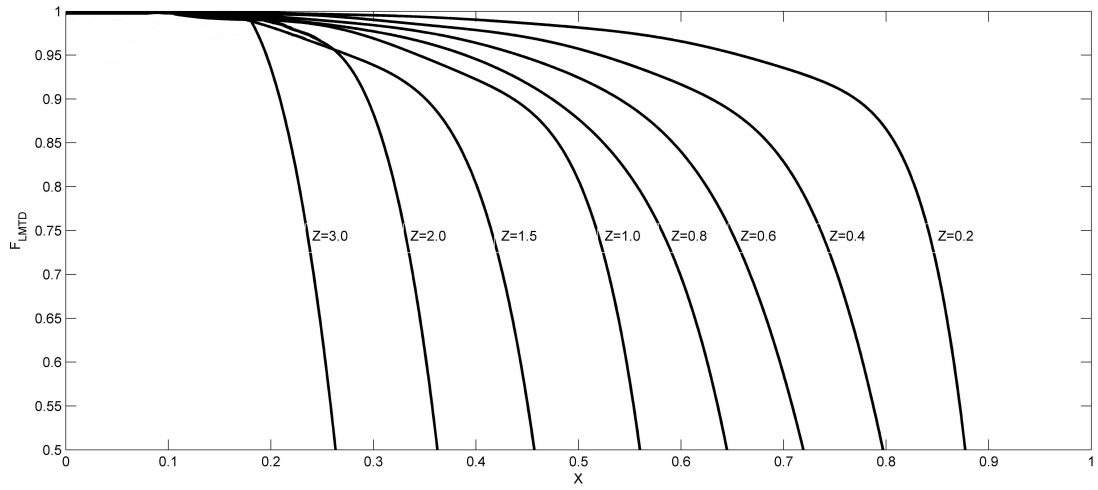

Figure 3.4: Correction factor plot for a shell and tube heat exchanger with one shell pass

3.3.3 Determination of Pressure and Friction Losses

The fluid friction associated with the flow through heat exchangers is accompanied by a pressure drop across the entire heat exchanger and has the effect of increasing the pumping power required, or in the case of a Stirling engine reducing the net power output of the engine. In any case this pumping loss has to be minimised. The pressure drop ΔP is due to fluid friction as it flows through the heat exchanger. Newtons law of viscosity states that shear stress τ between adjacent layers of fluid is proportional to the velocity gradient in these layers normal to the flow direction. In order to represent fluid flow, the mean bulk mass flow rate is often used, with the dynamic viscosity being a measure of the internal friction. Bretsznajder (1971) published graphs of dynamic viscosity *vs.* temperature and it is assumed throughout this thesis that the dynamic viscosity does not vary with pressure over the range of pressures used. The following equation, based on the temperature and the Sutherland constant can be used to determine the dynamic viscosity for gases.

$$\mu = \mu_0 \left(\frac{T_0 + T_{suth}}{T + T_{suth}} \right) \left(\frac{T}{T_0} \right)^{1.5} \tag{3.36}$$

The viscosity of liquids is more complex, as the additional forces between molecules become more important. This leads to additional contribution to the shear stress. The viscosities of the fluids in this work are based on published empirical data (Douglas *et al.*, 2005). The frictional drag force F is related to the shear stress τ as follows:

$$F = \tau\, A \tag{3.37}$$

Kays & London define a coefficient of friction Cf as the ratio of the shear stress to the dynamic head:

$$Cf = \frac{\tau}{0.5\,\rho\,\bar{V}^2} \tag{3.38}$$

Rewriting equation (3.37) in form of volume and diameter and combining with equation (3.38) gives,

$$F = \frac{2\,Cf\,\rho\,\bar{V}^2\,V}{d} \tag{3.39}$$

In the case of steady flow assumptions, the frictional drag force is equal to pressure drop force, thus:

$$F + \Delta P\, A_{cs} = 0 \tag{3.40}$$

Substituting for F from equation (3.39), the pressure drop is given by:

$$\Delta P + \frac{2Cf\rho\bar{V}^2V}{dA} = 0 \tag{3.41}$$

The pressure drop can be negative or positive, depending on the direction of flow. However the second term in equation (3.41) is always positive. As this statement violates the momentum conservation principle in the case of reversing flow, the friction coefficient can be multiplied by the Reynolds number to determine a Reynolds friction coefficient. Since the Reynolds number is always positive by definition, the pressure drop can be evaluated as follows:

$$\Delta P = -\frac{2\,Cf_{Re}\,\mu\,\bar{V}\,V}{d^2\,A} \tag{3.42}$$

This equation is more appropriate as it is always related to the sign of the velocity. Traditionally empirical data on the coefficient of friction is presented as a function of the Reynolds number and the formulas presented by Kays and London are

used depending on the heat exchanger configuration. The graph for circular pipes (Moody diagram) has led to a simplified equation depending on Reynolds numbers. The Blasius equation is valid for turbulent flow in smooth circular pipes ($Re > 4000$):

$$Cf_{Re} = 0.0791\, Re^{0.75} \tag{3.43}$$

3.4 Theory of the Stirling Engine

A Stirling engine as shown in Fig. 3.5, is a hot gas engine that makes use of the expansion of gases with temperature. From the ideal gas law it is obvious that whilst keeping the gas and its mass unchanged, the volume, the temperature and the pressure will change. Generally an engine consists of the following major components: a heater, a cooler, a regenerator, a compression space and an expansion space. Depending on the engine configuration there may be one or two cylinders containing the two working spaces. Ideally the heater and the cooler are kept at constant temperature to allow for continuous operation. Gamma type engines have a displacer and a power piston that are contained in two different cylinders. The advantage of this is the complete separation of the heater and cooler, which allows for more freedom when designing the heat source and heat sink for the engine. However, this increases the dead volume somewhat in comparison to alpha and beta configurations. Additionally, a small portion of the expansion process needs to take place in the compression space which leads to a reduction of specific power output. Gamma engines are therefore used when the advantages of having separate cylinders outweigh the specific power disadvantage. In order to evaluate the performance of a Stirling engine, the volume variations of the compression and expansion spaces with respect to the crank angle need to be determined. These variations in volume behave in a sinusoidal form, but in different ways according to the engine layout (i.e. alpha, beta, and gamma). Gustav Schmidt published an analysis in 1871 in which he obtained closed form solutions of the ideal isothermal model for the special case of sinusoidal volume variations of the working spaces with respect to the crank angle (Steimle *et al.*, 2007). The top dead volumes for expansion (DV_e) and for compression (DV_c) do not change with the crank angle (θ). The swept volume for the expansion space

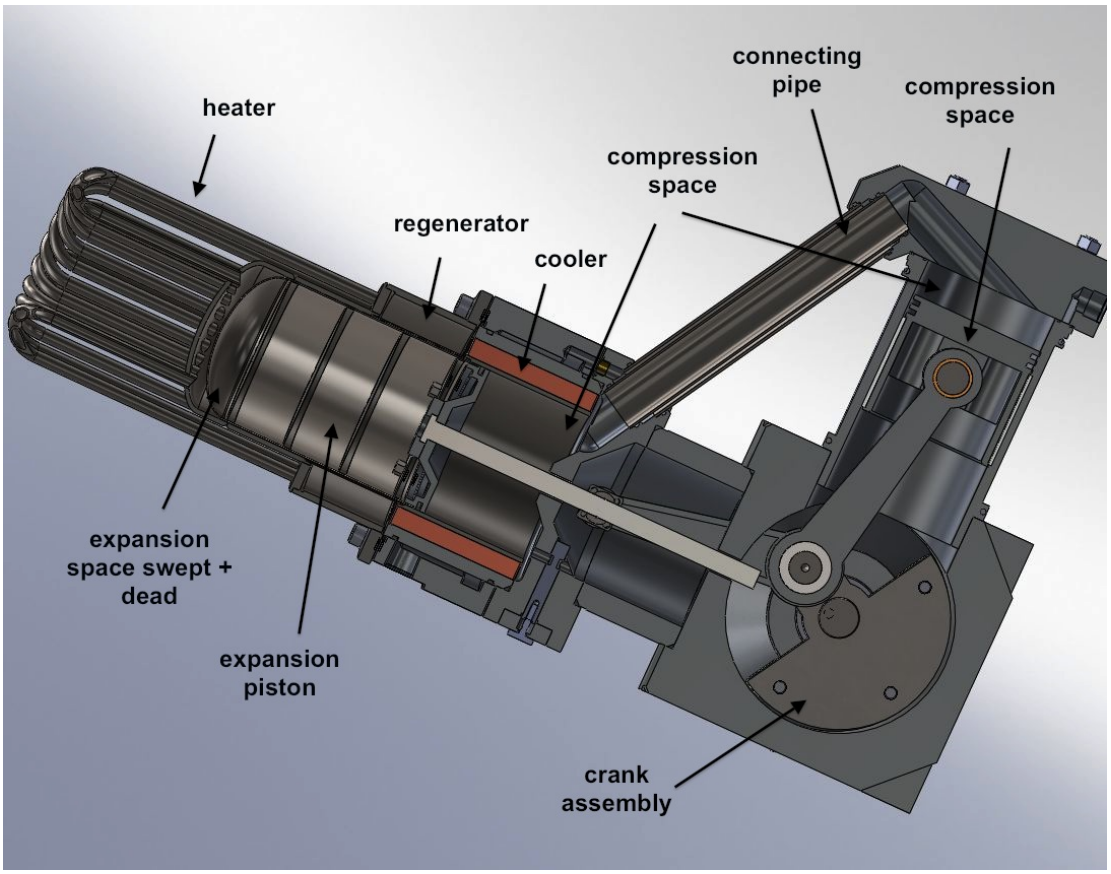

Figure 3.5: γ-type Stirling engine (cross-sectional cut)

varies with the crank angle and it will be of minimum value when the crank angle is 0°; and maximum when the crank angle is 180° (refer to Fig.3.6). Here, the convention is used to consider a crank angle of 0° as the position of 12 o'clock on a watch. The total volume for the expansion space then is the algebraic sum of the dead and swept expansion volumes as follows:

$$V_e = DV_e + 0.5SV_e\,(1 - \cos\theta) \tag{3.44}$$

The swept volume for the compression space (SV_c) varies with the crank angle. However, it is out of phase with the displacement of the expansion piston by 90°, which can be seen on Fig. 3.6. Additionally, some of the gas will be compressed in the cooler by the downward motion of the displacer piston. This additional

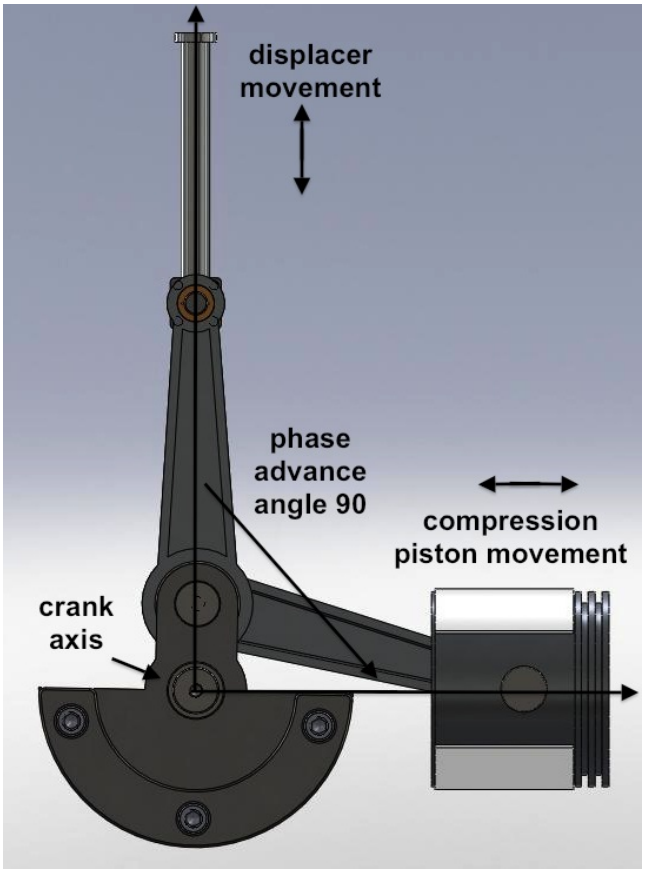

Figure 3.6: Diagram for the convention of crank angle and piston movement

compression space is the space in the displacer cylinder not occupied by the expansion space at this time. Hence it is of maximum value when the expansion space is at its lowest and vice versa. The total volume for the compression space then is the algebraic sum of all dead and swept compression spaces as follows:

$$V_c = DV_c + 0.5SV_e\,(1 + \cos\theta) + 0.5SV_c\,(1 - (\cos\,(\theta - 90°))) \tag{3.45}$$

3.4.1 Stirling Engine Cycle Analysis

The Stirling cycle is defined as a heat power cycle using isothermal compression and expansion and constant volume heating and cooling. The first cycle analysis published on Stirling engines is referred to as the Schmidt analysis. This analysis

gives a closed form solution rather than a prediction of the real cycle. This shortcoming can be derived directly from some of the assumptions of the Schmidt theory:

- there is no pressure nor heat loss in the heat exchanger
- the expansion process and the compression process are isothermal
- the working gas behaves as an ideal gas
- the expansion and compression dead spaces are at constant temperature during the cycle
- the regenerator gas temperature is an average of the expansion and compression temperature
- the expansion and compression volume variations are of the sinusoidal form

Figure 3.7 shows a layout of the engine divided in five cells with four walls separating them. For simplicity it is assumed that at the beginning of the cycle, the working gas flows from the compression space to the expansion space via the cooler, the regenerator and then the heater. These volumes are seen as open thermodynamic systems with a variable mass of working gas. The starting point of the analysis is that the total mass of gas in the engine is constant, thus:

$$m = m_c + m_k + m_r + m_h + m_e \tag{3.46}$$

Substituting into the ideal gas law, gives:

$$m = \frac{P\left(\dfrac{V_c}{T_k + \dfrac{V_k}{T_k} + \dfrac{V_r}{T_r} + \dfrac{V_h}{T_h} + \dfrac{V_e}{T_h}}\right)}{R} \tag{3.47}$$

This definition for the mass can be rewritten, whilst substituting equations (3.44) and (3.45) as follows:

$$m = \frac{P\,SV_e}{2\,R\,T_k}\left[\left(\varphi + \frac{T_k}{T_h} + \frac{SV_c}{SV_e}\right) - \frac{T_k}{T_h}\cos\theta - \frac{SV_c}{SV_e}\cos\left(\theta - 90^\circ\right)\right] \tag{3.48}$$

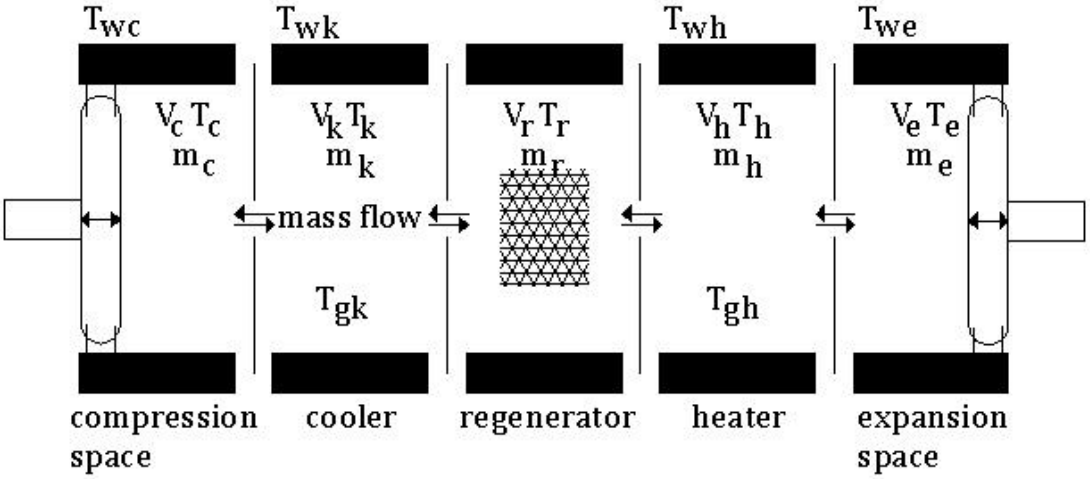

Figure 3.7: Five engine cells with separating walls

where, $\varphi = 2\frac{T_k}{T_h}\frac{DV_e}{SV_e} + 2\frac{V_r}{SV_e}\frac{T_k}{T_r} + 2\frac{T_k}{T_h}\frac{V_h}{SV_e} + 2\frac{T_k}{SV_e}\frac{V_k}{SV_e} + 1 + 2\frac{DV_c}{SV_e}$

A trigonometric substitution, derived from Pythagoras' right angle triangle, and applying standard trigonometric formulae, the following three parameters (t, v and ζ) can be deriveded and equation (3.48) can be rewritten in respect of pressure.

$(t = \frac{T_k}{T_h},\ v = \frac{SV_c}{SV_e}$ and $\zeta = \sqrt{v^2 + t^2})$

$$P = \frac{2\,R\,m\,T_k}{SV_e\,(\kappa - \zeta\cos(\beta - \theta))} \tag{3.49}$$

where, $\beta = \tanh\left[\frac{SV_c}{SV_e}\frac{T_h}{T_k}\right]$, $\chi = \frac{\zeta}{\kappa}$ and $\kappa = \varphi + \frac{T_k}{T_h} + \frac{SV_c}{SV_e}$

Equation (3.49) can be rewritten as follows:

$$P = \frac{2\,R\,m\,T_k}{SV_e\,[\kappa\,(1 - \chi\cos(\beta - \theta))]} \tag{3.50}$$

The mean pressure charge of the engine can be determined by integrating equation (3.50) over an entire cycle.

$$P_{mean} = \frac{2\,R\,m\,T_k}{SV_e\left(\kappa\sqrt{1+\chi^2}\right)} \tag{3.51}$$

Since the mean pressure charge is known at priori, equation (3.51) can be rewritten to determine the total mass of gas inside the engine.

$$m = \frac{P_{mean}\,SV_e\,\kappa\sqrt{1+\chi^2}}{2\,R\,T_k} \tag{3.52}$$

Now, substituting equation (3.51) into equation (3.50) will give a new equation for the engine pressure:

$$P = \frac{P_{mean}\sqrt{1-\chi^2}}{\kappa\zeta\cos\left(\beta-\theta\right)} \tag{3.53}$$

With regards to equation (3.53), in the particular case when $\cos\left(\beta-\theta\right) = -1$ then P becomes the minimum possible pressure inside the engine. Similarly, when $\cos\left(\beta-\theta\right) = 1$, then the pressure becomes the maximum possible pressure inside the engine. The work done by the system over a complete cycle is given by the cyclic integration of pressure in respect of volume ($P\delta V$):

$$\begin{aligned} & = W_e + W_c \\ W & = \int P\delta V_e + \int P\delta V_c \\ & = \int P\left(\frac{\delta V_e}{\delta\theta} + \frac{\delta V_c}{\delta\theta}\right)\delta\theta \end{aligned} \tag{3.54}$$

The net work done by the engine is the sum of the work done by the expansion and compression spaces. In order to determine this, the pressure from equation (3.53) as well as the derivatives of the expansion and compression volumes, equations (3.44) and (3.45) respectively, can be substituted into the equation for the work, equation (3.54), and integrated:

$$W_e = \frac{P_{mean}\,SV_e\,\pi\,\chi\,\sin\beta}{1+\sqrt{1-\chi^2}} \tag{3.55}$$

$$W_c = -\frac{P_{mean}\, SV_e\, \pi\, \chi\, t\, \sin\beta}{1+\sqrt{1-\chi^2}} \tag{3.56}$$

The total work output is then the sum of the work from the expansion and compression space and the indicated power output of the engine and the thermal efficiency can be determined as follows:

$$\dot{W} = (W_e + W_c) \times f \tag{3.57}$$

$$\eta_{th} = 1 - \frac{T_k}{T_h} \tag{3.58}$$

3.4.2 Third Order Design Method for Stirling Engines

The analysis in this work is based on the published work and third order method presented by Finkelstein as well as Urieli & Berchowitz (1984). This method has been proven an adequate tool for simulating Stirling engine performance. The model presented by them had to be reconfigured prior to being applied to the configuration of the engine used in this setup. Additionally, the heater, regenerator and cooler configurations had to be remodelled. In the previous analysis, the temperature in the compression and expansion space were kept constant. However, they will vary over the cycle due to the changes in pressure and volume in the respective working spaces. As a matter of fact the enthalpies flowing across the interfaces (ck) and (he), carry the respective adjacent temperatures and they are thus dependent on the direction of the flow of the gas. Applying the conservation of energy for the working gas to a generalised cell of the engine, the following equation can be written:

$$\delta Q + (cp\, T_i m_i - cpT_o m_o) = \delta W + cv\delta\,(m\, T) \tag{3.59}$$

It is generally assumed that the working gas in Stirling engines is behaving like an ideal gas and that the total mass of gas in the engine is constant (hence there is no leakage). The pressure inside the engine can be determined, according to

equation (3.4) as follows:

$$P = \frac{m\,R}{\frac{V_c}{T_c} + \frac{V_k}{V_k} + \frac{V_r}{T_r} + \frac{V_h}{T_h} + \frac{V_e}{T_e}} \tag{3.60}$$

Applying equation (3.59) to the compression/expansion space and considering continuity, the mass derivative in the compression/expansion space can be determined as follows:

$$\delta m_c = \frac{P\,\delta V_c + \frac{V_c \delta P}{\gamma}}{R\,T_{ck}} \tag{3.61}$$

$$\delta m_e = \frac{P\,\delta V_e + \frac{V_e \delta P}{\gamma}}{R\,T_{he}} \tag{3.62}$$

where: $\gamma = \frac{cp}{cv}$

The Van der Waals equation of state can be rewritten for a generalised cell of the engine in both its standard and differential form:

$$P\,V = m\,R\,T \tag{3.63}$$

$$\frac{\delta P}{P} + \frac{\delta V}{V} = \frac{\delta m}{m} + \frac{\delta T}{T} \tag{3.64}$$

Since the respective volumes and temperatures in each cell of the heat exchangers are constant, the differential form of the equation of state, equation (3.64), thus reduces to :

$$\frac{\delta m}{m} = \frac{\delta P}{P} \tag{3.65}$$

Differentiating the equation for the total mass of gas in the engine, equation (3.46), gives:

$$\delta m_c + \delta m_k + \delta m_r + \delta m_h + \delta m_e = 0 \tag{3.66}$$

Substituting equations (3.61) and (3.62), as well as equation (3.65) for each heat exchanger into the differential equation for the total mass of gas, equation (3.66),

the following equation for the differential form of the pressure can be determined:

$$\delta P = \frac{-\gamma P \left(\frac{\delta V_c}{T_c} + \frac{\delta V_e}{T_h}\right)}{\frac{V_c}{T_c} + \gamma \left(\frac{V_k}{T_k} + \frac{V_r}{T_r} + \frac{V_h}{T_h}\right) + \frac{V_e}{T_e}} \tag{3.67}$$

Applying the equation of state to the working spaces and differentiating, gives the temperature derivatives for the expansion and compression spaces, respectively:

$$\delta T_c = T_c \left(\frac{\delta P}{P} + \frac{\delta V_c}{V_c} - \frac{\delta m_c}{m_c}\right) \tag{3.68}$$

$$\delta T_e = T_e \left(\frac{\delta P}{P} + \frac{\delta V_e}{V_e} - \frac{\delta m_e}{m_e}\right) \tag{3.69}$$

In order to determine the heat in the different heat exchangers of the engine, the energy equation can be applied whilst substituting for the equation of state for a heat exchanger:

$$\delta Q = \frac{V\, \delta P\, cv}{R} - cp\,(T_i \dot{m}_i - T_o \dot{m}_o) \tag{3.70}$$

3.4.3 Performance Evaluation of a Stirling Engine

In every modern Stirling engine there are usually three different heat exchangers present, namely the heater, the cooler and the regenerator. According to the Schmidt theory they have no impact on the actual performance of a Stirling engine and do not contribute any net heat transfer over the cycle. Instead of isothermal behaviour, the working spaces in real machines tend to behave adiabatically. This implies that the net heat transferred over the cycle needs to be provided by heat exchangers. Extensive research on regenerators has been carried out by Allan Organ (1997) on whose work this regenerator analysis is based. Generally, a regenerator is cyclic by nature. In a first instance of a cycle, the hot gas flows from the heater to the cooler through the regenerator and during its pass transfers some of its heat to the regenerator matrix. This is referred to as a single blow. In the second instance of the cycle, the now cooled gas flows from the cooler back to the heater through the regenerator by *picking up* the previously stored heat. Hence at steady state the net heat transfer per cycle between the working gas

and the regenerator matrix is zero. The quality of the regenerator is defined on an enthalpy basis in respect of its effectiveness. An equivalent formulation can be obtained in the context of the ideal adiabatic cycle.

$$\varepsilon = \frac{heat\ from\ matrix\ to\ working\ gas\ during\ a\ single\ blow}{equivalent\ heat\ matrix\ to\ working\ gas\ in\ the\ regenerator\ in\ ideal\ model} \tag{3.71}$$

The regenerator effectiveness thus varies from 0 for no regenerator action to 1 for an ideal adiabatic model. The thermal efficiency of the ideal adiabatic cycle is given in terms of the energy values accumulated at the end of the cycle by:

$$\eta_{cycle} = \frac{q_h + q_k}{q_h} \tag{3.72}$$

The lower case q is used here to denote the heat at the end of a cycle. Note here that the heat absorbed by the cooler has a negative value as compared to a positive value for the heat added to the cycle in the heater. It follows that the thermal efficiency of the non-ideal adiabatic engine is given by:

$$\eta_{th} = \frac{W}{Q_h} = \frac{Q_h + Q_k}{Q_h} \tag{3.73}$$

In case of a non-ideal adiabatic regenerator, during the second instance of the single blow (from the cooler back to the heater), upon exiting the regenerator, the working gas will have a temperature somewhat lower than the that of the heater. The gas will need to be heated back to the heater temperature at the end of each cycle, in order to keep the heater temperature constant. Thus, there needs to be a constant external supply of heat equal to the amount lost in the regenerator. This amount of heat can be represented quantitatively as follows:

$$Q_h = q_h + q_r^{(1-\varepsilon)} \tag{3.74}$$

Consequently, the same happens in the reverse flow direction, i.e. from the heater to the cooler. Upon leaving the regenerator, the temperature of the working gas will be somewhat higher than that of the cooler. This requires additional heat rejection from the cooler during each cycle equal to the amount of heat not lost

in the regenerator.

$$Q_k = q_k - q_r^{(1-\varepsilon)} \tag{3.75}$$

Substituting Q_h, Q_k and ε_{th} in equation (3.73):

$$\varepsilon_{th} = \frac{\varepsilon_{cycle}}{1 + \dfrac{q_r^{(1-\varepsilon)}}{q_h}} \tag{3.76}$$

Figure 3.8 shows a temperature profile for a regenerator in order to rewrite equation (3.71) with respect to temperatures.

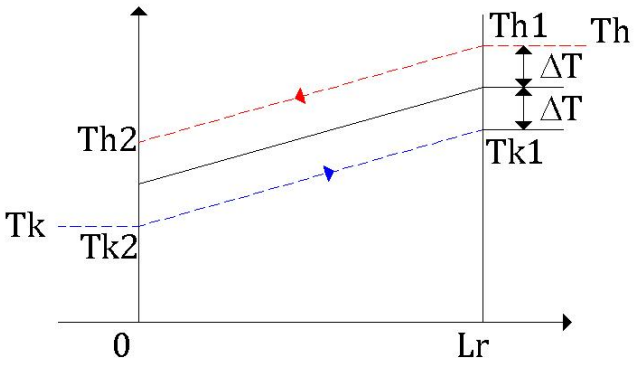

Figure 3.8: Regenerator temperature profile

$$\varepsilon = \frac{T_{h1} - T_{h2}}{T_{h1} - T_{k2}} \tag{3.77}$$

Assuming an equal difference in temperature difference on the hot and the cold sides and a linear temperature profile across the regenerator leads to the following:

$$2\Delta T = T_{h2} - T_{k2} \tag{3.78}$$

Combining these two equations,

$$\varepsilon = \frac{1}{1 + \dfrac{2\Delta T}{T_{h1} - T_{h2}}} \tag{3.79}$$

Considering the energy balance of any stream, the change in enthalpy is equal to the heat transfer from the stream to the regenerator, thus:

$$\dot{Q} = cp\,\dot{m}\,(T_{h1} - T_{h2}) = 2\,h\,A_{cs}\,\Delta T \tag{3.80}$$

Substituting in the above equation (3.79) for the regenerator effectiveness:

$$\varepsilon = \frac{1}{1 + \dfrac{cp\,\dot{m}}{h\,A_{cs}}} \tag{3.81}$$

Combining this equation for the regenerator effectiveness with the definition of the number of transfer units given in equation (3.82), adopted from Kays & London:

$$NTU = \frac{A\,U}{\Delta T} = \frac{h\,A_{cs}}{\rho\,\bar{V}\,cp\,A} = \frac{St\,A_{cs}}{2\,A} \tag{3.82}$$

The factor 2 in this equation is unusual, and stems from the fact that the Stanton number is usually defined for the transfer of heat from the gas stream to the matrix alone, whereas the NTU usage in this section is for overall transfer of heat from the hot stream to the regenerator matrix, and subsequently to the cold stream.

The other two heat exchangers in regards to Stirling engines are the heater and the cooler. They contribute towards the addition and rejection of heat, respectively. As mentioned in the regenerator analysis, they are required as it is impossible to design an ideal adiabatic regenerator and hence a constant update of the temperatures in the heater and the cooler are required. The analysis of the heater and cooler are very similar and will therefore be carried out in the same way. Similar to the regenerator, the effectiveness of the heater and cooler can be determined. Kays and London showed that for a regenerator type heat exchanger the effectiveness can be reduced to:

$$\varepsilon = \frac{NTU}{NTU + 1} \tag{3.83}$$

Unfortunately for the heater and the cooler, there is no simple relation between their respective effectiveness and the engine efficiency as with the regenerator. From the ideology of heat exchangers, it is obvious that the gas temperature

upon leaving the heater is lower than the heater wall temperature, whereas the temperature leaving the cooler is higher than its corresponding wall temperature. This has an impact on the engine efficiency in ways that the operating cycle takes place at a lower temperature differential than those of the heater and cooler walls. Determining the velocity of the gas in the engine, would not be of great use in Stirling engines. As a matter of fact, it will only give a numerical value of the velocity at a particular location, however would not take into account the direction of flow of the gas. A more useful term is the mass flux which takes into account the mass in– and out–flow to each cell of the engine as well as the operating speed and can be determined as follows, based on the mass conversation principle:

$$G_{flux} = \frac{(\dot{m}_i + \dot{m}_o)\,\omega}{2\,A} = \frac{(-\delta m_c - \delta m_k + \delta m_e + \delta m_h)\,\omega}{2\,A} \tag{3.84}$$

Applying the equation for convection heat transfer to the two heat exchangers, the net heat transferred over one single cycle can be obtained by dividing by the frequency of operation, thus:

$$Q_h + Q_{rloss} = \frac{h_h\,A_{cs,h}\;(T_{w,h} - T_h)}{f} \tag{3.85}$$

$$Q_k - Q_{rloss} = \frac{h_k\,A_{cs,k}\;(T_{w,k} - T_k)}{f} \tag{3.86}$$

Rewriting in respect of the gas temperatures:

$$T_h = T_{w,h} - \frac{(Q_h + Q_{rloss})\,f}{h_h\,A_{cs,h}} \tag{3.87}$$

$$T_k = T_{w,k} - \frac{(Q_k - Q_{rloss})\,f}{h_k\,A_{cs,k}} \tag{3.88}$$

Q_{rloss} is the net enthalpy loss in the regenerator that can be determined as follows:

$$Q_{rloss} = (1 - \varepsilon)\,(Q_{rmax} - Q_{rmin}) \tag{3.89}$$

Additional losses can be quantified as Q_{leak}. This is the leakage from the regen-

erator housing wall and is determined as described by Organ:

$$Q_{leak} = \frac{\frac{k\,A_{wall}}{l_r} \times (T_{w,h} - T_{w,k})}{f} \tag{3.90}$$

The pumping work is the sum of the pumping loss for each crank angle increment.

$$\dot{W}_{pump} = \sum_{i=0}^{360} \left(\frac{\theta_i \left(\Delta P_h + \Delta P_r + \Delta P_k\right) 0.5\, VSE\, \sin\theta_i}{f} \right) \tag{3.91}$$

3.5 Theory of Absorption Cooling

The thermo-chemical accumulator (TCA) is an absorption process that uses a working pair of Lithium-Chloride (LiCl) and water, in the liquid, vapour and solution phases as a solid sorbent. This process is significantly different from the traditional absorption processes in that it is a three phase process (solid, solution and vapour). All other absorption processes are two phase processes with either solution + vapour or solid + vapour. Figure 3.9 shows the schematic of a TCA unit, where the solution is pumped over a heat exchanger via a spreader arm to increase the wetted area and improve heat transfer. The process has been developed by the Swedish company ClimateWell. During desorption the solution comes closer and closer to saturation, and when it reaches saturation point further desorption at the heat exchanger results in the formation of solid crystals that fall under gravity into the vessel. Here they are prevented from following into the pump by a sieve, thus forming a form of slurry in the bottom of the vessel. This gives the TCA the following characteristics:

- High energy density storage in the solid crystals
- Good heat and mass transfer, as this occurs with a solution

For discharging, where the process is reversed, the saturated solution is pumped over the heat exchanger where it absorbs the vapour evaporated in the evaporator. The heat of evaporation is provided either by the building (cooling mode) or from the environment (heating mode). The solution becomes unsaturated on the heat

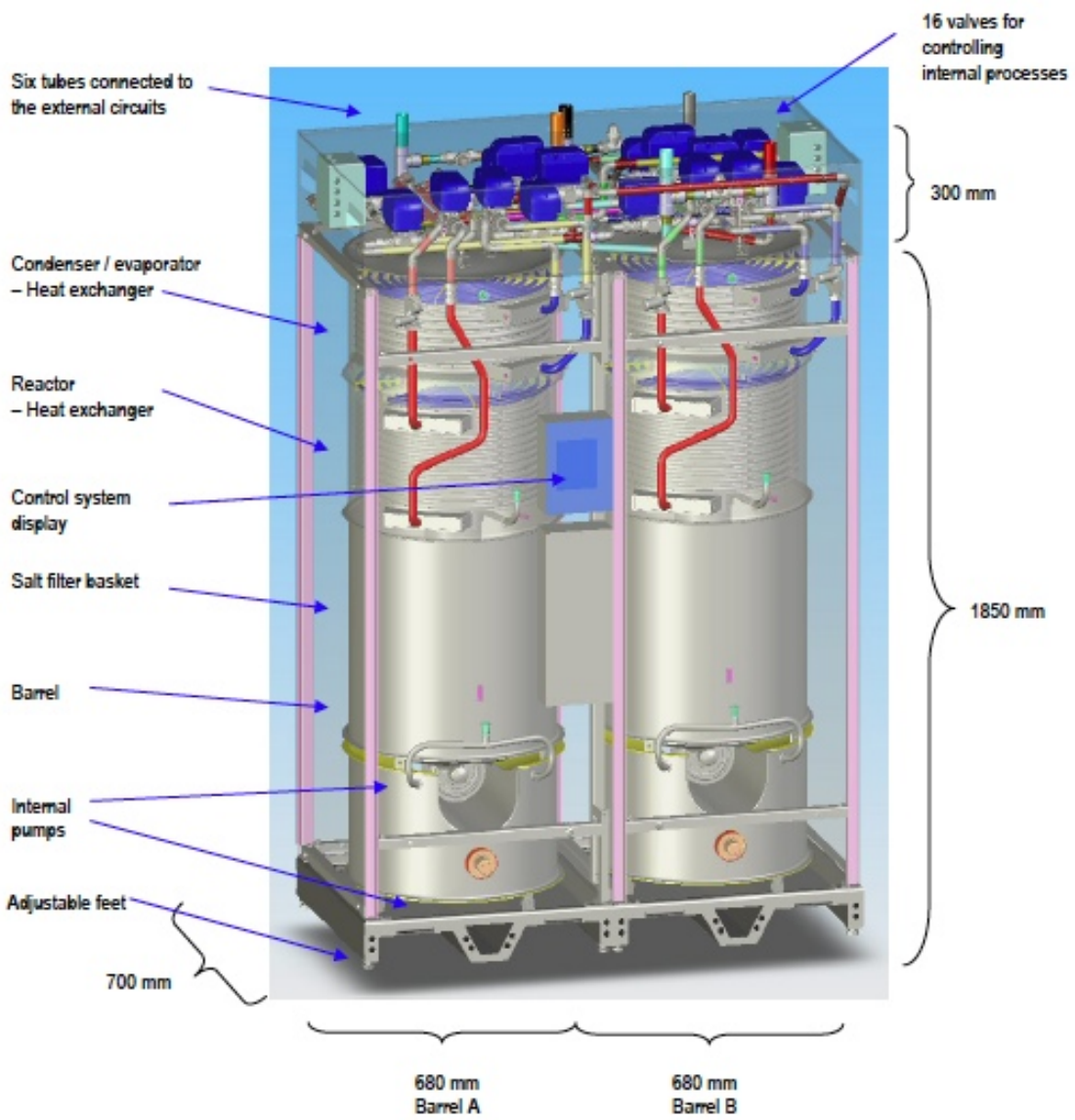

Figure 3.9: Schematic of a single TCA unit

exchanger, but when it falls into the vessel it has to pass through the slurry of crystals, where some of the crystals are dissolved to make the solution fully saturated again. In this way the solution is always saturated and the net result is a dissolving of the crystals into a saturated solution. The heat of condensation and binding energy release is transferred to the environment (cooling mode) or to the building (heating mode). Thus there is a flow of energy from the evaporator at low temperature to the reactor at moderate temperature. The first TCA units have been built using LiCl/water as the active pair, and with two parallel units connected via switching valves, so that one unit can be charged while the other is being discharged. A typical thermo-chemical accumulator unit consists of a reactor and condenser/evaporator with a vapour channel between them, as well as tanks for both water and the active salt solution. Vacuum conditions are assumed and each of the main sections has its own mass and associated heat loss coefficient. Heat of vaporisation, condensation and dilution are taken into account and a single UA-value (overall heat transfer coefficient for the whole heat exchanger area) is used as parameter for charge and one for discharge conditions. These UA-values are used to calculate the UA-values for the reactor and the condenser. There is a mixing flow between the reactor and the solution store, and between condenser and water store.

3.5.1 Energy Transfer of Heat Exchangers and Vapour in a TCA Unit

For simplicity, the condenser and the reactor are treated as though they each consist of two separate tanks.This allows considering the top tank as the exchange of energy between the tanks and the outside, and the bottom of the tank as a storage for the water or salt solution. Internal pumps assure the exchange of water/solution between the bottom tank and the top tank. Thus the condenser top is the condenser itself and the condenser bottom is the water store. Likewise, the reactor top is the reactor itself and the reactor bottom is the solution storage. It is assumed that for initial conditions, all salt is dissolved in the reactor. In the real system, the temperatures are depending on the heat transfer across the heat exchangers. And, similarly, the masses and salt concentrations are dependent on

the temperatures. **In order to express this mathematically, it is assumed that the system determines its initial conditions and then evaluates its corresponding temperature and mass values. Thus, the symbols on the left hand side of the subsequent equations refer to the adjusted values, whereas the ones on the right hand side refer to the outdated values.** Initially, all the temperatures for the reactor and condenser are set to the ambient temperature. The concentration of the solution can then be calculated as follows, depending on the quantities of water and salt in the respective tanks:

$$x_{LiCl} = \frac{m_{LiCl}}{m_{LiCl} + m_{H_2O} - m_{H_2O,ct} - m_{H_2O,cb}} \tag{3.92}$$

Based on this calculated solution concentration, the mass of water and solution in every part of the unit can be calculated, based on the volume of the reactor and the density of the salt, as follows:
mass of salt solution in the reactor top,

$$m_{ss,rt} = x_{LiCl}\, V_0\, \rho_{LiCl} \tag{3.93}$$

mass of water solution in the reactor top,

$$m_{ws,rt} = (1 - x_{LiCl})\ V\ \rho_{LiCl} \tag{3.94}$$

mass of salt solution in the reactor bottom,

$$m_{ss,rb} = m_{LiCl} - m_{ss,rt} \tag{3.95}$$

mass of water solution in the reactor bottom,

$$m_{ws,rb} = m_{H_2O} - m_{ws,rt} - m_{H_2O,ct} - m_{H_2O,cb} \tag{3.96}$$

Applying the principles of mass and energy transfer to any heat exchanger can be determined mathematically as expressed by equations (3.19 - 3.20), the energies transferred through the heat exchangers can be evaluated. Thus, for the

condenser heat exchanger power,

$$\dot{Q}_{cx} = \dot{m}_{cx}\, cp_{cx}\, (T_{cxi} - T_{cxo}) \tag{3.97}$$

for the reactor heat exchanger power,

$$\dot{Q}_{rx} = \dot{m}_{rx}\, cp_{cr}\, (T_{rxi} - T_{rxo}) \tag{3.98}$$

for the energy rate due to vapour for the condenser,

$$\dot{Q}_{vap,cx} = UA_{cx}\, (T_{cf} - T_{ct}) \tag{3.99}$$

The energy rate due to vapour in the reactor is dependent on the energy rate of the vapour in the condenser, based on the principle of energy balance. When the system is charging, ($\dot{Q}_{vap,cx} > 0$), part of the energy is used to vaporise the water and the rest to break the chemical bond to the salt. If the system is discharging, ($\dot{Q}_{vap,cx} < 0$),the energy stored by the salt is released because of the dilution of salt solution and the condensation of the water vapour.

$$\dot{Q}_{vap,rx} = \frac{-\dot{Q}_{vap,cx}\, (H_{vap} + H_{dil})}{H_{vap}} \tag{3.100}$$

The mass fraction of LiCl salt in the reactor is given as follows:

$$x_{LiCl,t} = \frac{m_{ss,rt}}{m_{ss,rt} + m_{ws,rt}} \tag{3.101}$$

The temperature difference between the reactor and the condenser during equilibrium is based on this salt concentration. Equation (3.102) presents this temperature difference for LiCl, which is fitted to data extrapolated from Conde (2004).

$$\Delta T = T_{rt} - \left(1.018 T_{rt} - 13.344 x_{LiCl,r} - 122.667 x_{LiCl,r}^2 - 0.212 x_{LiCl,r} T_{rt}\right) \tag{3.102}$$

The energy rate due to vapour in the condenser depends on the UA value of the heat exchanger in the condenser, the temperature of the water film on the heat exchanger surface as well as the temperature of the condenser top. The film

temperature of the condenser can be determined from the above heat transfer equations as follows:

$$T_{cf} = T_{ct} + \frac{(T_{rt} - T_{ct} - \Delta T)\, UA_{rx}}{UA_{rx} + UA_{cx}} \tag{3.103}$$

The film temperature at the reactor heat exchanger can be determined as follows:

$$T_{rf} = T_{cf} + \Delta T \tag{3.104}$$

3.5.2 Reactor Mass and Temperature Calculations

The mass of vapour is dependent on the energy rate due to vapour and the film temperatures of the surfaces of the heat exchangers over a period of time δt

$$m_{vap} = \frac{\dot{Q}_{vap,cx} \times \delta t}{H_{vap} + cp_{ste}\,(T_{cf} - T_{rf})} \tag{3.105}$$

The mass migrations between the reactor and the condenser due to vapour transport could go in either direction depending on whether the unit is charging or discharging. During the charging process, the vapour travels from the reactor to the condenser and vice versa for discharging. Therefore (for charging), some part of the water in the top tank of the reactor will go to the condenser and some solution will be pumped up to the top tank from the bottom one, so that the mass of solution in the top tank will be kept constant. Applying mass balance this gives:

$$m_{ws,rt} = m_{ws,rt} - m_{vap} \tag{3.106}$$

From the following equations the volume of the reactor top tank and the required mass to fill it up can be evaluated as follows:

$$V_{rt} = \frac{m_{ws,rt} + m_{ss,rt}}{\rho_{LiCl}} \tag{3.107}$$

$$m_{fill} = (V_0 - V_{rt})\, \rho_{LiCl} \tag{3.108}$$

There are three possibilities for equation (3.108): the bottom tank is empty ($m_{fill} = 0$), the solution is pumped from the bottom tank to the top one ($m_{fill} >$

0), or the solution is pumped from the top tank to the bottom ($m_{fill} < 0$). Depending on what direction the solution is being pumped, the masses of LiCl salt and water in the reactor can be determined according to the mass conversation equation by thus adjusting the previous determined masses for salt and water solutions.

$$m_{ws,rt} = m_{ws,rt} + m_{fill}\,(1 - x_{LiCl}) \tag{3.109}$$

$$m_{ws,rb} = m_{ws,rb} - m_{fill}\,(1 - x_{LiCl}) \tag{3.110}$$

$$m_{ss,rt} = m_{ss,rt} + m_{fill} x_{LiCl} \tag{3.111}$$

$$m_{ss,rb} = m_{ss,rb} - m_{fill} x_{LiCl} \tag{3.112}$$

The LiCl concentration and temperature of the top and the bottom tank can be determined using the mass and energy conservation principles as follows, based on the masses in the reactor:

$$x_{top} = \frac{m_{ss,rt}}{m_{ss,rb} + m_{ws,rt}} \tag{3.113}$$

$$x_{bottom} = \frac{m_{ss,rb}}{m_{ss,rb} + m_{ws,rb}} \tag{3.114}$$

$$T_{rt} = \frac{T_{rt}\, m_{rt} + T_{rb}\, m_{fill}}{m_{rt} + m_{fill}} \tag{3.115}$$

$$T_{rb} = \frac{T_{rb}\, m_{rb} + T_{rt}\, m_{fill}}{m_{rb} + m_{fill}} \tag{3.116}$$

The required amount of monohydrate crystals can be evaluated using Conde's published relationship for the concentration of crystals:

$$x_{mc} = -4.643 \times 10^{-06} T_{rt}^2 + 1.901 \times 10^{-03} T_{rt} + 0.411 \tag{3.117}$$

The molecular masses for Lithium-chloride ($42.4\ \frac{g}{mol}$) and water ($18\ \frac{g}{mol}$) is used here:

$$m_{mc} = 1.425 \times (x_{mc} - x_{top})\,(m_{ss,rt} + m_{ws,rt}) \tag{3.118}$$

The transport of the vapour can cause the solution in the top of the reactor to be concentrated or diluted. Therefore, extra water or salt are required to keep

the salt solution at its equilibrium state. The temperature changes due to the dissolution at the reactor top can be expressed as follows:

$$T_{rt} = T_{rt} + \frac{m_{mc}\, H_{sol}}{m_{rt}\, cp_{rx}} \tag{3.119}$$

If there is not enough solution of water available, then the required mass of monohydrate crystals is set to zero and the masses of the salt and water solution are adjusted as follows:

$$m_{ss,rt} = m_{ss,rt} + 1.425 \times m_{mc} \tag{3.120}$$

$$m_{ws,rt} = m_{ws,rt} + 0.298 \times m_{mc} \tag{3.121}$$

3.5.3 Condenser Mass and Temperature Calculations

The calculations for the condenser are less extensive as they are largely dependent on the calculations carried out for the reactor. The mass of the condenser is based on initial conditions and on the mass of vapour:

$$m_{cb} = m_{cb} + m_{vap} \tag{3.122}$$

$$m_{ct} = m_{ct} + m_{ws,ct} \tag{3.123}$$

The temperatures of the condenser top and bottom tank are dependent on whether the unit is charging or discharging. For charging ($m_{vap} > 0$):

$$T_{cb} = \frac{T_{cb}\,(m_{cb} - m_{vap}) + (T_{ct}\, m_{vap})}{m_{cb}} \tag{3.124}$$

For discharging ($m_{vap} < 0$):

$$T_{ct} = \frac{T_{ct}\,(m_{ct} + m_{vap}) - (T_{cb}\, m_{vap})}{m_{ct}} \tag{3.125}$$

Additionally the condenser temperatures need to be adjusted to account for the internal mixing pumps as follows:

$$T_{ct} = T_{ct} + \frac{T_{cb}\dot{m}_{cx}\delta t - T_{ct}\dot{m}_{cx}\delta t}{m_{cb}} \tag{3.126}$$

$$T_{cb} = T_{cb} + \frac{T_{ct}\dot{m}_{cx}\delta t - T_{cb}\dot{m}_{cx}\delta t}{m_{cb}} \tag{3.127}$$

The factor δt is required since the temperature change due to the pump is time-dependent and varies with the mass flow of the pump.

3.5.4 COP of a TCA Absorption Heat Pump

The coefficient of performance (COP) is the ratio of output to input energies. COP_{cool} is the thermal COP for producing cooling from the thermal source, and COP_{heat} is for the heat extracted during discharge for the given operating conditions. COP_{pump} is the thermal COP when the machine is used as a heat pump, with the energy that in cooling operation is dumped to ambient being used for heating. The heat input (Q_s) as well as the heat outputs (Q_{ac}) and (Q_{hs}) are determined with equation (3.19). The values are based on whether the system is charging or discharging as indicated in Table 3.1.

$$COP_{cool} = \frac{Q_{ac}}{Q_s} \tag{3.128}$$

$$COP_{heat} = \frac{Q_{hs,ch}}{Q_s} \tag{3.129}$$

$$COP_{pump} = \frac{Q_{hs,ch} + Q_{hs,dis}}{Q_s} \tag{3.130}$$

Table 3.1: System connections dependent on status

Status	**Heat source (Q_s)**	**Heat sink (Q_{hs})**	**Cooling (Q_{ac})**
Charging	Reactor	Condenser	not connected
Discharging	not connected	Reactor	Condenser

3.6 Theory of Combined Generation Systems

In this section, a theoretical analysis of combined heat and power (CHP), combined cooling and heating (CCH) and tri-generation (tri) is performed. Figure 3.10 shows a Sankey diagram of the energy flow for a CCH system. Furthermore,

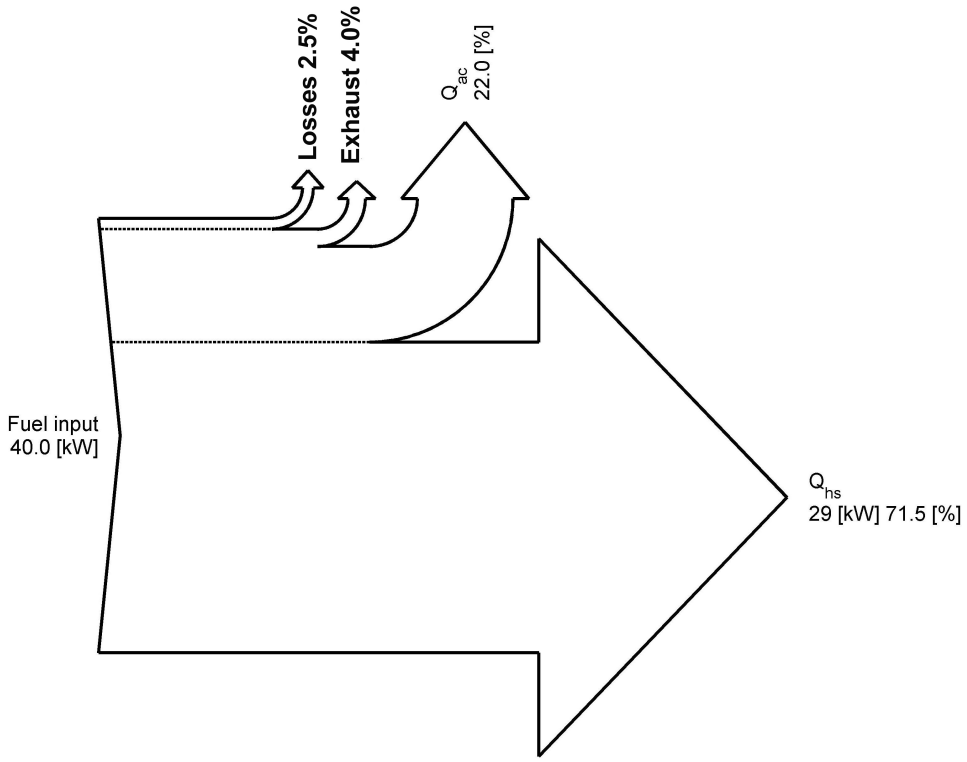

Figure 3.10: Sankey diagram for CCH

the discussion will involve a comparison of tri-generation system with the conventional power generation and cogeneration; and the comparison of tri-generation system with the separate generation system of power, heat and cooling. The investigated combined systems are made of a biomass combustion unit, a Stirling engine, a heat sink, and an absorption cooling unit. The heat released during the combustion of the biomass is used to drive the Stirling engine and the remaining flue gas heat is used to heat water. This heated water is then used to drive the absorption cooling cycle. A heat sink is required to dump the heat extracted during the cooling of the re-circulating cooling fluid cycle. The primary energy input

(Q_{pr}), in this case, is from biomass pellets supplied to the biomass combustion unit. The electrical power output (P_{el}) is generated by a generator coupled to the Stirling engine. The heat output from the heat sink (Q_{hs}) will be regarded as useful heat as it has the potential to be used in underfloor heating systems. The cooling output (Q_{ac}) is achieved from the heat input (Q_s) to the reactor in the absorption system. The useful heat output (Q_{wa}) from the biomass combustion unit in form of hot water is used for central heating.

The electrical power output: the electrical power output is directly measured by the Wattmeter.

The heat available in the exhaust: although this is a potential waste of heat there could be further uses such as pre-heating of the primary air inlet to the combustion chamber or use of a condensing boiler.

The useful energy output from combined heat and power and the thermal efficiency: this is the output if the heat from the combustion is used to drive the Stirling engine and provide hot water for heating systems:

$$Q_{CHP} = P_{el} + Q_h \tag{3.131}$$

$$\varepsilon_{CHP} = \frac{Q_{CHP}}{Q_{Pr}} \tag{3.132}$$

The useful energy output from combined cooling and heating: in this case the hot water is used to drive the absorption cooling unit, as tested in the laboratory.

$$Q_{CCH} = Q_{ac} + Q_{hs} \tag{3.133}$$

$$\varepsilon_{CCH} = \frac{Q_{CCH}}{Q_{pr}} \tag{3.134}$$

The useful energy output form tri-generation: in this case the previous two schemes will be combined to generate electrical power with the Stirling engine, cooling with the absorption unit and heat with the heat sink.

$$Q_{tri} = P_{el} + Q_{ac} + Q_{hs} \tag{3.135}$$

$$\varepsilon_{tri} = \frac{Q_{tri}}{Q_{Pr}} \tag{3.136}$$

3.6.1 Comparison of Combined Cooling and Heating with the Conventional Generation of Cooling and Heating

In order to find out how much energy savings can be achieved by combined cooling and heating generation, the system performances, discussed above, are compared to each other. In both systems, fuel is converted into cooling and heating. A conventional electrical driven air-conditioning unit and a heating boiler with oil is used for comparison. The thermal efficiency of the electrical power generation is:

$$\varepsilon_{el} = \frac{P_{el}}{Q_{Pr}} \tag{3.137}$$

The coefficient of performance (COP) of power driven (electrical) absorption cooling system is:

$$COP = \frac{Q_{ac}}{P_{el}} \tag{3.138}$$

Then, the primary energy input to the power driven absorption unit ($Q_{pr,ac}$) is based on equation (3.137):

$$Q_{pr,ac} = \frac{Q_{ac}}{COP\,\eta_{el}} \tag{3.139}$$

The efficiency of heating by conventional heating by use of an oil burner is determined by the heat supply for heating (Q_h) and the primary energy input to the burner ($Q_{pr,h}$).

$$\eta_h = \frac{Q_h}{Q_{pr,h}} \tag{3.140}$$

Based on these single generation efficiencies for cooling and heating, the total energy consumed for the separate generation system ($Q_{tot,sg}$) can be shown as:

$$Q_{tot,sg} = Q_{pr,ac} + Q_{pr,h} \tag{3.141}$$

The heat efficiency of separate generation is then:

$$\varepsilon_{tot,sg} = \frac{Q_{ac} + Q_h}{Q_{tot,sg}} \tag{3.142}$$

The primary energy input to the combined coolind and heating sytem (Q_{CCH}) is shown in equation (3.9) and the thermal efficiency of CCH is given by equation (3.134). The real saving in the primary energy consumption by using CCH system compared to the separate generation system is then:

$$\Delta Q_{sg} = Q_{tot,sg} - Q_{CCH} \tag{3.143}$$

The comparative savings of primary energy demand can be defined as a ratio of the saved primary energy in CCH to the primary energy consumption at separate generation system:

$$saving\ Q_{sg} = \frac{\Delta Q_{sg}}{Q_{tot,sg}} \tag{3.144}$$

3.6.2 Comparison of Tri-generation System with the Separate Generation System of Power, Heat and Cooling and the Combined Systems of CCH and CHP

In order to compare the overall efficiency of the systems, it is necessary to consider the systems under the same working conditions. The discussions below are based on the output of power, heating and cooling from tri-generation. In both systems, fuel is converted into electricity, heat and cooling. The domestic hot water is produced with an electrical hot water storage tank and the thermal efficiency of the DHW generation is:

$$\eta_{dhw} = \frac{Q_{dhw}}{P_{el}} \tag{3.145}$$

Based on the above single generation efficiencies, the total energy consumed for the separate generation system ($Q_{tot,sg}$) can be shown as:

$$Q_{tot,sg} = Q_{pr} + Q_{pr,ac} + Q_{pr,h} \tag{3.146}$$

The thermal efficiency of separate generation is then:

$$\varepsilon_{tot,sg} = \frac{P_{el} + Q_{ac} + Q_h}{Q_{tot,sg}} \tag{3.147}$$

The primary energy input to the tri-generation system (Q_{tri}) is shown in equation (3.9) and the thermal efficiency of tri-generation is given by equation (3.136). The real saving in the primary energy consumption by using tri-generation system compared to the separate generation system is then:

$$\Delta Q_{sg} = Q_{tot,sg} - Q_{tri} \tag{3.148}$$

The comparative savings of primary energy demand can be defined as a ratio of the saved primary energy in tri-generation to the primary energy consumption at separate generation system:

$$saving\ Q_{sg} = \frac{\Delta Q_{sg}}{Q_{tot,sg}} \tag{3.149}$$

Similarly, the real savings and comparative savings for tri-genetration over CHP systems can be determined as follows:

$$\Delta Q_{CHP} = Q_{CHP} - Q_{tri} \tag{3.150}$$

$$savin\ Q_{CHP} = \frac{\Delta Q_{CHP}}{Q_{CHP}} \tag{3.151}$$

And, the real savings and compartive savings for tri-genetration over CCH systems can be determined as follows:

$$\Delta Q_{CCH} = Q_{CCH} - Q_{tri} \tag{3.152}$$

$$saving\ \Delta Q_{CCH} = \frac{\Delta Q_{CHP}}{Q_{CHP}} \tag{3.153}$$

3.7 Conclusion

This chapter presented the theory necessary for the development of numerical and computational models to predict the performance of biomass combined generation schemes. The theory based on laws of Thermodynamics for the combustion of biomass will be used in the next chapter to develop an analytical model to estimate the combustion temperatures and combustion products from the burning of

solid biomass fuels. The theory of the shell and tube heat exchanger will be used to develop an analytical model to determine the heat transfer coefficients and surface areas involved. The equations presented for the Stirling engines will be used to first develop a tool to perform a simple Schmidt analysis and secondly a third order model of the gamma type engine tested in the later stages of this study. The absorption theory will be used to develop a model to predict the coefficient of performance of a thermo-chemical accumulator absorption unit for different inlet temperatures. All these models will later be used to conduct a performance analysis of the different key components in the system under various operating conditions. Eventually the model to compare different generating schemes will give useful insight when comparing the measured data with simulated models of different generating schemes during the discussion of the results.

Chapter 4

Computational Fluid Dynamics and Analytical Modelling

4.1 Introduction

This chapter describes the development of mathematical and CFD models for the biomass boiler, heat exchanger, the Stirling engine as well as the refrigeration system. All of these units form the basic components of the combined generation scheme under study in this thesis. An analytical model is developed to estimate the combustion temperatures and combustion products from the burning of biomass. This model is verified by taking the case for the combustion of pure Carbon in air. The computational fluid dynamics of the biomass boiler is used to visualise the flow pattern of the air and the water inside the combustor. This will give a qualitative insight into the flow of air and water prior to the testing. Potential areas for improvement could then be identified. An analytical model for shell and tube heat exchangers is developed in this chapter, to determine the heat transfer coefficients and surface areas. Additionally the correction factor for this type of heat exchanger is modelled based on Bowman's equations. A computational fluid dynamics analysis of the heat exchanger is carried out to visualise flow pattern inside the shell of the heat exchanger and to determine outlet temperatures depending on inlet flow properties and heat transfer coefficients determined by the analytical model. An analytical model of the Stirling engine is developed in this chapter. In a first step the Schmidt analysis is used to determine

the total mass of gas in the engine. In a second step a third order method is used to estimate the engine output and efficiency. This model is verified by detailed calculations for the engine with air as the working fluid at 10 *bar* pressure charge. A computational fluid dynamics model is also used to determine the heat transfer in the different heat exchangers of the engine as well as flow patterns for the gas and the cooling water across different parts for the engine. A working model for the refrigeration unit is developed to model the working conditions for different temperatures. The coefficient of performance determined by the model will be used to compare to real-life testing carried out in other studies.

4.2 Modelling of the Biomass Combustion

In this study, the combustion of biomass is used to simultaneously generate the required heat to drive the prime mover, a hot water heat exchanger and the cooling unit. The analytical model will investigate the combustion products released during the combustion, whereas the CFD model will investigate the heat distribution and flow through various combustor components.

4.2.1 Analytical Model of Biomass Combustion

This analytical model of biomass combustion is aimed to predict the products released during the biomass combustion and to determine the resulting temperature of these products. The model is based on the concept of 'adiabatic flame temperature'. In addition, it takes into account the dissociation that occurs in the products which results in a lowering of the flame temperature. A major impact on the results is the accuracy of the fuel data provided. As most often the elemental composition of the biofuels is unknown, the model will assume average values for the fuel type obtained from published data unless otherwise stated by the user input. Another assumption of the model is that only the following elements will be present in the fuel: Carbon, Hydrogen, Oxygen, Nitrogen and Sulphur. This assumption is reasonable as biomass is a hydrocarbon and it is burnt in atmospheric air. Sulfur being a rare part it is nevertheless included, in case some biomass samples do contain it. The input for the analytical model

of the biomass combustion is the type of fuel and the moisture content of the fuel sample. Although the calculations are based on the higher heating value, the moisture content will be used to determine the approximate value of the net calorific value. The option is available to choose a different chemical composition by choosing 'other' as fuel type. Figure 4.1 shows a flow diagram of the model. The data part reads the user input and looks up the chemical composition of the fuel. This allows determining the molar composition of the fuel by chemical balancing method. The higher heating value (HHV) can be determined either by user input or based on the fixed carbon (FC), volatile matter (VM) and ash content (ash). The correlation used is derived by literature as shown in equation (4.1) (Parikh *et al.*, 2005).

$$HHV = 0.3536\,FC + 0.1559\,VM - 0.0078\,ash \tag{4.1}$$

The lower heating value (LHV) is based on the HHV as well as the moisture content of the fuel. The correlation is adopted from the European standard (ISO, 2009c).

$$LHV = HHV \times (1 - 0.01\,MC) - 24.43 \times MC \tag{4.2}$$

The adiabatic flame temperature of the biomass is based on equation (3.6). The enthalpy of the reactants is kept at constant temperature and is of opposite sign to the higher heating value. In order to avoid confusion, the temperature of the reactants is not equal to the temperature of the products. The enthalpy of formation of pure oxygen and nitrogen is zero at standard atmospheric conditions. The enthalpies of each reactant can be determined based on the higher heating value and the total enthalpy of the products is the sum of the enthalpies of the individual elements. The temperature is initially set to 298 K. Once equation (3.2) is balanced, the K_p values for all combustion products can be determined. Rearranging equation (3.14) will result in equations of the 2^{nd} or 3^{rd} order. These equations are solved within the model and the mathematical solutions are checked for validity (i.e. negative values will be omitted). This change in combustion products obviously will result in a new temperature. The model will determine a new temperature and check the difference with the previous temperature. If the difference is less than 1%, the temperature is regarded as stable and the output

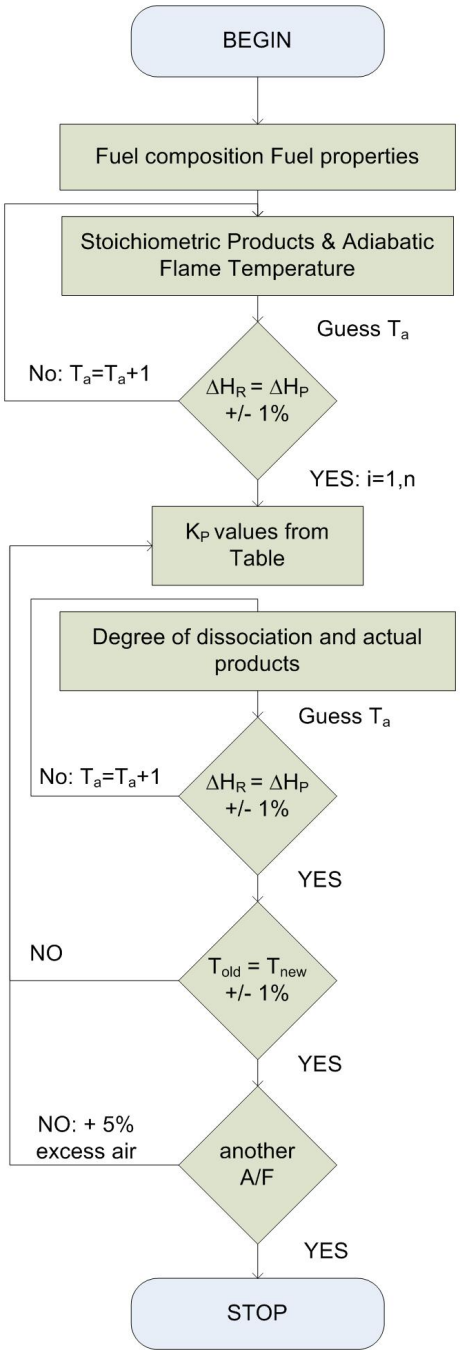

Figure 4.1: Flow diagram for the biomass combustion model

will be generated. The model writes the quantity of combustion products and their resulting temperature for air excess values ranging from 100% to 500%.

4.2.2 Verification of the Analytical Model of Biomass Combustion

The model proposed to estimate the combustion of biomass needs to be verified in order to accept any results obtained and presented. There are different methods to verify a model, namely by comparing the results to either real life tests, published data or meticulous hand calculations. The verification for the previously described model, the combustion of pure Carbon is presented analytically step by step and then compared to the model output. Since this simplified model contains all the calculations involved in the model (the exact same equations are used for all elements in the fuel), this exercise is sufficient to validate the results obtained by the model. The stoichiometric equation (3.6) reduces to:

$$C + (O_2 + 3.76\, N_2) \rightarrow CO_2 + 3.76\, N_2 + E \tag{4.3}$$

The higher heating value (HHV) for pure carbon, of molar mass $M = 12kg/kmol$ is taken from reference (Keating, 2007) to be $32.79\, MJ/kg$. The enthalpy of pure carbon is then given as:

$$H = -\frac{HHV}{M} = \frac{32790}{12} = -2732.5\, kJ/kmol \tag{4.4}$$

Using the simplified form for the conservation of energy principle, the adiabatic temperature can be determined as follows:

$$\begin{aligned} H(C) + H(O_2) &= H_f(CO_2) + 3.76 H_f(N_2) \\ -2732.5 + 0 &= [-393520 + (56.205\,(T_i - 298))] \\ &\quad +3.76\,[0 + (33.707\,(T_i - 298))] \end{aligned} \tag{4.5}$$

Equation (4.5) can be solved for (T_i) by an iterative process using an initial guess value for the temperature (T_i) and then increasing this guess temperature repeatedly by $0.001\, K$ until the equation converges. For this particular case this

amounts to a value of 2434.215 K. Correlations for K_p values were determined from tabulated data of K_p with temperature, taken from reference (Al-Shemmeri, 1993). For carbon dioxide this correlation is:

$$\ln K_p = (26.168 \times \ln T_{ad}) - 212.14 \tag{4.6}$$

where, T_{ad} is the adiabatic temperature determined by equation (4.5). This gives a value for $\ln K_p = -8.09$. Now equation (3.14) can be solved for ϑ as follows:

$$\begin{aligned} \left[K_p^2 - 1\right] \vartheta^3 + \left[\left(2\, K_p^2\, n_t\right) - \left(2\, K_p^2\, n_{CO_2}\right)\right] \vartheta^2 \;+\; & \left[\left(K_p^2\, n_{CO_2}^2\right) - \left(4\, n_t\, K_p^2\, n_{CO_2}\right)\right] \vartheta \\ \left[2\, n_t\, K_p^2\, n_{CO_2}^2\right] \;=\; & 0 \end{aligned} \tag{4.7}$$

This equation is of the general third order from, which by definition can lead to up three possible roots for ϑ, depending on the occasion. These roots can be determined by using an adapted method based on the solution proposed by Ferro and Cardan (Weintraub, 2009, see). However, not all of these theoretical solutions are adequate for the purpose of this model. As a matter of fact, imaginary and negative solutions as well as solutions for ϑ in excess of the original amount of moles present are impossible and thus will be neglected here. A generalised form of the third order equation with one unknown, in this case ϑ, can be written as follows:

$$a\, \vartheta^3 + b\, \vartheta^2 + c\, \vartheta + d = 0 \tag{4.8}$$

The known variables for the above equation are determined as follows:

$$\begin{aligned} \ln K_p = -8.09 \;&\Rightarrow\; K_p = e^{-8.09} \\ n_{CO_2} &= 1 \\ n_{N_2} &= 3.76 \\ n_t = 1 + 3.76 \;&\Rightarrow\; n_t = 4.76 \end{aligned} \tag{4.9}$$

Inputing all known variables into equation (4.7) and rearranging in the above format results in the following substitutions:

$$\begin{aligned} a &= \left(e^{-8.09}\right)^2 - 1 = -0.999 \\ b &= \left(2 \times \left(e^{-8.09}\right)^2 \times 4.76\right) - \left(2 \times \left(e^{-8.09}\right)^2 \times 1\right) = 7.07 \times 10^{-7} \\ c &= \left(\left(e^{-8.09}\right)^2 \times 1^2\right) - \left(4 \times 4.76 \times \left(e^{-8.09}\right)^2 \times 1\right) = -1.69 \times 10^{-6} \\ d &= 2 \times 4.76 \times \left(e^{-8.09}\right)^2 \times 1^2 = 8.95 \times 10^{-7} \end{aligned} \tag{4.10}$$

According to Ferro and Cardan a 'Δ' parameter can be determined which will then permit to determine the roots of the equation.

$$\Delta = \left(\frac{q}{2}\right)^2 + \left(\frac{p}{3}\right)^3 \tag{4.11}$$

where:

$$\begin{aligned} p &= \frac{c}{a} - \frac{b^2}{3a^2} \\ q &= \frac{d}{a} - \frac{bc}{3a} + 2\left(\frac{b}{3a}\right)^3 \end{aligned} \tag{4.12}$$

This gives values for $p = 1.69 \times 10^{-6}$, $q = -8.95 \times 10^{-7}$ and $\Delta = 2 \times 10^{-13}$. Since this value of Δ is positive, according to Ferro and Cardan, there will be two real roots as for equation (4.7) as follows:

$$\vartheta_1 = \sqrt[3]{-\frac{q}{2} + \sqrt{\Delta}} - \frac{p}{3 \times \sqrt[3]{-\frac{q}{s} + \sqrt{\Delta}}} - \frac{b}{3a} = 0.0095 \tag{4.13}$$

$$\vartheta_2 = 0 \tag{4.14}$$

This realistic solution of $\vartheta_1 = 0.0095$ represents the amount of moles of carbon monoxide formed during the dissociation of carbon dioxide with oxygen. Thus, equation (4.3) can be rewritten as follows:

$$C + (O_2 + 3.76N_2) \rightleftharpoons 0.9905CO_2 + 0.0095CO + 3.76N_2 + 0.00475O_2 \tag{4.15}$$

The dissociation of H_2O follows the same set of equation as the dissociation of N_2. Similar as for the K_p values for the dissociation of CO_2, a correlation for K_p value for N_2 was determined from tabulated data as follows:

$$\ln K_p = (89.045 \times \ln T_{ad}) - 740.43 \tag{4.16}$$

This gives a value for $\ln K_p = -46.11$. The dissociation of N_2 into nitrogen is determined by solving equation (3.14) as follows:

$$[-K_p - 4]\,\vartheta^2 + [(n_{N_2}\,K_p) - (n_t\,K_p)]\,\vartheta + [K_p\,n_{N_2}\,n_t] = 0 \tag{4.17}$$

This equation is of the general second order form, which by definition can lead to up to two possible roots for ϑ, depending on the occasion. Similar, as for the solving method of the third order equation, negative values and values in excess of the original amount of moles will be disregarded. A generalised form of the second order equation with one unknown, in this case ϑ, can be written as follows:

$$a\,\vartheta^2 + b\,\vartheta + c = 0 \tag{4.18}$$

The known variables for the above equation are determined as follows:

$$\begin{aligned} \ln K_p = -46.11 \quad &\Rightarrow \quad K_p = e^{-46.11} \\ n_{N_2} = 3.76 \\ n_t = n_{CO} + n_{CO_2} + n_{O_2} + n_{N_2} \quad &\Rightarrow \quad n_t = 4.76 \end{aligned} \tag{4.19}$$

Inputing all known variables into equation (4.17) and rearranging in the above format results in the following substitutions:

$$\begin{aligned} a &= \left(e^{-46.11} - 4\right) = -4 \\ b &= \left(3.76 \times e^{-46.11}\right) - \left(4.76 \times e^{-46.11}\right) = -9.44 \times 10^{-21} \\ c &= e^{-46.11} \times 3.76 \times 4.76 = 1.69 \times 10^{-19} \end{aligned} \tag{4.20}$$

As for the third order equation, a 'Δ' parameter can be determined as follows:

$$\begin{aligned} \Delta &= b^2 - 4ac = \left(-9.44 \times 10^{-21}\right)^2 - \left(4 \times (-4) \times 1.69 \times 10^{-19}\right) \\ \Delta &= 2.70 \times 10^{-18} \end{aligned} \tag{4.21}$$

Since this value for Δ is positive, there will be two distinct real roots to equation (4.17):

$$\vartheta_1 = \frac{-b + \sqrt{\Delta}}{2a} = -2.05 \times 10^{-10} \tag{4.22}$$

$$\vartheta_2 = \frac{-b - \sqrt{\Delta}}{2a} = 2.05 \times 10^{-10} \tag{4.23}$$

For obvious reasons ϑ_1 will be neglected. The only realistic solution ϑ_2 needs to be multiplied by a factor of two as the equations are all based on the dissociation of $N_2 \rightleftharpoons 2\,N$. So the updated equation for the combustion of carbon becomes:

$$\begin{aligned} C + (O_2 + 3.76N_2) \rightleftharpoons 0.9905CO_2 &+ 0.0095CO + 3.76N_2 \\ &+ 0.00475O_2 + 4 \times 10^{-10} N_2 \end{aligned} \tag{4.24}$$

The dissociation of H_2, O_2,and NO follows the same set of equation as the dissociation of N_2. Now the adiabatic flame temperature can be re-evaluated according to equation (4.5), taking into account the enthalpies for newly added combustion products. The energy balance is evaluated at each step, similar as for the adiabatic flame temperature until this condition is satisfied within 1 K is met. Then the process is terminated and the final temperature is taken as the solution for the new flame temperature. At this new temperature dissociation of all elements is reevaluated until the temperature difference between the previous iteration and current iteration becomes 0.1% or less.

Since the combustion of pure Carbon is used here, no water should be present in the combustion products and hence no hydrogen based dissociation should occur. Table 4.1 shows the output from the model in comparison with the hand by hand calculations. The calculated value is the numerical value determined with the analytical model until convergence is met.

Table 4.1: Model output for different iterations and calculated value for the final iteration

	CO_2	CO	NO	O_2	O (10^{-6})	N_2	N (10^{-12})	T [K]	%
it = 1	1	0	0	0	0	3.760	0	2434.21	n/a
it = 10	0.936	0.004	0.002	0.022	25.7	3.759	63.3	2327.01	0.31
it = 20	0.902	0.003	0.002	0.027	15.7	3.759	10.6	2271.96	0.19
it = 30	0.879	0.002	0.002	0.028	10.7	3.759	9.26	2234.22	0.15
it = 40	0.861	0.002	0.002	0.027	7.76	3.759	5.38	2206.44	0.11
it = 45	0.854	0.002	0.002	0.027	6.73	3.759	4.21	2194.58	0.10
calc	0.853	0.002	0.002	0.027	6.69	3.759	4.19	2195.01	n/a

4.2.3 Verification of the General CFD Flow Analysis Applied to a Thermal Situation

An experiment is conducted to compare the results with the ones obtained through Solidworks FlowSimulation. For this a small square wind-tunnel of 152 mm width

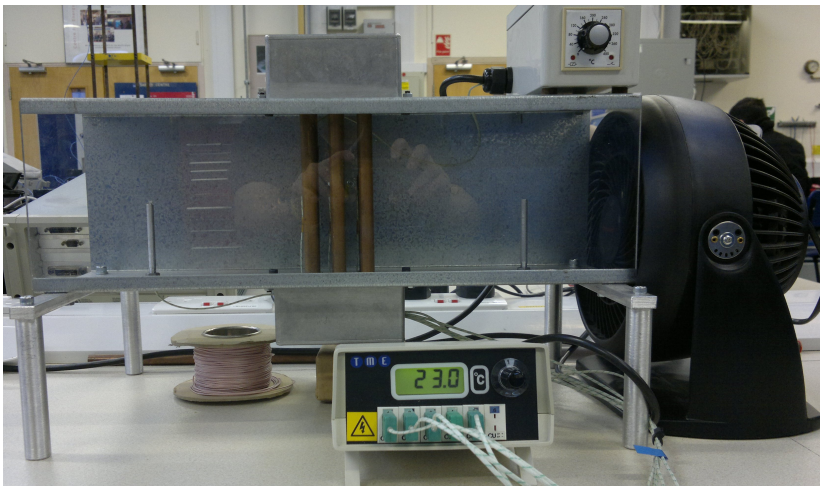

Figure 4.2: Side view of the wind-tunnel experiment to validate CFD flow results

and 500 mm length is built, as shown in Fig. 4.2. Nine copper hollow rods are placed upright in the middle of the wind-tunnel. A heating element rated at 22 W is placed inside each copper rod. A fan is used to cause forced convection across

the tube banks with flow direction from right to left. The velocity is determined with a Pitotstatic tube at the outlet of the wind-tunnel. A micro-manometer was used to measure the kinetic pressure at this location, as 36 mmH_2O. This reading in mmH_2O can be converted to a reading in Pa as follows:

$$P = \rho\, g\, h \tag{4.25}$$

where h is the value measured by the micro-manometer in m. This gives a kinetic pressure of $P = 353.16\, Pa$. Applying Bernoulli's equation to the case of a pitotstatic tube it can be shown that:

$$\bar{V} = \sqrt{\frac{2\, P}{\rho}} \tag{4.26}$$

This pressure equals to a velocity of $\bar{V} = 24.26\ m/s$. This exact experiment

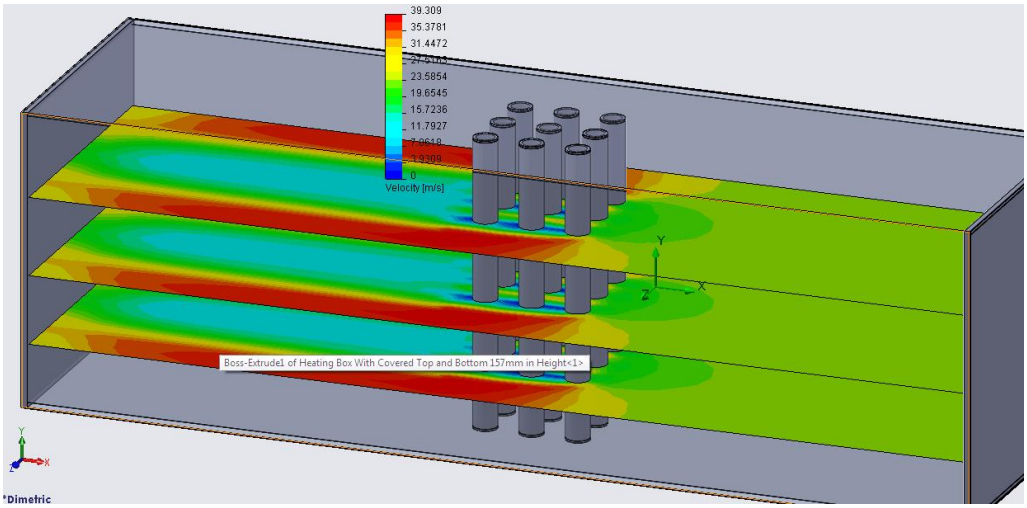

Figure 4.3: Side view of the velocity distribution on the three horizontal levels across the wind-tunnel

was set up in Solidworks. After applying the same boundary conditions for the heating elements and roughness factors on the sides of the wind-tunnel and the rods as well as modelling the fan; FlowSimulation was used to determined the velocity distribution inside the wind-tunnel and determine an average outlet ve-

locity. Figure 4.3 shows the velocity distribution on three horizontal planes across the length of the wind-tunnel. The disturbance to the flow caused by the tube arrangement causes the air to go turbulent and at increased velocity due to the mass continuity principle. FlowSimulation determines an average velocity at the outlet of 23.5 m/s. This is within 3% of the experimental value. This allows the conclusion that the velocity determined by FlowSimulation is within acceptable margins of error. Additionally the flow distribution provided by FlowSimulation will be useful information as this will not be possible to visualise on the actual model of the biomass combustion unit. The findings from this comparison permit to accept the results on flow distribution across the biomass unit as valid for the purpose of this study.

4.2.4 Computational Fluid Dynamics of the Biomass Combustion System

This section presents an investigation of the combustion system performance using computational fluid dynamics software. The investigation will include velocity profiles and flow patterns across the boiler and the combustion chamber of the biomass unit used for testing described in the following chapters. Figure 4.4 shows a cross-sectional view of the Carborobot Farmer F40. The unit is rated at 40 kW maximum output and burns either coal or biomass in pellet, log and chip form. The combustor is composed of a rotary grate of which the speed can be adjusted according to the type of fuel burnt. Since, it is unknown at priori how the combustion gases will flow through the system, and as this can not be determined in real-life tests, a CFD analysis is used to determine the flow pattern and velocity vectors across the unit. Additionally, CFD is used to determine the flow pattern of the water across the boiler. The unit is modelled according to the dimensions provided by the manufacturer and the outer walls of the unit are modelled based on the insulating material used in the actual system. The mass flow rates for the water (0.194 kg/s) and air (0.05 kg/s) are set to the values recommended for good operating conditions by the manufacturer. The direction of flow for the water is used in the same way as in the real-life tests, which is in an updraft direction to exit the shell at the top. All openings of the system, e.g. ash

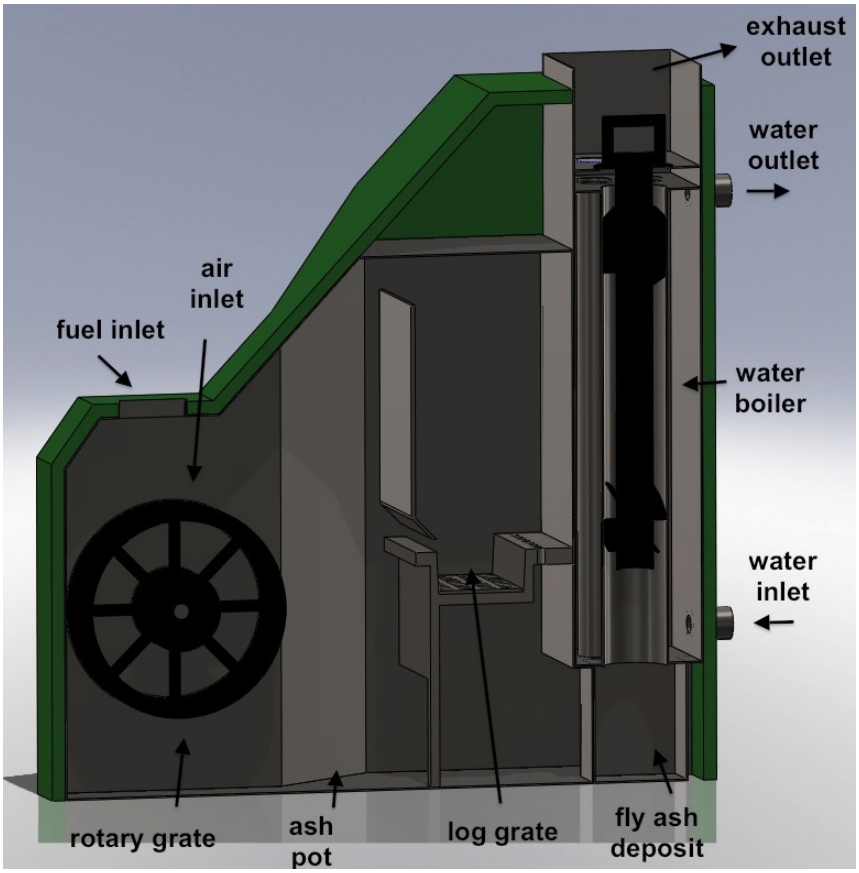

Figure 4.4: Cross-sectional view of the Carborot F40 with annotations

port, fuel inlet, are sealed in the CFD model and are treated as insulated walls. A downside of the model will be the lack of leaks that cannot be accounted for and hence the modelled results will not represent any influence that leaks will have in the real system. Additionally, the system is modelled to generate a constant heat output of 40 kW at the combustion place on the rotary grate. In order to reduce run-time and allow for a finer mesh, there will be two different tests carried out: the flow pattern of the combustion gases and the flow pattern of the water in the boiler. Figure 4.5 shows the flow pattern of the combustion gases across the combustion chamber and through the tubes of the boiler. A lot of turbulence and high velocity can be noticed across the tubes. This enhances the heat transfer to the water which is additionally enhanced by finned cleaning tubes inside the

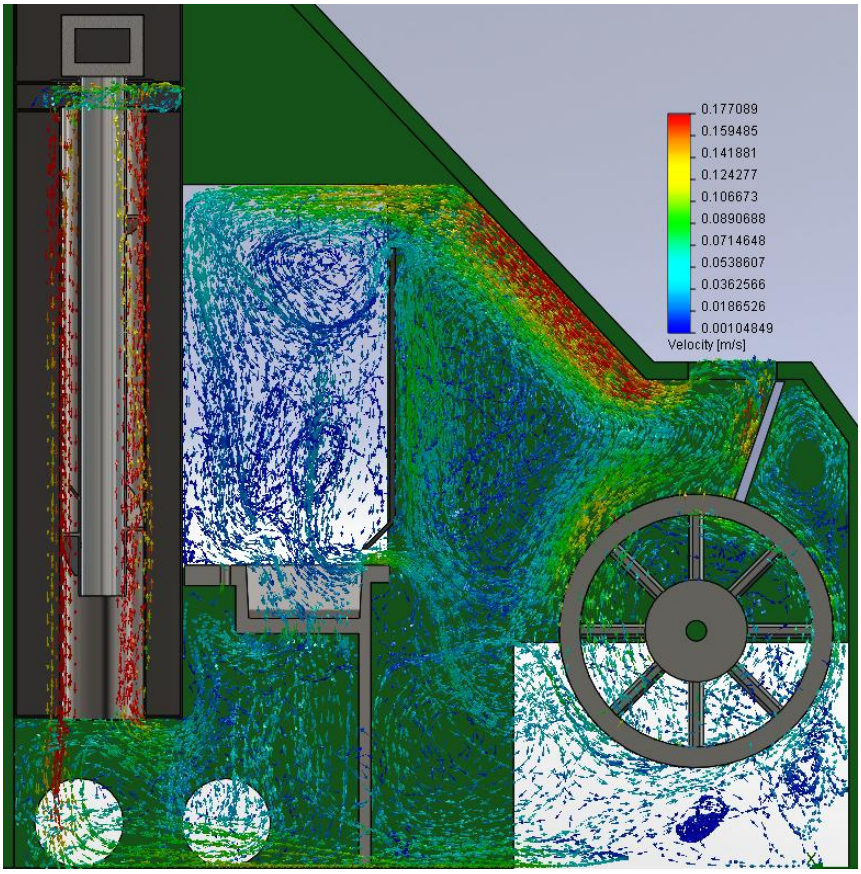

Figure 4.5: Cross-sectional view of the air flow inside the Carborot F40

tubes of the boiler. These cleaning tubes, as shown on Fig. 4.6 act similar to baffles and are used to remove ash deposit inside the tubes. The two openings at the bottom of the boiler are fly ash removal ports, and the opening in the middle is the log wood chamber door. Figure 4.7 shows the flow pattern of the water inside the boiler of the Carborobot F40. As the water enters the boiler at the bottom, the natural updraft directs the water flow towards the boiler outlet, caused by the raising of the hotter water due to reduced density. This forces the hot water to leave at the top of the boiler. For the purpose of this experiment, the water inlet temperature was set to $60°C$ and the water leaving the system had an average temperature of $85°C$.

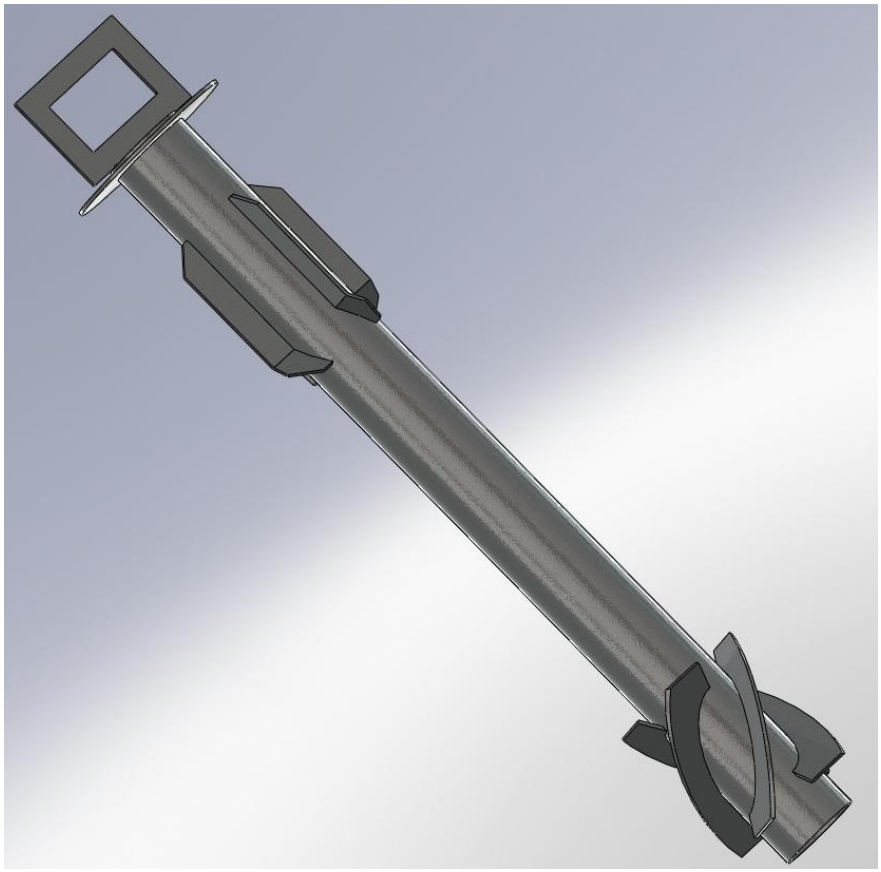

Figure 4.6: Carborot F40 boiler tubes with ash removal fins

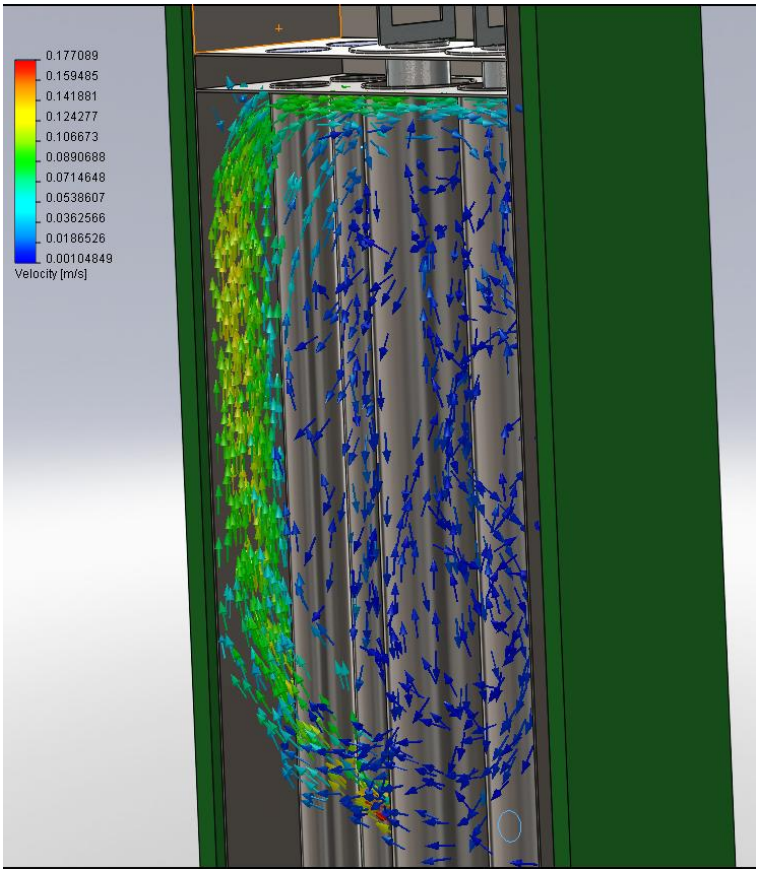

Figure 4.7: Velocity vectors of the water flow inside the boiler of the Carborobot F40

4.3 Modelling of Heat Exchangers for Biomass Applications

In this study, all heat exchangers used are of the shell and tube type. There is one heat exchanger in the biomass generator to transfer the heat from the combustion gases to the water. There are two more, as depicted on Fig.4.8 that are used once in the heat sink circuit and once in the cooling circuit driven by the TCA unit. The heat exchangers inside the TCA unit are not investigated as such as their geometrical measurements are unknown, however, their UA values have been provided by ClimateWell to be used in the calculations in section 4.5. The analytical model will investigate the tube and shell side properties of a shell and tube exchanger, with particular interest to the heat transfer coefficient, that will later be used in the performance evaluation model. The CFD investigation will look at the flow pattern across the tube banks and in the headers and the heat transfer across the tubes.

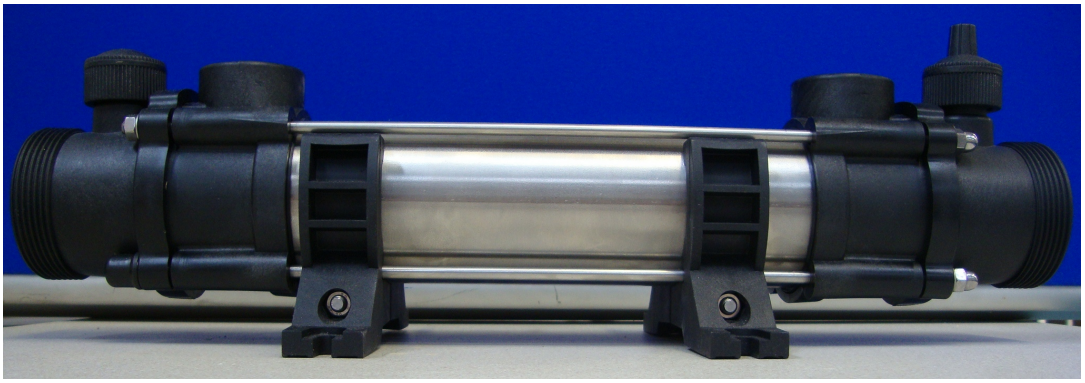

Figure 4.8: Elecro shell and tube heat exchanger

4.3.1 Analytical Model of Shell and Tube Heat Exchangers

This analytical model of heat exchanger analysis is intended to evaluate the heat transfer coefficient and surface areas for shell and tube exchangers. The model is

based on convective heat transfer theory. The thermal conductivity for the stainless steel tubes is taken from textbooks to be 14.9 W/mK. The fluid properties for the water/glycol mixture (15%) are obtained with the following correlations fitted from data for the temperature range of $-5°C$ to $50°C$ within 1% accuracy (Anon., 2011b).

$$\rho = -0.0024\,T^2 - 0.2343\,T + 1027.3 \tag{4.27}$$

$$cp = 0.00001\,T^2 + 0.0019\,T + 3.8555 \tag{4.28}$$

$$k = -0.000008\,T^2 + 0.0018\,T + 0.4878 \tag{4.29}$$

$$\mu = \left(0.00003\,T^4 - 0.0089\,T^3 + 1.01\,T^2 - 69.58\,T + 2460.4\right) \times 10^{-5} \tag{4.30}$$

The input data for the model requires the geometrical properties for the tube side and for the shell side. These include inside and outside diameters, tube and shell length, number of tubes, flow rates, the expected temperatures for the inlets and outlets and the circuit in which the heat exchanger is used. The temperatures do not have to be exact values, yet the LMTD is used in the above correlation for the fluid properties. Alternatively, default temperatures for the correlations are used depending on the circuit in which the heat exchanger is used and depending on tube or shell side. From this input data, the model determines cross-sectional areas, wetted areas, volumes and hydraulic diameter for one tube, all tubes and the shell. The fluid properties are determined as well as the Prandtl, Nusselt and Reynolds number for both tube and shell side. The corresponding heat transfer coefficient is then determined depending on the flow regime (turbulent or laminar). The overall heat transfer coefficients for both sides can then be calculated.

4.3.2 Verification of the Analytical Model of Heat Exchangers

The model described above is verified with the calculations for the shell and tube heat exchanger used in the heat sink and cooling circuits of the system. These temperatures are the recommended operating temperatures by ClimateWell, the manufacturer of the refrigeration system. The working model will be based on

these parameters in order to compare the results obtained to establish the suitability of the chosen heat exchanger. Additionally, this will be the preferred operating conditions of the real-life system and hence best represents actual working conditions. The default temperatures, capital T for hot fluid and lower case t for cold fluid streams, used in the model are as follows:

- For cooling system: $T_i = 20^\circ\,C$; $T_o = 22^\circ\,C$; $t_i = 10^\circ\,C$; $t_o = 21^\circ\,C$
- For heat sink system: $T_i = 35^\circ\,C$; $T_o = 30^\circ\,C$; $t_i = 15^\circ\,C$; $t_o = 55^\circ\,C$

Table 4.2: Dimensions of the shell and tube heat exchanger

Parameter	**Unit**	**Tubes**	**Shell**
ID	mm	6.17	65.06
OD	mm	7.01	68.30
Tubes		37	n/a
Length	mm	320	310
Flow rate	m^3/hr	0.70	6.00

From the data in Table 4.2, the geometrical parameters e.g. perimeter, surface areas, cross-sectional areas can be determined. The equations used as well as the results are shown in Table 4.3. The logarithmic mean temperature difference is

Table 4.3: Geometrical data for the shell and tubes

Parameter	**Equation**	**Unit**	**Value**
A_{cs} tubes	$n_t \times \frac{\pi\,(ID)^2}{4}$	$10^{-3}\,m^2$	1.106
A_{cs} shell	$\frac{\pi\,(ID)^2}{4} - \left(n_t \times \frac{\pi\,(OD_t)^2}{4}\right)$	$10^{-3}\,m^2$	1.896
P_x tubes	$\pi \times ID \times n_t$	m	0.717
P_x shell	$\pi \times OD_t \times n_t$	m	0.815
A tubes	$ID \times \pi\, timesL \times n_t$	m^2	0.229
A shell	$OD \times \pi \times L \times n_t$	m^2	0.253
V tubes	$A_{cs} \times L$	$10^{-4}\,m^3$	3.539
V shell	$A_{cs} \times L$	$10^{-4}\,m^3$	5.878
d_H tubes	$\frac{4\,A_{cs}}{P_x}$	$10^{-3}\,m$	6.17
d_H shell	$\frac{4\,A_{cs}}{P_x}$	$10^{-3}\,m$	9.305

calculated using the theory described in Chapter 3, the equation for a correction factor F is used. The $LMTD$ is calculated as follows:

$$LMTD = \frac{\Delta T_o - \Delta T_i}{\ln \frac{\Delta T_o}{\Delta T_i}} = \frac{(22-21)-(20-10)}{\ln \frac{22-21}{20-10}} = 3.9^\circ\, C \tag{4.31}$$

The parameters for the correction factor are thus:

$$X = \frac{t_o - t_i}{T_i - t_i} = \frac{21-10}{22-10} = 0.917 \tag{4.32}$$

$$Z = \frac{T_i - T_o}{t_o - t_i} = \frac{22-20}{21-10} = 0.182 \tag{4.33}$$

$$\Psi = \frac{1 - \frac{X\,Z-1}{X-1}}{Z - \frac{X\,Z-1}{X-1}} = \frac{1 - \frac{0.917\times 0.182-1}{0.917-1}}{0.182 - \frac{0.917\times 0.182-1}{0.182-1}}$$

$$\Psi = 0.917 \tag{4.34}$$

The correction factor for the logarithmic mean temperature difference is the obtained as follows:

$$F_{LMTD} = \frac{\left(\frac{\sqrt{Z^2+1}}{Z-1}\right)\ln\left(\frac{1-\Psi}{1-Z\,\Psi}\right)}{\ln\left(\frac{\frac{2}{\Psi}-1-Z+\sqrt{Z^2+1}}{\frac{2}{\Psi}-1-Z-\sqrt{Z^2+1}}\right)} = \frac{\left(\frac{\sqrt{0.182^2+1}}{0.182-1}\right)\ln\left(\frac{1-0.917}{1-0.182\,0.917}\right)}{\ln\left(\frac{\frac{2}{0.917}-1-0.182+\sqrt{0.182^2+1}}{\frac{2}{0.917}-1-0.182-\sqrt{0.182^2+1}}\right)}$$

$$F_{LMTD} = 0.39 \tag{4.35}$$

The corrected $LMTD$ can be then be evaluated:

$$F_{LMTD} = 0.39 \times 3.9^\circ = 1.19^\circ\, C \tag{4.36}$$

The properties for the water/glycol mixture are obtained by using the correlations presented above. Table 4.4 shows the results for the above temperatures for the heat exchanger being used in the distribution circuit in comparison with published data by Munson *et al.* (2009). The values of the fluid flow properties,

Table 4.4: Correlated and published data for density, specific heat capacity, thermal conductivity and viscosity

	T	$\boldsymbol{\rho}$	$\boldsymbol{cp}$	$\boldsymbol{k}$	$\boldsymbol{\mu}$
unit	$°C$	kg/m^3	kJ/kgK^{-1}	W/mK^{-1}	$10^{-5}\,kg/ms^{-1}$
t_m (corr)	15.5	1023.09	3.887	0.514	159.32
t_m (lit)	15.5	1023.12	3.885	0.513	160.62
T_m (corr)	21.0	1021.32	3.900	0.522	136.80
T_m (lit)	21.0	1021.34	3.896	0.521	139.81

e.g. velocity, Prandtl and Reynolds, etc. will be shown in Table 4.5. The output

Table 4.5: Fluid properties for the tube and shell side of the heat exchanger

Parameter	**Equation**	**Unit**	**Value**
$\bar{V}$ tubes	$\frac{\dot{V}}{A_{cs}}$	m/s	0.18
$\bar{V}$ shell		m/s	0.88
Pr tubes	$\frac{cp\,\mu}{k}$		12.05
Pr shell			10.22
Re tubes	$\frac{\rho\,\bar{V}\,d_H}{\mu}$		714
Re shell			6113
Nu tubes			4.10
Nu shell			104.70
h tubes	$\frac{Nu\,k}{d_H}$	W/m^2K^{-1}	341.00
h shell		W/m^2K^{-1}	5872.34

from the model is generated in Table 4.6. The percentage difference for the U values between the model output and the calculated value above varies between -0.1% – 0.2%. This error is negligible as it is most likely due to rounding off numbers differently between the methods.

4.3.3 Verification of the CFD Heat Transfer Model Applied to a Plate Fin

In order to verify the heat transfer simulation results obtained through commercial software packages, the heat transfer along a flat plate fin is considered.

Table 4.6: Output from the heat exchanger evaluation model in comparison with calculated values

Parameter	Unit	Calculated	Model
A_{cs} tubes	mm^2	1106	1106.27
A_{cs} shell	mm^2	1896	1896.44
$\bar{V}$ tubes	m/s	0.18	0.18
$\bar{V}$ shell	m/s	0.88	0.88
Re tubes		714	698
Re shell		6113	6133
h tubes	W/m^2K^{-1}	341.00	341.41
h shell	W/m^2K^{-1}	5872.34	5873.66
U tubes	W/m^2K^{-1}	319.45	319.79
U shell	W/m^2K^{-1}	212.28	211.94

The theoretical and experimental results are compared to the results obtained in Solidworks Simulation and Ansys, software packages available in the University Engineering department. For conventional purposes, the left hand side of the fin is kept at a constant temperature of $60°C$. Thermocouples are attached along the plate at 6 locations as shown in Fig. 4.9. The same locations were used in the software model. The experimental results were recorded once the base tempera-

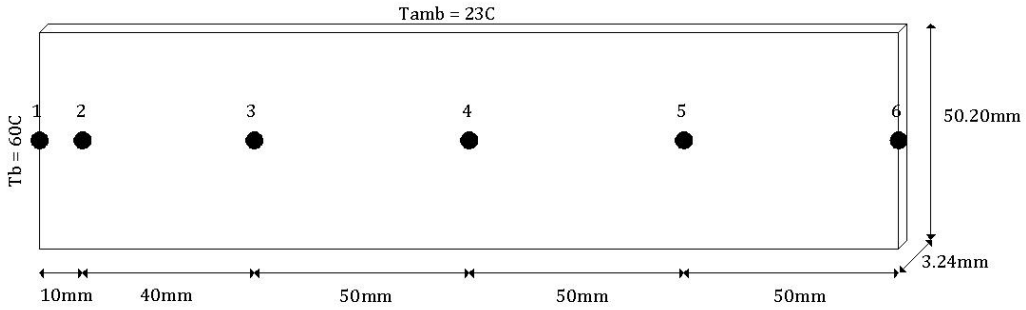

Figure 4.9: Plate fin with thermocouple locations

ture reached $60°C$. The thermal conductivity of the aluminium alloy plate was taken from the manufacturer as 16 W/mK^{-1} and the heat transfer coefficient of the un-insulated fin was determined as 14.9 W/m^2K^{-1}, based on the formula for

free convection on plate fins established by Kays and London. In this particular example there are a total of five elements with six nodal points spaced unevenly. The stiffness matrix, ($[k_s]$), and thermal load matrix, ($\{F\}$), are adopted from Moaveni (2003) as follows:

$$\left[\ k_s\ \right] = \frac{k\,A}{L}\begin{bmatrix}1 & -1\\ -1 & 1\end{bmatrix} + \frac{h\,P_x\,L}{6}\begin{bmatrix}2 & 1\\ 1 & 2\end{bmatrix} + h\ \ A\begin{bmatrix}0 & 0\\ 0 & 1\end{bmatrix} \tag{4.37}$$

$$\left\{\ F\ \right\} = \frac{h\,T_{amb}\,P_x\,L}{2}\begin{Bmatrix}1\\ 1\end{Bmatrix} + h\ \ T_{amb}\ \ A\begin{Bmatrix}0\\ 1\end{Bmatrix} \tag{4.38}$$

The third argument in the stiffness matrix and the second argument in the thermal load matrix are known as the end convection term and will only be considered for element 5. For the first element, the stiffness and load matrices are calculated as follows (all dimensions are in mm):

$$\begin{aligned}[k_s]^{(1)} &= \frac{0.16\times 50.20\times 3.24}{10}\begin{bmatrix}1 & -1\\ -1 & 1\end{bmatrix}\\ &\quad + \frac{0.0000149\times 2\times(50.20+3.24)\times 10}{6}\begin{bmatrix}2 & 1\\ 1 & 2\end{bmatrix}\\ [k_s]^{(1)} &= \begin{bmatrix}2.608 & -2.600\\ -2.600 & 2.608\end{bmatrix} \qquad (4.39)\\ \{F\}^{(1)} &= \frac{0.0000149\times 23\times 2\times(50.20+3.24)\times 10}{2}\begin{Bmatrix}1\\ 1\end{Bmatrix}\\ \{F\}^{(1)} &= \begin{Bmatrix}0.183\\ 0.183\end{Bmatrix} \qquad (4.40)\end{aligned}$$

The stiffness matrices for element 2 to 4 can be evaluated in the same way and become:

$$[k_s]^{(2)} = \begin{bmatrix}0.672 & -0.640\\ -0.640 & 0.672\end{bmatrix} \tag{4.41}$$

$$[k_s]^{(3)} = [k_s]^{(4)} = \begin{bmatrix}0.547 & -0.507\\ -0.507 & 0.547\end{bmatrix} \tag{4.42}$$

The load matrices for element 2 to 4 then become:

$$\{F\}^{(2)} = \begin{Bmatrix} 0.733 \\ 0.733 \end{Bmatrix} \tag{4.43}$$

$$\{F\}^{(3)} = \{F\}^{(4)} = \begin{Bmatrix} 0.916 \\ 0.916 \end{Bmatrix} \tag{4.44}$$

For element 5 the stiffness matrix looks as follows:

$$\begin{aligned} [k_s]^{(5)} &= 0.52 \begin{bmatrix} 1 & -1 \\ -1 & 1 \end{bmatrix} + 0.014 \begin{bmatrix} 2 & 1 \\ 1 & 2 \end{bmatrix} \\ &\quad + 0.0000149 \times 50.20 \times 3.24 \begin{bmatrix} 0 & 0 \\ 0 & 1 \end{bmatrix} \\ [k_s]^{(5)} &= \begin{bmatrix} 0.547 & -0.507 \\ -0.507 & 0.549 \end{bmatrix} \end{aligned} \tag{4.45}$$

For element 5 the thermal load matrix looks as follows:

$$\begin{aligned} \{F\}^{(5)} &= 0.983 \begin{Bmatrix} 1 \\ 1 \end{Bmatrix} + 0.0000149 \times 23 \times 50.20 \times 3.24 \begin{Bmatrix} 0 \\ 1 \end{Bmatrix} \\ \{F\}^{(5)} &= \begin{Bmatrix} 0.916 \\ 0.971 \end{Bmatrix} \end{aligned} \tag{4.46}$$

Assembling all the elements leads to the global conductance matrix $[k_s]^{(G)}$ and the global thermal load matrix $\{F\}^{(G)}$.

$$[k_s]^{(G)} = \begin{bmatrix} 2.608 & -2.600 & 0 & 0 & 0 & 0 \\ -2.600 & 3.280 & -0.640 & 0 & 0 & 0 \\ 0 & -0.640 & 1.219 & -0.507 & 0 & 0 \\ 0 & 0 & -0.507 & 1.094 & -0.507 & 0 \\ 0 & 0 & 0 & -0.507 & 1.094 & -0.507 \\ 0 & 0 & 0 & 0 & -0.507 & 0.549 \end{bmatrix} \tag{4.47}$$

$$\{F\}^{(G)} = \begin{Bmatrix} 0.183 \\ 0.916 \\ 1.648 \\ 1.831 \\ 1.831 \\ 0.971 \end{Bmatrix} \tag{4.48}$$

Applying the boundary condition $T = 60° C$, the final set of linear equations becomes:

$$\begin{bmatrix} 1 & 0 & 0 & 0 & 0 & 0 \\ -2.600 & 3.280 & -0.640 & 0 & 0 & 0 \\ 0 & -0.640 & 1.219 & -0.507 & 0 & 0 \\ 0 & 0 & -0.507 & 1.094 & -0.507 & 0 \\ 0 & 0 & 0 & -0.507 & 1.094 & -0.507 \\ 0 & 0 & 0 & 0 & -0.507 & 0.549 \end{bmatrix} \begin{Bmatrix} T_1 \\ T_2 \\ T_3 \\ T_4 \\ T_5 \\ T_6 \end{Bmatrix} = \begin{Bmatrix} 60 \\ 0.916 \\ 1.648 \\ 1.831 \\ 1.831 \\ 0.971 \end{Bmatrix} \tag{4.49}$$

In order to find a solution for this equation, the inverse matrix for the stiffness matrix needs to be computed:

$$[k_s]^{(G)^{-1}} = \begin{bmatrix} 1 & 0 & 0 & 0 & 0 & 0 \\ 0.931 & 0.358 & 0.2772 & 0.202 & 0.164 & 0.151 \\ 0.707 & 0.272 & 1.394 & 1.035 & 0.839 & 0.775 \\ 0.535 & 0.203 & 1.035 & 2.233 & 1.809 & 1.671 \\ 0.426 & 0.164 & 0.839 & 1.809 & 3.065 & 2.829 \\ 0.393 & 0.151 & 0.775 & 1.671 & 2.829 & 4.432 \end{bmatrix} \tag{4.50}$$

Now multiplying the inverse of the stiffness matrix with the global load matrix gives the numerical values for the temperatures at the different nodal points as follows:

$$\begin{Bmatrix} T_1 \\ T_2 \\ T_3 \\ T_4 \\ T_5 \\ T_6 \end{Bmatrix} = \begin{Bmatrix} 60.00 \\ 57.44 \\ 49.17 \\ 42.43 \\ 38.75 \\ 37.54 \end{Bmatrix} \tag{4.51}$$

The same boundary conditions and fin plate dimensions are applied in Ansys and Solidworks. Figure 4.10 shows the nodal temperatures at the same locations as above determined by Ansys. Figure 4.11 shows a plot of the nodal temperatures obtained through experimental investigation, Ansys, Solidworks and numerical modelling. The variation for the different methods ranges within -12 % – -0.5% for the experimental results; -9 % – 0% for Ansys; and -3.5% – 0% for Solidworks in comparison to the analytical results. As expected, the biggest error is for the experimental values as they include human error and the results are time-dependent. The system is heated until a base temperature of $60°C$ is reached.

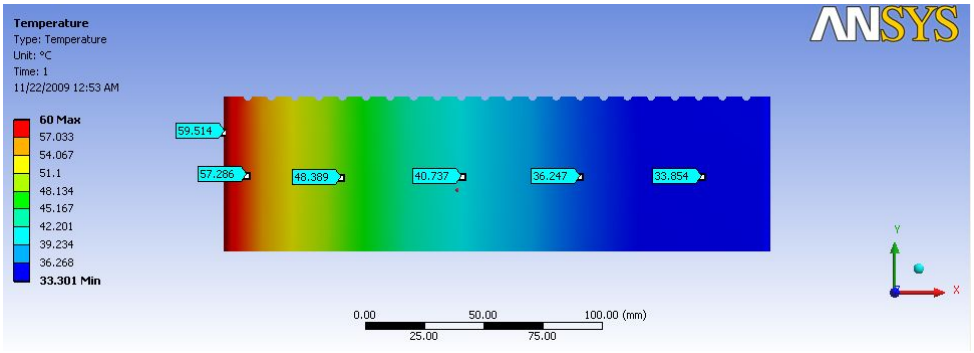

Figure 4.10: Ansys result plot of nodal temperatures across a plate fin

Upon this, the nodal temperatures are obtained through K-type thermocouples. Taking into account these errors would bring the result closer to the numerical values. The rig used in the experiment has a holder at the opposite side to the heating element, which acts partially as a heat sink. Additionally, the heat transfer coefficient and heat capacity values are not necessarily exactly the same as in the actual values for the experiment.

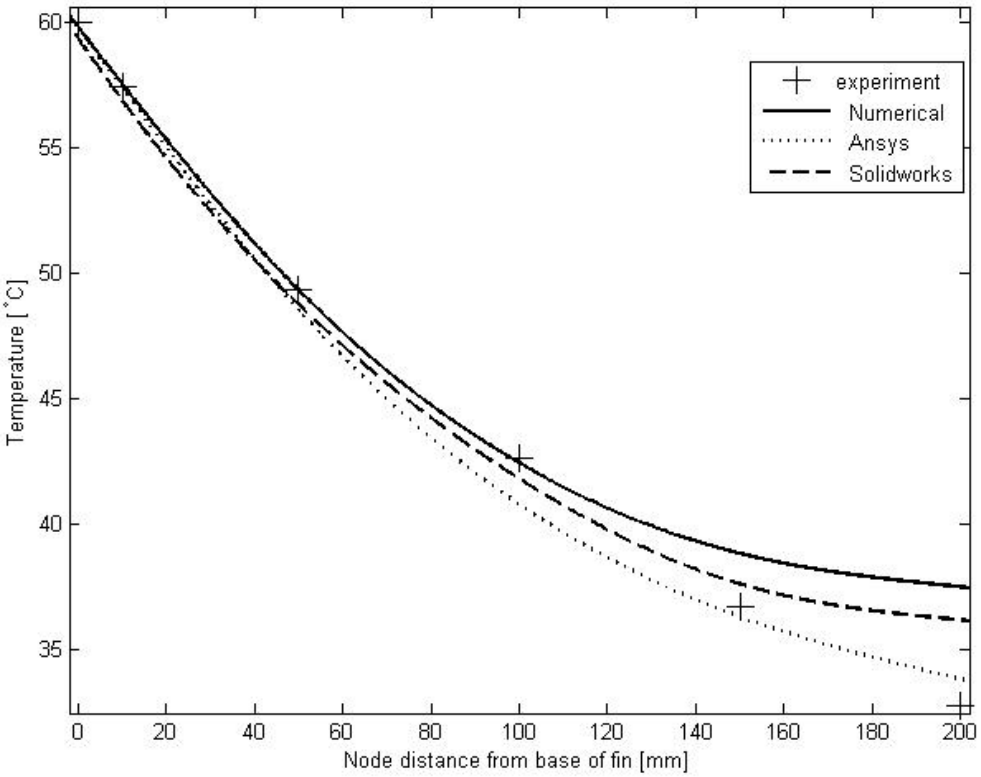

Figure 4.11: Comparison between experimental, numerical, Ansys and Solidworks results

4.3.4 Computational Fluid Dynamics of the Shell and Tube Heat Exchanger

This section describes the CFD model of the shell and tube heat exchanger used in the test rig. The heat exchanger is modelled according to manufacturing specifications in Solidworks. The FlowSimulation in Solidworks is used to model the flow of the water across the heat exchanger and the heat transfer from the hot to the cold fluid. A symmetry plane across the middle of the heat exchanger is used in to order to save CPU time for the convergence of the results. The domain fluid is set to water at an initial temperature of 293.16 K. The turbulence is set to turbulent in the shell and laminar inside the tubes based on the Reynolds numbers from the analytical model. This is based on the calculations carried out and presented above in Table 4.6. The mass flow rates are set to the values recommended by the manufacturer as outlined in Table 4.2. The shell inlet temperature is set to 318.16 K and the tube inlet temperature is set to 293.16 K.

The velocity in the shell side accelerated to a maximum of 12 m/s, however, this is at the outlet of the header tank where the water flow gets funnelled through to the outside of the domain, and varies between 0.01 m/s and 3.5 m/s within the actual shell. The velocity inside the tubes varies between 0.05 m/s to 0.25 m/s which corresponds well with an average calculated value of 0.18 m/s. The velocity variation for the shell and tubes are shown in Figs. 4.12 and 4.13, respectively. The legends are adapted to the minimum and maximum values of the corresponding sides of the heat exchanger. The average temperature drop from shell inlet to shell outlet is 7.2 K and the temperature is shown in Fig. 4.14. The average temperature rise from tube inlet to tube outlet is 3.9 K and the temperature distribution across the tubes is shown in Fig. 4.15.

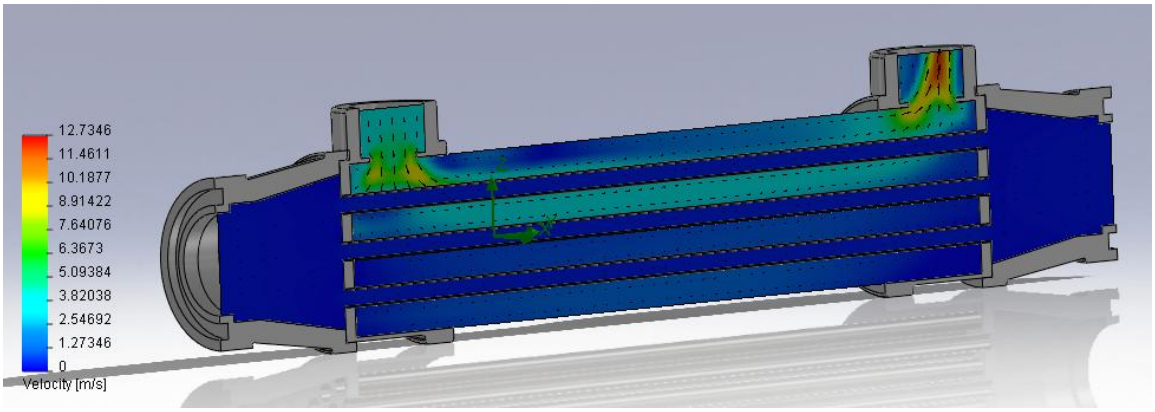

Figure 4.12: Velocity profile inside the shell

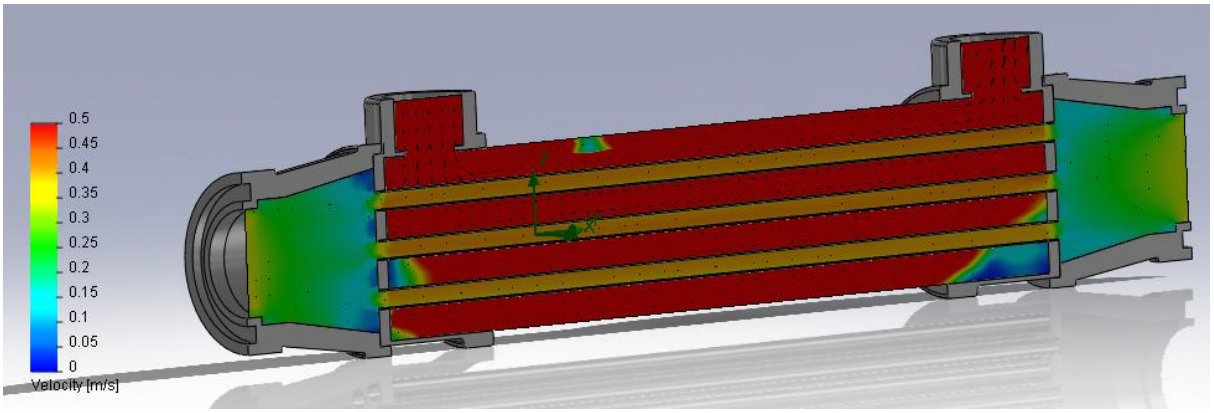

Figure 4.13: Velocity profile inside the tubes

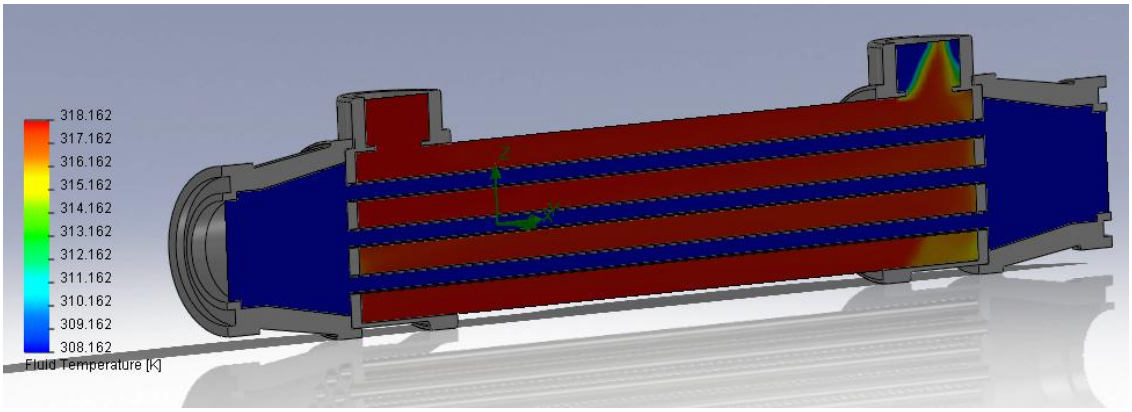

Figure 4.14: Temperature distribution across the shell

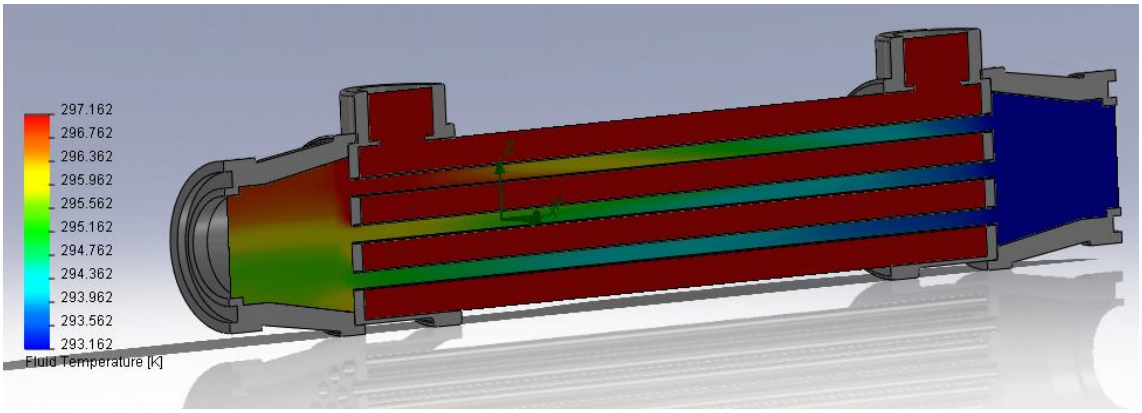

Figure 4.15: Temperature distribution across the tubes

4.4 Modelling of a γ-type Stirling Engine for Biomass Applications

As mentioned before, there are three different types of Stirling engines, namely alpha, beta and gamma. The gamma engine used in this study was originally developed by Dieter Viebach in 1992. The drawings of the engine are available under the Creative-commons licensing rights. The engine specifications are listed in Table 4.7 and the notations refer to Fig. 3.5. Numerous design changes were carried out over the years through communities of users. Roughly 120 engines were officially built until 2004. From the literature review it was determined that, although the gamma engine tends to have slightly larger dead volumes than either the alpha or the beta engine, there is a complete separation between the heat exchangers associated with the expansion and the compression working space. This is caused by the two pistons being housed in separate cylinders. The advantage is that the two cylinders can be sized independently. The analytical

Table 4.7: Stirling engine specifications

Parameter	**Unit**	**Value**
Engine type	n/a	γ
Bore compression piston	mm	85
Bore expansion piston	mm	96
Stroke compression	mm	183.5
Stroke expansion	mm	167.5
Cooling fluid	n/a	water
Heater arrangement	n/a	tubular
Cooler arrangement	n/a	fins
Regenerator arrangement	n/a	mesh wire

model will be developed to investigate the effects of changing the type of gas and the gas pressure charge on actual work output, pressure drop, mass of gas and efficiency. The computational fluid dynamics will look at the simulation of the flow and heat transfer in various parts of the engine.

4.4.1 Analytical Model of a γ-type Stirling Engine

The computer model generated is divided into two parts. The first part uses the Schmidt analysis to determine the total mass of gas in the heat exchanger (A1-A3).The second part is a third order analysis of the Stirling engine to determine the work output and efficiency (B1-B5). Figure 4.16 shows a layout of the major steps invoked by the software. In section (A1) the user input is read by the macro and stored in variables and the initial conditions for temperatures are set as well as the gas properties depending on the type of gas used as working fluid. In section (A2), the free flow area, void volume, wetted area and hydraulic diameter are determined for the heater, cooler and regenerator, respectively. These are dependent on the geometric shape of the heat exchangers and are programmed to account for the type used in the engine of this study; tubular for the heater, finned for the cooler and mesh wire for the regenerator. In section (A3), a Schmidt analysis is carried out for this gamma type engine. This is used to determine the total mass of the working gas in the engine.

In the second part, the computation of numerous differential equations is required and an iterative solution approach is applied. As mentioned in the theory, the heater and cooler temperatures specified by the user are not equal to the temperatures of the respective working spaces due to the impossibility of 100% heat transfer in the heater and cooler. Hence, an iterative method is used, which can be compared to a warm-up period of the engine, until the temperatures are balanced. This means that the temperatures at the end of the cycle will be more or less equal to the temperatures at the beginning of the cycle. This temperature difference is set to 1 degree and is limited by a maximum number of iterations of 10 (but this can be modified by the user). Secondly, the equations above are partially dependent on derivative forms of their corresponding equations. Hence, at priori, it is unknown what happens to the different values for each crank angle increment of the engine. Analysing the obtained equations shows a set of seven ordinary differential equations (T_e, T_c, Q_k, Q_r, Q_h, W_e and W_c). In order to solve this set of equations, the system is regarded as an initial value problem, where the equations are integrated from the known initial state. The classical fourth order Runge-Kutta method is used here. In section B1, the initial conditions are set as

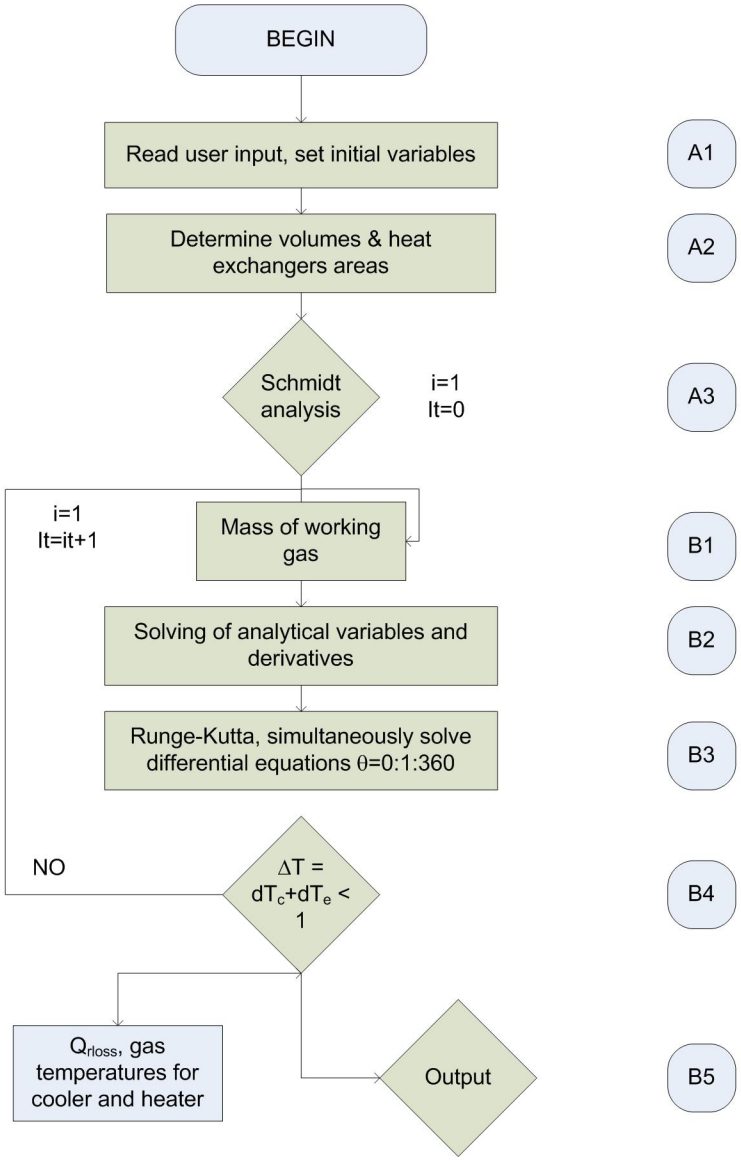

Figure 4.16: Flow diagram for the Stirling model

well as the resetting of the values for Q and W to zero at the beginning of each cycle. In section B2, the analytical variables and derivatives for pressure, masses and volumes are computed and in section B3, the seven ordinary differential equations are solved with a step increment of one degree crank angle (0.0174 rad) over an entire cycle. In section B4, the sum of the absolute temperature difference between beginning and end of the cycle is evaluated. If the sum is higher than 1, then the temperatures at the beginning and the end of the cycle are not yet balanced and require a new cycle run with the initial temperatures for the heater and cooler now being the temperatures determined for the end of the cycle. When the temperature difference computed in B4 becomes less than 1, then two options are presented in B5. The heat loss and resulting gas temperatures have or have not yet been computed. It can be seen that the actual gas temperature will be less than the determined wall temperature. This will generate a more realistic gas temperature. Once they are computed the condition of ΔT is re-checked and if still true, the results are presented. If the condition is not satisfied, the iteration is run once more. A $P - V$ graph is plotted once for the Schmidt analysis and once for the more realistic simulation of the engine. Table 4.8 shows the input parameters that are required from the user in order to compute the results. The dimensions shown in this table, are taken from the engine used in the test stage of this study. The operational values are realistic values that will be targeted when running the engine. The sinusoidal volume variation of the compression and the expansion space, as described by equations (3.44) and (3.45) can be plotted over an entire cycle (360°). Figure 4.17 shows a plot of the volume variations over an entire cycle for the test engine with the interconnecting heat exchanger spaces omitted. Once these data have been read, the properties for the chosen gas are determined by the macro. These values are presented in Table 4.9. Now the geometrical parameters for all three heat exchangers (heater, regenerator and cooler) can be determined. Table 4.10 presents cross-sectional and free flow area, volume and hydraulic diameter for all three heat exchangers. As the inlet and outlet temperatures are not of main interest at this time (compared to the actual temperature difference), the regenerator temperature is determined with

Table 4.8: Input parameter/specifications used for the analytical model of the Stirling engine

Parameter	Symbol	Definition	Unit	Value
Engine	SV_e	expansion swept vol.	cc	607.30
	SV_c	compression swept vol.	cc	595.41
	DV_e	expansion dead vol.	cc	150.70
	DV_c	compression dead vol.	cc	170.78
Heater	d_i	tube inner diameter	mm	6.0
	L_h	tube length	mm	362.8
	n_t	number of tubes	n/a	20
Regenerator	d_i	inner diameter	mm	97.6
	d_o	outer diameter	mm	133.7
	L_r	length	mm	65.6
	por	mesh porosity	n/a	0.90
	t_m	mesh wire thickness	mm	0.05
Cooler	L_{fin}	fin length	mm	11.0
	t_{fin}	fin thickness	mm	1.0
	w_{fin}	fin width	n/a	84.0
	n_{fin}	number of fins	n/a	144
	d_i	inner diameter	mm	101.0
	d_o	outer diameter	mm	125.0
Operation	gas	type of gas (Ai, He, H)	n/a	he
	P_m	mean pressure charge	Pa	1000000
	ΔT_h	hot side temperature diff.	K	873.0
	ΔT_k	cold side temperature diff.	K	293.0
	f	frequency	Hz	13.33
	rev	revolutions per minute	rpm	800

Table 4.9: Gas properties for the Stirling engine model

Parameter	Unit	Air	Helium	Hydrogen
γ	n/a	1.40	1.67	1.40
R	$J/kgmol^{-1}$	287.00	2078.60	4157.20
μ	$10^{-6}\, kg/ms^{-1}$	17.08	18.55	8.35
T_{suth}	K	112.00	80.00	84.40
cv	kJ/kgK^{-1}	0.718	3.103	10.393
cp	kJ/kgK^{-1}	1.005	5.181	14.550

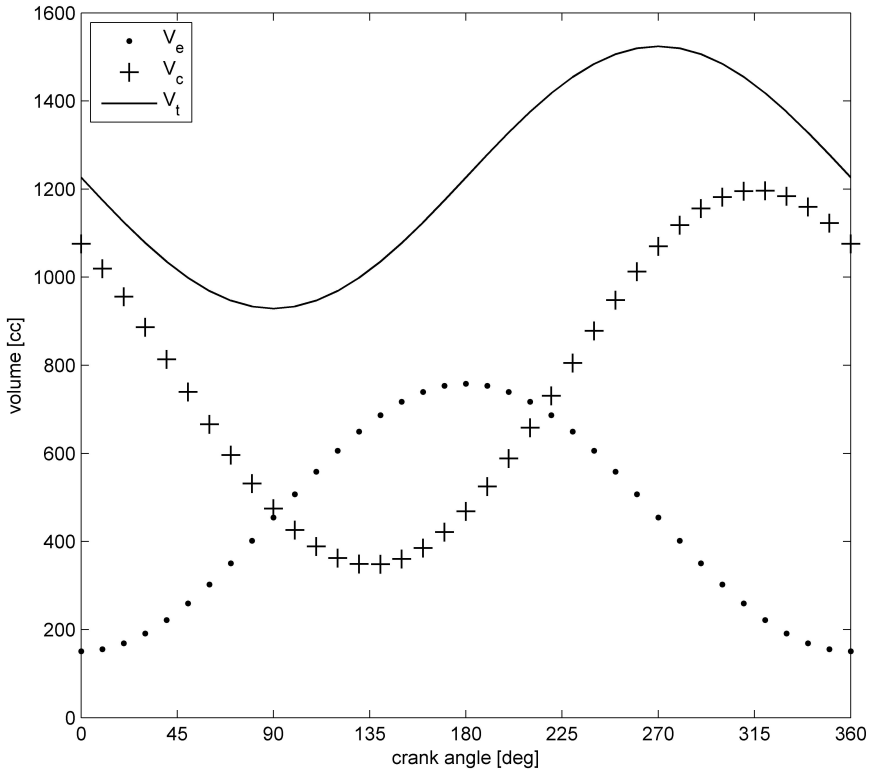

Figure 4.17: Volume variations with crank angle for the γ-type Stirling engine

the logarithmic mean temperature difference:

$$T_r = \frac{t_h - t_k}{\ln \frac{t_h}{t_k}} = \frac{873 - 293}{\ln \frac{873}{293}} = 531.25\ K \tag{4.52}$$

The various parameters described in chapter 3 that are required to determined

the total mass of gas in the engine, are calculated as follows:

$$\begin{aligned}\varphi &= 2\frac{T_k}{T_h}\frac{DV_e}{SV_e} + 2\frac{V_r}{SV_e}\frac{T_k}{T_r} + 2\frac{T_k}{T_h}\frac{V_h}{SV_e} + 2\frac{T_k}{SV_e}\frac{V_k}{SV_e} + 1 + 2\frac{DV_c}{SV_e} \\ &= 2\times\frac{293}{873}\times\frac{150.70}{607.30} + 2\times\frac{441.04}{607.30}\times\frac{293}{531.25} + 2\times\frac{293}{873}\times\frac{205.16}{607.30} \\ &\quad +2\times\frac{293}{873}\times\frac{224.78}{607.30} + 1 + 2\times\frac{170.78}{607.30} \\ \varphi &= 3.005 \end{aligned} \tag{4.53}$$

Table 4.10: Geometrical parameters for the heater, regenerator and cooler

Parameter	**Unit**	**Heater**	**Regenerator**	**Cooler**
A_{cs}	$10^{-3}\,m^2$	0.566	6.733	0.268
A	m^2	0.137	3.920	0.302
V	$10^{-3}\,m^3$	0.205	0.441	0.225
d_H	$10^{-3}\,m$	6.000	4.500	2.980

$$\kappa = \varphi + \frac{T_k}{T_h} + \frac{SV_c}{SV_e} = 3.005 + \frac{293}{873} + \frac{595.41}{607.30} = 4.321 \tag{4.54}$$

$$\beta = \tanh\left[\frac{SV_c}{SV_e}\frac{T_h}{T_k}\right] = \tanh\left[\frac{595.41}{607.30}\times\frac{873}{293}\right] = 71.10^\circ \tag{4.55}$$

$$\begin{aligned}\zeta &= \sqrt{\left(\frac{SV_e}{SV_c}\right)^2 + \left(\frac{T_k}{T_h}\right)^2} = \sqrt{\left(\frac{607.30}{595.41}\right)^2 + \left(\frac{293}{873}\right)^2} \\ \zeta &= 1.074 \end{aligned} \tag{4.56}$$

$$\chi = \frac{\zeta}{\kappa} = \frac{1.074}{4.321} = 0.249 \tag{4.57}$$

Now the total mass of gas (Helium) in the engine can be determined as follows:

$$\begin{aligned} m &= \frac{P_{mean}\, SV_e\, \kappa\sqrt{1+\chi^2}}{2\, R\, T_k} \\ &= \frac{1000000 \times 607.30 \times 10^{-6} \times 4.321 \times \sqrt{1+0.249^2}}{2 \times 2078.6 \times 293} \\ m &= 2.22\, g \end{aligned} \tag{4.58}$$

The total work done in the expansion and compression space is respectively:

$$\begin{aligned} W_e &= \frac{P_{mean}\, SV_e\, \pi\, \chi\, \sin\beta}{1+\sqrt{1-\chi^2}} \\ &= \frac{1000000 \times 607.30 \times 10^{-6} \times \pi \times 0.249 \times \sin 71.10^\circ}{1+\sqrt{1-0.249^2}} \\ W_e &= 229.32\, J \end{aligned} \tag{4.59}$$

$$\begin{aligned} W_c &= -\frac{P_{mean}\, SV_e\, \pi\, \chi\, t\, \sin\beta}{1+\sqrt{1-\chi^2}} \\ &= -\frac{1000000 \times 607.30 \times 10^{-6} \times \pi \times 0.249 \times \frac{293}{873} \times \sin 71.10^\circ}{1+\sqrt{1-0.249^2}} \\ W_c &= -76.63\, J \end{aligned} \tag{4.60}$$

The efficiency of the engine can be determined as follows:

$$\eta = \frac{W_e + W_c}{W_e} = \frac{229.32 - 76.63}{229.32} = 66.58\% \tag{4.61}$$

Once the total mass of gas in the engine is determined, the third order analysis of the engine can be carried out. In a first stage, the model uses an iterative approach to determine the conditions of the engine over one cycle. The criterion for convergence is governed by the temperature difference between beginning and end of the cycle of the heater and the cooler. At priori, this difference is set to less than 1 K. This results in the model calculating all values for a number of iterations until steady-state operations are reached. Each iteration is carried out for an entire cycle. All calculations are carried out for a crank angle of zero before the angle is increased by 1 K degree. For each crank angle the following

calculations are carried out first. Since the calculations are dependent on the crank angle, the following hand by hand calculations are for a crank angle of 0°. The pressure, equation (3.60), and the derived pressure derivative, equation (3.67) in the engine are as follows:

$$\begin{aligned} P &= \frac{m\,R}{\frac{V_c}{T_c}+\frac{V_k}{V_k}+\frac{V_r}{T_r}+\frac{V_h}{T_h}+\frac{V_e}{T_e}} \\ &= \frac{0.00222\times 2078.6}{\frac{0.0010706}{293}+\frac{0.000225}{293}+\frac{0.000441}{531.25}+\frac{0.000205}{873}+\frac{0.000151}{873}} \\ P &= 816.33\,kPa \end{aligned} \tag{4.62}$$

$$\begin{aligned} \delta P &= \frac{-\gamma P\left(\frac{\delta V_c}{T_c}+\frac{\delta V_e}{T_h}\right)}{\frac{V_c}{T_c}+\gamma\left(\frac{V_k}{T_k}+\frac{V_r}{T_r}+\frac{V_h}{T_h}\right)+\frac{V_e}{T_e}} \\ &= \frac{-1.67\times 816331\times\left(\frac{-0.0003}{293}+\frac{0}{873}\right)}{\frac{0.0010706}{293}+1.76\times\left(\frac{0.000225}{293}+\frac{0.000441}{531.25}+\frac{0.000205}{873}\right)+\frac{0.000151}{873}} \\ \delta P &= 202.11\,kPa \end{aligned} \tag{4.63}$$

The masses of gas for the different cells can be determined by the gas law equation:

- compression: $m_c = 1.442\,g$
- cooler: $m_k = 0.301\,g$
- regenerator: $m_r = 0.326\,g$
- heater: $m_h = 0.092\,g$
- expansion: $m_e = 0.068\,g$

The mass derivatives for the compression and expansion spaces are calculated as follows:

$$\begin{aligned} \delta m_c &= \frac{P\,\delta V_c+\frac{V_c\delta P}{\gamma}}{R\,T_c k} \\ &= \frac{816331\times(-0.0003)+\frac{0.001076\times 202114}{1.67}}{2078.6\times 293} \\ \delta m_c &= -0.188\,g/s \end{aligned} \tag{4.64}$$

$$\begin{aligned}
\delta m_e &= \frac{P\,\delta V_e + \frac{V_e \delta P}{\gamma}}{R\,T_h e} \\
&= \frac{816331 \times 0 + \frac{0.000151 \times 202114}{1.76}}{2078.6 \times 873} \\
\delta m_e &= 0.01\ g/s
\end{aligned} \tag{4.65}$$

The mass derivatives for the three heat exchangers are as follows:

$$\delta m_k = \frac{\delta P\, m_k}{P} = \frac{202114 \times 0.301}{816331} = 0.075\ g/s \tag{4.66}$$

$$\delta m_r = \frac{\delta P\, m_r}{P} = \frac{202114 \times 0.326}{816331} = 0.081\ g/s \tag{4.67}$$

$$\delta m_h = \frac{\delta P\, m_h}{P} = \frac{202114 \times 0.092}{816331} = 0.023\ g/s \tag{4.68}$$

$$\tag{4.69}$$

The seven derivatives, determined in chapter 3 (expansion and compression temperature derivatives, the heat derivative for the heater, regenerator and cooler as well as the derivative of the expansion and compression work), are determined by applying the 4^{th} order Runge-Kutta method (Haiber *et al.*, 1989, see). The detailed calculations are shown for the heat changes in the cooler. For the cooler, the initial value for Q_k is set to zero, as no heat has passed through the cooler at the start of the simulation. The initial crank angle is zero and the final crank angle for the Runge-Kutta method is set to 1°, which is the next crank angle in the overall simulation. The derivative of Q_k can be calculated for the initial step.

$$\begin{aligned}
\delta Q_k &= \frac{V_k\,\delta P\, cv}{R} - cp\ (T_i\,\dot{m}_i - T_o\,\dot{m}_o) \\
&= \frac{0.000225 \times 202114 \times 3103}{2078.6} \\
&\quad -5181 \times \left(293 \times 0.188 \times 10^{-3} - 293 \times (0.188 - 0.075) \times 10^{-3}\right) \\
\delta Q_k &= -44.82
\end{aligned} \tag{4.70}$$

This value for δQ_k can then be used in the Runge-Kutta method in order to determine the value for Q_k after an increment of 1°. This amounts to $Q_k = -0.779\ J$. The value obtained for Q_k by the model in the first iteration from 0° to 1° crank angle is $Q_k = -0.782\ J$. The model was forced to stop after one

iteration in order to obtain this result. The slight difference in value arises from rounding off numbers in the calculations carried out by hand. This value for Q_k will now become the new starting value for the Runge-Kutta for the next crank angle. Similarly, the values for Q_h, Q_r, $\dot{W}_c$, $\dot{W}_e$, T_e and T_c are calculated. Once all these calculations have been computed over one cycle, the model determines the difference between heater and cooler temperatures between values at the beginning and the end of the cycle. If this difference becomes less than 1 K, the model assumes steady state conditions, otherwise another iteration is performed. Table 4.11 presents the values determined by the model for the particular case of the default values presented in Table 4.7. The model determines steady state conditions after 4 iterations, as shown by the error value.

The temperatures for expansion and compression determined by the model after one cycle are $T_e = 760.12\ K$ and $T_c = 282.88\ K$, respectively. The error is then calculated as follows:

$$error = |T_{c,1} - T_{c,2}| + |T_{e,1} - T_{e,2}| \tag{4.71}$$

The absolute values are used in order to determine the numerical difference, independent of the mathematical sign. The subscript 1 and 2 refer to the beginning and end of the cycle, respectively. Using the values for the first iteration gives an error value of 123 K . This is obviously larger than 1 K, the specified error, hence the engine is not in steady state conditions and the model runs another iteration. The temperatures determined so far do not take into account the losses

Table 4.11: Temperature and error results for the different iterations

Iteration	T_e $[K]$	T_c $[T]$	**error**
0	873.00	293.00	n/a
1	760.12	282.88	123.00
2	748.13	279.99	14.88
3	747.00	279.06	2.05
4	747.02	278.75	0.30

due to pumping and heat losses. These need to be evaluated and the temperature adjusted accordingly. The method is the same for all three heat exchangers and is

shown here for the regenerator as it is the first one to be carried out by the model. The net heat loss for the regenerator requires the effectiveness of the regenerator. The Stanton number for this particular heat exchanger, adopted from Kays and London, is given as:

$$St = \frac{0.46\, Re^{-0.4}}{Pr} = \frac{0.46 \times 33.76^{-0.4}}{0.71} = 0.16 \tag{4.72}$$

Here, the Reynolds number is the average value over one cycle. From this the number of transfer units and the heat exchanger effectiveness can be determined, as shown in equations (3.82) and (3.83), respectively:

$$NTU = \frac{St\, A_{cs}}{2\, A} = \frac{0.16 \times 3.92}{2 \times 6.73 \times 10^{-3}} = 46.6 \tag{4.73}$$

$$\varepsilon = \frac{NTU}{NTU + 1} = \frac{46.6}{46.6 + 1} = 0.979 \tag{4.74}$$

Over the first cycle, the minimum and maximum heat loss in the regenerator are included in the net heat loss for the regenerator as follows:

$$Q_{rloss} = (1 - \varepsilon)\,(Q_{max} - Q_{min}) = (1 - 0.979)\,(1400 - 0) = 29.4\ J \tag{4.75}$$

The Reynolds friction coefficient can be determined based on the average Reynolds number over one cycle:

$$Cf_{Re} = 54 + 1.43\, Re^{0.78} = 54 + 1.43 \times 33.76^{0.78} = 76.26 \tag{4.76}$$

The pressure loss in pipes can be rewritten in respect of the regenerator flow direction:

$$\begin{aligned} \Delta P &= \frac{2\, Cf_{Re}\, L\, V\, G_{flux}\, \mu}{m\, d^2} \\ &= \frac{2 \times 76.26 \times 65.5 \times 10^{-3} \times 0.441 \times 10^{-3} \times 0.90 \times 2.91 \times 10^{-5}}{0.301 \times 10^{-3} \times (0.45 \times 10^{-3})^2} \\ \Delta P &= 1889.32\ Pa \end{aligned} \tag{4.77}$$

The mass flux G_{flux} takes into account the mass in– and out–flow to the regenerator as well as the engine operating speed ω, and can be determined as

follows:

$$\begin{aligned} G_{flux} &= \frac{(\dot{m}_i + \dot{m}_o)\,\omega}{a\,A} = \frac{(-\delta m_c - \delta m_k + \delta m_e + \delta m_h)\,\omega}{2\,A} \\ &= \frac{(0.188 - 0.075 + 0.01 + 0.022) \times 10^{-3} \times 83.78}{2 \times 0.00673} \\ G_{flux} &= 0.90 kg/m^2 s^{-1} \end{aligned} \tag{4.78}$$

The heat transfer coefficient for the heater can be determined as follows:

$$h = \frac{C f_{Re}\,\mu\,cp}{2\,d\,Pr} = \frac{32.47 \times 3.93 \times 10^{-5} \times 5181}{2 \times 0.006 \times 0.71} = 775.97 W/m^2 K^{-1} \tag{4.79}$$

Now the actual gas temperature in the heater can be determined according to equation (3.87), based on the engine frequency f:

$$T_h = T_{w,h} - \frac{(Q_h + Q_{rloss})\ f}{h\,A} = 760.12 - \frac{(202.17 + 29.4) \times 13.33}{775.78 \times 1.37} = 757.22\ K \tag{4.80}$$

Now the iteration can be run again with the new temperatures for the expansion and compression spaces. The total heat losses and inputs to the engine can then be determined. The heat at the end of the cycle is multiplied by the frequency to obtain an overall cycle value as follows:

$$\begin{aligned} \dot{Q}_{act} &= (Q_h + Q_{rloss} + Q_{leak}) \times f \\ &= (201.87 + 29.488.85) \times 13.33 \\ \dot{Q}_{act} &= 4267.19\,W \end{aligned} \tag{4.81}$$

where Q_{leak} is the leakage from the regenerator housing wall and is determined as follows:

$$Q_{leak} = \frac{\frac{k\,A_{wall}}{l_r} \times (T_{w,h} - T_{w.k})}{f} = \frac{\frac{25 \times 0.0065}{0.0655} \times (760.12 - 282.88)}{13.33} = 88.82\ J \tag{4.82}$$

The actual work output by the engine takes account of the pumping losses as follows:

$$\dot{W}_{act} = \dot{W}_c + \dot{W}_e - \dot{W}_{pump} = -1536.35 + 3151.95 - 83.96 = 1531.64\,W \tag{4.83}$$

The overall efficiency of the engine can then be determined as follows:

$$\eta = \frac{\dot{W}_{act}}{\dot{Q}_{act}} = \frac{1531.64}{4267.19} = 35.9 \tag{4.84}$$

4.4.2 Verification of the Analytical Model of a γ-type Stirling Engine

Table 4.12 and Table 4.13 give the output from the computer model for the above described engine parameters. The results obtained differ slightly from the calculated values, this is generally due to the different methods of rounding off numbers used. The difference between computed and calculated values for the actual work, actual heat input and efficiency are 0.1%, 1.2% and 1.1%, respectively. Figure 4.18 shows a plot of the total engine pressure versus the total

Table 4.12: Output from the Schmidt analysis

Symbol	**Description**	**Unit**	**Model**	**Calculated**
m	mass	kg	2.22	2.22
W_e	expansion work	J	219.6	229.3
W_c	compression work	J	-73.7	-76.6
Power	power	W	1945.6	2035.4
η	efficiency	n/a	66.4%	66.6%

volume of the engine, based on the results obtained by the method derived from the 'Schmidt' analysis and Fig. 4.19 shows the results for the third order analysis.

Table 4.13: Output from the third order analysis

Symbol	Description	Unit	Model	Calculated
$\dot{Q}_k$	heat to the cooler	W	2129.13	1979.39
$\dot{Q}_r$	heat to the regenerator	W	215.26	215.21
$\dot{Q}_h$	heat to the heater	W	2695.53	2690.93
$\dot{W}$	total power output	W	1614.13	1613.72
η	efficiency	n/a	59.9%	59.9%
$\dot{Q}_{rloss}$	regenerator net loss	W	396.13	391.9
$\dot{Q}_{rwl}$	regenerator wall leakage	W	1121.58	1183.97
$\dot{W}_{pump}$	pumping loss	W	83.96	83.96
$\dot{W}_{act}$	actual power	W	1530.18	1531.64
$\dot{Q}_{act}$	actual heat input	W	4213.24	4267.19
η_{act}	actual thermal efficiency	n/a	36.3%	35.9%

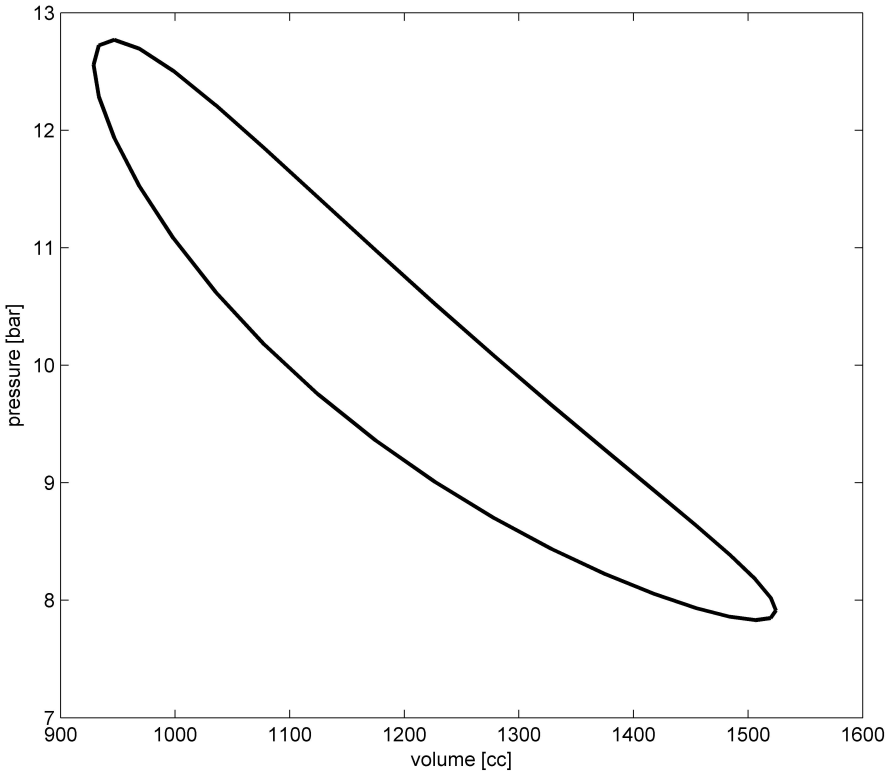

Figure 4.18: Schmidt P-V diagram for a γ-type Stirling engine

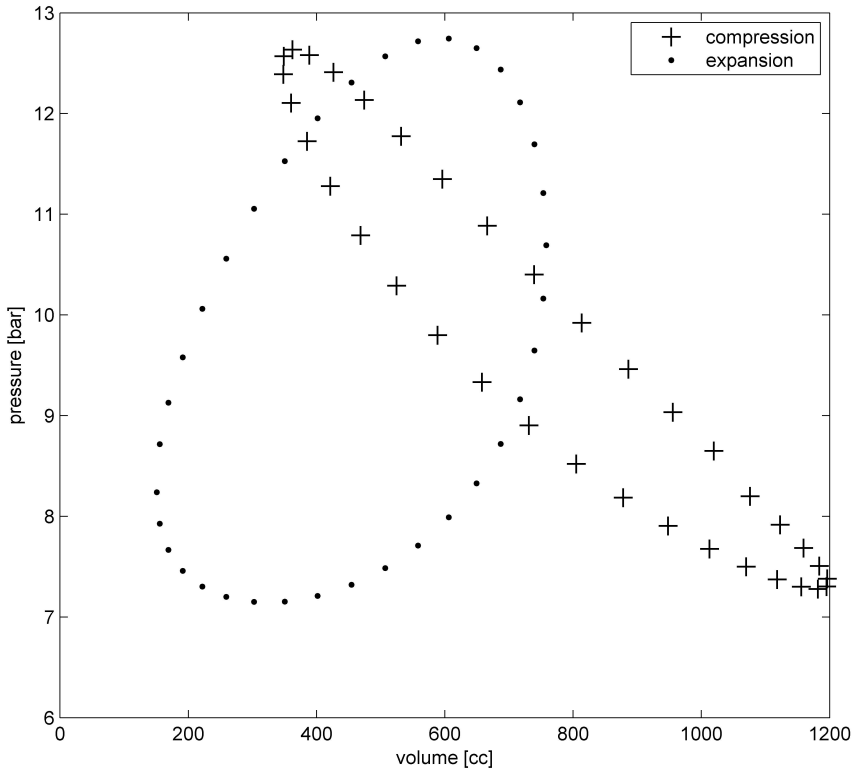

Figure 4.19: P-V diagram for a γ-type Stirling engine from the 3^{rd} order analysis

4.4.3 CFD Analysis of the γ-type Stirling Engine

The CFD analysis of the Stirling engine is divided into three parts. In a first part, the gas flow from the regenerator to the expansion space is analysed along with the heating of the gas in the heater. In a second part, the flow of the gas and the water from the cooler to the compression space header and in a third part, the flow of both gas and water in the compression space and its header. For all three investigations, the heat exchange between the hot gas and the water is determined. For the first two tests, the inlet temperature of the working gas is set to the regenerator temperature of 531.25 K, same as for the model, and for the third test the inlet parameters are based on the outlet results from the second test. For the first test, the heat transfer coefficient of the heater tubes is set to 800 W/m^2K^{-1} as determined earlier by the analytical model. The outside bulk temperature surrounding the heater is kept constant at 873 K. This temperature is the same as the one used in the model. The inlet mass flow to the regenerator is set to 0.8 g/s as determined by the model for standard air with a pressure charge of 10 MPa. The expansion piston is not included in the model and it is assumed that the gas will enter the expansion space at its maximum volume. The graphs legends, for the CFD results, are adjusted to minimum and maximum temperature for the respective fluid for that particular test. This will give a more detailed picture of the temperature changes for the various investigations. The orange arrows are used to show the direction of flow of the fluid, and is only used for viewing purposes. Figure 4.20 shows the temperature increase of the gas as it flows from the regenerator through tubes to the expansion space determined by SolidWorks FlowSimulation. The highest temperature of the gas is achieved at the bend of the heater U-tubes. The heat input was directed towards the centre of the all the bends to cause uniform heat distribution on all tubes. The results show a gradual increase of the temperature, as expected until the gas flows from the tubes into the expansion space. The expansion of the gas causes the temperature to drop. The outflow at the bottom of the expansion space is set to atmospheric conditions. Figure 4.21 shows the air velocity through the tubes as determined by the CFD model to be uniform across the tubes. As the tube diameter neither increases nor decreases no change in velocity should be

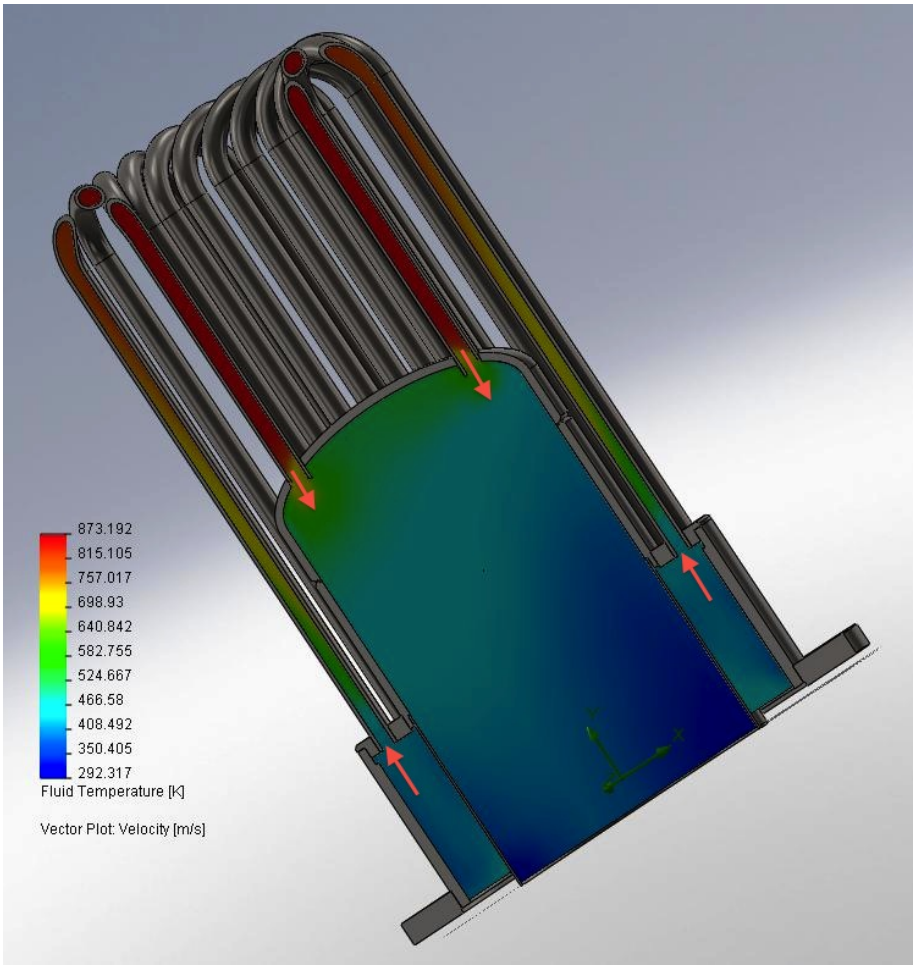

Figure 4.20: Temperature profile for the heater at 10bar air

expected. However in the u-bend there will be a slight increase of temperature due to the different curvature radius of the bend. As the gas has a 'longer' path to travel at the outer bend radius, the velocity is expected to increase compared to gas travelling along the inside curvature radius. The second test was used to determine the water and gas flow as well as the heat transfer between the two fluids. The water inlet parameters were set to 293 K and 10 $litre/hr$ water flow. The gas flow direction is arbitrarily chosen to flow from the regenerator to the cooler towards the compression space. The inlet mass flow is set to 2.7 g/s for air at 10 MPa pressure charge with a temperature of 531.25 K, as previously

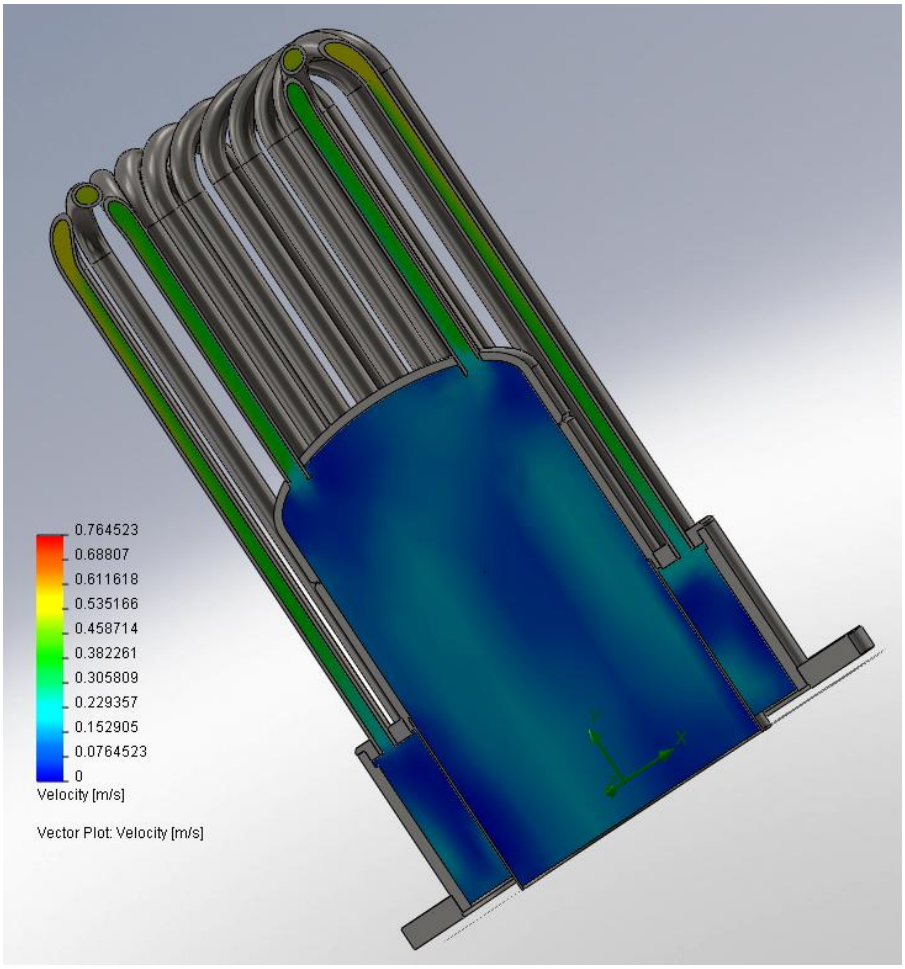

Figure 4.21: Velocity distribution for the heater at 10bar air

stated. The third test determines the temperature changes in the compression space and its respective header. The inlet temperatures for this third test are based on the outlet flow temperature and velocities, determined by the second test described above. These temperatures had been evaluated at 311.8 K and 346.3 K for water and gas respectively. This reflects a temperature drop for the gas in the cooler and connecting tubes of 185 K and a rise for the water temperature of 18.6 K. Figure 4.22 shows the gas temperature as it enters the cooler from the regenerator. The gas temperature upon entering the cooler is set to the regenerator exit temperature (facing the cooler with the direction of flow

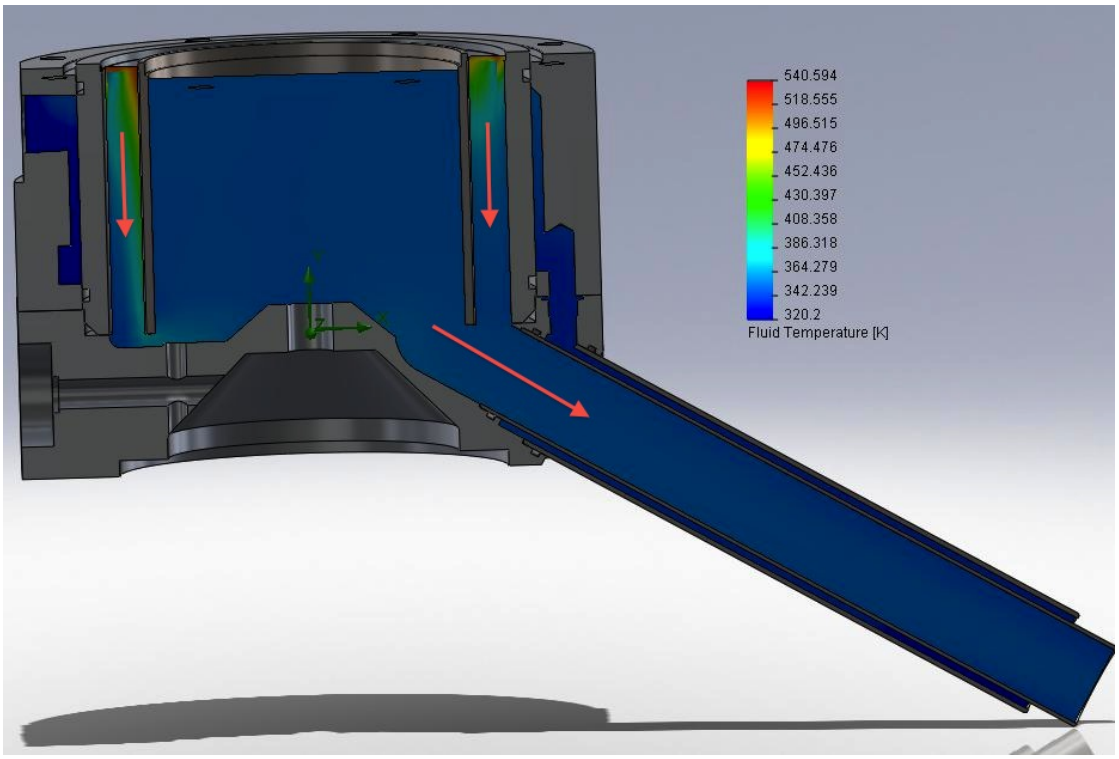

Figure 4.22: Gas temperature profile for the cooler and its connecting tubes

being towards the cooler). This temperature then gradually drops to around 346 K at the end of the cooler where the gas enters the compression space inside the expansion cylinder. The flow of gas is then directed towards the connecting pipes, leading the gas towards the compression space, Fig. 4.26. Additionally, cooling takes place via a double-pipe heat exchanger where the cooling fluid flows in the outer tube and the gas in the inner tube prior to entering the compression header. Figure 4.23 shows the flow pattern of the gas from the cooler (after leaving the regenerator), through the compression space of the expansion cylinder towards the compression header. An obvious increase in velocity is observed in the connecting pipe, caused by the reduced diameter normal to the flow. The flow of gas upon leaving the cooler shows a lot of turbulence inside the compression space. Figure 4.24 shows the increase in water temperature as it flows around the cooler and then down into the connecting pipe. The water temperature is increased by almost 20 K. At the end of the connecting tubes (before reaching

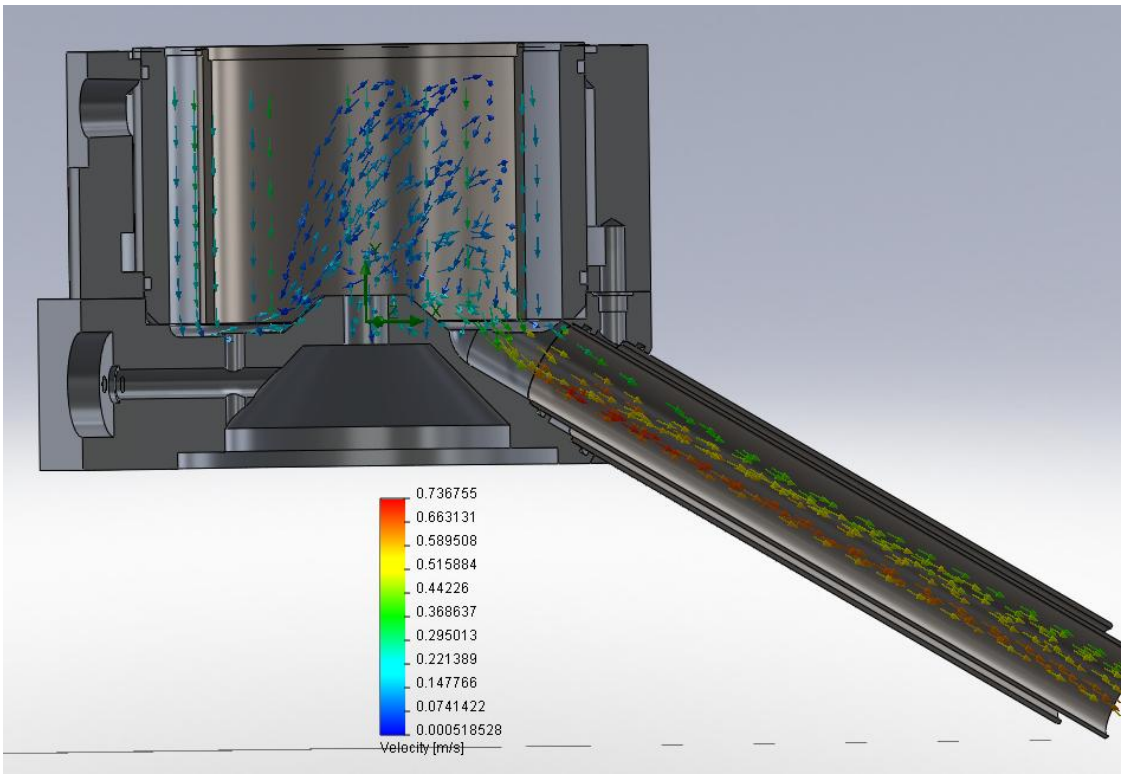

Figure 4.23: Gas velocity vectors across the cooler and its connecting tubes

the compression header, omitted from Fig. 4.24), there seems to be a decrease of the water temperature. However, as can be seen from Fig. 4.25, the water flow does not affect this region of the pipe. The flow is directed upwards due to internal turbulences in the water flow. The flow pattern is shown on Fig. 4.25 and shows some turbulences occurring at the connecting point between the cooler and the piston mounting plate, as well as on the thinner regions of the cooling jacket. There is a slight increase in temperature for the water in the bottom part of the cooling jacket. Although Fig. 4.25 is a cross-section view of the cooler and the connecting tubes, the results are not subject to this cross-sectional cut and show the water flow around the outside of the expansion cylinder inside the cooling jacket. Equally, the water flow inside the outer (connecting) tube seems to flow inside the inner tube. This is due to the imperfections of 2D representations of 3D results. Figure 4.26 shows the velocity variation through the compression

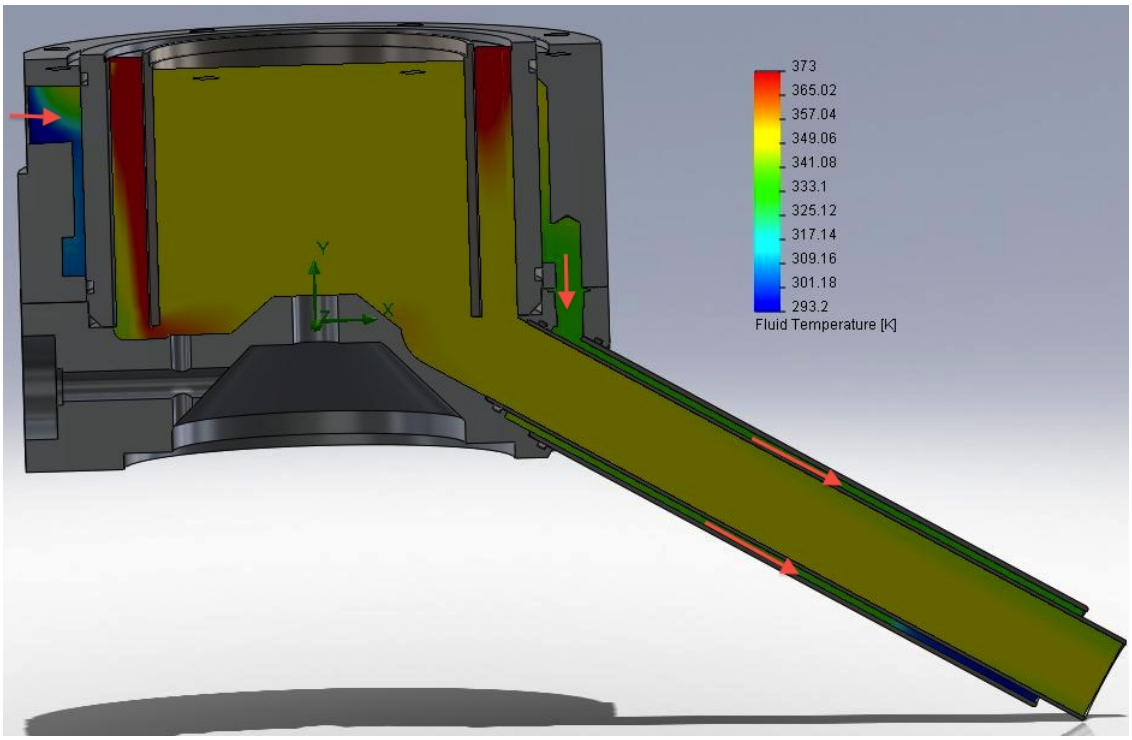

Figure 4.24: Water temperature profile for the cooler and its connecting tubes

header and space for the working gas. An increase of velocity can be observed at the bend of the compression header, where the gas changes its flow direction by almost 120°. Once the gas is fully compressed here, it will change its flow direction again and flow back through the connecting pipes into the cooler. The water temperature is shown on Fig. 4.27. The bars cause the water to flow evenly along the length of the cooling jacket and hence cause an additional cooling in the compression space. The importance of the directing bars in the cooling jacket can be seen in Fig. 4.28, which shows the velocity and flow pattern of the water from underneath the cooling jacket. As mentioned before, there is some slight turbulence when the water exits the connecting pipes to enter the compression header. Figure 4.29 gives a better view of this flow inside the compression header, which funnels the water from the connecting pipe into the cooling jacket and then back out into the open. From the compression header, the water is then evenly distributed via the connecting holes into the cooling jacket of the compression

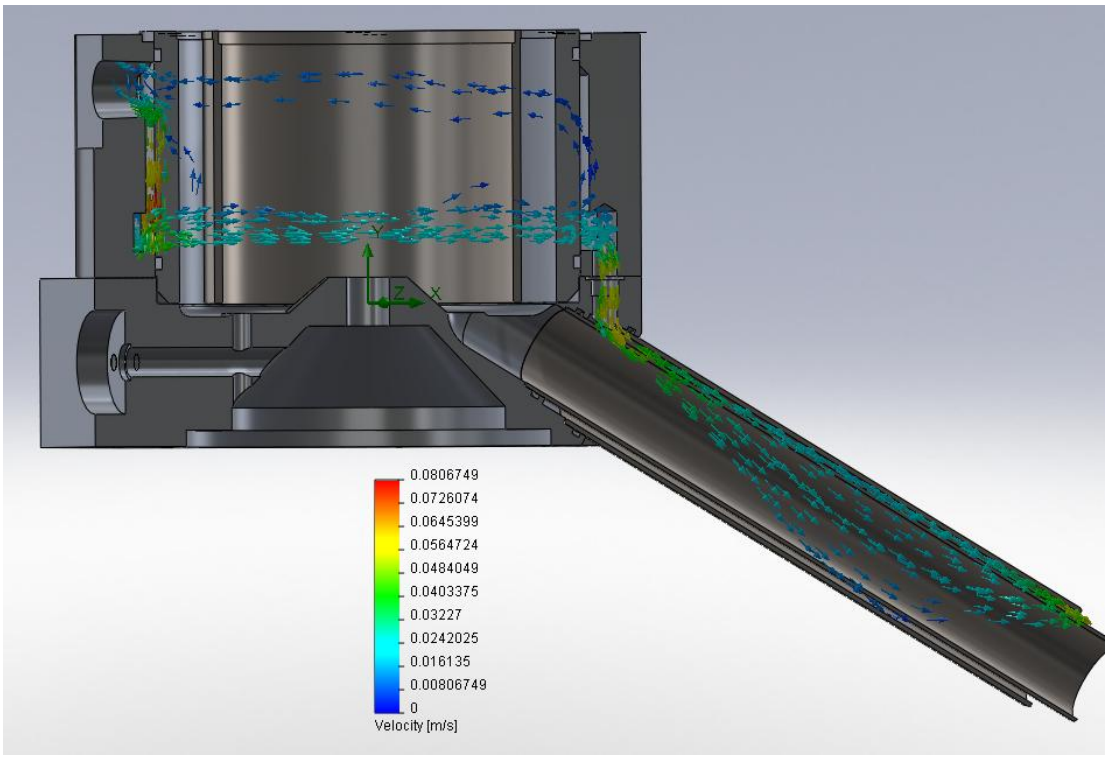

Figure 4.25: Water velocity vectors across the cooler and its connecting tubes

space.

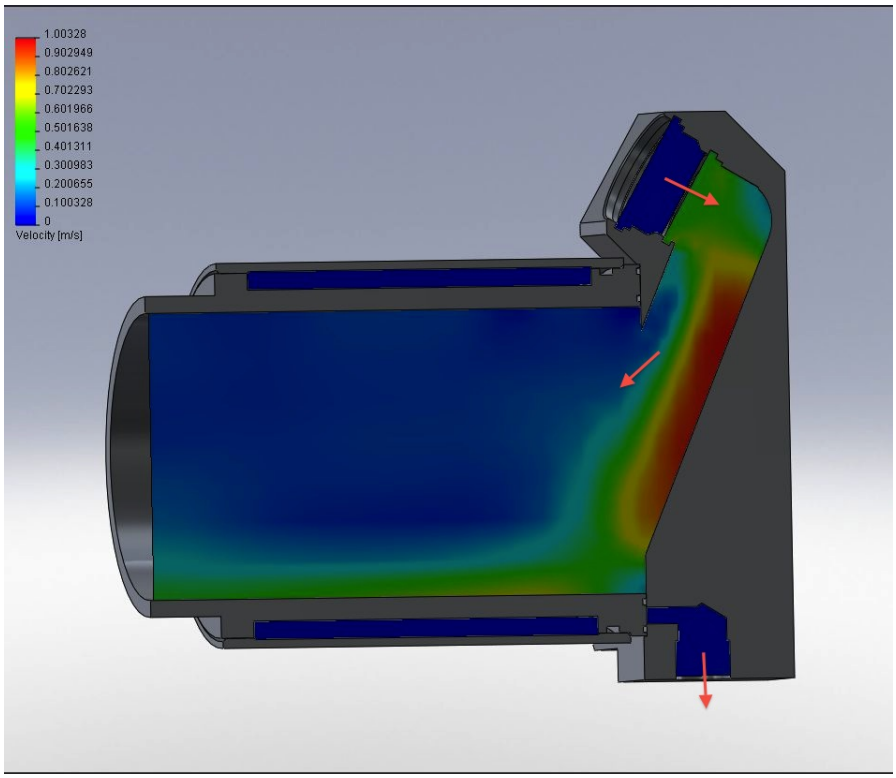

Figure 4.26: Gas velocity distribution in the compression space and its header

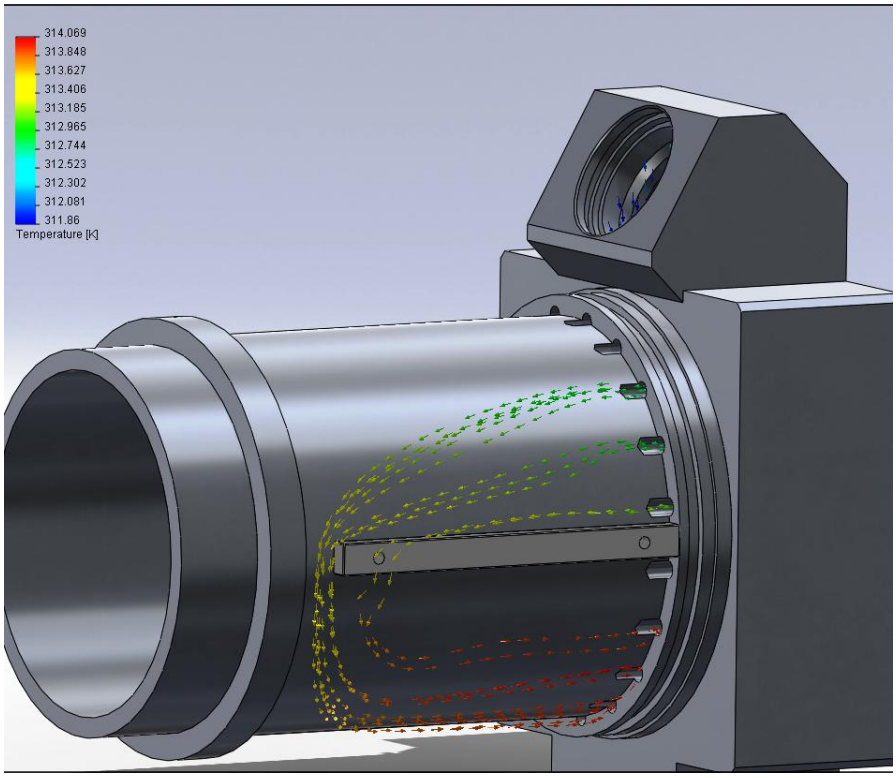

Figure 4.27: Water temperature variations in the cooling jacket of the compression space

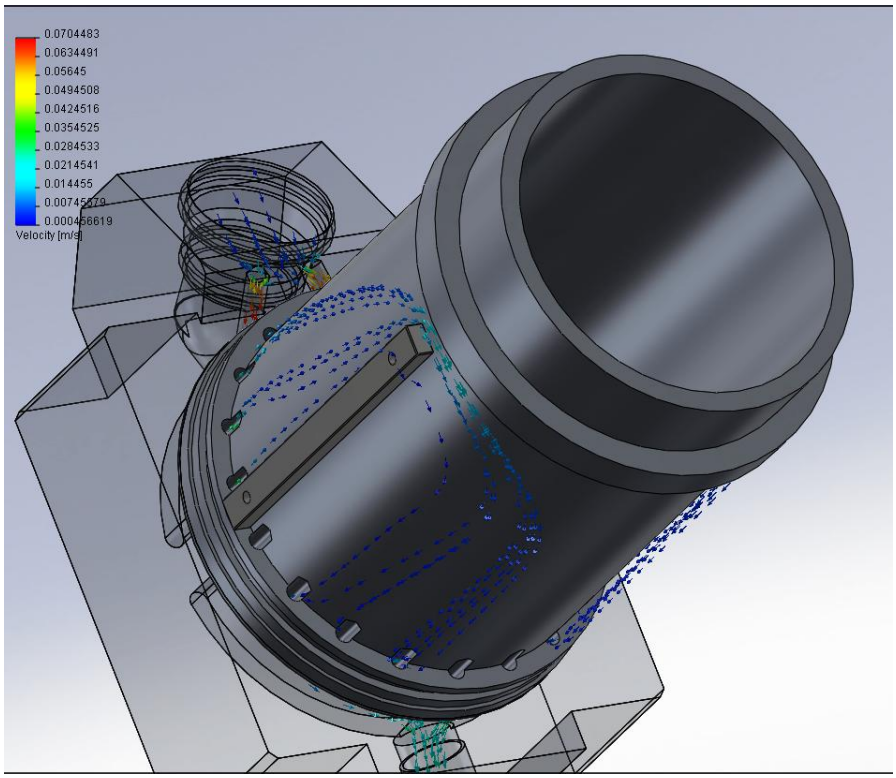

Figure 4.28: Water velocity vectors in the cooling jacket of the compression space (bottom view)

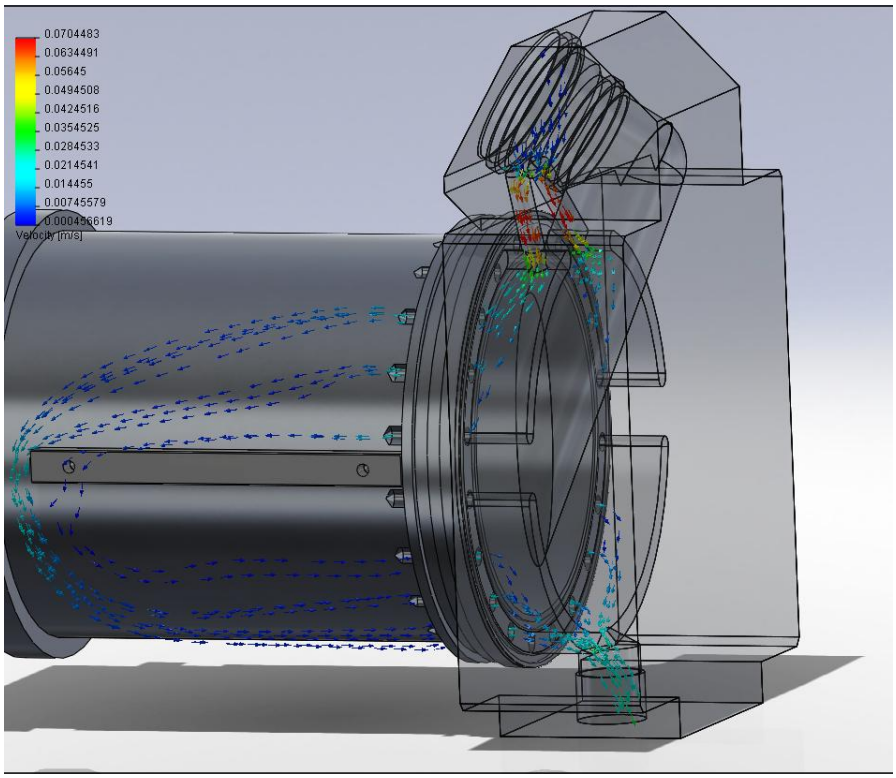

Figure 4.29: Water velocity vectors in the cooling jacket of the compression space (side view)

4.5 Modelling of the Absorption Cooling Process for Biomass Applications

In this project, a thermo-chemical accumulator (TCA) is used to store heat from a biomass boiler and release it in the form of heat (heat sink) or cooling. The TCA unit is based on Lithium Chloride (LiCl) absorption technology developed by ClimateWell. This section will describe an analytical model of the TCA absorption.

4.5.1 Analytical Model of the Thermo Chemical Accumulator Absorption Cooling Process

The TCA system used in this project is comprised of two barrels and a control unit. The control unit regulates the pumps in the system and determines which barrel is being charged and discharged. There are no calculations involved and the whole process is based on decision (`If...else`) statements depending on the information supplied to the control unit from the temperature sensors built into the system. Vacuum conditions are assumed and each of the main sections has its own mass. The heat of vaporisation, condensation and dilution is taken into account. A set value for the heat loss factor for the heat exchangers is used, as provided by the manufacturer. The UA–values for the reactor and the condenser are calculated based on these values. There is a mixing flow between the reactor and the solution store, and between the condenser and the water store. The model uses a fixed number of internal time steps for every output time step in order to iterate to a solution. The condenser and the reactor are treated as though they each consist of two separate vessels. The top vessel is used to exchange energy between vessel and outside, and the bottom vessel is used to store the water or salt solution. Similar to the actual machine, the barrel is charged to a certain limit, before a swapping procedure is initiated. This swap period allows the systems to redirect flow and regulate the speed for the internal pumps. Since the system will always charge one unit while the other one discharges; the heat source and the distribution system are only ever connected to one internal circuit whereas the heat sink is always connected to two circuits. To account for this, the flow rate

for the heat sink is assumed to split evenly between the two units. The internal pumps are regulated according to the status of the unit. The water mixing flow for the charging unit is set to 0 kg/h and for the discharging unit it is set to 150 kg/h. The solution mixing flow is always set to 327 kg/h. These are set values for all modes of the unit, i.e. charging and discharging. Since the system is made up of two units, the swap duration is required to allow the pumps to re-adjust to new conditions. This means that once a barrel is fully charged, before it can start discharging, the pump for the water mixing needs to be regulated from 150 kg/h to 0 kg/h. The system constantly monitors the level of charge/discharge of the unit. A unit is considered fully charged when the salt concentration in the reactor reaches 95% and cannot be "dried" any further. The unit is considered being fully discharged when the water level in the water store goes below 12 kg. The length of the swap period is limited to either half an hour or if the temperature of the condenser is 1°C below the set cooling temperature (whichever comes first).

In this model, the inlet temperatures to the system are kept constant for all three circuits. Obviously, in reality this is not the case and they fluctuate depending on the use of the circuits. For example, the heat sink return temperature largely depends on the capacity of the circuit to dissipate the heat from the incoming water and its temperature. For example, the heat sink return temperature largely depends on the capacity of the circuit to dissipate the heat from the incoming water and its temperature. The parameters that are used in the model have been obtained from the manufacturer. Some of them, e.g. heat loss factors, are based on empirical results conducted by ClimateWell during the course of the design of the unit and at times represent average values, yet are assumed satisfactory for the model used here. These parameter values are regrouped in Table 4.14. Table 4.15 shows the input data for the model. The time length of the simulation is set to 24 hours. This timeframe is used to assure at least one complete charge and discharge cycle of the barrel is carried out with at least one instance of swapping. The model iterates for a set number of times between each time increment. The following steps, as shown in Fig. 4.30,are consecutive steps carried out in each iteration of the model, and the decisions the model takes at the end of each run. At the beginning of each simulation, the model loads the design parameters and reads the user input. Then equations (3.92–3.96) are run

Table 4.14: Input parameter/specifications used for the analytical model of the TCA unit

Symbol	Description	Unit	Value
m_{LiCl}	total mass of LiCL	kg	53.9
m_{H_2O}	total mass of water	kg	117.1
$m_{H_2O,cb}$	initial mass of water in condenser bottom	kg	50
$m_{H_2O,ct}$	initial mass of water in condenser top	kg	1
T_{cx}	initial temperature of condenser	$°C$	20
T_{rx}	initial temperature of reactor	$°C$	20
V_{rt}	capacity of reactor top vessel	m^3	0.016
UA_{ch}	UA value for charging heat exchanger	J/sK^{-1}	4030
UA_{dis}	UA value for discharging heat exchanger	J/sK^{-1}	2870
m_{cb}	mass of empty condenser bottom	kg	3
m_{ct}	mass of empty condenser top	kg	15
m_{rt}	mass of empty reactor top	kg	5
m_{rb}	mass of empty reactor bottom	kg	3
UA_{cb}	heat loss factor for condenser bottom	J/sK^{-1}	2.5
UA_{ct}	heat loss factor for condenser top	J/sK^{-1}	10.56
UA_{rt}	heat loss factor for reactor top	J/sK^{-1}	5
UA_{rb}	heat loss factor for reactor bottom	J/sK^{-1}	2.5
cp_{cx}	specific heat capacity for condenser	J/kgK^{-1}	4190
cp_{rx}	specific heat capacity for reactor	J/kgK^{-1}	2600
cp_{ste}	specific heat capacity for steam	J/kgK^{-1}	1650
H_{sol}	heat of dissolution	kJ/kg	281
ρ_m	density of LiCl mono-hydrate crystals	kg/m^3	1780
ρ_s	density of LiCl solution	kg/m^3	1220

to determine the initial conditions of the system (A1). The system then determines the status of the system (charge/discharge) and adjusts the direction of the different flows accordingly (A2). During the first run, the concentrations of LiCl and solutions are based on the parameters listed above. Subsequently, the model runs a number of iterative steps to reach the first time increment (A3). After each iteration the model checks the time parameter (δt) to determine if one cycle of 5 minutes has been completed (A4). If not, the model returns to the beginning of step (A3). Otherwise the program checks the time parameter (t) to determine if the simulation is finished (A5). If not, the model returns to the beginning

Table 4.15: Input data used for the analytical model of the TCA unit

Symbol	Description	Unit	Value
m_{hs}	mass flow of heat sink loop fluid	kg/s	25
T_{hs}	heat sink return temperature	$°C$	31
m_s	mass flow of heat source loop fluid	kg/s	17
T_{rxi}	heat source inlet temperature	$°C$	115
m_{ac}	mass flow cooling loop fluid	kg/s	23
T_{ac}	cooling fluid return temperature	$°C$	18
T_{amb}	ambient temperature	$°C$	20
T_{cxoset}	cooling output set temperature	$°C$	5
T_{rxoset}	heating output set temperature	$°C$	20

of step (A2). At the end of each time increment, the values are updated and the model verifies the charge/discharge status of the unit and if necessary if the swap period is over. At the end of a swap, the model determines the charge or discharge status based on the previous status of the unit. Otherwise, the system determines the energies and the coefficients of performance.

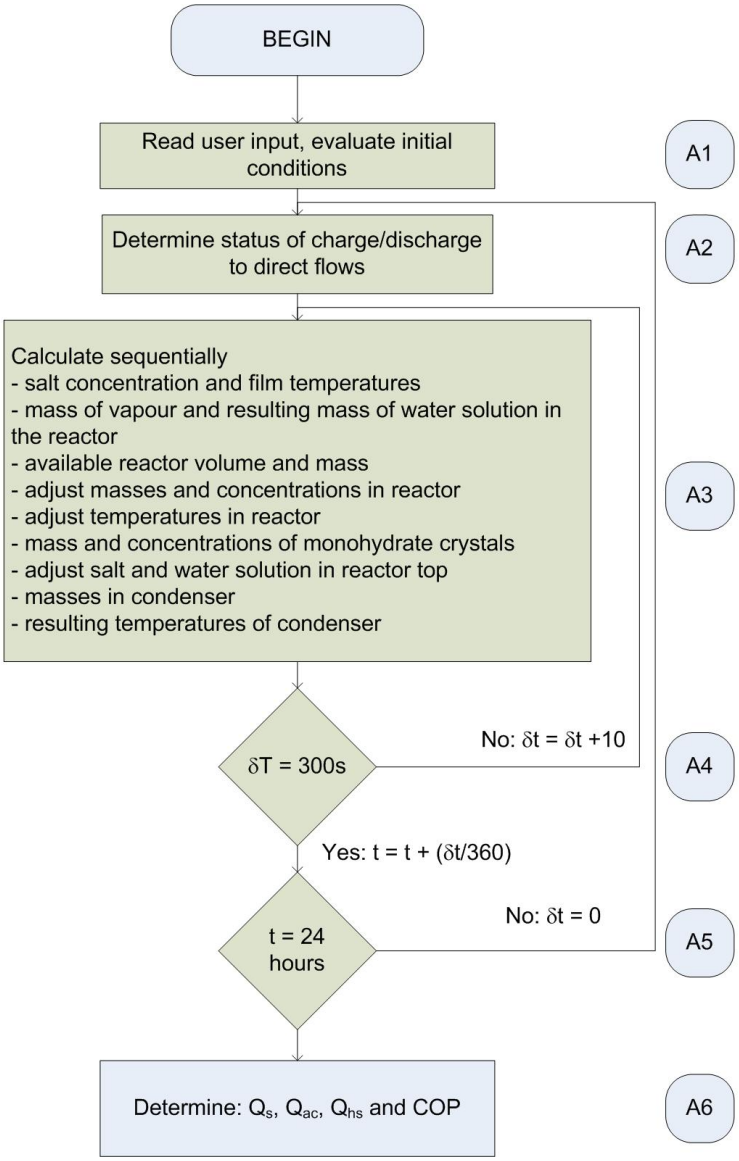

Figure 4.30: Flow diagram for the TCA model

4.5.2 Verification of the Analytical TCA Model

The inlet temperatures to the unit from the heat source ($115°C$), distribution circuit ($18°C$) and heat sink ($31°C$) are set to fixed values for the model. Figure 4.31 shows the variation of the average salt concentration in the unit over a period of 24 hours. The status of the machine starts with a charging procedure and then enters a swap period after 5 hours of running time (as indicated by 'swap' on the figure). During the charge, the salt concentration increases as the heat provided to the machine is used to dry the salt. During the discharge phase, the salt is wetted again and the concentration drops. Figure 4.32 shows the outlet temperatures

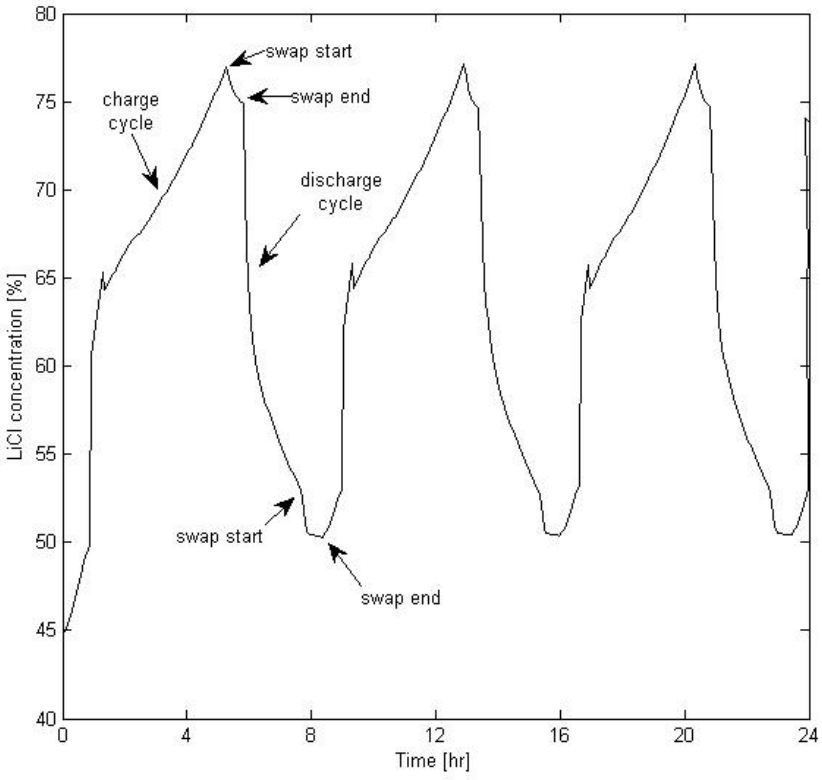

Figure 4.31: Salt concentration of the TCA unit with indicated 'swap' periods

for the condenser and reactor. The drop in temperature in the discharge phase is corresponding with providing cooling. However, the temperatures will differ

in the real system as inlet temperatures are not constant but vary according to their load. Table 4.16 shows the COPs for this unit determined by the model, as

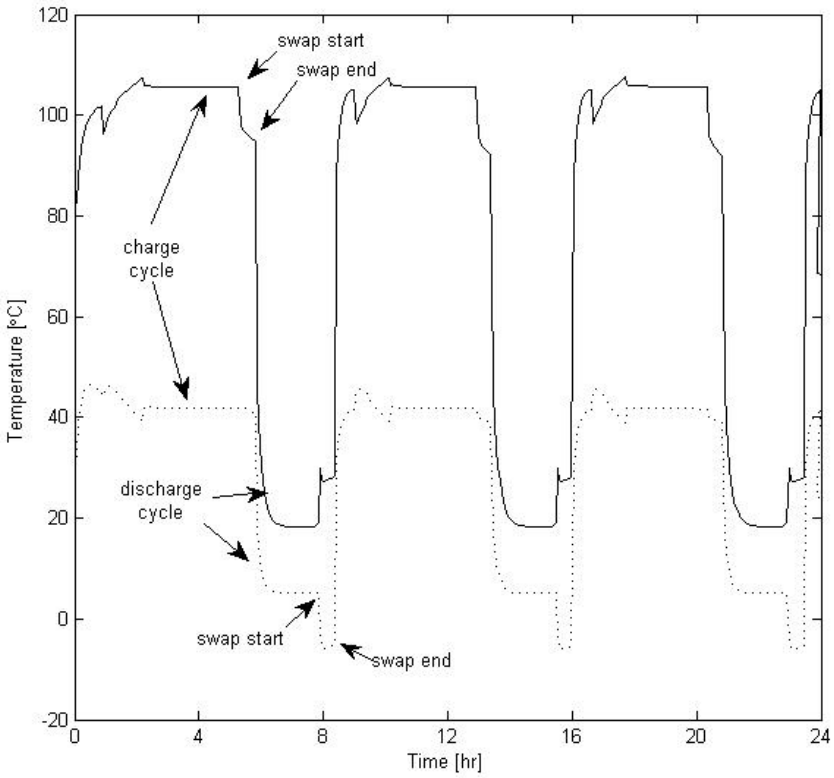

Figure 4.32: Outlet temperatures for condenser and reactor

well as the COPs determined by ClimateWell design calculations. Although, the cooling COP is stated as 0.68, installed systems all show a COP varying between 0.52 and 0.57. The present study estimates a COP closer to the realistic system as the design calculations by ClimateWell.

Table 4.16: Comparison of COP results

Parameter	ClimateWell	Present Study	Relative Error
COP_{cool}	0.68	0.61	10.29%
COP_{heat}	0.79	0.69	14.78%
COP_{pump}	1.41	1.42	-0.71%

4.6 Modelling of the Combined Generation Systems

The following model is developed to determine the performance of the proposed combined and tri-generation systems. Additionally, a comparison is added to compare the combined systems to the tri-generation system as well as a comparison between the tri-generation and the separate single generation of power, heating and cooling. Table 4.17 shows the input data for the performance evaluation model. It is assumed that depending on material and installation methods,

Table 4.17: Input data for the performance evaluation model

Symbol	Unit	Description	Value
$\dot{m}_{fuel}$	g/s	mass flow rate of fuel	3.33
LHV	MJ/kg	lower heating value	14.00
η_{cc}	n/a	combustion efficiency	0.80
P_{el}	kW	electrical output	0.50
$\dot{m}_{water}$	kg/s	water flow rate	0.10
Q_{hs}	kW	heat output from heat sink	22.7
Q_{ac}	kW	cooling output	9.70
η_{el}	n/a	conventional power efficiency	0.33
COP	n/a	COP for electrical AC unit	0.33
Q_{dhw}	kW	domestic hot water demand	3.5

the efficiencies for underground heating is set to 80%, for central heating to 93% and for air cooling unit to 85%. For the underground heating this means that only 80% of the heat available in the heat sink circuit will actually be used for heating purposes. Additionally, it is assumed that 3.5 kW will be consumed to generate domestic hot water. (Equivalent to 15 m^3 p.a. per person in a four-person house heated from 15°C to 45°C. Below are the equations to determine the performances of combined power and heating (CHP), combined cooling and heating (CCH) and tri-generation (tri):

$$\varepsilon_{CHP} = \frac{P_{el} + Q_h}{Q_{pr}} = \frac{0.5 + (0.8 \times 22.7)}{2.33 \times 10^{-3} \times 15.96 \times 1000 \times 0.} = 56.6\% \tag{4.85}$$

$$\varepsilon_{CCH} = \frac{Q_{ac} + Q_{hs}}{Q_{pr}} = \frac{(0.85 \times 9.7) + (0.8 \times 22.7)}{2.33 \times 10^{-3} \times 15.96 \times 1000 \times 0.9} = 79.9\% \tag{4.86}$$

$$\begin{aligned} \varepsilon_{tri} &= \frac{P_{el} + Q_{ac} + Q_{hs}}{Q_{pr}} \\ &= \frac{0.5 + (0.85 \times 9.7) + (0.8 \times 26.2)}{2.33 \times 10^{-3} \times 15.96 \times 1000 \times 0.9} \\ \varepsilon_{tri} &= 89.9\% \end{aligned} \tag{4.87}$$

The equivalent savings in total primary energy supply can then be evaluated with the following respective equations:
combined power and heat with power only:

$$\Delta Q_{el} = \frac{56.5 - 33}{33} = 71\% \tag{4.88}$$

tri-generation with combined power and heat:

$$\Delta Q_{CHP} = \frac{89.9 - 56.5}{56.5} = 59.1\% \tag{4.89}$$

tri-generation with power and cooling:

$$\Delta Q_{CCH} = \frac{89.9 - 79.9}{89.9} = 12.5\% \tag{4.90}$$

Comparing the performance of the proposed tri-generation system with the conventional separate generation system of power, heat and cooling, is included in the model. The overall performance of the combination of all separate generation systems can be determined as follows:

$$\begin{aligned} \varepsilon_{tot,sg} &= \frac{P_{el} + Q_{ac} + Q_h}{Q_{tot,sg}} \\ &= \frac{0.5 + (0.85 \times 9.7) + (0.8 \times 26.2)}{\frac{0.5}{0.33} + \frac{9.7}{0.33 \times 0.33} + \frac{26.2}{0.9}} \\ \varepsilon_{tot,sg} &= 25.6\% \end{aligned} \tag{4.91}$$

The equivalent saving of primary energy demand can then be evaluated as follows:

$$\Delta Q_{tot,sg} = \frac{Q_{tot,sg} - Q_{pr}}{Q_{tot,sg}} = \frac{115.8 - 33.04}{115.8} = 71.5\% \tag{4.92}$$

Table 4.18 shows a comparison with the results determined by the model and the hand calculations. Slight differences are due to rounding of numbers.

Table 4.18: Comparison between computed and calculated values

Symbol	Description	model	calculated
ε_{CHP}	combined power and heating	56.6%	56.5%
ε_{CCHP}	combined cooling and heating	79.9%	79.9%
ε_{tri}	tri-generation	89.8%	89.9%
ΔQ_{el}	power vs CHP	71.1%	71.0%
ΔQ_{CHP}	CHP vs tri-generation	59.0%	59.1%
ΔQ_{CCH}	CCH vs tri-generation	12.5%	12.5%
$\varepsilon_{tot,sg}$	separate systems performance	25.6%	25.6%
$\Delta Q_{tot,sg}$	comparative saving sg vs tri	71.4%	71.5%

4.7 Conclusion

This chapter provided the development of the mathematical and CFD models for the biomass boiler, main type of heat exchanger, the Stirling engine as well as the thermo–chemical accumulator.

The analytical model to estimate the combustion temperatures and various combustion products from solid biofuels was verified and can thus be used in the next chapter with confidence on the obtained results. The results then will be compared to empirical data. The computational fluid dynamics investigation of the biomass boiler shows the flow pattern for air and water inside the unit. The installation of additional fins on the gas side of the heat exchanger could give a potential increase of heat transfer in the boiler.

The analytical model for shell and tube heat exchanger determines the heat transfer coefficients and surface areas. The equations for the correction factor for this type of heat exchanger are in accordance with published graphs. Hence, the

equations can be used in the model and do not require additional user input. The computational fluid dynamics analysis of the heat exchanger visualises the flow pattern inside the shell of the heat exchanger. The outlet temperatures determined by the analysis are within the load requirements for the heat exchanger.

The analytical model of the Stirling engine determines in a first step the total mass of gas in the engine. In a second step, a third order method determines a realistic preview of the engine output and efficiency. This model is verified by detailed calculations for the engine with air as the working gas at 10 *bar* pressure charge. The computational fluid dynamics model visualises the flow of the gas and the cooling water across different parts for the engine. The heat transfer and temperature distribution show the expected duty of the engine.

The working model of the TCA absorption cooling unit demonstrated an agreement for the coefficient of performance with reported values by the manufacturers. This model will be used in the next chapter to simulate various situations depending on inlet temperatures.

The flow velocity results obtained in Solidworks Flowsimulation are verified with a simple investigation of flow distribution across staggered tubes in a windtunnel. The result for the velocity at the outlet is in accordance with the correlated value obtained from the empirical data. The results due to heat transfer obtained by Solidworks are satisfactory compared to Ansys as well as empirical data and calculated data for the temperature distribution across a plate fin.

Chapter 5

Experimental Setup and Plan

5.1 Introduction

This chapter describes the tests carried out during the course of this study. The tests include performance analysis of the biomass boiler as a stand alone water boiler and as a heat source for the absorption unit. The absorption unit will be tested as a cooling output only and in combined cooling and heating mode by utilising the heat dumped in the heat sink of the system. All these tests include emission measurements for various operating conditions. The main parameter changed in the tests will be the Reynolds number of the heat source flow circuit (the heating output of the biomass boiler). The Stirling engine will be run as a cooling generator to determine its working conditions and determine any possible leaks and problems. The engine will be run at different speeds and pressures to highlight changes in operating conditions. The properties of a variety of solid biomass fuels will be investigated and these results will be included in the discussion of the emissions and efficiency results. All the equipment used for the measurements will be explained along with the calibration procedures used. Additionally an uncertainty analysis on all measurements will be conducted to present errors in measurements for the results presented in the next chapter.

5.2 Experimental Setup

In this study, the combustion of biomass is used to generate the required heat to provide heat to a hot water heat exchanger and the cooling unit. The test rig consists of a biomass boiler, an absorption cooling unit, two heat exchangers and a cooling water reservoir as shown in Fig. 5.1. Additionally, the schematic of the Stirling engine test bay is shown. Besides the basic equipment for setting up the proposed (CCH) system, in order to evaluate their respective performances, the power output from the engine; the emissions from the biomass combustion exhaust gas; the heat output from the heat sink in heat exchanger 1 ($HE1$), the cooling effect from heat exchanger 2 ($HE2$), and boiler heat output (Q_h), a series of data collection instruments need to be selected and installed. These instruments include a data logger and a PC computer for logging data; an orifice plate to measure the air flow rate into the combustor; a fuel flow rate system to measure fuel consumption; electrical meters to measure the power input to the engine (generator); a pitot tube to measure the exhaust gas flow rate; thermocouples to measure air temperature, exhaust gas temperature and water temperatures at various key locations of the system; emission analysers to measure the contents in the exhaust gas; and water flow meters. The following sub-sections will describe the apparatuses and instruments used in the test rig. The completed test rig is shown in Fig. 5.2.

5.2.1 Carborobot Farmer F40

The automatic biomass heating boiler of Carborobot, Fig.5.3, is a modern heating system manufactured in Hungary. The farmer model is typically used in rural areas and is suitable for burning pellets, corn, wheat as well as entire logs. The boiler can be used for the heating of large family residences with a nominal heat output of up to $40kW$. The system has to be adjusted for the various types of fuel, in order to achieve optimum fuel feed rates. This should allow for a good control on the fuel consumption during the testing of the system. The specifications of the Carborobot F40 are presented in Appendix B1. The following parameters are required to evaluate the performance of the biomass unit:

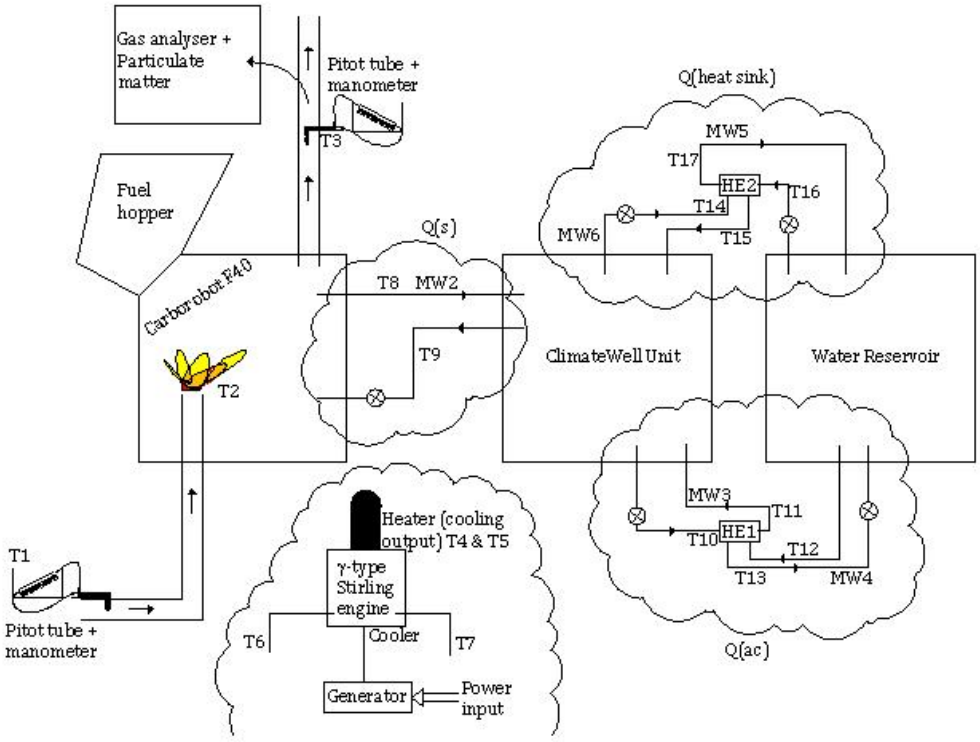

Figure 5.1: Schematic diagram of the experimental test setup

- Energy input
- Heat output
- Thermal efficiency
- Emissions

In order to evaluate these parameters, the following instruments are used:

- An adjustable orifice plate to measure the air mass flow rate to the combustor

  The temperature at the inlet to the orifice is assumed to be equal to the ambient temperature ($T1$). A manometer is used to measure the pressure drop across the orifice to evaluate the air flow to the combustor.

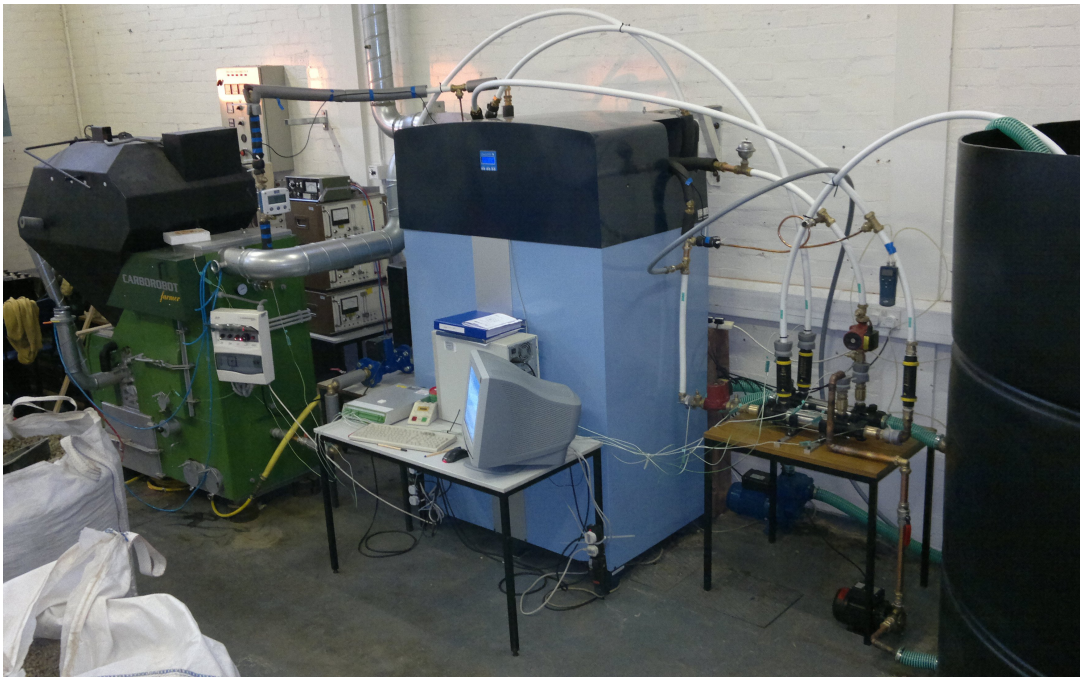

Figure 5.2: Test rig assembly and data acquisition equipment

- Fuel measurement device
  This consists of a timer and a scale to measure the fuel put into the hopper at the beginning of the test and the mass of fuel left in the hopper once the test is stopped.

- Combustor room temperature
  A thermocouple ($T2$) will be placed inside the combustion chamber to measure the temperature. The location is chosen in a way that the thermocouple will measure the actual air temperature and not the radiating temperature from the fire.

- Engine emissions
  Four infra-red exhaust gas analysers and a magneto-dynamic oxygen analyser are used to measure CO_2, CO, HC, NO_x and O_2 contents in the exhaust gas. A Dynoptic single pass optical particulate monitor is used to measure the particulate concentration in the exhaust gas.

Figure 5.3: Carborobot Farmer F40

- Air flow and temperature of the exhaust gas
  The air flow of the exhaust gas is monitored by using a pitotstatic tube connected to a micro-manometer. Thermocouple ($T3$) will measure the exhaust temperature.

- Calorific value of the fuel
  The calorific value of the fuel is determined with a PARR 1341 bomb calorimeter.

- Water flow measurement and temperatures
  The water flow ($MW1$) in the heating circuit of the hot water is measured with a digital water meter. The temperature for the outlet is measured with thermocouple ($T8$) and the return temperature is measured with thermocouple ($T9$).

5.2.2 γ-type Stirling Engine

As mentioned before the γ-type Stirling engine used in this study was originally developed by D. Viebach. The drawings are currently available under the "Creative Common's" licensing scheme and an assembly drawing can be obtained for free from Viebach. For this study, different elements of the original design were changed. The regenerator is made of stainless steel mesh wire wool and the cooler is made from aluminum fins provided by GDM Heat transfer Ltd. All the drawings were drawn and checked in Solidworkds to prevent manufacturing delays. The actual manufacturing was partially done by Staffordshire University, ELTH S.A. (L) and outside contractors supplied by the university. Figure 5.4 shows an assembly of the heater and Fig. 5.5 shows the assembled crankcase with the two working pistons (for the displacer only the mounting plate is shown). Figure

Figure 5.4: Heater assembly

5.6 shows the compression cylinder lining without the cooling jacket. The divider

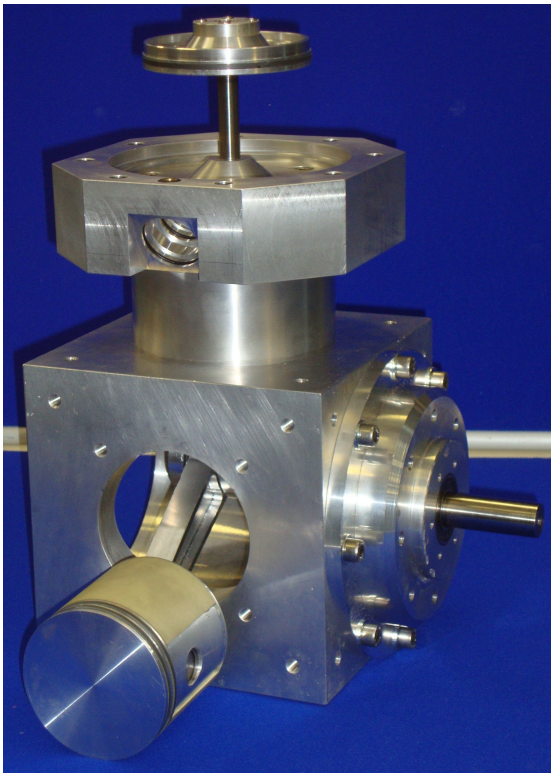

Figure 5.5: Crankcase assembly

bars (white ABS polymer) are used to direct the flow and obtain uniform cooling in the compression space. The majority of parts are made from an aluminum alloy (5083). The heater and the expansion piston are made from stainless steel (316) and the polymers (divider bars and washers) are made from POM. As oil rings are not feasible for Stirling engines, all piston rings and bearings were made from Iglidur W300 form IGUS. Figure 5.7 shows the displacer piston made from stainless steel (304). The engine is connected to a Leroy Somer generator Fig. 5.8 and the specifications of the LSRPM Leroy-Somer generator are listed in Appendix B2. The following parameters are required to evaluate the performance of the engine:

- Temperatures
- Power input

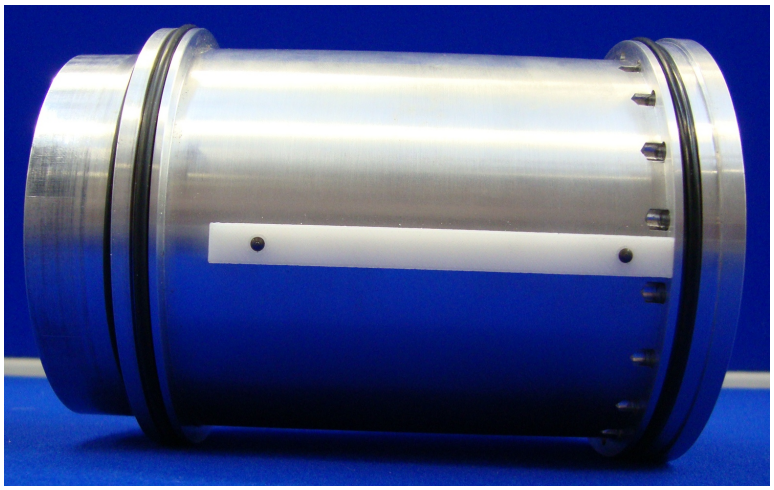

Figure 5.6: Compression cylinder lining

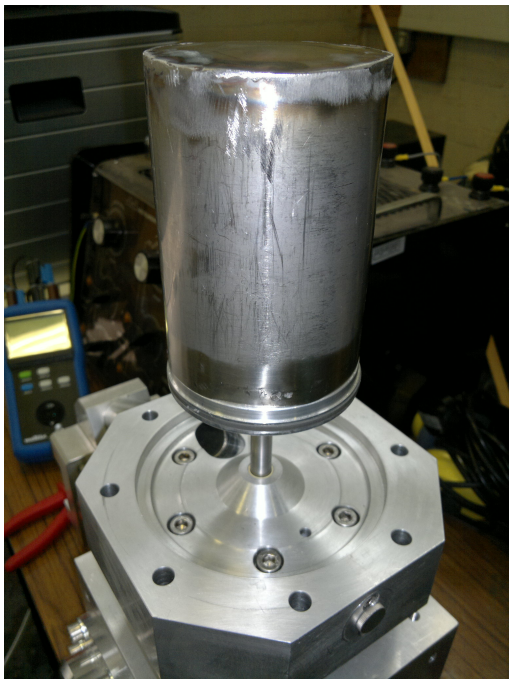

Figure 5.7: Displacer piston mounted on the displacer base

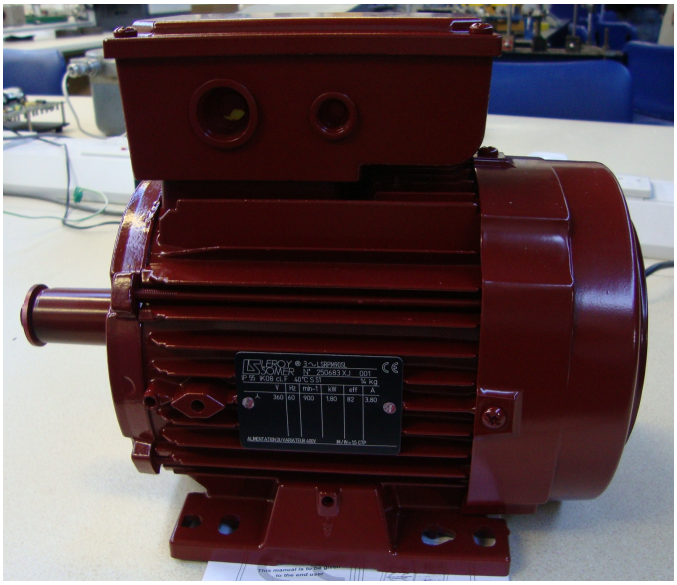

Figure 5.8: Leroy-Somer LSRPM90SC generator

In order to evaluate these parameters, the following instruments are used:

- Thermocouples
  The temperature at the heater is measured with thermocouples ($T4$) and ($T5$), the cooling inlet is measured with thermocouple ($T6$) and the outlet with ($T7$).

- Power meter
  The power input to the generator is directly measured by a FLUKE1735 Power meter connected between the Unidrive and the generator.

5.2.3 Shell and Tube Heat Exchanger

The shell and tube heat exchangers are manufactured by Elecro in the United Kingdom. They have a nominal capacity of 25 kW and are standard equipment for swimming pool heating. The hot fluid circuit is connected to the shell side and the cold fluid circuit is connected to the tube side of the heat exchanger. Figure 5.9 shows the two heat exchangers (with pumps) connected to their respective circuits. The specifications of the Elecro Heat Exchanger are listed in Appendix

B3. There are two heat exchangers of this type installed in the system,namely

Figure 5.9: Elecro heat exchangers installed with their respective connections and pumps

($HE1$) and ($HE2$); one to transfer the heat from the reservoir to the cooling circuit (Q_{ac}) and one to transfer the heat from the heat sink circuit (Q_{hs}) to the reservoir. The following instruments are used to measure the parameters that were necessary to determine the performance of the two heat exchangers.

- Thermocouples
  For ($HE1$), the temperatures on the tube side are measured with thermocouple ($T10$) for the inlet and ($T11$) for the outlet. On the shell side, ($T12$) is used for the inlet and ($T13$) for the outlet. For ($HE2$), the temperatures on the shell side are measured with thermocouple ($T14$) for the inlet and ($T15$) for the outlet. On the tube side, ($T16$) is used for the inlet and ($T17$) for the outlet.

- Water flow measurement
  The water flow across the heat exchangers is measured with a spring activated water meter for ($MW3$) and ($MW4$) for the tube and shell side in

heat exchanger ($HE1$) as well as the tube side ($MW5$) in heat exchanger ($HE2$). The water flow ($MW6$) on the shell side in heat exchanger ($HE2$) is correlated with the pressure drop across an orifice plate manufactured according to British Standards.

5.2.4 ClimateWell TCA Absorption Unit

The ClimateWell thermo chemical accumulator stores the supplied energy inside and then releases it in form of heating or cooling when required. For the purpose of this evaluation, the heat and cooling generated by the system will be constantly swapped with a large reservoir tank. Figure 5.10 shows a view of a unit that is used for the testing. The nominal cooling output is rated at 10 kW depending on the inlet temperatures for the heat source and heat sink. In order to run the

Figure 5.10: ClimateWell TCA unit

unit, three different circuits need to be connected to it. These are labelled as:

- (Q_s), for the heat source and providing the hot water from the biomass unit
- (Q_{hs}), for the heat sink and providing cooling water to dump the excess heat
- (Q_{ac}), for the cooling and providing a heat source to be cooled in cooling mode

In order to determine the performance of the unit, the biomass boiler, the heat exchangers ($HE1$) and ($HE2$) as well as the reservoir need to be connected and monitored as discussed above. Additionally, the software supplied for the unit will be used to collect all the temperatures, flow rates and pump settings within the unit. It is assumed that the software and the monitoring devices inside the unit are in working conditions as they can be neither calibrated nor replaced. The specifications of the ClimateWell absorption cooling unit are listed in Appendix B4.

5.3 Data Acquisition and Instrumentation

The data acquisition and instrumentation for the test rig are shown in Fig. 5.1; it consists of the following components:

- A data logger for the recording of the thermocouples;
- Thermocouples to measure air temperature and exhaust gas temperature at different points;
- Air pressure measured by a mercury barometer;
- Air flow rate measured by an orifice plate;
- Fuel consumption;
  The fuel flow in this study is measured by adding a known quantity of fuel into the empty hopper. At the end of each test, the remaining quantity of fuel is measured and subtracted from the initial quantity of fuel added to the hopper. This amount is the fuel consumed over the length of the test.

In order to determine the fuel flow in kg/s, it is sufficient to divide the fuel quantity measured (kg) by the length of the test (s).

- Exhaust gas flow rate measured by a pitotstatic tube;
- Water flows measured by different types of flow meters;
- Electrical power measured by an electrical multi-meter;
- Engine emissions measured by the infra-red gas analysers, the magneto-dynamic oxygen analyser and the single pass opacity meter.

All necessary calibration and set up procedures are explained later in this chapter (section 5.5. Calibration)

5.3.1 Data Acquisition System and Software

A H.E.A.T Technology Division Data Logger, Fig. 5.11, is used in the experiments to log the data provided by the thermocouples. It is a microprocessor controlled computer interface that has multi-channel analogue and digital input and output capabilities. As the interface has its own microprocessor and independent memory, it is possible to set up the system to return data from most standard transducers in the form required by the data logging software. The interface may be simply configured either as a data logger or a combined data logger and controller, and is operated on a computer serial link responding to simple (ASCII) alphanumeric commands and returning numeric data. Commands and data are transferred via a 5–wire RS232 ribbon serial link using ASCII Character string sent and received by a controlling IBM compatible computer running the HEAT Technology Data Logging software. Once all of the required channels have been set up to return data in the format required by the software, then the whole system configuration maybe stored to disc. 15 Differential DC FSD (20 mV (High gain) or 80 mV) are available. These may be configured as thermocouple input channels and on board cold junction compensation is standard for both type T and type K thermocouples. The data from the ClimateWell is read by the provided software (CWIC). It allows reading all the temperatures, energies, and flow rates in the two barrels.

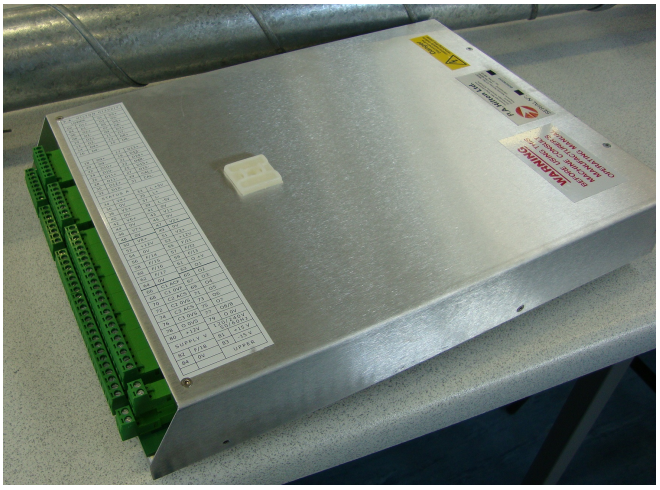

Figure 5.11: H.E.A.T. Technology Division Data Logger

5.3.2 Temperature Measurements

The data acquisition system used, provides connections for temperature measurement using K–type thermocouples. The K–type thermocouple (Copper / Copper - Nickel) is extensively used in low to moderate temperature applications, and provides excellent repeatability within the intended temperature range considered. British standard for output of K–type thermocouples, BS EN 60584-1 Part 4:1996 states a continuous working temperature range of $0°C$ to $1100°C$, and a short interval working range of $-180°C$ to $1350°C$. In accordance with BS EN 60584-2:1993, the K–type thermocouple offers a high output tolerance value of $1.5°C$ (Class 1) between the temperature range of $-40°C$ to $+375°C$; and $0.004(t)$ between the range of $375°C$ to $1000°C$. The thermocouples used in the tests are made by TC Ltd., Uxbridge (United Kingdom).

5.3.3 Air Pressure Measurement

A mercury barometer, Fig. 5.12, made by Short & Mason Company, London, is used for the reading of ambient air pressure. The specification of the mercury barometer, with calibration traceable to British Standard BS 2520:1983.

Figure 5.12: Barometer used in the present study

5.3.4 Air Flow Measurement

The air supply is measured by an adjustable orifice plate as shown in Fig. 5.13. The diameter of the inlet (d_1) is 80 mm and the restriction diameter of the orifice plate (d_2) is set to 60 mm. The air entering the engine passes first through the orifice plate, the pressure drop across the orifice plate being a measure of the air flow rate. This is the common method of measuring the air flow rate into the combustor. If this pressure drop is small, as it has to be if the orifice is not to throttle the air flow into the combustor, the incompressible form of the energy (Bernoulli) equation may be used (Douglas *et al.*, 2005). This means that the velocity of the air through the orifice plate is related to the pressure drop across the orifice plate by the following expression:

$$\bar{V} = Cd \sqrt{\frac{1}{1-\beta^4}} \sqrt{\frac{2\,\Delta P}{\rho}} \tag{5.1}$$

where: $\beta = \frac{d_2}{d_1}$, and C_d is the coefficient of discharge for the orifice plate.
The orifice plate was made according to the British Standard (BS EN ISO 5167-1:1997), the coefficient of discharge is: $C_d = 0.6$. An inclined manometer is used to measure the effect of pressure drop ΔP. Equation (5.2) can then be substituted into equation (5.1)

$$\Delta P = \rho\, g\, h \tag{5.2}$$

where h denotes the height read of the manometer.
Applying the conservation of mass principle:

$$\dot{m} = Cd\, \rho\, \bar{V}\, A \tag{5.3}$$

Figure 5.13: Orifice plate mounted at the air inlet to the combustor

Hence:

$$\dot{m} = Cd\, A \sqrt{\frac{1}{1-\beta^4}}\, \sqrt{2\, \rho_{air}\, \rho_{water}\, g\, h} \tag{5.4}$$

5.3.5 Exhaust Gas Flow Measurement

A pitotstatic tube connected to a manometer will be used to determine the flow rate of the exhaust gas. The tube will be inserted next to thermocouple ($T3$), in order to compensate the density fluctuations caused by the change of temperature. The specifications of the manometer used are listed in Appendix B6. The pitotstatic tube (named after Henri Pitot) measures a fluid velocity by converting the kinetic energy of the flow into potential energy. The conversion takes place at the stagnation point, located at the tube entrance facing the fluid flow. A pressure, higher than the free stream pressure (i.e. dynamic), results from the kinetic to potential conversion. This static pressure is measured by comparing it to the flow's dynamic pressure with a differential manometer. Evaluated at two different points along a streamline, the Bernoulli equation yields:

$$\frac{P_1}{\rho\, g} + \frac{\bar{V}_1^2}{2\, g} + z_1 = \frac{P_2}{\rho\, g} + \frac{\bar{V}_2^2}{2\, g} + z_2 \tag{5.5}$$

Now, assuming that $z_1 = z_2$ and that point 2 is a stagnation point (i.e. $\bar{V}_2 = 0$), then:

$$\bar{V}_1 = \sqrt{\frac{2\,\Delta P}{\rho}} \tag{5.6}$$

Thus the mass flow rate of exhaust gas can be determined as:

$$\dot{m} = A\,\sqrt{2\,\rho_{air}\,\rho_{water}\,g\,h} \tag{5.7}$$

5.3.6 Water Flow Measurements

In the system there are five water flow rates to measure. Three different methods of water flow measurements are used in the system. This is due to different natures of flow regime and the various pipe diameters. The following methods are used:

- Digital flow meter (Fig. 5.14) to measure flow ($MW1$)
- Spring activated flow meter (Fig. 5.15) to measure flows ($MW3$), ($MW4$) and ($MW5$)
- Pressure drop across an orifice plate to measure ($MW6$)

The first two devices can be read directly over a period of time to get the flow rate. For the orifice plate, the pressure drop is converted similar to the method used for the air flow measurement. The conical type orifice plate used here, is manufactured according to British standard BS EN ISO 5167-2:2003.

5.3.7 Emission Measurements

The analysis of exhaust emission is an important part of this project. For this purpose, a Magneto-dynamic oxygen analyser, Infra-red gas analysers and a Dynoptic opacity meter to measure particulate matter were used to detect O_2 (Fig.5.16), CO, CO_2, Hexane, NO_x (Fig. 5.17) and particulate matter (Fig. 5.18). The specifications of the analysers are shown in Appendix B7, B8 and B9, respectively.

Figure 5.14: Digital flow meter to measure flow rate ($MW1$)

Figure 5.15: Spring based flow meter to measure flow rates ($MW3$), ($MW4$) and ($MW5$)

Figure 5.16: Magneto-dynamic oxygen analyser

Figure 5.17: Infra-red NO_x gas analyser

Figure 5.18: Dynoptic opacity particulate monitor

5.3.8 Solid Biofuels Properties

Different fuels will be used for the different tests. A bomb calorimeter PARR 1341, Fig. 5.19, will be used to determine the energy content of the fuel (EN14918). Additional tests will be carried out to determine the volatile matter (EN15148), moisture content (EN14774), bulk density (EN15103) and ash content (EN14775) according to the current European standards. The fixed carbon content is dependent on the content of ash, moisture and volatile matter. The properties of the fuels are determined by analysing the moisture content for the different fuels. All tests are carried out at least three times in accordance with the respective standards. In each test a sample of 1 g of fuel is crushed, weighed in a crucible and heated in an oven. The following heating procedures are carried out:

- Moisture content (MC)
  - Heat evenly at 105°C for two hours
  - Weigh sample and heat for another hour until weight stays constant
  - Weigh sample with crucible
- Ash content (ash)
  - Heat evenly to 250°C for two hours

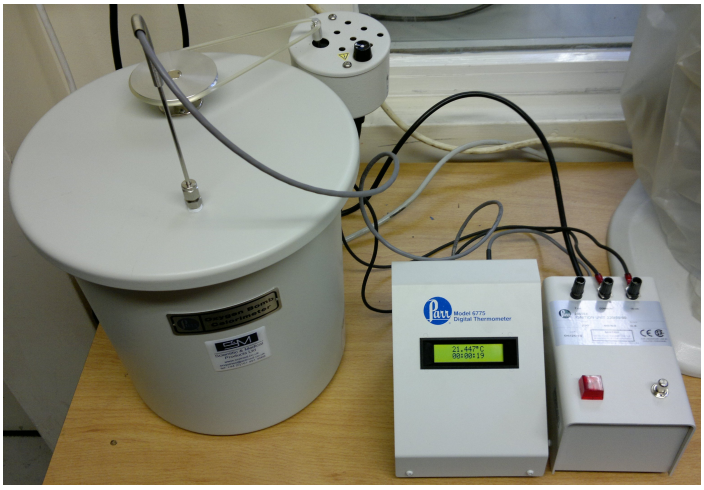

Figure 5.19: PARR bomb calorimeter

  - Increase temperature to 550°C and heat for another 2–3 hours
  - Weigh sample with crucible

- Volatile matter (VM)
  - Put sample with crucible in oven preheated to 900°C for seven minutes
  - Weigh sample with crucible

The fixed carbon (FC) content is calculated based on the above results. In order to determine the different values, the following calculations are carried out based on the measured values of weight:

$$MC = \frac{m_1 - m_2}{m_1 - m} \tag{5.8}$$

$$ash = \frac{m_2 - m}{m_1 - m} \times \frac{100}{100 - MC} \tag{5.9}$$

$$VM = \left(\frac{m_1 - m_2}{m_1 - m} - MC\right) \times \frac{100}{100 - MC} \tag{5.10}$$

$$FC = 1 - MC - ash - VM \tag{5.11}$$

where subscript 1 refers to the sample before the heating procedure, subscript 2 refers to the sample after the heating procedure and m is the weight of the empty

crucible

5.4 Test Plan and Procedure

A test plan is designed to study the performance of single generation of domestic hot water (DHW) and combined cooling and heating (CCH):

- Theoretical analysis and computational simulations; these include the performance evaluations of the combustion unit, the Stirling engine and the absorption cooling unit. Additionally a comparison between conventional single power generation and /combined generation is performed.
- Experimental investigation, including performance evaluations and emissions under various test conditions.

The experimental plan is to investigate the performance of the system in parts and as a whole. These experiments include: (1) the performance tests of biomass combustion for heat purposes; (2) the performance tests of the Stirling engine; (3) the performance tests of the absorption cooling unit; and (4) the performance tests of the total system. A computing model has been developed (Chapter 4) for the total system. The model is divided into 5 sub-models: the biomass combustion model is used to determine the combustion performance and combustion products; the heat exchanger model is used to calculate the performance of the heat exchanger; the Stirling model is used to calculate the performance of the γ-type Stirling engine; the absorption cooling model is used to calculate the performance of the ClimateWell unit; and the model of the CHP/tri-generation is used to calculate the overall performance of the system and compare it to conventional single generation. In conjunction with these models and simulations, a series of experiments are designed to test the performance of the combustor, the Stirling engine, the absorption unit and the biomass combustion.

5.4.1 Experimental Plan for Boiler Performance

A series of tests are designed to evaluate the performance of the biomass combustion unit, which are shown in Table 5.1. In these tests, the performance of the

boiler is evaluated for different Reynolds numbers; and the required parameters shown in Table 5.2, were recorded in order to evaluate:

- Fuel consumption
- Heat dissipation to the water
- Heat dissipation to exhaust gas
- Emissions from the combustion of solid biomass

These tests are done on different days and in different ambient conditions as the weather changed. Three test series are carried out to obtain consistency between the test results and account for fluke results.

Table 5.1: Carborobot Farmer F40 test series

	Reynolds number			
Test series	**23704**	**29570**	**37540**	**46605**
Test series 1	BT11	BT21	BT31	BT41
Test series 2	BT12	BT22	BT32	BT42
Test series 3	BT13	BT23	BT33	BT43

5.4.2 Experimental Plan for Stirling Engine Performance

A series of tests are designed to evaluate the working conditions and the performance of the γ-type Stirling engine, which are shown in Table 5.3. The engine is run as cryocooler in these tests, where the nominal charge pressure of the engine is varied between atmospheric and 10 bar in increments of 2.5 bar. The required parameters, shown in Table 5.4, were recorded in order to evaluate:

- Power input
- Temperature output at the 'heater' tubes
- Temperature output at the 'cooler'

Table 5.2: Carborobot test parameters

Symbol	**Description**	**Unit**	**Value**
P_{air}	ambient air pressure	$mmHg$	
Δh_1	air flow inlet	mmH_2O	
Δh_2	air flow exhaust gas	mmH_2O	
$\Delta MW1$	water flow volume	m^3	
$\Delta fuel$	fuel quantity	kg	
Δt	test duration	s	
$T1$	ambient air temp.	$°C$	
$T2$	combustion temp.	$°C$	
$T3$	exhaust gas temp.	$°C$	
$T8$	hot water temp.	$°C$	
$T9$	return water temp.	$°C$	
CO	carbon monoxide	ppm	
CO_2	carbon dioxide	%	
C_6H_14	hexane	ppm	
NO_x	nitric oxide	ppm	
O_2	oxygen	%	
PM	particulate matter	mg/m^3	

Table 5.3: γ-type Stirling engine test series

	Pressure charge				
Test series	0 *bar*	2.5 *bar*	5 *bar*	7.5 *bar*	10 *bar*
Test series 1	ST11	ST21	ST31	ST41	ST51
Test series 2	ST12	ST22	ST32	ST42	ST52
Test series 3	ST13	ST23	ST33	ST43	ST53

Table 5.4: γ-type Stirling engine test parameters

Symbol	Description	Unit	Value
Δt	test duration	s	
$T4$	heater temperature	$°C$	
$T5$	heater temperature	$°C$	
$T6$	cooling inlet	$°C$	
$T7$	cooling outlet	$°C$	
V	Voltage	V	
I	Current	A	

These tests are done on different days and different ambient conditions as the weather changed. Three test series' are carried out to obtain consistency between the test results and account for fluke results. Additional tests will be carried out with the simulation model developed during the course of this project. The simulations will be used to determine the working conditions of the engine when used to drive a generator to output electricity.

5.4.3 Experimental Plan for Absorption Cooling Performance

A series of tests are designed to evaluate the performance of the TCA absorption cooling unit, which are shown in Table 5.5. All the tests will be carried out for a range of heat sink inlet temperatures and a range of different cooling inlet temperatures. The parameters, shown in Table 5.6, were recorded in order to evaluate:

- Primary energy input
- Heat absorbed from the heat source
- Cooling output from the unit
- Emissions

These tests are done on different days and different ambient conditions as the weather changed. Three test series are carried out to obtain consistency between the test results and account for fluke results.

Table 5.5: Absorption performance test series for cooling only

	Reynolds number		
Test series	**12710**	**21185**	**29660**
Test series 1	AT11	AT21	AT31
Test series 2	AT12	AT22	AT32
Test series 3	AT13	AT23	AT33

5.4.4 Experimental Plan for Solid Biofuels Properties

As mentioned above the fuel properties will be carried out according to new European standards regarding 'solid recovered biofuels'. Since the physical appearance of the different fuel types used is not the same, the bulk density is determined for each fuel. This can then be used to determine an energy density for each fuel based on their calorific value. First the bulk density as received will be determined. For all tests, unless otherwise specified, the results are based on the masses of the samples before and after the test series.

Three test series are carried out in order to get three replications. The average value will then be rounded to the nearest 10 kg/m^3. The bulk density on a dry basis is dependent on the moisture content. The moisture content is carried out by drying a sample of 1 g of fuel in an oven at constant temperature according to EN14774-3. Three tests are carried out and the average mean of duplication is reported to the nearest 0.1%.

The ash content is determined by heating, after drying, a sample of 1 g of fuel in an oven at initial temperature to allow the volatiles to leave the sample before ignition. Then the temperature will be raised further until there is no more weight change in the sample (at least 2 hours). The tests will be repeated and the mean of duplication is reported to the nearest 0.1%.

In order to determine the volatile matter content in the fuels, a sample of 1g of fuel is heated at a high temperature for a short period of time according to the

Table 5.6: Absorption cooling unit test parameters

Symbol	Description	Unit	Value
P_{air}	ambient air pressure	$mmHg$	
Δh_1	air flow inlet	mmH_2O	
Δh_2	air flow exhaust gas	mmH_2O	
$\Delta MW1$	water flow volume	m^3	
$\Delta MW3$	water flow volume	m^3	
$\Delta MW4$	water flow volume	m^3	
$\Delta fuel$	fuel quantity	kg	
Δt	test duration	s	
$T1$	ambient air temp.	$°C$	
$T2$	combustion temp.	$°C$	
$T3$	exhaust gas temp.	$°C$	
$T8$	hot water temp.	$°C$	
$T9$	return water temp.	$°C$	
$T10$	HE1 tube side inlet	$°C$	
$T11$	HE1 tube side outlet	$°C$	
$T12$	HE1 shell side inlet	$°C$	
$T13$	HE1 shell side outlet	$°C$	
CO	carbon monoxide	ppm	
CO_2	carbon dioxide	%	
C_6H_{14}	hexane	ppm	
NO_x	nitric oxide	ppm	
O_2	oxygen	%	
PM	particulate matter	mg/m^3	

procedure detailed in standard EN15148. The result is reported as the mean of duplicate determinations rounded to the nearest 0.1%.

The fixed carbon content is derived by subtracting the wt% for moisture, ash and volatile matter from 100.

The calorific value of the fuels is carried out according to EN14918 with a PARR 1341 bomb calorimeter. Three tests are carried out along with an additional test to determine the bomb calorimeter's own energy content and allow for calibration. The net calorific value is then calculated based on the formulas presented in the standard. The results determined by these tests will be used as the input parameter for the biomass combustion model described in the previous

chapter.

5.4.5 Experimental Plan for CCH Performance

A series of tests were designed to evaluate the total combined cooling and heating performance (CCH), which are shown in Table 5.7. In these tests the flow rate of the heat source circuit is varied for different Reynolds numbers. The following are determined to evaluate the performance of the proposed CCH system:

- Primary energy input
- Heat absorbed in the absorption unit
- Heat dissipated to the exhaust gas
- Heat dissipated to the heat sink circuit
- Cooling output from the unit

In addition to the parameters presented in Table 5.6, the parameters in Table 5.8 are recorded.

Table 5.7: Absorption performance test series for CCH

	Reynolds number		
Test series	**12710**	**21185**	**29660**
Test series 1	CCT11	CCT21	CCT31
Test series 2	CCT12	CCT22	CCT32
Test series 3	CCT13	CCT23	CCT33

5.4.6 Test Procedure

In line with the test plan, a series of tests were performed to examine the performance of the combustion unit, the Stirling engine, the absorption unit, the biomass properties, and CCH system, which comes to a total of 101 tests (these include the necessary test for the fuel properties). The performance tests have

Table 5.8: Absorption cooling unit test parameters for CCH

Symbol	Description	Unit	Value
$\Delta MW5$	water flow volume	m^3	
$\Delta MW6$	water flow volume	m^3	
$T14$	HE2 shell side inlet	$°C$	
$T15$	HE2 shell side outlet	$°C$	
$T16$	HE2 tube side inlet	$°C$	
$T17$	HE2 tube side outlet	$°C$	

been based on the Reynolds number in the heat source flow circuit. The difference in the values between heating only and the absorption tests is due to the different pressure drops encountered. The following procedure was used for every set of results that were taken from the test system:

- All instrumentation needed for the collection of data from the system was installed and tested.
- The electrical power and control side connections were checked for integrity and safety.
- The exhaust fans were turned on and the combustion unit was lit in accordance with the manufacturer‘s start up procedure.
- The combustion chamber was left to warm up.
- During this period, the ambient barometric air pressure was recorded along with all the water meter levels.
- Upon reaching $50°C$ water temperature inside the boiler, the water pump regulating the boiler circuit was switched on.
- The absorption unit control regulated the valves for the heat source, heat sink and cooling circuit.

5.5 Calibration

This section discusses the calibration of all sensors and instruments used in the experiments. The mercury barometer for measuring atmospheric pressure; the manometers for measuring air (gas) flow rates; the scales for weighting fuel quantities and samples; and the digital multi-meters for measuring power, voltage and current, are all calibrated by the manufacturers and checked regularly. Hence, they are not included in the following discussion.

5.5.1 Calibration of Gas Analysers

Prior to testing, the analysers were calibrated by using the special gases supplied by BOC Ltd. Calibration was conducted in–house at the University, using the standard gases. The following procedure was used to calibrate the analysers:

- Switch on the power of the analysers; leave them on for at least one hour until the analysers are in stable conditions; then start the calibration procedure.
- Zero setting: dry air was pumped into the analysers, while the needle gauge was adjusted until the analysers read zero.
- Span: the span gases were used. The span controls were adjusted to read the corresponding indications of 830 ppm for CO, 3.15% for CO_2, 1470 ppm for NO_x, and 850 ppm for hexane. When these were completed, the analysers were ready for use.

Prior to testing, the oxygen analyser was calibrated by using the zero gas and span gas.

- Zero: a zero gas (high purity nitrogen) was used at a pressure between 2.3 to 70 kPa. The zero adjust screw on the side of the analyser was adjusted to obtain an indication of 00.0% on the display.
- Span: the span gas (clean dry air) was at a pressure between 2.3 to 70 kPa. The span control was adjusted to obtain a corresponding indication of 21.0%.

5.5.2 Calibration of Thermocouples

The thermocouples used in the tests are of the K–type. The thermocouples were calibrated at two known set points using crushed ice and boiling water, supplemented by a series of randomly taken temperature measurements using a precision hand held FLUKE Digital Thermometer, which has a range of $-200°C$ to $1370°C$, and an accuracy of 0.1% of reading. The thermocouples were placed into a mounting disc that had been prepared, which ensured that the thermocouples and thermometers remained exactly positioned equally-spaced around the body of the heating bath, equally distant both from each other and form the centralised heating source. The mounting disc would also ensure that the instruments were inserted into the heating bath at the same depth. To determine the lower set point, finely crushed ice from distilled water was prepared and packed into the heating bath ($1000\,ml$). The mounting disc was fitted to the heating bath and the thermocouples and thermometers inserted into the crushed ice water. The thermocouples were left in direct contact with the crushed ice water for some time in order for minor temperature fluctuations to stabilise. Once the crushed ice had begun to melt, the reference FLUKE digital thermometer and Mercury thermometer recorded the temperature. After some time, only a marginal melting of the ice had been observed and so another series of temperature measurements were taken. As the ice began to melt, the reducing volume was replaced with chilled water in order to maintain a working volume of $1000\,ml$. Once there was sufficient liquid content to cover the heating element of the bath, the heating bath was switched on. As the water temperature slowly increased, temperature recordings were taken at about $10°C$ intervals of the thermocouples and FLUKE digital thermometer. When the water began to boil (upper set point) a series of recordings was taken. The thermocouples were left in direct contact with the boiling water as no discernible fluctuations of the indicated readings could be seen, and a final set of readings were taken. This procedure was repeated several times and the corresponding calibration data generated for each thermocouple. Two further tests confirmed that the correlations were repeatable to within accuracies of $\pm 0.2°C$.

5.5.3 Data Logging System Configuration

The interface is connected to the computer using a 5-wire RS232 ribbon serial lead to a 25-pin IBM compatible D connector with the other end of the serial lead using the 25 to 9 way adapter inserted into a COM port. To configure the data logger, designated channels are assigned to the appropriate sensor, using the Heat Technology Data Logging software provided. The thermocouples are connected to the Data Acquisition System using the screwed terminal connectors situated on the front of the unit. The channels on the data logger were configured for high gain, as shown in Table 5.9.

Table 5.9: Data logging interface configuration and calibration

Channel	**Label**	**Temperature**	**Calibration**
1	$T1$	ambient air	$T_h = 0.9891 \times T1 - 0.1383$
2	$T2$	combustion	$T_h = 0.9949 \times T2 - 0.0751$
3	$T3$	exhaust gas	$T_h = 1.0045 \times T3 + 0.5937$
4	$T4$	heater tubes	$T_h = 1.0014 \times T4 - 1.2023$
5	$T5$	heater tubes	$T_h = 1.0014 \times T5 - 1.1474$
6	$T6$	cooling inlet	$T_h = 0.9997 \times T6 + 0.0307$
7	$T7$	cooling outlet	$T_h = 0.9982 \times T7 - 0.5045$
8	$T8$	hot water outlet	$T_h = 0.9984 \times T8 + 0.1533$
9	$T9$	return water inlet	$T_h = 0.9995 \times T9 + 0.0313$
10	$T10$	HE1 tube inlet	$T_h = 1.0002 \times T10 - 0.1881$
11	$T11$	HE1 tube outlet	$T_h = 0.9936 \times T11 - 0.0743$
12	$T12$	HE1 shell inlet	$T_h = 1.0011 \times T12 + 0.2111$
13	$T13$	HE1 shell outlet	$T_h = 0.9867 \times T13 - 0.6099$
14	$T14$	HE2 shell inlet	$T_h = 0.9928 \times T14 + 0.2150$
15	$T15$	HE2 shell outlet	$T_h = 1.0046 \times T15 + 0.4246$
16	$T16$	HE2 tube inlet	$T_h = 0.9898 \times T16 + 0.0436$
17	$T17$	HE2 tube outlet	$T_h = 0.9890 \times T17 + 0.3119$

5.5.4 Calibration of Bomb Calorimeter

The results obtained from the bomb calorimeter test include the effective heat capacity of the test equipment. In order to correct the results for this equipment's dependent variable, the calorimeter needs to be 'standardised'. This en-

ergy equivalent factor represents the energy required to raise the temperature of the calorimeter by one degree. This requires a series of standardisation tests from which an average can be taken to represent the true correction factor. The procedure for the standardisation test is exactly the same as for testing a fuel sample. However, the sample used is a pellet of calorific grade benzoic acid weighing no less than 0.9 and no more than 1.25 g. After the test, the correction factor can be determined as follows (here the equations and material properties are used as provided by the manufacturer):

$$W = \frac{H \times m + e_1 + e_3}{t} \tag{5.12}$$

where:
W = energy equivalent of the calorimeter in $cal/^{\circ}C$
H = heat of combustion of the standard acid sample in $cal/^{\circ}C$
m = mass of the standard benzoic acid sample in grams
t = net corrected temperature rise in $^{\circ}C$
e_1 = correction factor for the heat of formation of nitric acid in calories
e_3 = correction factor for the heat of combustion of the firing wire in calories

The calibration of the tests determined an average value for W of $2469.219 cal/^{\circ}C$.

5.5.5 Calibration of Double Pass Particulate Monitor

The DSL-330 Particulate Monitor is an in-situ analyser that relies on the local plant structure to determine both the length and angular alignment of its light path. This means that, after installing the DSL-330 in the exhaust pipe, the following procedures had to be carried out in order to achieve an optimal working condition of the particulate monitor.

- Head alignment; this optimises the mounting angle of the Reflector and TRX heads to achieve the largest possible measured signal with the least gain.
- Automatic Gain Correction; this adjusts the gain applied to the measurement signal to achieve an amplified signal that is within the required voltage range.

- Zero adjustment to $0.0\,mg/m^3$ particulate under clear path conditions; this adjusts the instrument's span setting to define the bottom scale.
- Upscale calibration; this involves using the density scale factor to force the particulate reading to match independent reference measurements taken coincidentally.

Regular calibration routines are required to guarantee optimum operating conditions of the device. The calibration is carried out by connecting the DSL-330 to a PC with the operating software, supplied by the manufacturer. The calibration tab of the user interface leads through the various steps of the calibration procedure, which involves several opacity filters. The main calibration is carried out by the software.

5.6 Error Analysis

Errors always exist when measurements are made during an experiment. These errors can be divided into two types: systematic and random errors.

Systematic errors are those which remain constant during the process of measurement for a given value measured. It causes repeated measurements to be in error by the same amount from each experiment. If an infinite number of readings are taken, the difference between their mean reading and true reading is the systematic error. It can be minimised by proper calibration or correction. The estimation of systematic error is related to the construction and calibration of the instruments. Typical systematic errors are from: errors from a single calibration; errors of determination of the constants in the working formula of a measuring method; errors due to truncating instead of rounding of results of measurements. The inaccuracy of systematic error correction results in a residual systematic uncertainty. The systematic uncertainties of instruments are usually provided by the manufacturer in the manuals.

Random errors are those that produce variation (not predictable) in repeated measurements of the same quantity. It is the variation between the instrument reading and the mean of all readings. It is different for every reading and hence it cannot be removed. The factors that introduce random error are uncertain

by nature. Typical random errors are those caused by inaccurate reading of the scale of a measuring instrument or by the scatter of the output signal of an instrument. The effect of random errors on the random uncertainty may be reduced by averaging multiple results of tests carried out under the same conditions. Random uncertainty is normally evaluated by the statistical analysis of repeated measurements and referred as experimental standard deviation. Error analysis, which can be estimated as the probable error in experimental results, are discussed in the standards BS ISO 5168:2005 (Measurement of fluid flow); BS ISO TR 7066-1:1997 (Assessment of uncertainty) and PD 6461-4:2004 (General metrology). The following error analysis and uncertainty calculations are based on the methods described in these standards and relevant textbooks (Hughes & Hase, 2010).

The relative uncertainty and percentage uncertainty can be expressed mathematically as follows:

$$Relative\ uncertainty = \frac{Absolute\ uncertainty\ in\ a\ measurement}{Size\ of\ a\ measurement} \tag{5.13}$$

Uncertainty rules can be written for standard operations in algebra, as outlined below:

$$(A \pm \Delta A) + (B \pm \Delta B) = (A + B) \pm (\Delta A + \Delta B) \tag{5.14}$$

$$(A \pm \Delta A) \times (B \pm \Delta B) = (A \times B) \pm \left(\frac{\Delta A}{A} + \frac{\Delta B}{B}\right) \tag{5.15}$$

The propagation of measurement uncertainties, when there is a known mathematical relationship between the results (Y) and subsidiary quantities ($x_1, x_2, \ldots, x_k$) can be expressed as follows:

$$Y = f\left(x_1, x_2, \ldots, x_k\right) \tag{5.16}$$

$$\frac{\delta Y}{\delta x_i} = \frac{\delta f}{\delta x_i}, \quad (i = 1, 2, \ldots, k) \tag{5.17}$$

Now the systematic uncertainty can be written as:

$$e_s = \sqrt{\Sigma \left(\frac{\delta f}{\delta x_i} e_{sx_i}\right)^2} \tag{5.18}$$

Thus, the random uncertainty (experimental standard deviation) of the results (Y) is given by:

$$e_r = \sqrt{\Sigma \left(\frac{\delta f}{\delta x_i} e_{rx_i} \right)^2} \tag{5.19}$$

The total uncertainty, in its relative form, of the test results can then be determined by combining the systematic and random uncertainties. The methods used are the additive or the root-sum-square model of combination:

$$U_{ADD} = \Delta e_s + \Delta e_r \tag{5.20}$$

$$U_{RSS} = \sqrt{(\Delta e_s)^2 + (\Delta e_r)^2} \tag{5.21}$$

5.6.1 Temperature Measurement Uncertainty

All the temperature measurements listed in Fig. 5.1 are carried out by Class 1 K type thermocouples. The systematic uncertainty for the thermocouples is taken from the technical specifications issued by the manufacturer, as specified in Table 5.10. The random uncertainty for thermocouple ($T1$) is based on a typical value

Table 5.10: Technical specifications of K type thermocouple

Temperature range	**Systematic error**	**Systematic uncertainty**
$-40°C$ to 375°	$\pm 1.5°C$	$\Delta e_s = 0.4\%$
$375°C$ to 1000°	$\pm 0.4\%$	$\Delta e_s = 0.4\%$

of $18°C$ and a probable random error of $0.18°C$. The random uncertainty thus becomes:

$$\Delta e_r = \frac{0.18}{18} = 1.00\% \tag{5.22}$$

Combining the systematic and random uncertainty by linear additive (ADD) and root-sum-square (RSS) methods for thermocouple ($T1$) yields:

$$U_{ADD} = 0.004 + 0.01 = \pm 1.40\% \tag{5.23}$$

$$U_{RSS} = \sqrt{0.004^2 + 0.01^2} = \pm 1.08\% \tag{5.24}$$

Table 5.11 shows the uncertainties for all the thermocouples used in the present study.

Table 5.11: Uncertainty of thermocouples used in the present study

Thermocouple	**Random**	**Systematic**	U_{ADD}	U_{RSS}
$T1$	0.40%	1.00%	1.40%	1.08%
$T2$	0.40%	0.05%	0.45%	0.40%
$T3$	0.40%	0.70%	1.10%	0.81%
$T4$	0.40%	0.32%	0.72%	0.51%
$T5$	0.40%	0.98%	1.38%	1.06%
$T6$	0.40%	0.61%	1.01%	0.73%
$T7$	0.40%	0.45%	0.85%	0.60%
$T8$	0.40%	0.44%	0.84%	0.59%
$T9$	0.40%	0.25%	0.63%	0.47%
$T10$	0.40%	0.19%	0.59%	0.44%
$T11$	0.40%	0.77%	1.17%	0.87%
$T12$	0.40%	1.02%	1.42%	1.10%
$T13$	0.40%	0.95%	1.35%	1.03%
$T14$	0.40%	0.97%	1.37%	1.05%
$T15$	0.40%	1.19%	1.59%	1.26%
$T16$	0.40%	0.74%	1.14%	0.84%
$T17$	0.40%	0.77%	1.17%	0.87%

5.6.2 Air Flow Measurement Uncertainty

The random and the systematic uncertainty for the air flow measurement is based on the equations from the propagation of measurement uncertainties in the British standard BS EN ISO 5168:2005.

$$e_s = \sqrt{\left(e_{s_{Cd}}\frac{\delta\dot{m}}{\delta Cd}\right)^2 + \left(e_{s_d}\frac{\delta\dot{m}}{\delta d}\right)^2 + \left(e_{s_\rho}\frac{\delta\dot{m}}{\delta\rho}\right)^2 + \left(e_{s_h}\frac{\delta\dot{m}}{\delta h}\right)^2} \tag{5.25}$$

$$e_r = \sqrt{\left(e_{r_{Cd}}\frac{\delta\dot{m}}{\delta Cd}\right)^2 + \left(e_{r_d}\frac{\delta\dot{m}}{\delta d}\right)^2 + \left(e_{r_\rho}\frac{\delta\dot{m}}{\delta\rho}\right)^2 + \left(e_{r_h}\frac{\delta\dot{m}}{\delta h}\right)^2} \tag{5.26}$$

For relative uncertainty:

$$\Delta e_s = \frac{e_s}{\dot{m}} = \sqrt{\left(e_{s_{Cd}}\frac{1}{Cd}\right)^2 + \left(e_{s_d}\frac{2}{d}\right)^2 + \left(e_{s_\rho}\frac{1}{2\rho}\right)^2 + \left(e_{s_h}\frac{1}{2h}\right)^2} \tag{5.27}$$

$$\Delta e_r = \frac{e_r}{\dot{m}} = \sqrt{\left(e_{r_{Cd}}\frac{1}{Cd}\right)^2 + \left(e_{r_d}\frac{2}{d}\right)^2 + \left(e_{r_\rho}\frac{1}{2\rho}\right)^2 + \left(e_{r_h}\frac{1}{2h}\right)^2} \tag{5.28}$$

Systematic uncertainties are introduced by the construction of the orifice; the recommended value of Cd, the systematic uncertainty of the density of air and the reading of the manometer. Based on a Reynolds number of 2×10^4, the following systematic errors are determined:

- For the coefficient of discharge of the installed orifice plate:
  - Average: $Cd = 0.60$
  - Possible error: $\Delta Cd = 0.005$
  - Systematic error: $\Delta e_{s_{Cd}} = \frac{0.005}{0.60} = 0.83\%$
- For the free flow area through the orifice (the diameter will be considered)
  - Diameter of orifice: $d = 60\,mm$
  - Possible error $\Delta d = 0.01\,mm$
  - Systematic error: $\Delta e_{s_d} = \frac{0.01}{60} = 0.02\%$
- For the reading of the manometer
  - Range of the manometer: 0–100 mmH_2O
  - Possible reading error: $0.05\,mmH_2O$
  - Systematic error: $\Delta e_{s_h} = \frac{0.05}{100} = 0.05\%$

The systematic uncertainty of the density of air is determined by combining the systematic uncertainties from measuring the pressure (0.04%), the temperature (0.4%) and the gas constant R (0.35%, $287 \pm 1\ J/kgK^{-1}$):

$$e_{s_\rho} = \sqrt{0.0004^2 + 0.004^2 + 0.0035^2} = 0.53\% \tag{5.29}$$

Therefore, the relative systematic uncertainty for the density of air at ambient conditions becomes:

$$\Delta e_{s_\rho} = \frac{0.0053}{1.2} = 0.44\% \tag{5.30}$$

Now the relative systematic uncertainty for the mass flow of air can be evaluated:

$$\begin{aligned} \Delta e_s &= \sqrt{\left(e_{s_{Cd}}\frac{1}{Cd}\right)^2 + \left(e_{s_d}\frac{2}{d}\right)^2 + \left(e_{s_\rho}\frac{1}{2\rho_{air}}\right)^2 + \left(e_{s_h}\frac{1}{2h}\right)^2} \\ &= \sqrt{0.0082^2 + (2\times 0.0002)^2 + (0.5\times 0.0044)^2 + (0.5\times 0.0005)^2} \\ \Delta e_s &= 0.85\% \end{aligned} \tag{5.31}$$

The random uncertainty, or the component experimental standard deviation, is zero for the coefficient of discharge and the diameter of the orifice. The one for the density of air is determined from the random errors of pressure and temperature measurement ($T1$):

$$e_{r_\rho} = \sqrt{0.0051^2 + 0.01^2} = 1.12\% \tag{5.32}$$

Hence the relative random uncertainty for the density of air is:

$$\Delta e_{r_\rho} = \frac{0.0112}{1.2} = 0.94\% \tag{5.33}$$

The relative random uncertainty is based on a typical reading of $h = 0.192 mmH_2O$ and a probable random error of 0.005 mmH_2O:

$$\Delta e_{r_h} = \frac{0.005}{0.192} = 2.60\% \tag{5.34}$$

Now the relative random uncertainty for the mass flow of air can be evaluated:

$$\begin{aligned} \Delta e_r &= \sqrt{\left(e_{r_\rho}\frac{1}{2\rho}\right)^2 + \left(e_{r_h}\frac{1}{2h}\right)^2} \\ &= \sqrt{(0.5\times 0.0094)^2 + (0.5\times 0.026)^2} \\ \Delta e_r &= 1.32\% \end{aligned} \tag{5.35}$$

Combining the systematic and random uncertainty by linear additive (ADD) and root-sum-square (RSS) methods for the air flow measurement yields:

$$U_{ADD} = 0.0085 + 0.0132 = \pm 2.17\% \tag{5.36}$$

$$U_{RSS} = \sqrt{0.0085^2 + 0.0132^2} = \pm 1.57\% \tag{5.37}$$

5.6.3 The Other Measurements Uncertainties

Applying the same uncertainty calculation principle to the other measurements, the final results are shown in Table 5.12. The detailed process of error analysis is reported in Appendix B.

Table 5.12: Measurement uncertainties

Parameter	**Instrument**	**Range**	**Syst.**	**Rand.**	$\boldsymbol{U_{ADD}}$	$\boldsymbol{U_{RSS}}$
P_{air} (Pa)	Mercury barometer	678 to 720 $mmHg$	0.04%	0.51%	0.55%	0.51%
fuel flow rate	scale	6.5 to 10.5kg	0.00%	2.52%		
	timer	0.0 to 24hr	0.00%	2.46%		
	$\dot{m}_{fuel}$	kg/s	0.00%	5.16%	5.16%	5.16%
exhaust gas flow rate	manometer	0-100 mmH_2O	0.00%	2.86%		
	ρ_{H_2O}	$997.1kg/m^3$	0.50%	–		
	gravity	$9.81m/s^2$	0.50%	–		
	conversion	mmH_2O to Pa	0.71%	2.86%		
	ρ_{air} 100°C	0.946 kg/m^3	0.56%	0.92%		
	gas flow	kg/s	1.27%	3.77%	5.04%	3.98%
Air flow intake	diameter of orifice	$d = 60mm$	0.02%	–		
	C_d	0.60	0.82%	–		
	manometer	0-100 mmH_2O	0.05%	2.71%		
	ρ_{air} 25°C	1.2 kg/m^3	0.44%	0.94%		
	air flow	kg/s	0.85%	1.43%	2.28%	1.67%

Table 5.12: Measurement uncertainties

Parameter	Instrument	Range	Syst.	Rand.	U_{ADD}	U_{RSS}
MW1	reading	m^3	0.01%	1.71%		
	ρ_{H_2O}	$986.7 kg/m^3$	0.50%	–		
	water flow	kg/s	0.51%	1.71%	2.22%	1.67%
MW3	water flow	lit/min	4.00%	0.42%		
	ρ_{H_2O}	$986.7 kg/m^3$	0.50%	–		
	water flow	kg/s	4.50%	0.42%	4.92%	4.52%
MW4	water flow	lit/min	4.00%	0.42%		
	ρ_{H_2O}	$986.7 kg/m^3$	0.50%	–		
	water flow	kg/s	4.50%	0.42%	4.92%	4.52%
MW5	water flow	lit/min	4.00%	1.39%		
	ρ_{H_2O}	$986.7 kg/m^3$	0.50%	–		
	water flow	kg/s	4.50%	1.39%	5.89%	4.71%
MW6	diameter of orifice	$d = 33mm$	0.03%	–		
	C_d	0.6117	0.82%	–		
	manometer	0-1 bar	0.10%	0.19%	1.05%	0.88%
Electrical input	voltage	57-480 V	0.50%	0.81%	1.31%	0.95%
	current	0.01-10 A	1.00%	4.49%	5.49%	4.60%
	power factor	0.000-1.000	1.00%	4.75%	5.75%	4.85%
	power	kW	Power errors are calculated by adding the errors of voltage and current. Error due to PF: specified error $\times(1 - [PF])$			
O_2 content	O_2 analyser	$0 - 100\%$	0.05%	1.77%	1.82%	1.77%
Exhaust emissions	CO	$0 - 0.5\%$	2.00%	4.60%	6.60%	5.02%
	CO_2	$0 - 20\%$	2.00%	4.53%	6.53%	4.95%
	NO_x	0-10 000 ppm	2.00%	7.27%	9.27%	7.54%
	C_6H_{14}	0-5 000 ppm	2.00%	5.01%	7.01%	5.39%
Particulate matter	PM	0-1 000 mg/m^3	2.00%	8.04%	10.04%	8.29%
Q_{pr}	fuel flow	kg/s	0.00%	5.16%		
	NCV	MJ/kg	0.73%	–		
	Q_{pr}	kW	0.73%	5.16%	5.89%	5.21%

Table 5.12: Measurement uncertainties

Parameter	Instrument	Range	Syst.	Rand.	U_{ADD}	U_{RSS}
Q_s	MW1	kg/s	0.51%	1.71%		
	cp	kJ/kgK	4.00×10^{-5}	–		
	(T8)	$°C$	0.40%	0.44%		
	(T9)	$°C$	0.40%	0.25%		
	Q_s	kW	1.13%	2.40%	3.71%	2.73%
Q_{ac}	MW3	kg/s	4.50%	0.42%		
	cp	kJ/kgK	1.90×10^{-6}	–		
	(T10)	$°C$	0.40%	0.19%		
	(T11)	$°C$	0.40%	0.77%		
	Q_{ac}	kW	5.30%	1.38%	6.68%	5.48%
Q_{hs}	MW6	kg/s	0.86%	0.19%		
	cp	kJ/kgK	5.72×10^{-6}	–		
	(T14)	$°C$	0.40%	0.97%		
	(T15)	$°C$	0.40%	1.19%		
	Q_{hs}	kW	1.66%	2.35%	4.01%	2.88%
Q_{ex}	gas flow	kg/s	1.27%	3.77%		
	cp	kJ/kgK	2.24×10^{-5}	–		
	(T1)	$°C$	0.40%	1.00%		
	(T3)	$°C$	0.40%	0.70%		
	Q_{ac}	kW	2.07%	5.47%	7.55%	5.85%

5.7 Conclusion

This chapter describes the tests carried out during the course of this study. All the equipment used for the measurements is explained in detail along with the calibration procedures used. Additionally an uncertainty analysis on all measurements is conducted to present errors in measurements for the results presented in the next chapter. All the tests are now set up and all the equipment is calibrated according to the manufacturer's specifications. Along with the extensive uncer-

tainty analysis, the results obtained in the described tests can now be discussed in the next chapter without scrutinizing their validity.

Chapter 6

Results and Discussion

6.1 Introduction

A series of tests were carried out according to the test plans described in the previous chapter for the performance evaluation and comparison with different generation schemes.

- The performance of the biomass boiler for different Reynolds numbers, based on the water flow, for hot water generation and as the heat source for the absorption cooling unit.
- The emissions of the biomass boiler when it is operated as a single generation or as the heat source for the absorption unit.
- The performance of the heat sink circuit for both charging and discharging cycles.
- The performance of the air conditioning circuit.
- The coefficient of performance of the absorption unit for different heat sink inlet temperatures.
- The working conditions of the Stirling engine as a cooler.
- The total performance for combined cooling and heating.

Two different generation schemes (conventional single hot water generation in a biomass boiler and combined cooling and heating) for different flow regimes on the water side are investigated. These flow regimes were obtained by different pump settings. For each Reynolds number, the hot water output, fuel consumption, thermal efficiency and emissions were investigated. Additionally, the coefficient of performance for the absorption unit was analysed for different heat sink and cooling loads. The Stirling engine was mounted on a test bed while connected to a generator. The generator was used to drive the crankshaft of the Stirling engine and thus reversing the thermal cycle process. The electric power, in this case, is considered the power input and the cooling generated at the heater tubes will be regarded as the net power output. In order to determine the energy input to the biomass combustion system, the biomass properties as outlined in the previous chapter are investigated prior to any testing. The results from these tests are presented in this chapter with relevant discussions. The boiler, engine, heat exchanger and absorption performance simulation as well as the biomass combustion prediction model results are compared to the data gathered in the tests.

6.2 Biomass Combustion Performance and Products

This section will present a discussion of the results obtained through the fuel properties test, the performance evaluation of the biomass boiler, and the emissions from different fuels under various combustion loads.

6.2.1 Biomass Fuel Properties

The biomass properties are carried out in accordance with the new European standards regarding 'solid recovered biofuels'. Different types of biomass are tested and the fuels were obtained from a local distributor, through a partner agreement, or imported from Luxembourg. Table 6.1 gives an overview of the different fuels with the name used in the subsequent sections of this study. The first test carried out is the moisture content as this is required for the evaluation

Table 6.1: Type of fuels used in the test series

Fuel	Country	Origin	Dried	Product	Certified
UK pellets	UK	wood	yes	pellets	?
DIN pellets	L	wood	yes	pellets	DIN+
Agripelelts	UK	?	yes?	pellets	?
Misc. pellets	UK	Miscanthus	yes	pellets	no
Misc. raw	UK	Miscanthus	yes	shredded [1]	no
Straw / lime	UK	Straw	yes	pellets [2]	pending
Misc. log good	UK	Miscanthus	yes (a lot)	log [3]	pending
Misc. log bad	UK	Miscanthus	yes (a lot)	log	pending

[1] Fig. 6.1
[2] Fig. 6.2
[3] Fig. 6.3

Figure 6.1: Shredded Miscanthus

Figure 6.2: Straw pellets dia: $\pm$ 6 mm

Figure 6.3: Miscanthus logs 60 mm $\times$ 60 mm

of all other tests. As a matter of fact the results presented will all be based on the dry basis of the fuel (d) or as received (ar). Figure 6.4 shows a bar chart of the moisture content for the different fuels tested in accordance with EN14774-3. All fuels comply with the current legislations of the DIN plus 51731 as well as the more stringent ÖNorm M7135 which indicates a moisture content of less than 12%. From the results of the Miscanthus based fuels it becomes obvious that the decrease in moisture content is directly proportional to the energy used for drying purposes. The shredded fuel has the highest value (11%) and the logs of good quality have the lowest value (7%) as raw Miscanthus was transformed into logs by a hot extrusion process. Figure 6.5 shows the bulk density as received as well as the bulk density on a dry basis. As expected the shredded Miscanthus has a relatively low bulk density (300 kg/m^3) compared to the other fuels (500–700 kg/m^3). These are typical values as reported in referenced literatures. The bulk

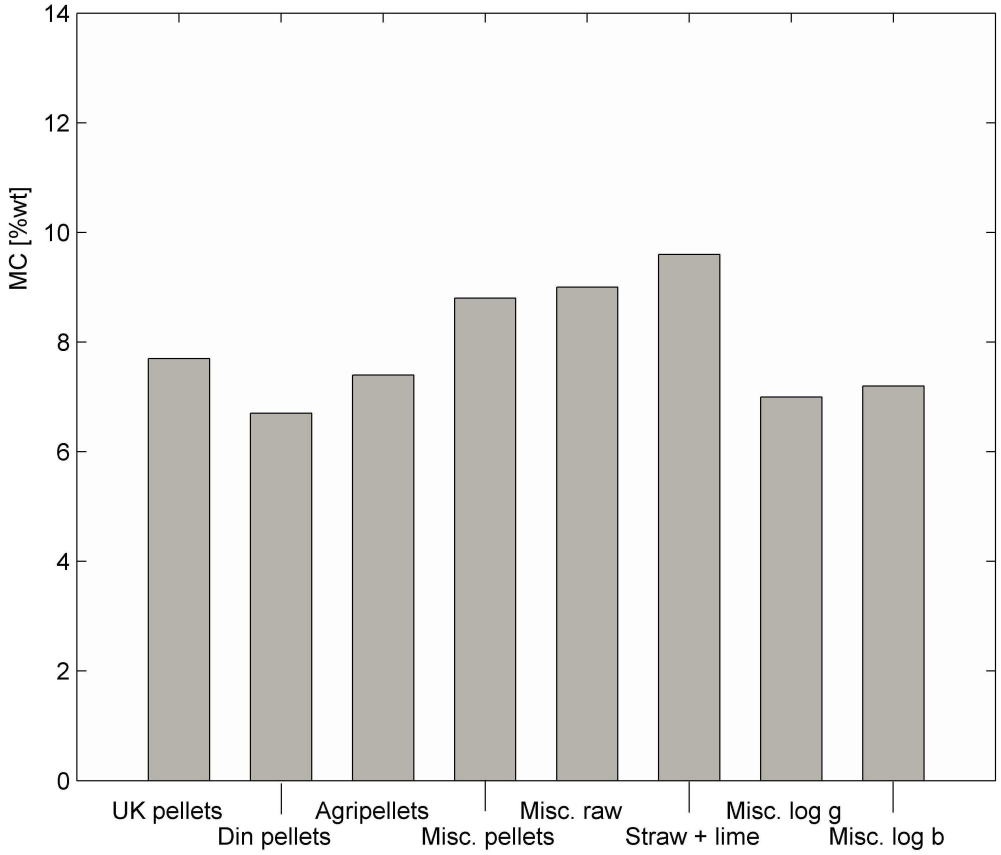

Figure 6.4: Moisture content for the different fuel samples

density, although it shows the mass/volume ratios of the fuels, it does not take into account the actual energy content. As a result, the product of bulk density and energy content is used as the energy density. Figure 6.6 shows the ash content for the various fuels tested. As expected the highest ash content is observed for the straw based biomass with a value in excess of 12%. The UK pellets and Din pellets are the only two samples that meet the current DIN 51731 norm of a value less than 1.5%. Only the Din pellets meet the ÖNorm of less than 0.5% for wood based pellets. An increase in ash content should have a lowering effect on the calorific value of the sample tested. Figure 6.7 shows the volatile matter of the different fuels tested. All the samples tested are close to 75% with the lowest values for the straw (70%) and the highest for Miscanthus logs tested. Figure 6.8

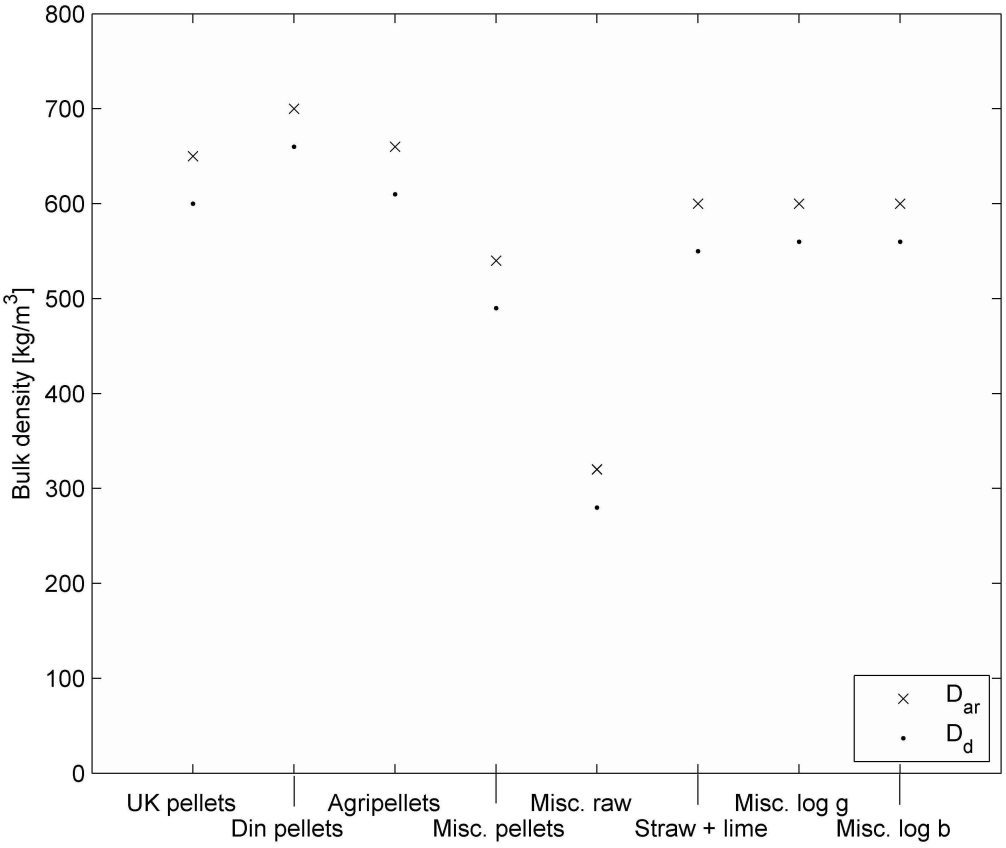

Figure 6.5: Bulk densities for the different fuel samples

shows the fixed carbon content for the different fuels investigated. Similar as for the volatile matter an increase in fixed carbon content should reflect an increase in energy content. Since the fixed carbon content is determined algebraically based on the previous three test results, the values are merely a reflection of the above results. Hence, a high moisture content (Misc. raw) and/or high ash content (straw + lime) will result in a low fixed carbon content as shown by the plotted results. The last test, regarding the properties of biofuels, was the higher heating value determined by a PARR bomb calorimeter. Figure 6.9 shows the heating values for the various fuels tested. The majority of the fuels have a higher heating value varying between 18 MJ/kg and 19 MJ/kg as recommend by the DIN and ÖNorm. The shredded Miscanthus (Misc. raw) as well as the straw have a lower

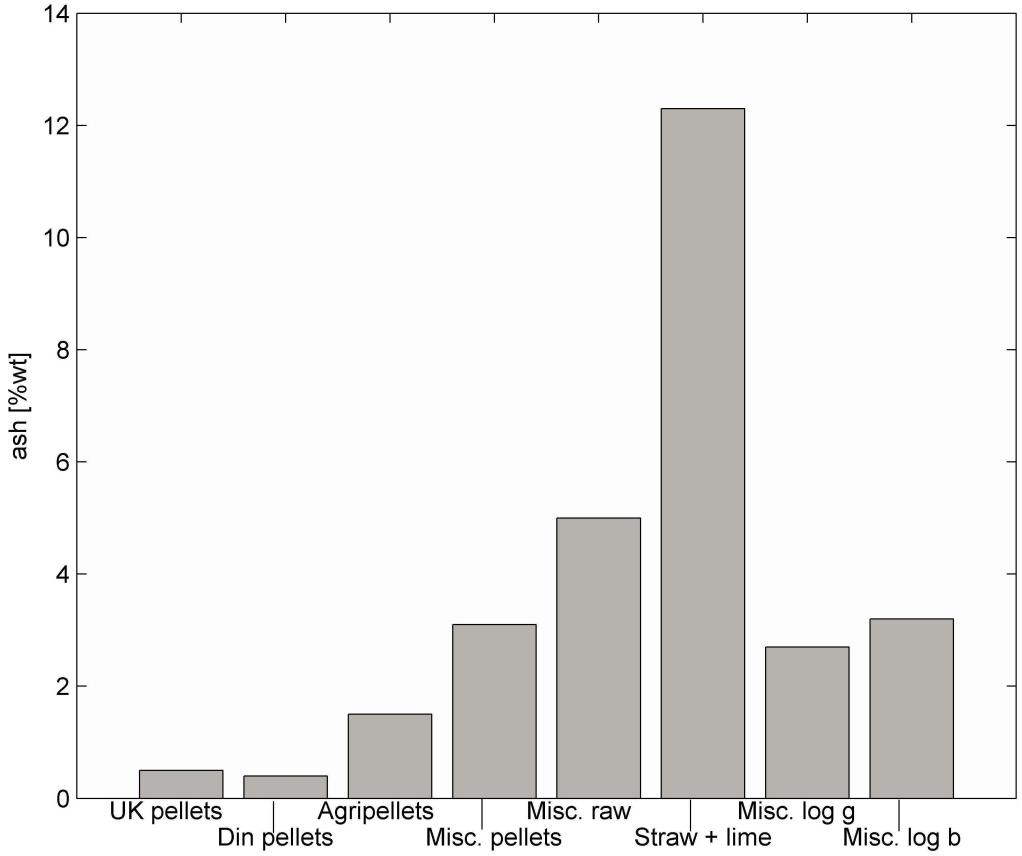

Figure 6.6: Ash content for the different fuel samples

heating value in accordance with the above discussions. In addition, Fig. 6.9, shows the energy density for the fuels (cf. bulk density). This energy density is presented in $MJ/litre$ which allows comparison with fossil fuels (e.g. heating oil 37.3 $MJ/liter$). Also, this gives an idea of the amount of space required for fuel storage for residential housing for example. The results show that the shredded form of Miscanthus requires a lot more storage compared to the pellets and log form of the fuel.

Figure 6.10 shows the ash content for the different fuels plotted against their respective heating value. As mentioned above an increase in ash content results in a decrease of the heating value. Additionally, the results show, as expected, that there is a linear relation between ash and energy content for solid biomass

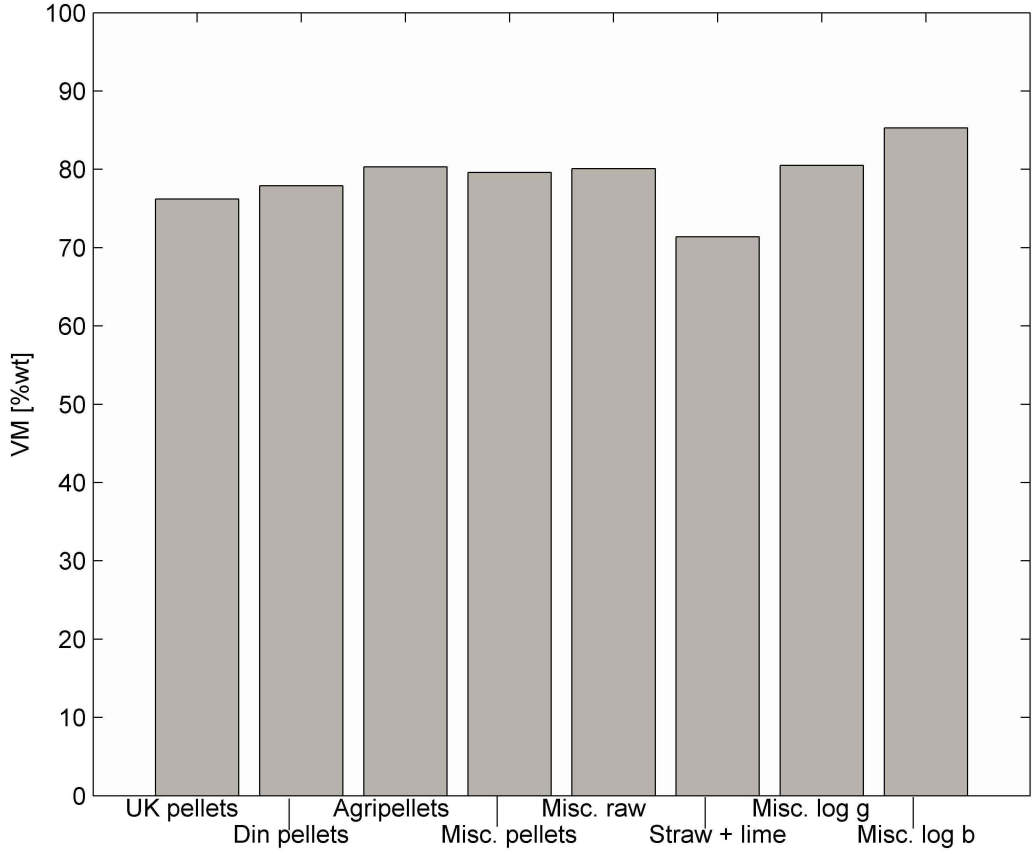

Figure 6.7: Volatile matter content for the different fuel samples

fuels. Figure 6.11 shows the sum of the volatile matter and fixed carbon content (useful energy) plotted against the heating values for the different fuel samples investigated. As mentioned above, an increase in volatile matter and fixed carbon content will result in an increased heating value for solid biomass fuels. Additionally, there is a linear relation between the sum of the volatile matter and fixed carbon content and the higher heating values. The two correlations are then compared to other similar correlations, presented in the literature by Parikh *et al.* (2005). Figure 6.12 shows a comparison of the measured values for the heating value against the predicted one with five different equations, three from the literature and two presented in this study. The correlations from the study, based on the measurements in this study, have an average absolute error varying

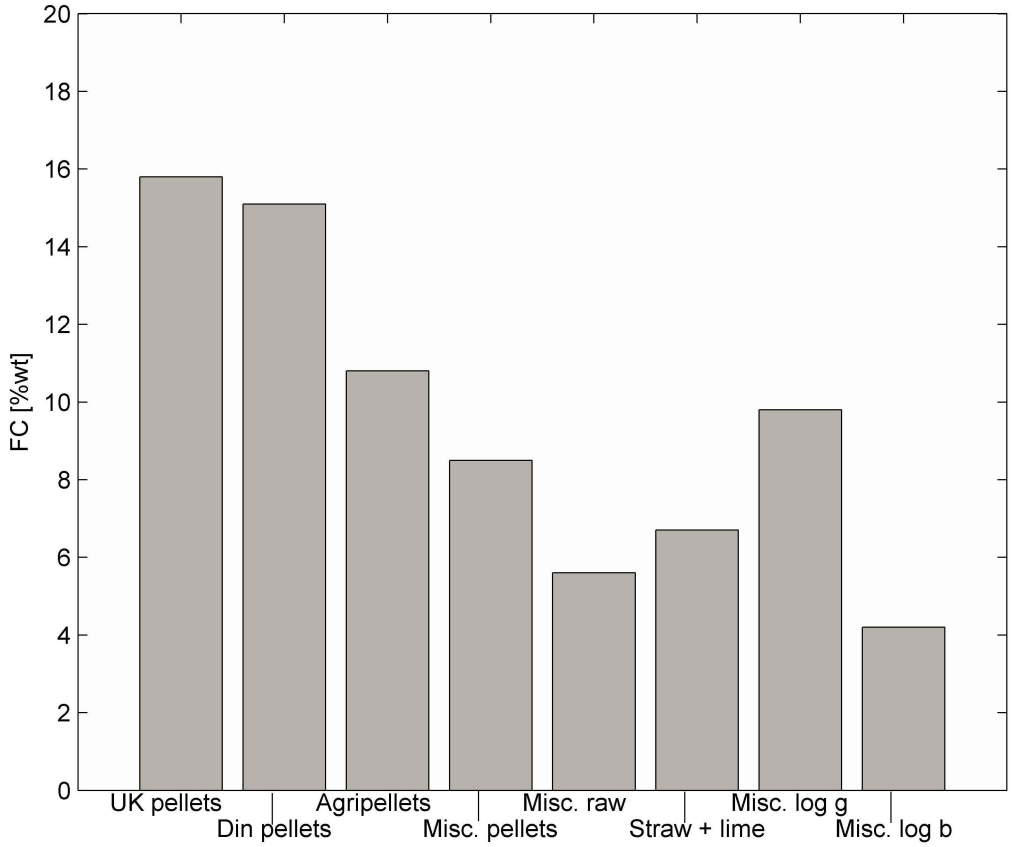

Figure 6.8: Fixed carbon content for the different fuel samples

from 5.13% – 11.9%. The correlation of HHV with ash, presented in this study has an average absolute error of 1.06%; and the one with the volatile matter and fixed carbon content has an average absolute error of 0.68%. Thus these two correlations are validated for solid biofuels with similar properties.

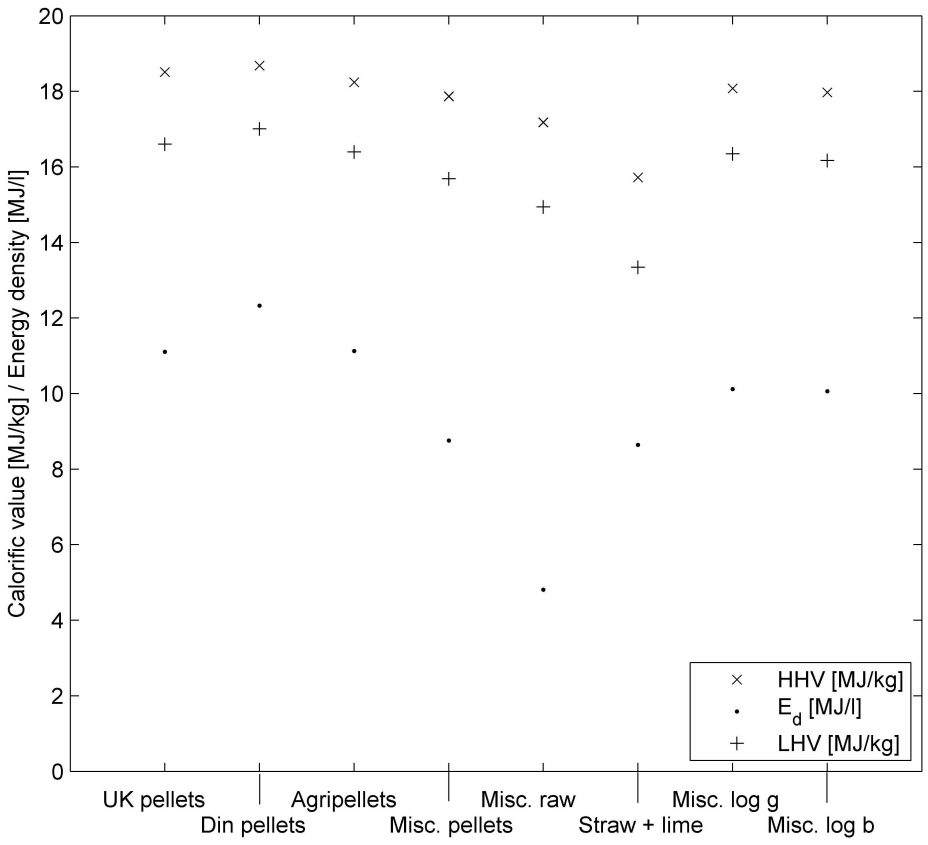

Figure 6.9: Energy content for the different fuel samples

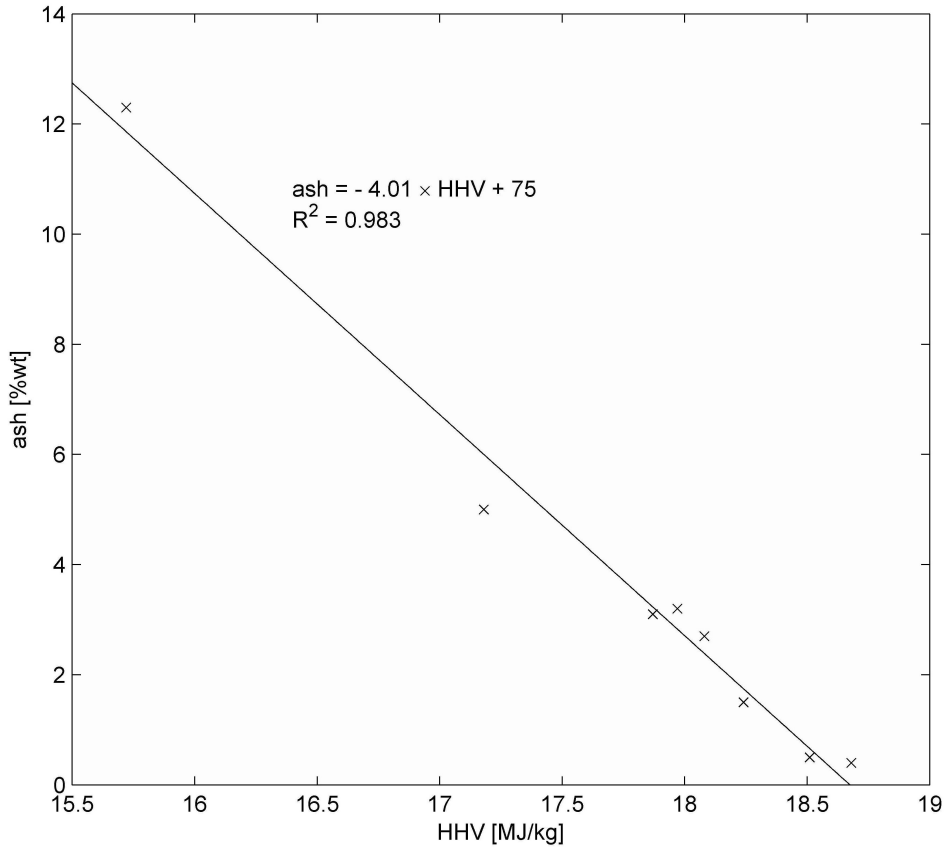

Figure 6.10: Ash content vs. higher heating value for the different fuel samples

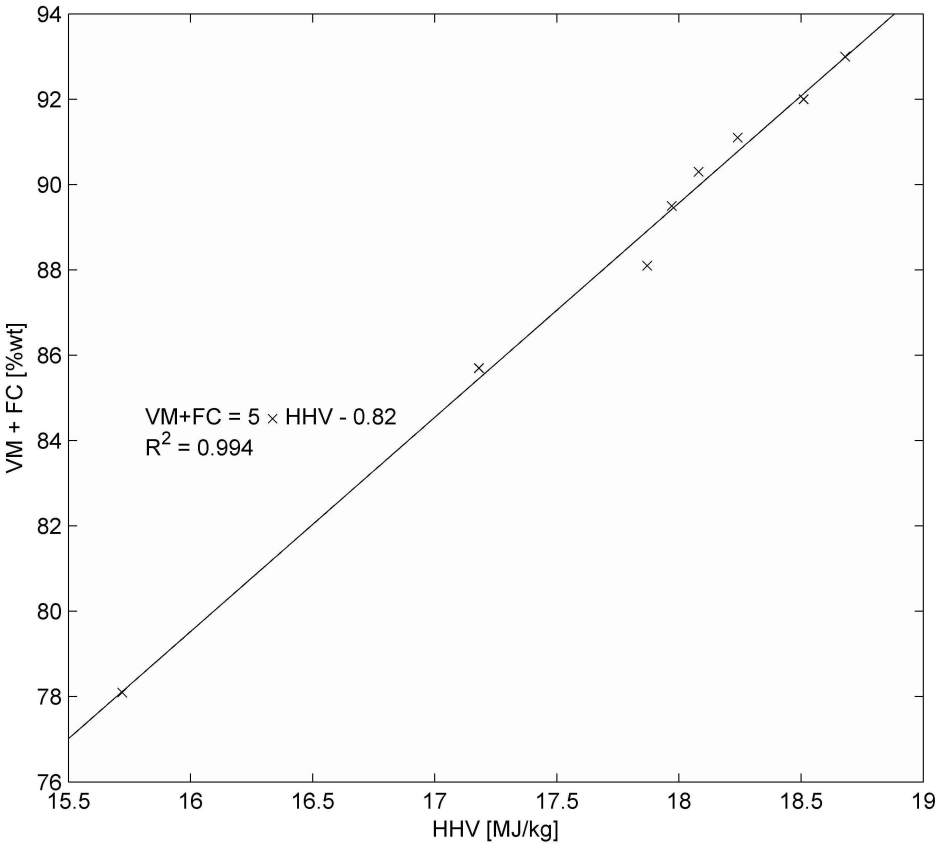

Figure 6.11: Volatile matter and fixed carbon vs. HHV for the different fuel samples

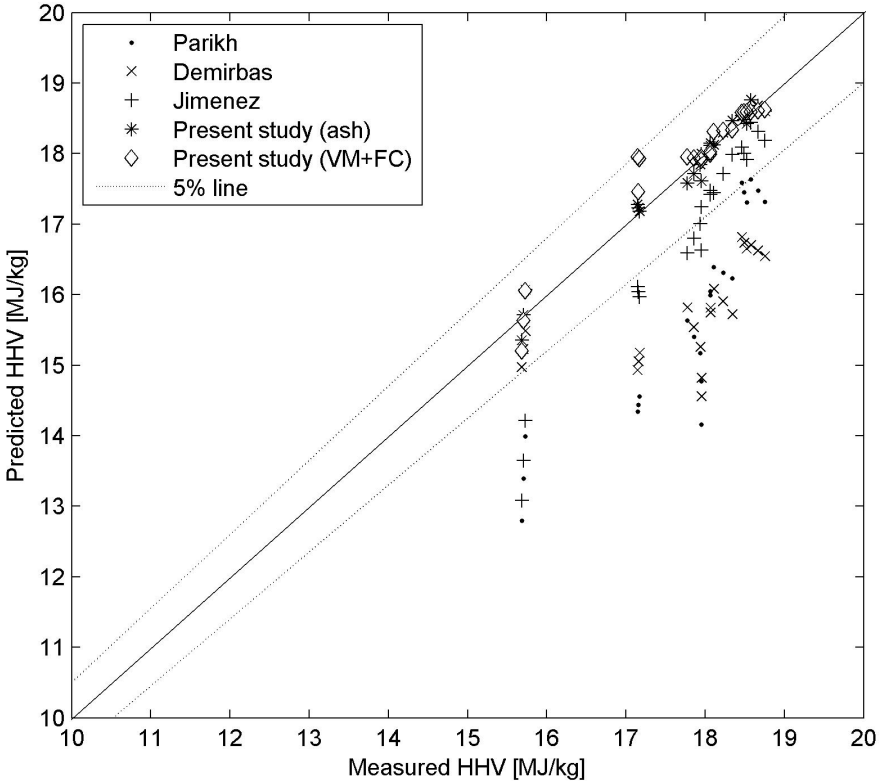

Figure 6.12: Accuracy of measured and correlated HHV

6.2.2 Performance Evaluation of the Biomass Boiler

A series of tests were conducted to evaluate the biomass boiler as a conventional domestic hot water system. The planned tests are outlined in the previous chapter and the final test results are presented in Figs. 6.13 – 6.17.

Figure 6.13 shows the net heat input (Q_{in}) for different Reynolds number in comparison with the net output (Q_{wa}) and the exhaust heat (Q_{ex}). The inlet heat to the system varies between 22kW and 24kW. This is influenced by the fuel regulation which was controlled to prevent a boiling of the water. This gives a constant fuel input for all tests. The net heat output in the water peaks at a Reynolds number of 38,000, before it starts dropping again. This should be reflected in a maximum efficiency at this Reynolds number. The measured heat left in the exhaust is constant at around 2 kW. Although this seems reasonably low (only 8% of the heat input), there is another average unaccounted loss of 15 kW (60% of the heat input). There are indeed numerous amounts of leaks, and although the majority had been sealed, the fan provided by the manufacturer appeared to be too powerful for the system. This resulted in too much air being introduced into the system between the combustor and the boiler, a flight path of almost two meters and thus causing too much cooling to the combustion gases. Figure 6.14 shows the variation of specific fuel consumption with Reynolds number. The specific fuel consumption is based on the net useful heat output and since the overall consumption of fuel was kept reasonably constant, it can indeed be observed that the SFC is at its lowest for a Reynolds of 38000. The average specific fuel consumption is approximately 0.7 kg/kW. According to manufacturers claims this value varies between 0.3-2.4 kg/kW with a heat output varying between 5 kW and 40 kW per operating hour. The results for SFC can be combined with the fuel consumption to determine the heat output per hour for the test series. Figure 6.15 shows the fuel consumption for different tests in comparison with Reynolds numbers. The average fuel consumption for the different tests is approximately 6.5 kg/hr, resulting in a net heat output of 9.3 kW. This is relatively low in comparison to the stated manufacturer's output possibilities of 40 kW. Figure 6.16 shows the variation of the thermal efficiency for single generation of domestic hot water for various Reynolds numbers. As

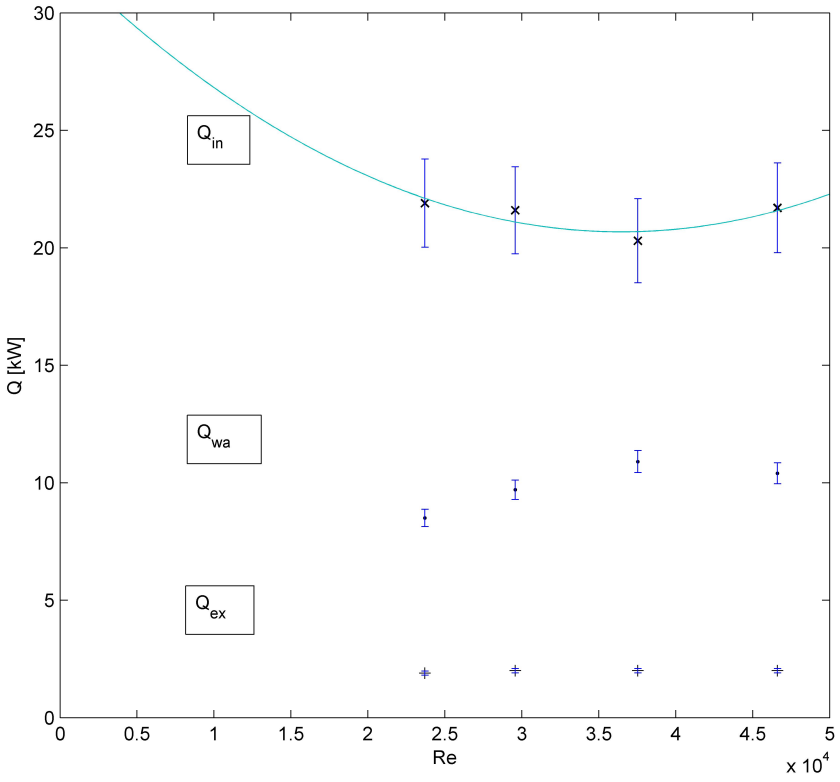

Figure 6.13: Comparison of inlet and outlet heat

mentioned previously, the thermal efficiency peaks around a value of 38000 for Reynolds number. The average thermal efficiency varies between 30% and 45% for all tests. Reducing the number of leaks and improving the control of the combustion fan could raise the net heat output and thus increase the thermal efficiency. Additionally, an increased demand of hot water should provide potential to increase the thermal efficiency. Figure 6.17 shows the net heat output for single generation of hot domestic water for different Reynolds number. The error bars represent the total errors (U_{ADD}) of $\pm 4.97\%$, determined by the error analysis outlined in the previous chapter.

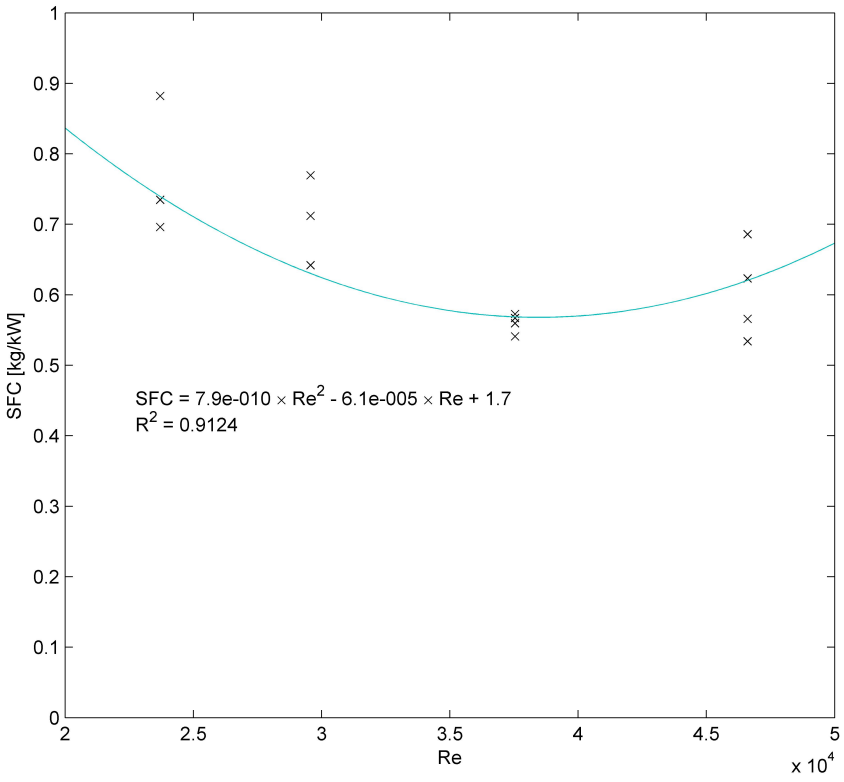

Figure 6.14: Comparison of specific fuel consumption

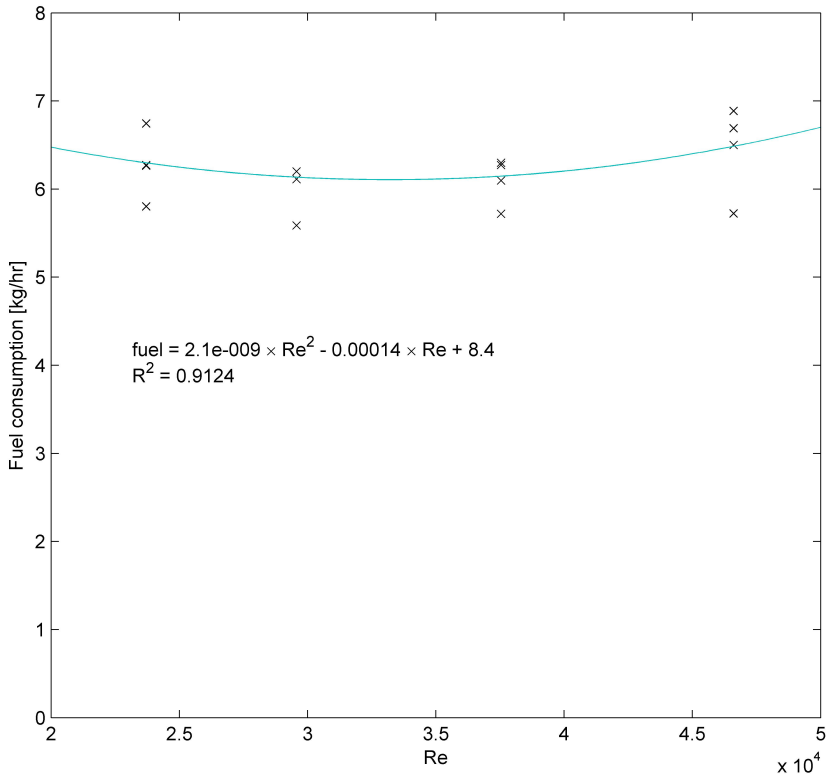

Figure 6.15: Comparison of fuel consumption

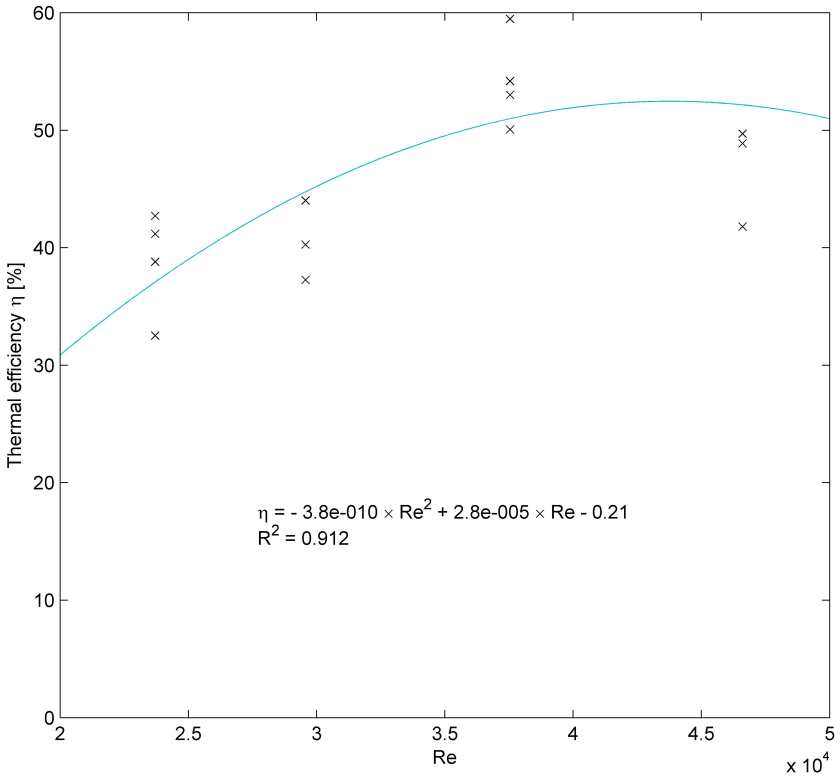

Figure 6.16: Comparison of thermal efficiency for single generation of *DHW*

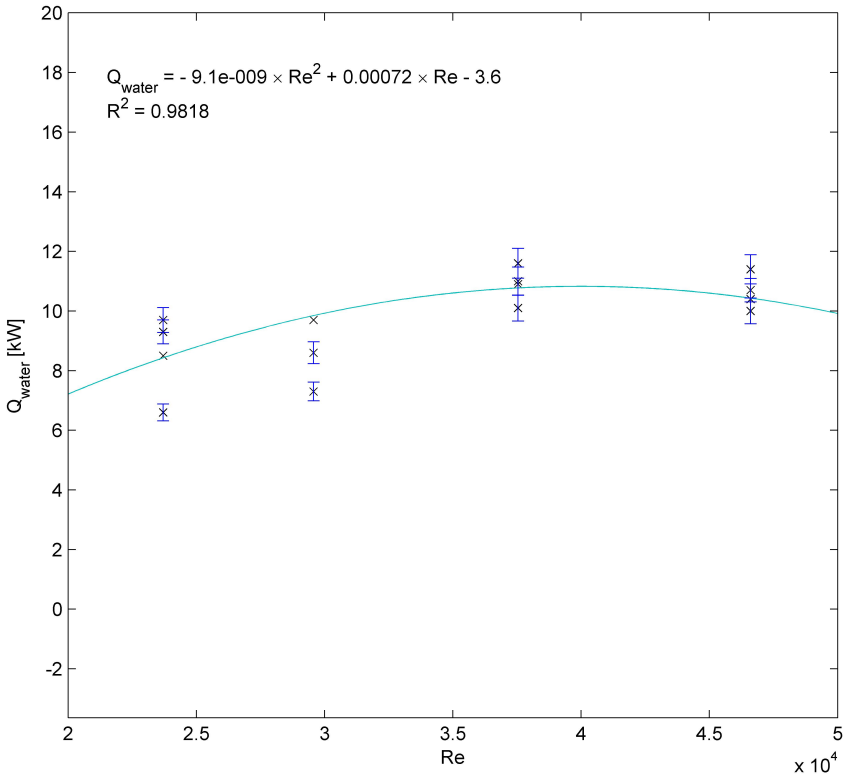

Figure 6.17: Comparison of net heat output

6.2.3 Emissions for Single Generation of DHW

The emissions from the combustion of different biomass are presented in Figs. 6.18 – 6.22. All results are plotted against the net useful energy output and are presented for the Miscanthus pellets and logs as well as for the straw/lime pellets.

Figure 6.18 shows the emissions of carbon dioxide for different straw and Miscanthus pellets and logs measured during single generation of hot water. The results are plotted in grams per net kWh energy output. The error bars indicate the determined U_{rss} error for the CO_2 emission equipment. It can be observed that there is a decrease in CO_2 emission with increased energy output. The dotted lines indicate the estimated values by the model developed in chapter four. The results compare well for Miscanthus and are within 12% of the average measured value (within 7% of the maximum error). The logs of Miscanthus show a higher emission of CO_2 than the pellets. Additionally, as mentioned before, the types of biomass analysed are carbon neutral as the CO_2 released during the combustion will be used to grow new biomass in a relatively short time-period. Referring to Fig. 6.4, it can be observed that a higher content of fixed carbon will lead to a comparatively higher output of CO_2. Figure 6.19 presents the emissions of carbon monoxide for Miscanthus pellets and logs as well as straw pellets for single generation of hot water. The logs have a lower emission of CO compared to the pellets. The emissions are presented in milligram per MJ net energy output and thus reduce with increased net output. The error bars are based on the U_{rss} value determined for the carbon monoxide analyser. The results are compared to a study (EMEP) conducted by Hobson & Thistlethwaite (2003) as part of the emission factor program task 7. Overall the emission are lower than observed by this study which combines average (av.) with lower (l.) and higher (h.) confidence levels for emissions in Europe for residential biomass combustion units. Figure 6.20 shows the emission of nitric oxide for Miscanthus pellets and logs as well as straw pellets for single generation of domestic hot water. The results are presented in milligrams per MJ of net energy output. It can be observed that the emissions reduce with increased output and that the straw has higher NO_x emissions than the Miscanthus. As matter of fact the straw did produce a higher flame temperature which should result in a higher

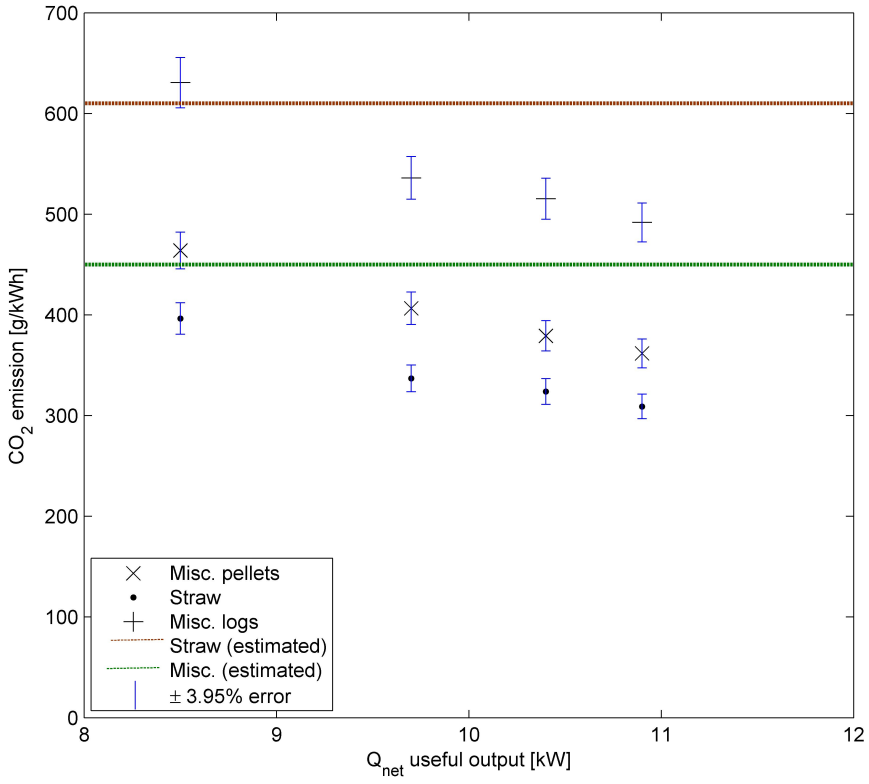

Figure 6.18: Emissions of CO_2 for different fuels against net energy output

NO_x formation, which was also reported in numerous other studies. The emission of NO_x is compared to EMEP data and it can be shown that straw resulted in a higher output than the average published data, although the Miscanthus was within the maximum value (8% for average measured values). From the fuels analysed in this study, it can be observed that the calorific value is indirectly proportional to the emissions of NO_x. Figure 6.21 shows the emissions of hexane for Miscanthus logs and pellets as well as straw pellets for single generation of hot domestic water only. The emissions decrease with increased net energy output similar to the other pollutants. The logs emit almost three times as much as the pellets. Referring to Fig. 6.4, it can be observed that a higher content of fixed carbon will lead to a comparatively higher output of hexane. Figure 6.22 shows

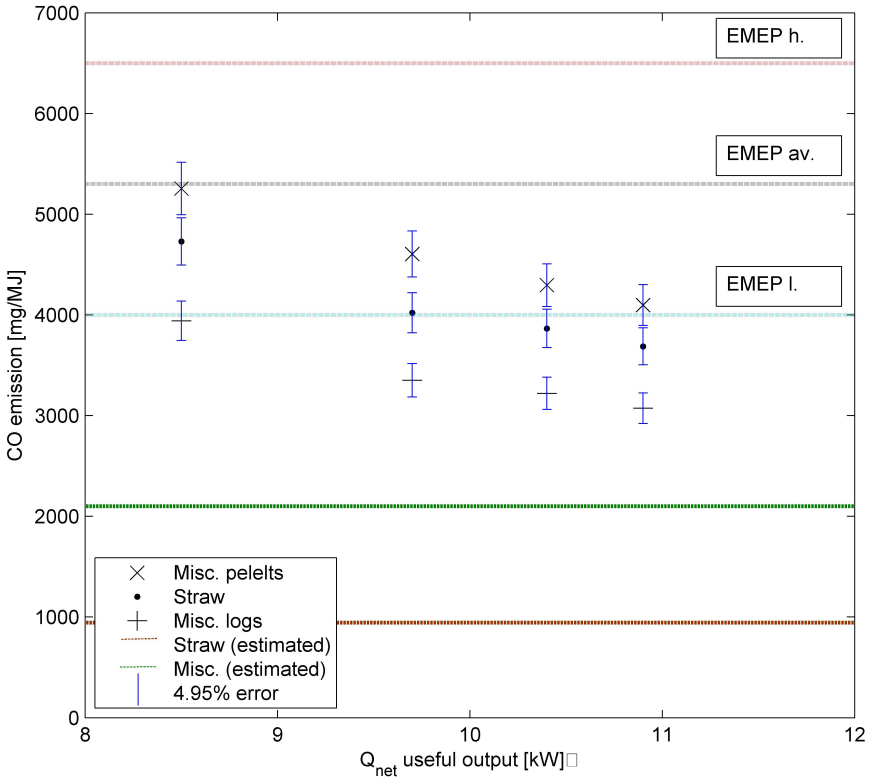

Figure 6.19: Emissions of CO for different fuels against net energy output

the particulate emissions for Miscanthus logs and pellets as well as straw pellets. As for the other pollutants the emissions decrease with increased energy output. The limits shown on the graph are taken from Caserini *et al.* (2010) who compiled average emissions of PM_{10} particulates for various burning units. Although the emissions for the pellets are well within the average reported values, the emissions for the logs are considerably lower than the reported ones. Obviously the boiler used in this study is different in its layout from conventional log burners and there is a considerable flight path through the unit before the installation of the measuring device, which will cause a decrease in fly-ash and smoke. Additionally, the logs used are not conventional wood logs but are pressed Miscanthus logs, as shown on Fig. 6.3.

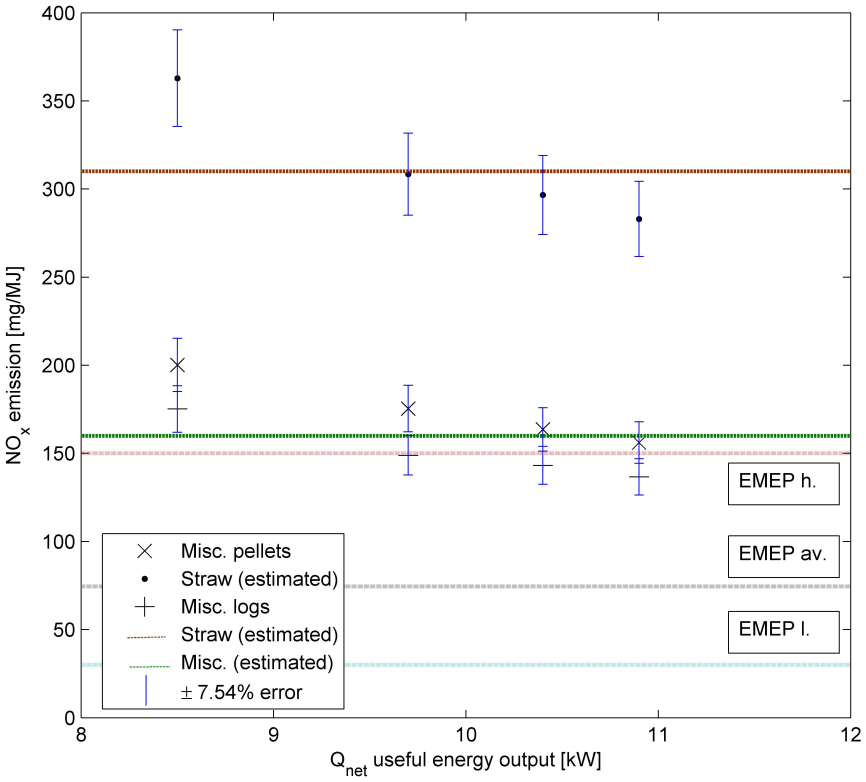

Figure 6.20: Emissions of NO_x for different fuels against net energy output

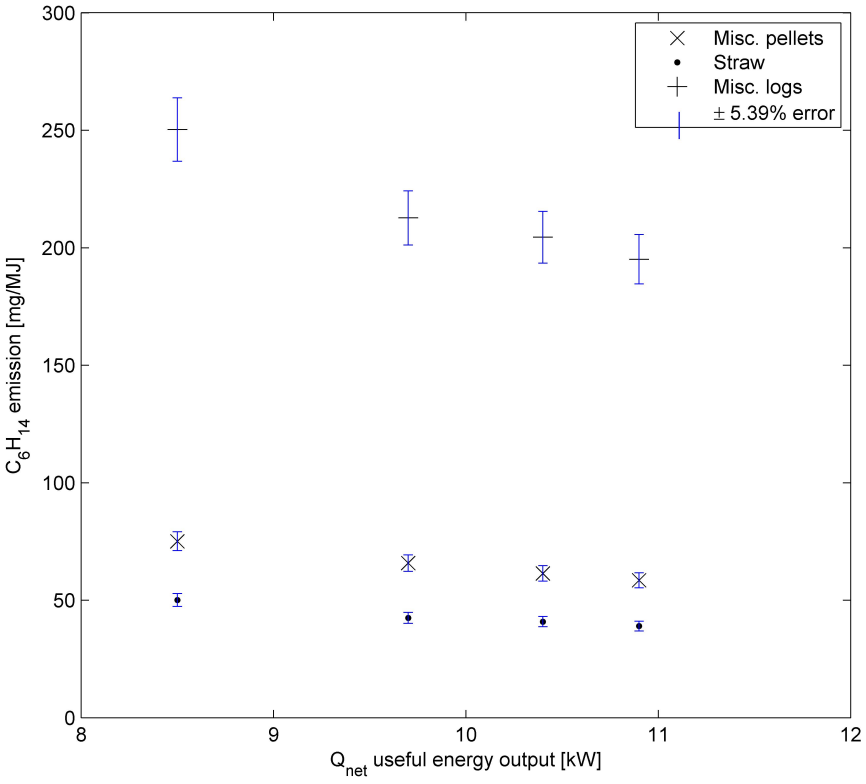

Figure 6.21: Emissions of C_6H_{14} for different fuels against net energy output

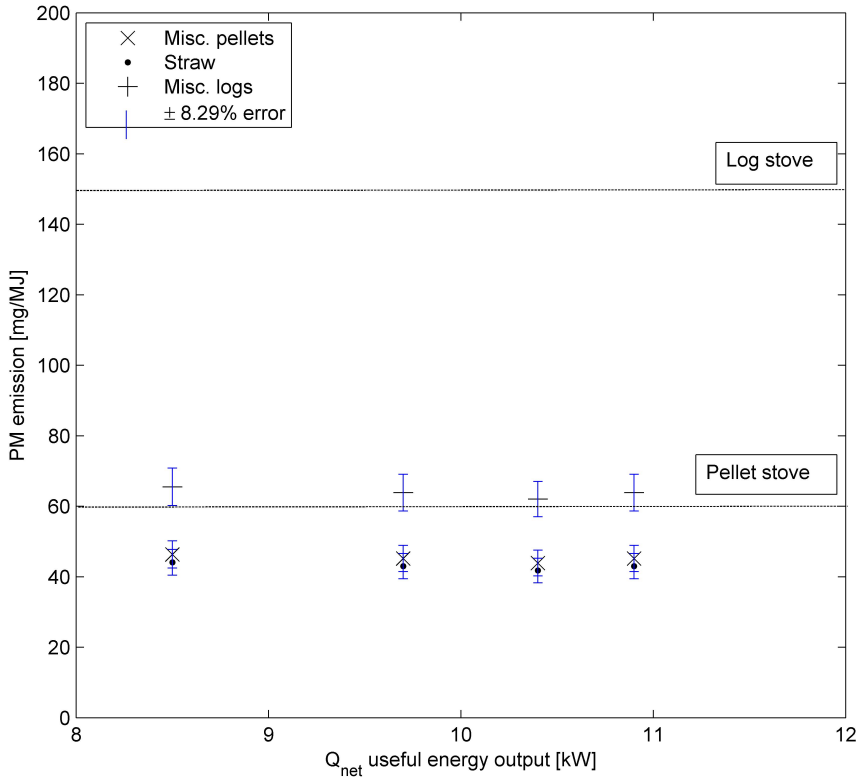

Figure 6.22: Particulate emissions for different fuels against net energy output

6.3 Stirling Engine Performance Analysis

Several simulations of the working behaviour of the Stirling engine are carried out with different working gases at different nominal charge pressures. The tests of the actual built machine are limited due to the laboratory layout. It is indeed not possible to account for the cooling water required when connected to the three phase connection to the generator. It was thus decided to run the engine as a cooler, by means of running the crankcase of the generator at different speeds and charge pressures. This will result in the reverse Stirling cycle process and the 'heater' tubes will act as a cooler.

6.3.1 The Effect of Changing Gas and the Pressure

The computer model developed in chapter four is used here to determine the effect of changing the nominal charge pressure as well as the working gas inside the engine. Three different gases will be used: Helium, Hydrogen and atmospheric air. The charge pressures will be varied from zero bar to 15 *bar* in increments of 2.5 *bar*.

Figure 4.17 shows the variation of the compression, expansion and total volume as a function of the crank angle. The compression volume reaches its maximum value when the cycle has not yet begun, because the flow direction of the working gas has been arbitrarily set to flow from the compression space to the expansion space. From the compression space the working gas is pumped through the cooler, the regenerator and the heater to the expansion space. After the gas has fully expanded in the expansion space, the gas flows back to the compression space. Figure 6.23 shows the variation of the working gas temperature in the expansion, compression space and regenerator as well as the heater and cooler temperature as a function of the crank angle. The temperature within the compression and expansion space increases due to the decreasing total volume before the volume starts to increase again. As the volume increases, the cooling occurs due to the expansion of the gas and the temperature in the compression and expansion spaces decrease. The pressure for the individual cells of the engine shows very little differences, which reflects the assumptions made for the pressure equation Eq.(3.49). Figure 6.24 shows the P–V diagram for the expansion

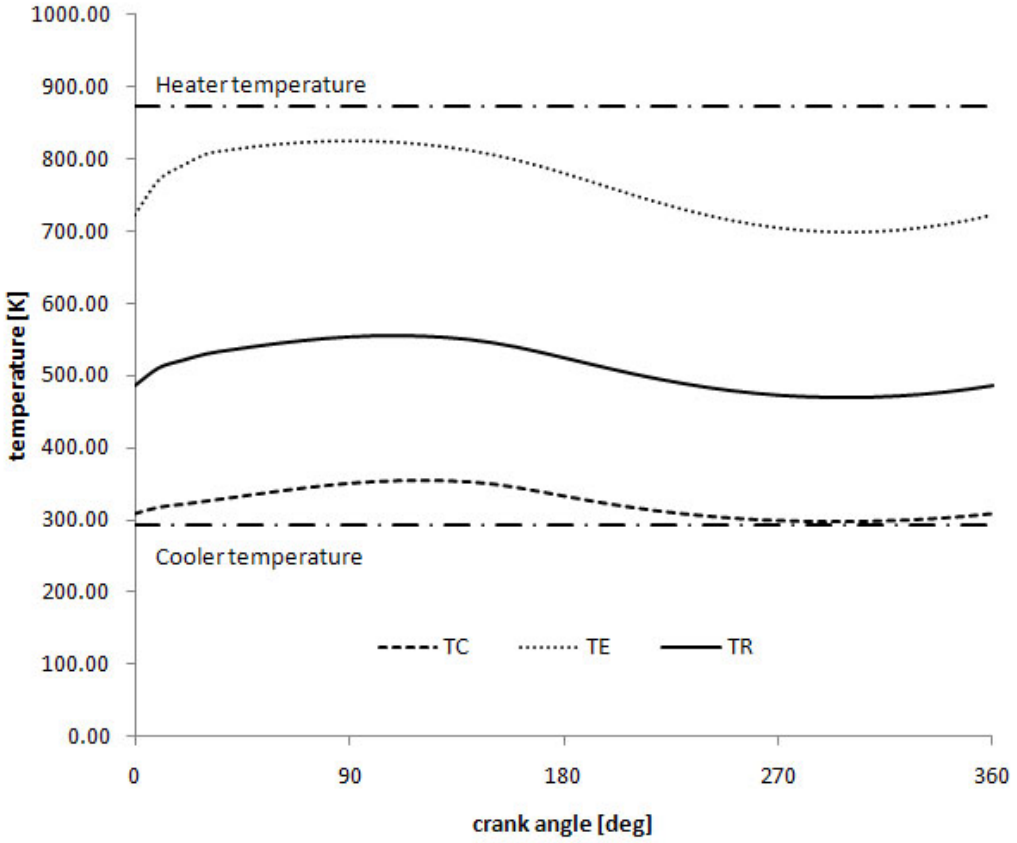

Figure 6.23: Temperature variations as a function of crank angle

and compression spaces for air, Hydrogen and Helium at 10 *bar* charge pressure. As the pressures are identical across the engine (for each cycle step), the actual pressure in the expansion space is equal to the sum of pressure in the compression space and the pressure losses due to pumping friction. The shape of the graphs are very similar for the three different working gases and since the work output is the mathematical integral of this graphical shape, there should be little difference between the work output for the different gases at equal charge pressure. Figure 6.25 shows the pressure drop for the three heat exchangers for air and Hydrogen at 10 *bar* nominal pressure charge as a function of crank angle. The pressure drops are shown with positive values for comparison, although the numerical values are negative for crank angles ranging from 140° to 330°. The negative or positive

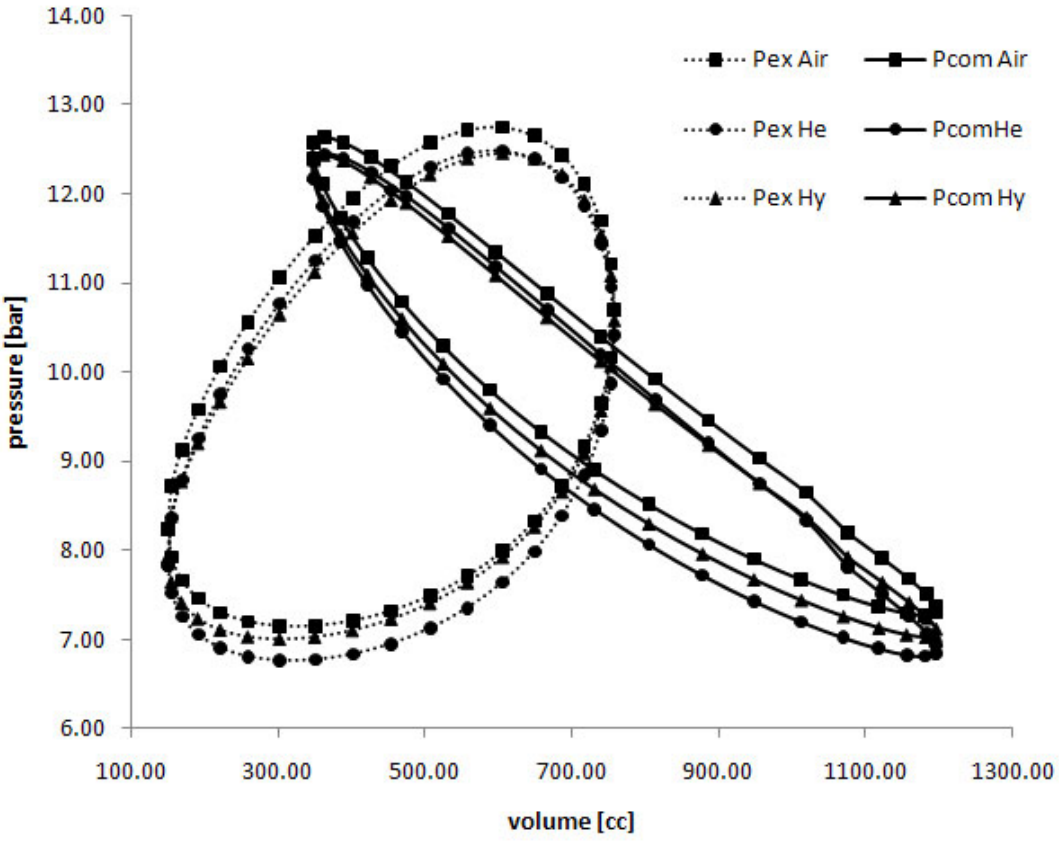

Figure 6.24: P–V diagram at 10 *bar* charge pressure

sign of the value of the pressure drops are relating to the direction of flow of the working gas. From the graph it can be observed that the pressure drop for air is of a higher magnitude than the one for Hydrogen. The calculations showed that the pressure drop for Helium was slightly higher than the one for Hydrogen and would overcrowd the graph. This shows that there is more work required to push the air around the engine than the other two working gases. For each of the three working gases the highest pressure drop is noticed in the regenerator with the lowest pressure drop in the cooler as the pressure drop is directly proportional to the Reynolds friction factor. Figure 6.26 shows the variation of the total mass of working gas as a function of the nominal charge pressure for all three working gases. Considerable differences can be noted with a total mass of air of 16.05 g

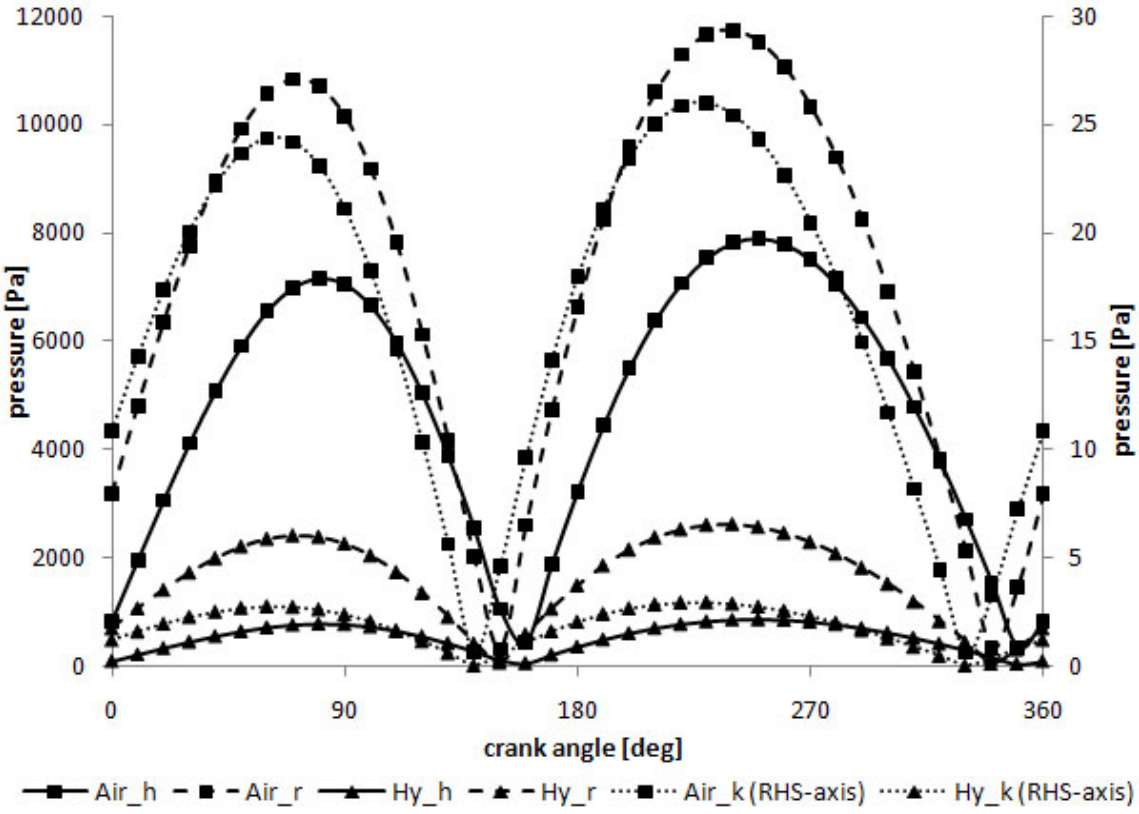

Figure 6.25: Pressure drop in the heat exchangers at 10 *bar*

(10 *bar*) in comparison to 2.22 g and 1.11 g for Helium and Hydrogen respectively. This is reflected on the amount of work required to push the gas around the engine, resulting in increased pressure drops for air compared to the other two gases. These differences in pressure drop for the different gases will have an impact on the actual work output and the efficiency of the engine. Figure 6.27 shows the variation of compression, expansion and total actual work output for air as a function of crank angle for 10 *bar*. The results show that there is an increase in work for increased pressure as expected. As the compression volume is decreasing, the work done by the compression space is of increasing negative magnitude as work is required to compress the gas. Similarly, as the expansion volume is increasing, the work done by the expansion space on the displacer is of

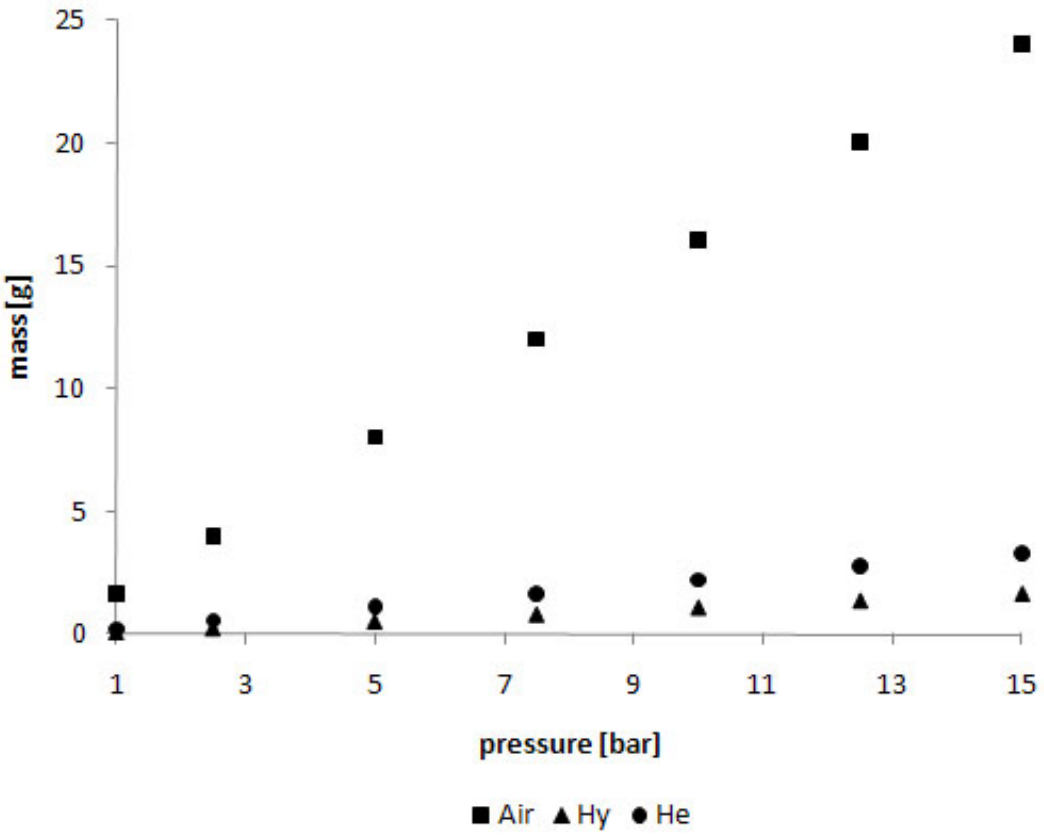

Figure 6.26: Total mass of working gas in the engine

increasing positive magnitude. At the end of the cycle, the values for W_e and W_c are equal to the values of heat transferred in the heater and cooler respectively.

Figure 6.28 shows the variation of thermal efficiency for all three working gases as a function of the nominal pressure charge. As expected, from the previous discussion points, there is a notable increase of thermal efficiency for increased nominal pressure charge. However, this difference becomes less significant above 7.5 *bar*. The difference in efficiency for air at 7.5 *bar* and 15 *bar* is less than 4% whereas the actual work output for the same pressure conditions is about 100%. This obviously reflects a higher heat input at 15 *bar* than at 7.5 *bar*. As a matter of fact the heat required is almost doubled. The engine was originally designed for a 10 *bar* nominal charge, which obviously shows a good work output

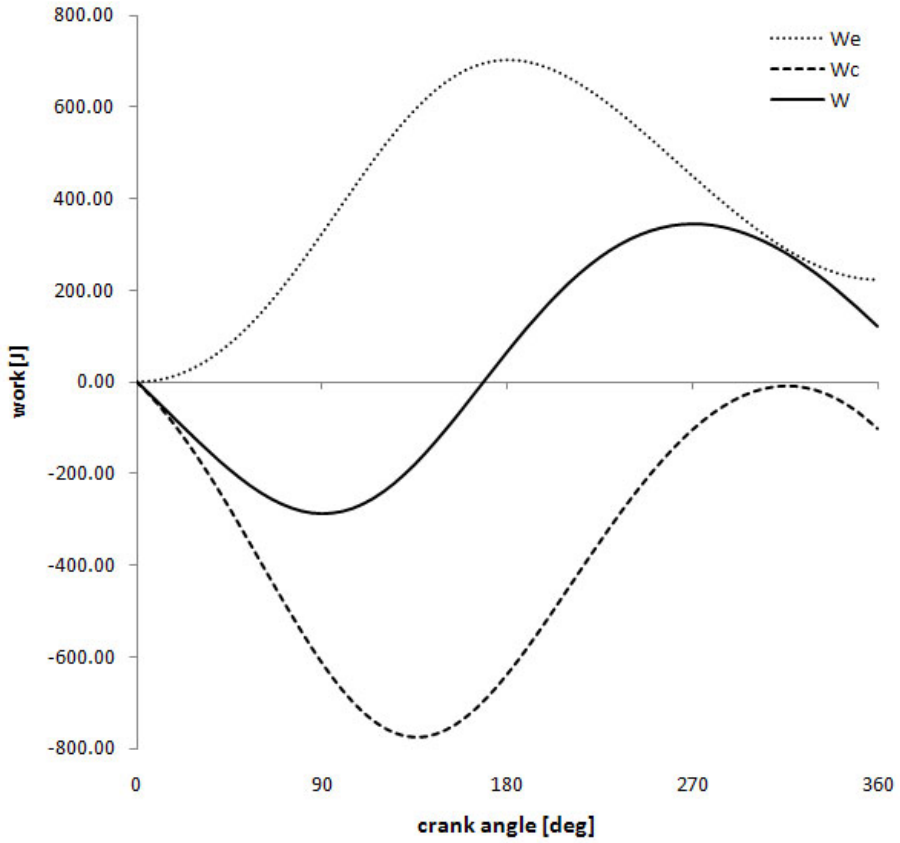

Figure 6.27: Actual work output for air at 10 *bar*

and efficiency. Increasing the pressure to 15 *bar* will increase the work output, however, it is not certain if the engine will actually be able to withstand those pressures from a stress related point of view.

6.3.2 The Stirling Engine as a Cooler

The Stirling engine was used in a Leroy-Somer test bench. This setup was used as the engine crankcase had been adjusted during the design to fit the mounting rail available in the bench. The generator was used in a known break assembly to determine its torque parameter. Figure 6.29 shows the torque against current for the generator. These was necessary to determine the torque delivered to the engine crankshaft at know values of current. After all the connections to the

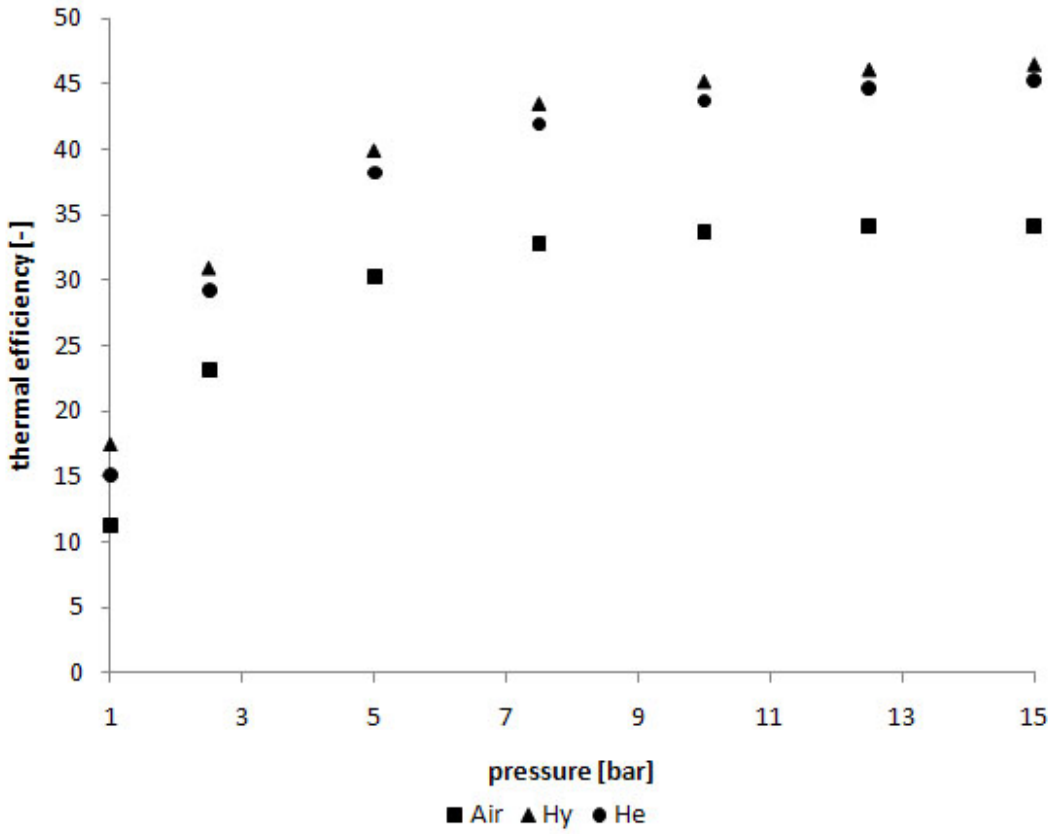

Figure 6.28: Comparison of thermal efficiency for all gases

generator were made, a Unidrive was used to run the engine at various speeds. Initially the engine was not pressurized and the pressure bypass valve was left open to allow the pistons to run free in the cylinders for a while. The pressure bypass valve was then closed and the engine speed was reduced to 150 rpm. Figure 6.30 shows the apparent power and the power of the generator. The temperatures at the heater bars reduced from ambient temperature of $30°C$ to $8°C$. Figure 6.31 shows a printout of the oscilloscope connected to an ampere-meter of the generator. This was used to keep an eye on a uniform power delivery to the generator and the engine. For the actual test the engine was pressurized and then left to run for a few minutes to get the generator up to temperature. Then the pressure bypass valve was closed and the engine started to work by dropping

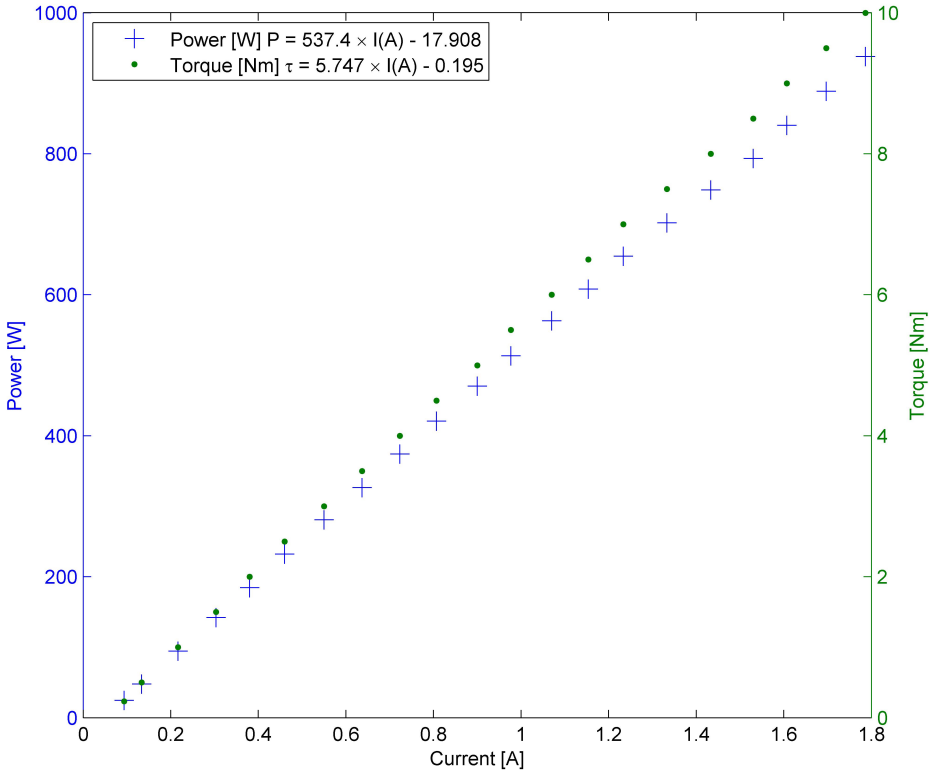

Figure 6.29: Torque and power calibration graph

the temperature at the heater tubes. Figure 6.32 shows a variation of the cooling temperature over a 15 minutes period. After this timeframe the temperatures became stable. There is an average temperature drop of $4°C$ when increasing the charge pressure to 2.5 *bar* compared to 0 *bar*. The inlet temperature to the heater drops a few degrees initially after that it becomes stable. Increasing the pressure further resulted in a lot of vibrations between the engine and the generator. Although numerous attempts were carried out to counteract the vibrations by means of installing dampers. Unfortunately it was not possible to reduce these vibrations to a satisfactory level and the piston kept jamming inside the cylinder.

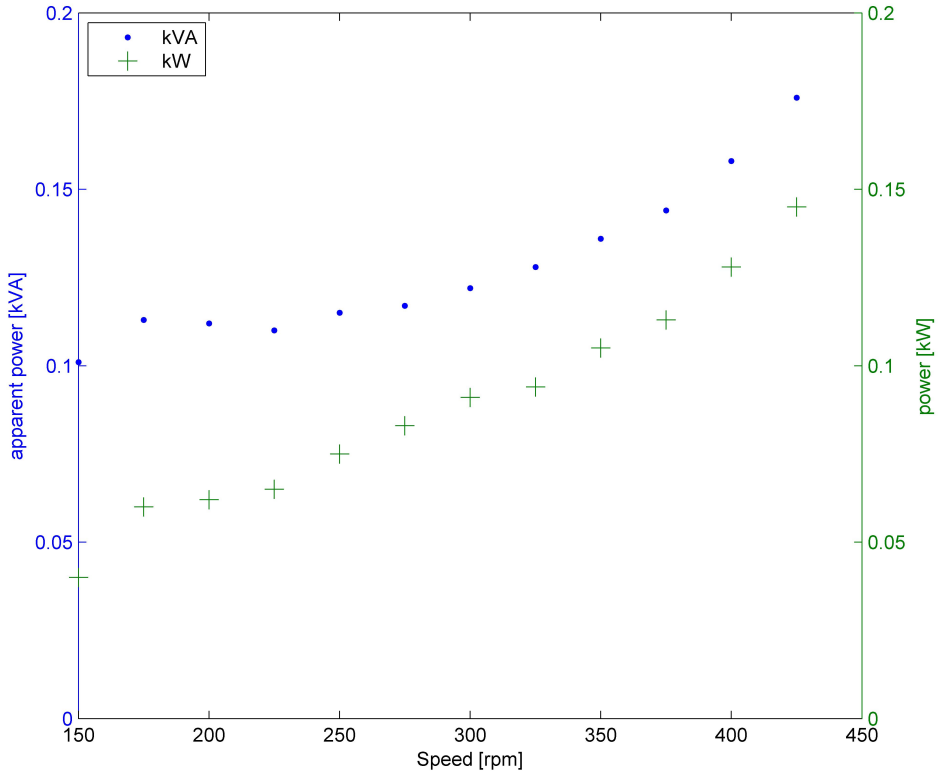

Figure 6.30: Apparent and true power at 0 *bar* pressure

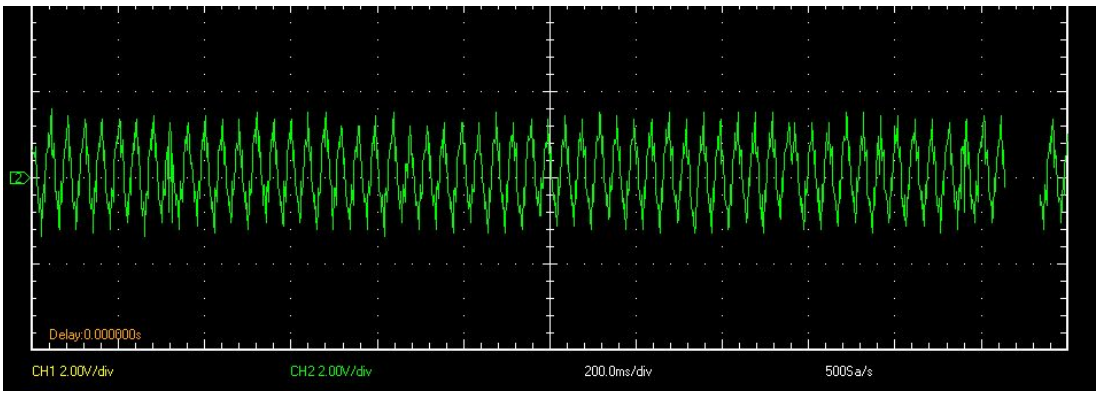

Figure 6.31: Oscilloscope screen shot for the ampere-meter

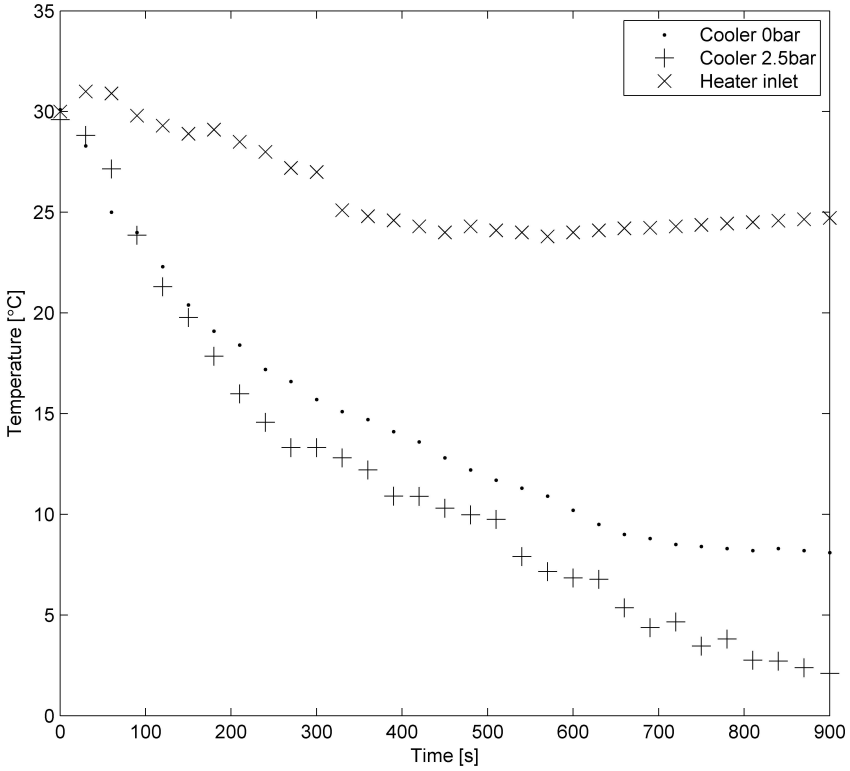

Figure 6.32: Variation of cooling temperature output of the Stirling engine

6.4 Absorption Cooling Performance Analysis

This section will present a discussion of the performance of the absorption unit when run as a cooling only or combined heating and cooling system. The emissions measured will be compared for the different modes under various heating loads. Additionally the model developed in chapter four will be used to estimate the COP for different inlet temperatures of the heat source, the cooling load and the heat sink.

6.4.1 Comparison of COP for Different Operating Conditions

For all the simulations the mass flow rates for all three circuits are kept constant, and it is assumed that a specific heat capacity for each circuit is satisfactory. Thus, only the changes in temperature will have an impact on the performance of the system. From the definition of the cooling COP, it can be deduced that an increased COP is due to either an increased cooling output with constant heat input or the rate of heat input is smaller than the rate of cooling output. Similar it can be said that a decrease in heat input will result in an increase cooling output, if the COP is increasing and a decrease in cooling output, if the COP is decreasing. Figures 6.33 – 6.37 show a comparison of cooling COP against heat source temperature for various cooling temperatures based on different heat sink temperatures. From a general point of view it can be seen that an increase in heat source temperature results in a higher COP while keeping the cooling temperature constant. The simulations are all run for heat load temperatures varying between $80°C$ and $110°C$. For the lower cooling temperatures ($18°C$–$22°C$) a high heat sink will not compute results for heat source temperatures below $95°C$. An additional data point for $102.5°C$ was added for the $30°C$ heat sink results. It has to be said that parameters outside these tested values are at not within the minimum working conditions of the unit and thus would not contribute to any useful discussion. Additionally, it can be seen that the COP is improved by reducing the heat sink inlet temperature. Figure 6.33, cooling temperature set to $18°C$, shows that lowering the heat sink inlet temperature

from $30°C$ to $20°C$, the cooling COP can be improved from 0.35 to 0.65. An important aspect for this study is that lowering the heat source temperature from $95°C$ to $85°C$ the same COP could be achieved. In the practical range for biomass hot water applications this gives a COP between 0.35 and 0.43. Figure

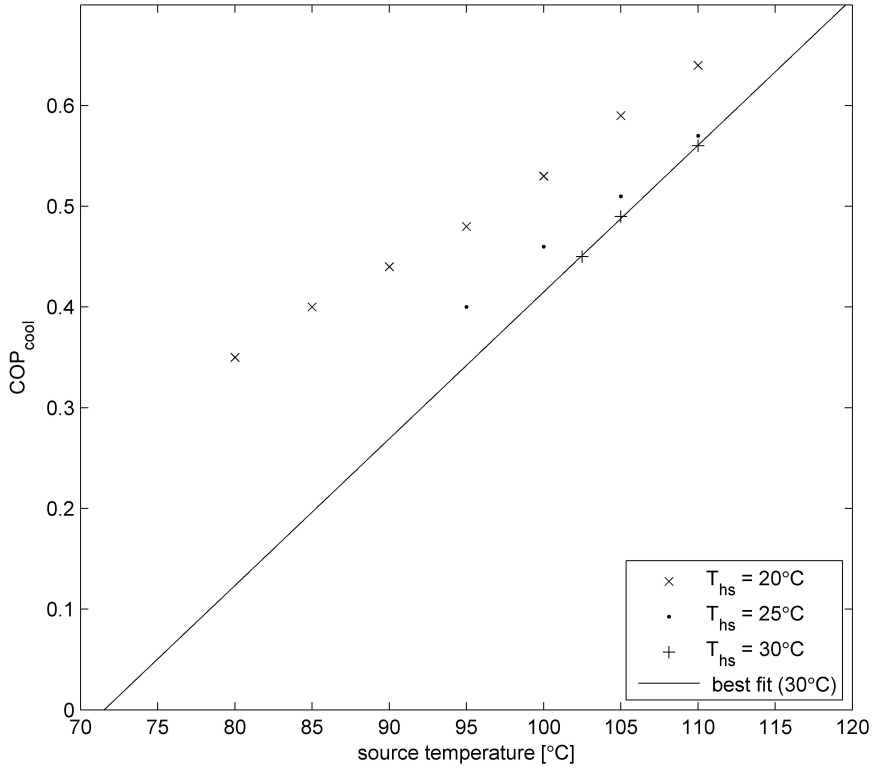

Figure 6.33: COP against heat source temperature for $18°C$ cooling temperature

6.34, cooling temperature set to $20°C$, shows that COP can be increased by approximately 0.1 by keeping the heat source and cooling temperatures constant and lowering the heat sink from $30°C$ to $20°C$. Depending on the heat sink temperature, the COP varies between 0.35 and 0.45 for heat source temperatures in the range of $80°C$ to $90°C$. Figure 6.35, cooling temperature set to $22°C$, shows that increasing the cooling temperature from $20°C$ to $22°C$, decreases the COP between 0.20 and 0.50, as expected by the definition of the cooling COP. Similar

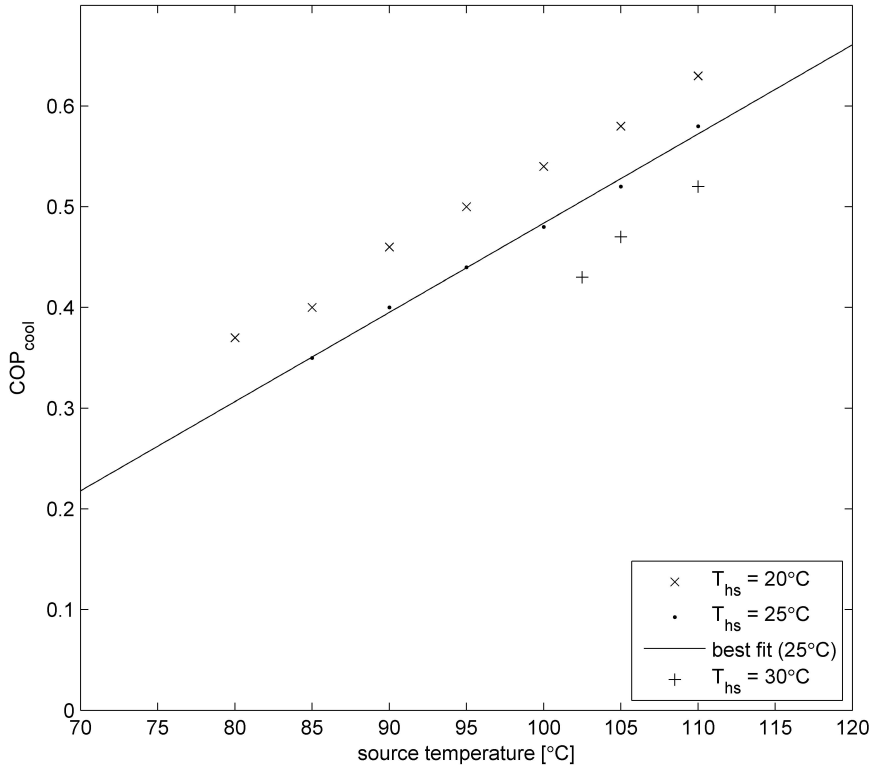

Figure 6.34: COP against heat source temperature for $20°C$ cooling temperature

as before lowering the heat source can be compensated by lowering the heat sink temperature as well. For heat source temperatures from $80°C$ to $90°C$ the COP varies between 0.30 and 0.43. Figure 6.36, cooling temperature set to $24°C$, shows similar behaviour as the previous figures. The COP for the targeted heat source range varies between 0.30 and 0.44. Figure 6.37, cooling temperature set to $26°C$, shows almost identical COP values as for a cooling temperature of $24°C$. This means that the rate of change for the cooling output is similar to the rate of change in heating input. Thus, there is no gained improvement by increasing the cooling temperature, nor decrease in improvement by an elevated cooling temperature depending on the climate region the system is installed in. Figure 6.38 shows the variation of cooling COP against cooling temperature for different heat source

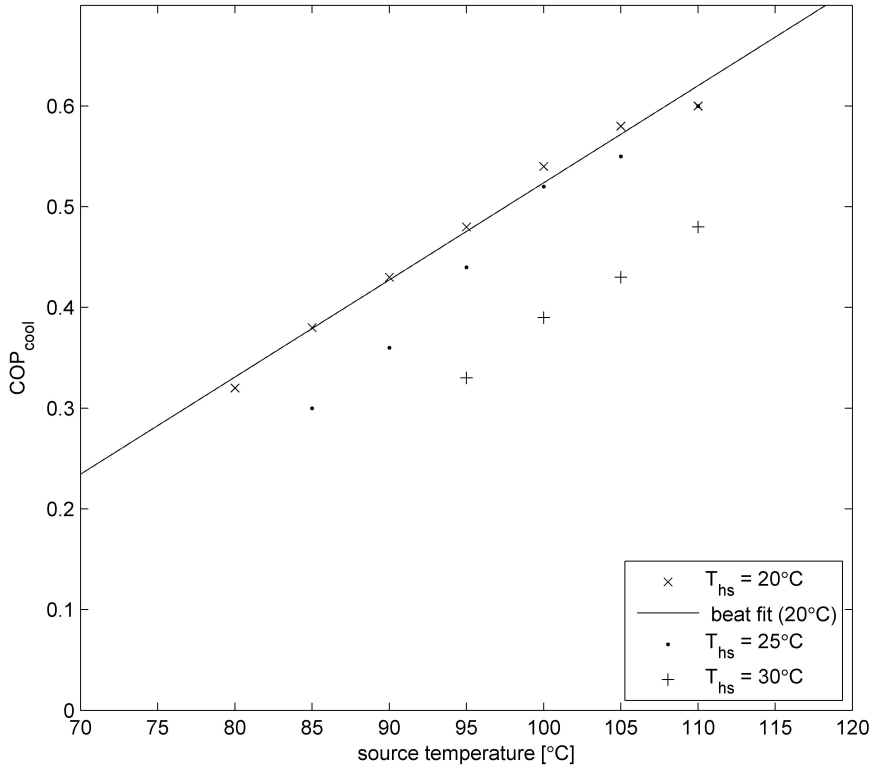

Figure 6.35: COP against heat source temperature for $22°C$ cooling temperature

temperatures while keeping the heat sink constant at $20°C$. It can be seen that for the lower region of the heat source temperatures there is a decrease in COP when increasing the cooling temperature above $22°C$. In the targeted heat source range ($80°C$ to $90°C$) the best COP should be achieved at cooling temperatures in the range of $18°C$ to $20°C$. The manufacturers actually recommend that the inlet cooling temperature should not exceed $21°C$ for reasons of performance. Figures 6.39 –6.40 show the variation of COP against heat source temperature, for a range of cooling load temperatures, for heat sink temperatures of $25°C$ and $30°C$, respectively. As mentioned before the lower heat sink temperature gives better results for COP and higher heat source temperature gives in return higher COP. Again, this shows that the target range of heat source temperatures for

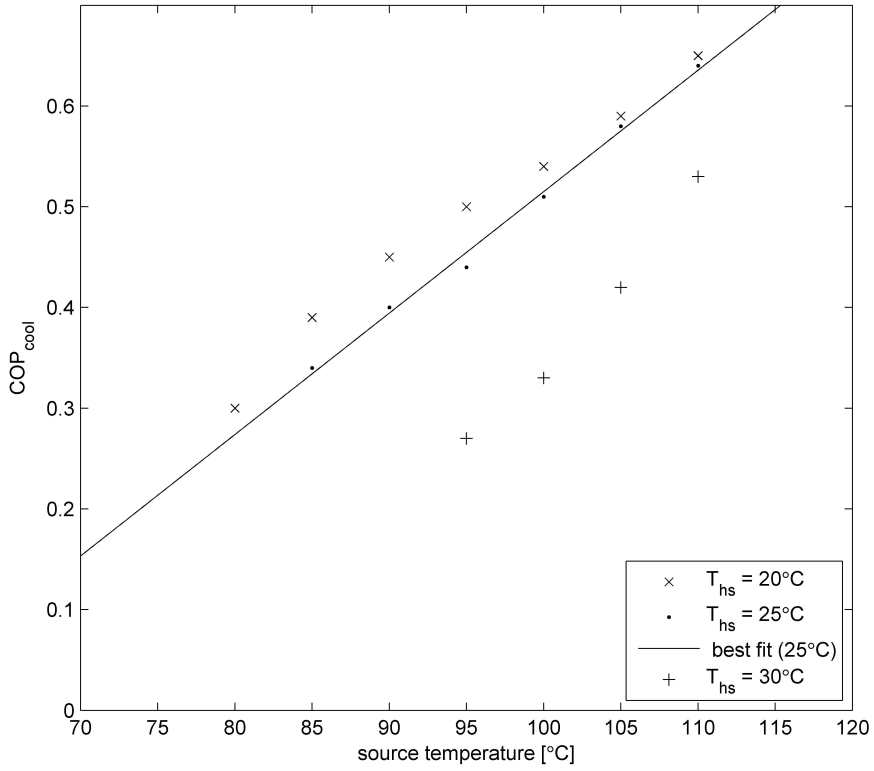

Figure 6.36: COP against heat source temperature for $24°C$ cooling temperature

biomass can be used, however there will be drop in COP.

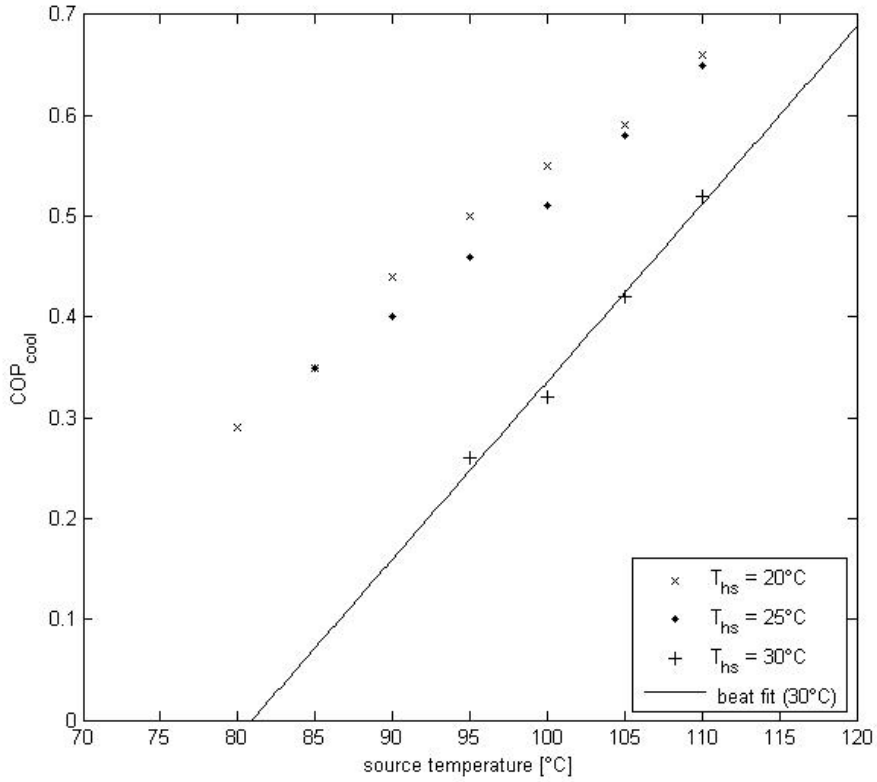

Figure 6.37: COP against heat source temperature for $26°C$ cooling temperature

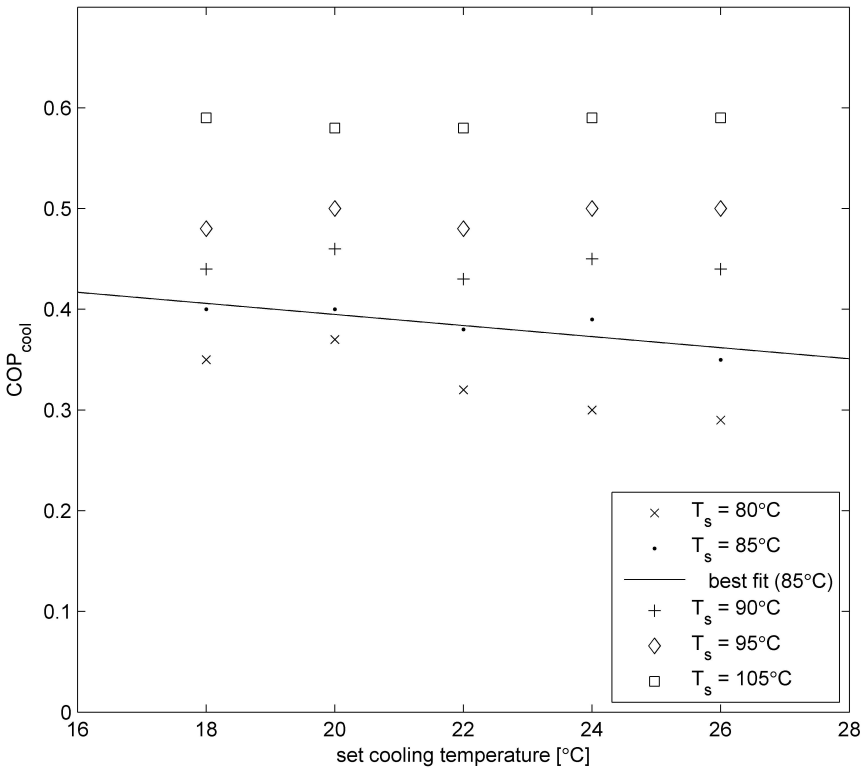

Figure 6.38: COP against cooling temperature for $20°C$ heat sink temperature

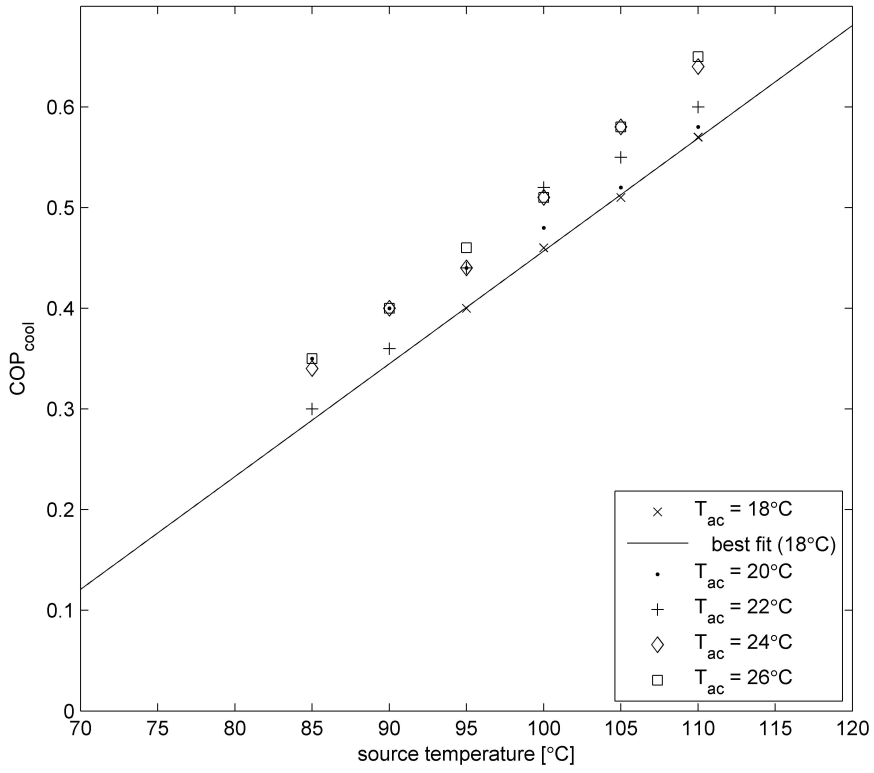

Figure 6.39: COP against heat source temperature for $25°C$ heat sink temp.

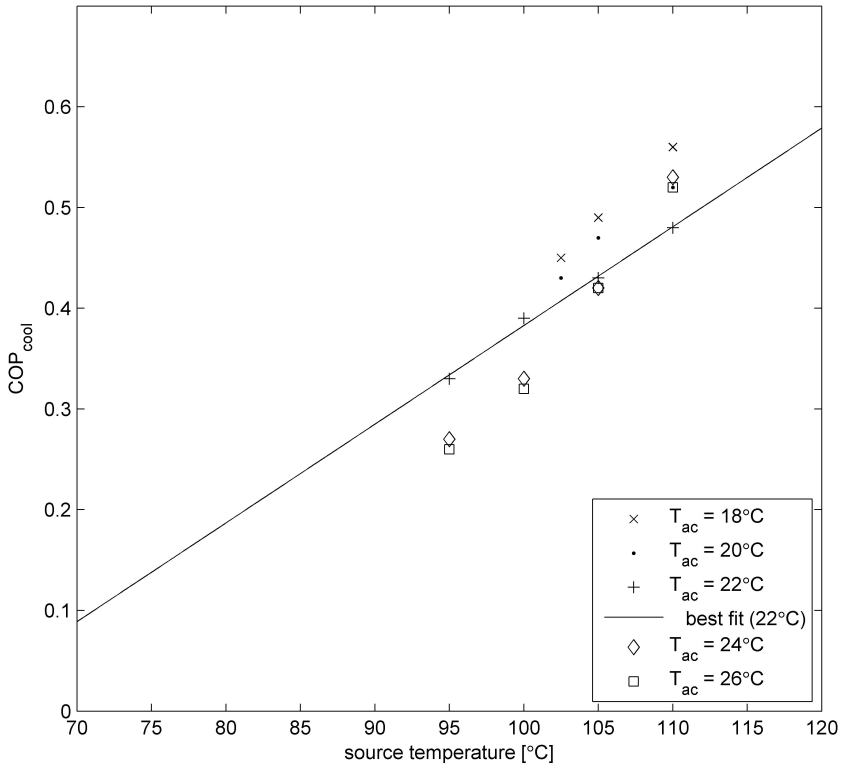

Figure 6.40: COP against heat source temperature for $30°C$ heat sink temp.

6.4.2 Single Generation of Cooling

A series of tests were conducted to evaluate the absorption unit in cooling mode only. The planned tests are outlined in the previous chapter and the final test results are presented in Figs. 6.41 – 6.43.

Figure 6.41 shows the variation of the cooling COP with different Reynolds numbers. These refer to the flow pattern in the heat source circuit and are set by

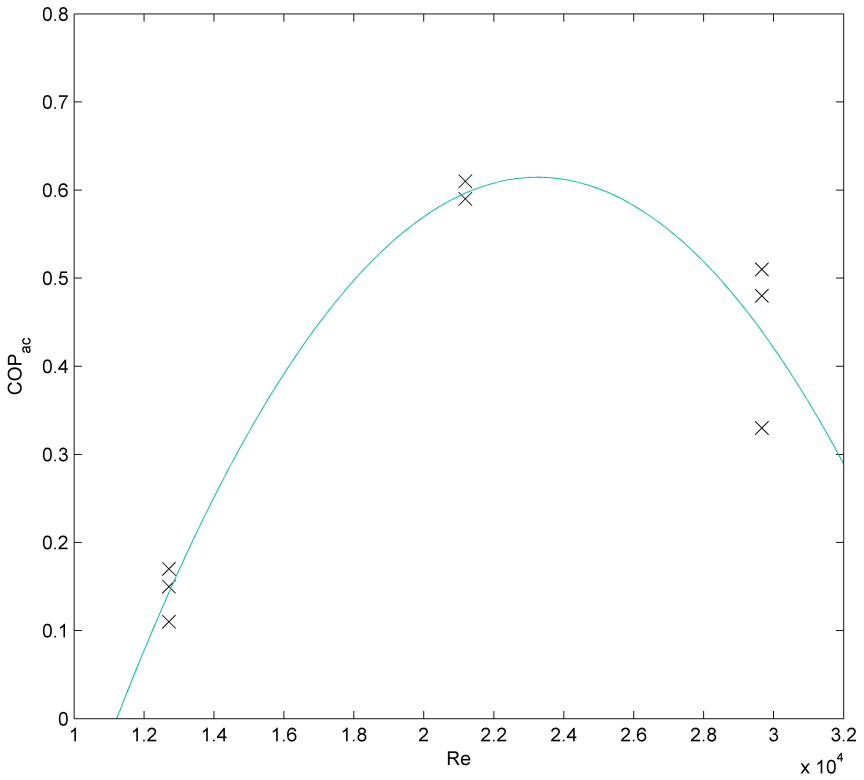

Figure 6.41: Cooling COP for different Reynolds numbers

the different pump settings. The cooling COP's used are based on average heat loads of the system. The highest cooling COP is measured for the middle region of the Reynolds numbers tested, roughly 21000. At the lower end of the flow spectrum, Q_s was indeed to low to charge the system in a constant manner. This resulted in a lot of opening and closing of the valves inside the unit as the system

will only open the valves once enough heat is available to charge the machine (assuming it is in charging mode). At the higher end of the flow spectrum, Q_s was too high to be absorbed entirely by the system. This resulted in a lot of heat being dumped to the heat sink of the system (this will be shown in the next section). The corresponding value of the cooling COP for the mid-level Reynolds numbers is slightly higher than expected from the computed values. This is influenced by the considerable lower heat sink temperature of 20° due to severe weather conditions in December 2010. Figure 6.42 shows the variation of the cooling COP with time. The graph also shows the variation of the cooling load temperature over the same time period, this indicates how the cooling COP increases with decreasing temperature. The initial rise at the first 5 minutes shows how the system stabilises until it gets to steady state conditions. Figure

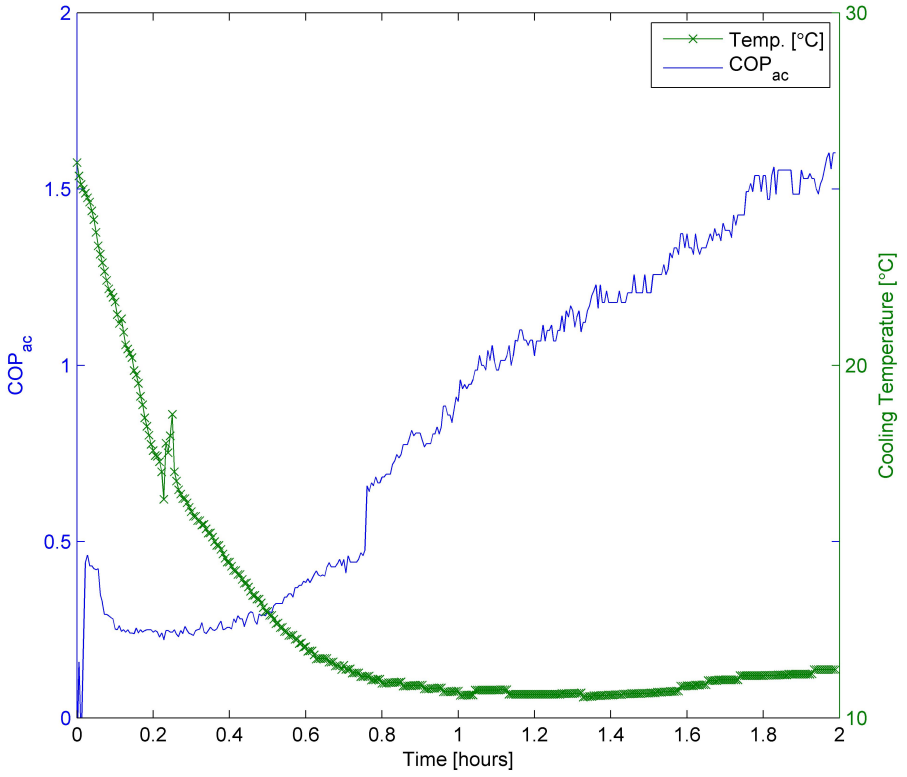

Figure 6.42: COP and cooling temperature against time

6.43 shows the variation of the cooling COP with time as well as the variation of the inlet temperature of the heat source. Since the cooling COP increases with increased heat source load, the cooling load must be increasing faster than the heat load. As mentioned before the cooling COP is the ratio of cooling load and heat source load.

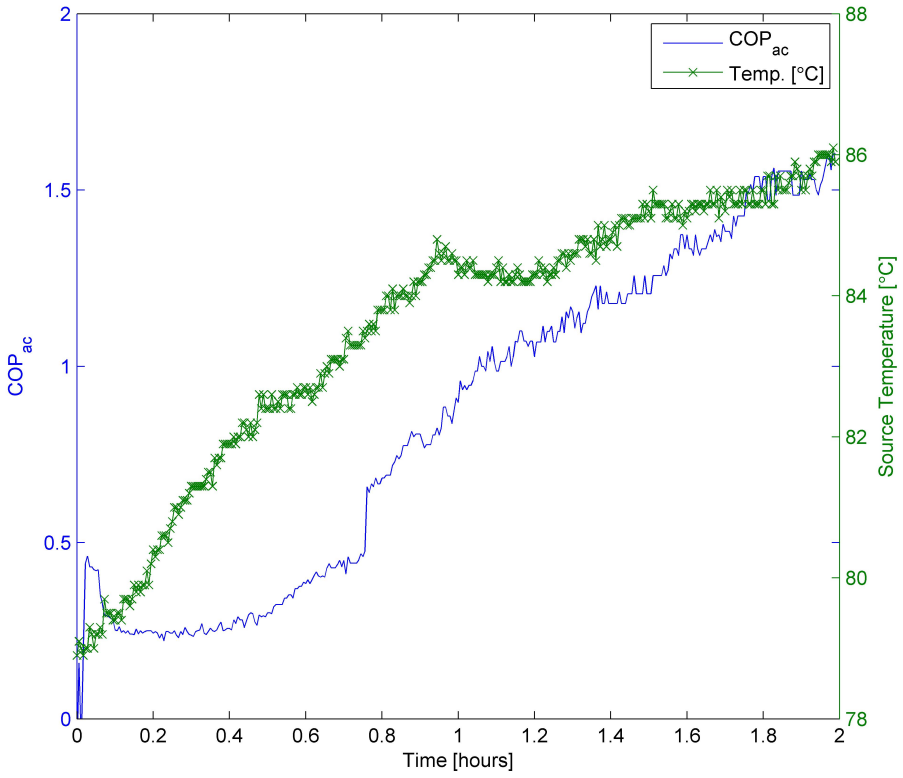

Figure 6.43: COP and heat source temperature against time

6.4.3 Combined Cooling and Heating

A series of tests were conducted to evaluate the absorption unit combined cooling and heating mode. The planned tests are outlined in the previous chapter and the final test results are presented in Figs. 6.44 – 6.46. Figure 6.44 shows the variation of the heating COP and heat sink temperature with time. Since the decrease of heat sink temperature is due to a decrease in heat being dumped, it is only safe to say that the heating COP will decrease as well. As the heating COP is based on the heat being dumped by the discharging cycle, this will give cause to an increase in cooling COP, as shown on Fig.6.42. Figure 6.45 shows the

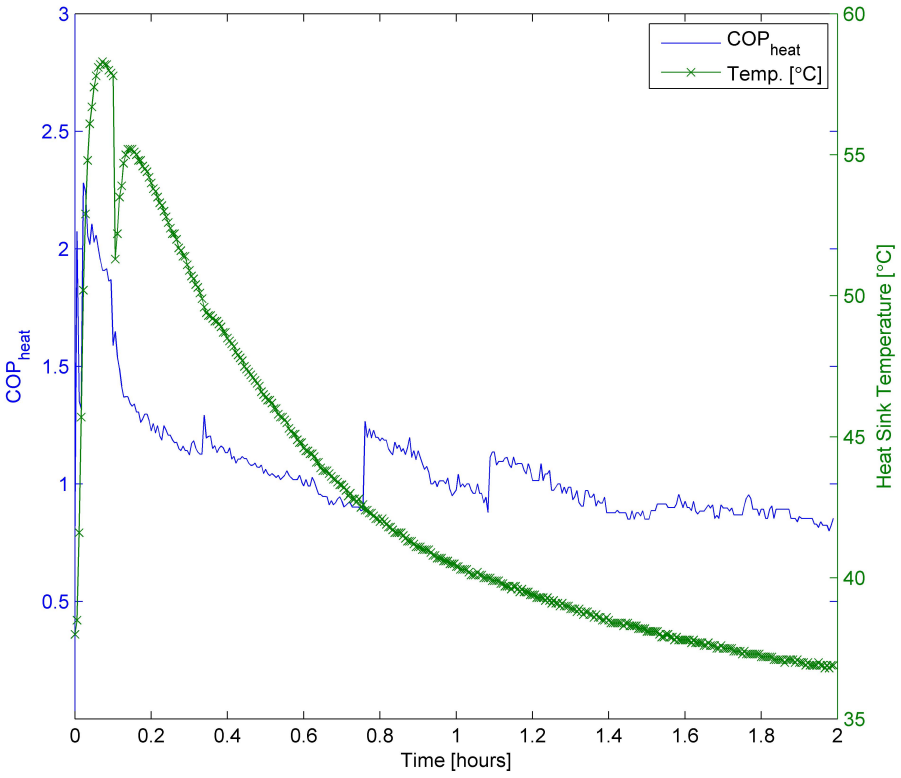

Figure 6.44: Heating COP and heat sink temperature against time

variation the heat pump COP and the heat sink temperature with time. Similarly as for the heating COP, there is a decrease of COP with a decrease of the heat

sink temperature, as less heat is being dumped to the system. The difference in the two COP's is that here the system is being considered as a heat pump and it is taking into account the heat being dumped during charge and discharge of the system. The high heat sink temperature in the first 20 minutes is due to a lot of the heat from the heat source being dumped and only a small portion of the available heat is being absorbed by the salt. This is reflected on Fig. 6.42 by a low cooling COP over the same length of time. Figure 6.46 shows a comparison

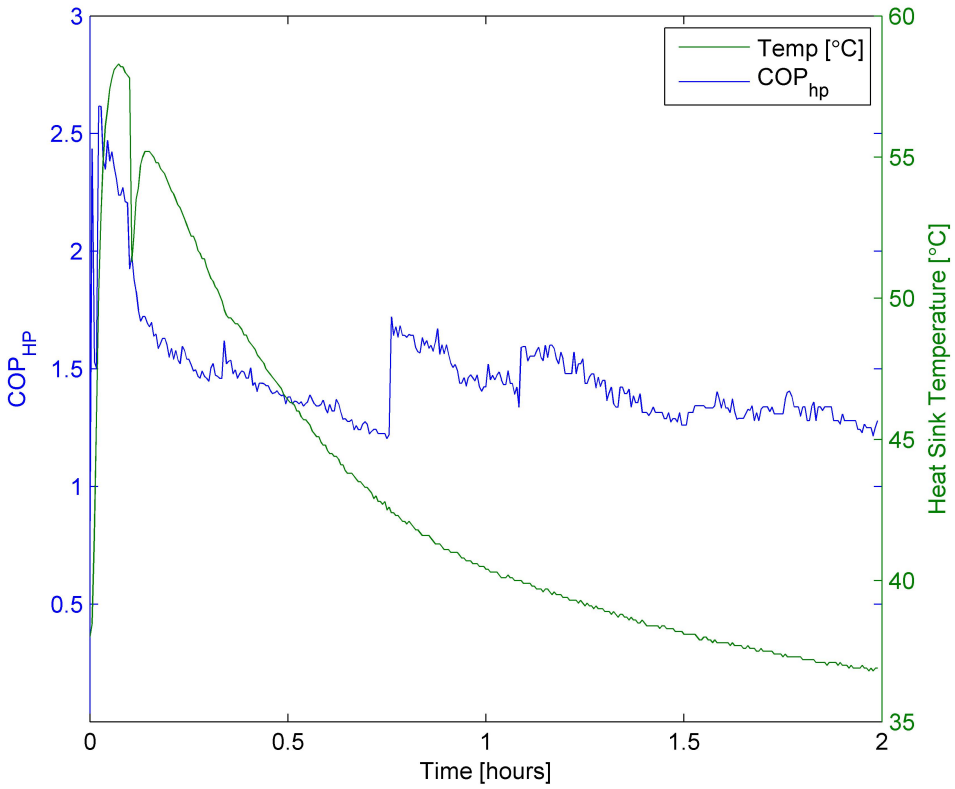

Figure 6.45: Heat pump COP and heat sink temperature against time

of all COP's in respect with Reynolds number. In the lower regions for Reynolds number, both cooling and heating COP are at their lowest, with the heat pump COP considerably high. As mentioned before, the heat source was not available constantly and thus a lot of the heat was being dumped to the heat sink for the

charging cycle. At mid-region of the Reynolds numbers investigated, the cooling COP is at its highest, resulting at lower heat and heat pump COP's, as more heat is being absorbed and less heat is being dumped. At the higher end of the Reynolds numbers used, the cooling COP decreases again as too much heat was delivered to the system, in comparison to the cooling output, and this resulted in an increased dumping of waste heat to the heat sinks.

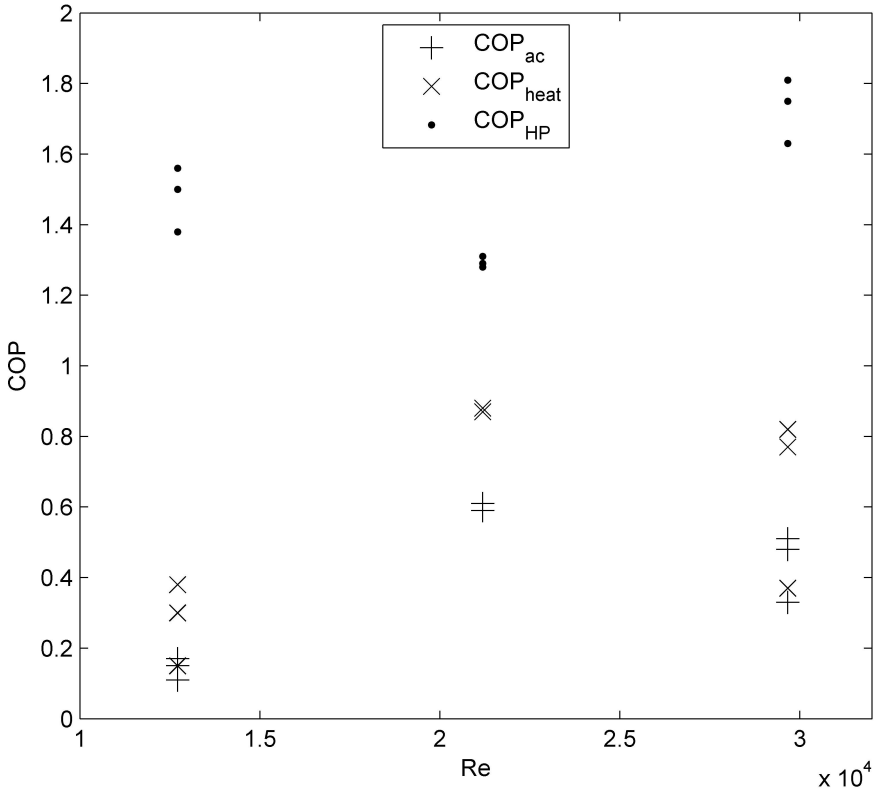

Figure 6.46: Comparison of all COP's

6.4.4 Emissions for Cooling Only and CCH

The emissions from the combustion of different biomass to drive an absorption refrigeration unit are presented in Figs. 6.47 – 6.51. All results are plotted against the net useful energy output and are presented for the Miscanthus pellets only. Figure 6.47 shows the emissions of carbon dioxide for different Reynolds numbers emitted during cooling and combined cooling and heating. The results are plotted in grams per net kWh energy output. The error bars indicate the determined U_{rss} error for the CO_2 emission equipment. It can be observed that there is a decrease in CO_2 emission with increased energy output (CCH) and with increased Reynolds number. Although there is a decrease in cooling COP with the higher value for Reynolds, there is no increase in CO_2. As a matter of fact the decrease in cooling COP is largely due to lesser efficient operating conditions for the cooling side of the system at higher Reynolds numbers. Figure 6.48 presents the emissions of carbon monoxide for Miscanthus pellets for single generation of cooling only and CCH. The emissions are presented in milligram per MJ net energy output and reduce with increased net output. The error bars are based on the U_{rss} value determined for the carbon monoxide analyser. The results are compared to a study (EMEP) conducted by Hobson & Thistlethwaite (2003) as part of the emission factor program task 7. Overall the emissions are lower than observed by this study which combines average (av.) with lower (l.) and higher (h.) confidence levels for emissions in Europe for residential biomass combustion units. Only the lower Reynolds number for cooling only shows an above average value, but as mentioned before this due to a poor utilisation of the available heat. There is a substantial decrease of emissions when comparing the combined mode of cooling and heating with cooling only. Figure 6.49 shows the emission of Nitric oxide for Miscanthus pellets for single generation of cooling only and CCH. The results are presented in milligrams per MJ of net energy output. It can be observed that the emissions reduce with increased output and decrease with increased Reynolds number. The emission of NO_x is compared to (EMEP) data and it can be shown that emissions from combined cooling and heating are within the limits observed by the study. The emissions for cooling only are higher than the highest observed levels, similar to the results for DHW

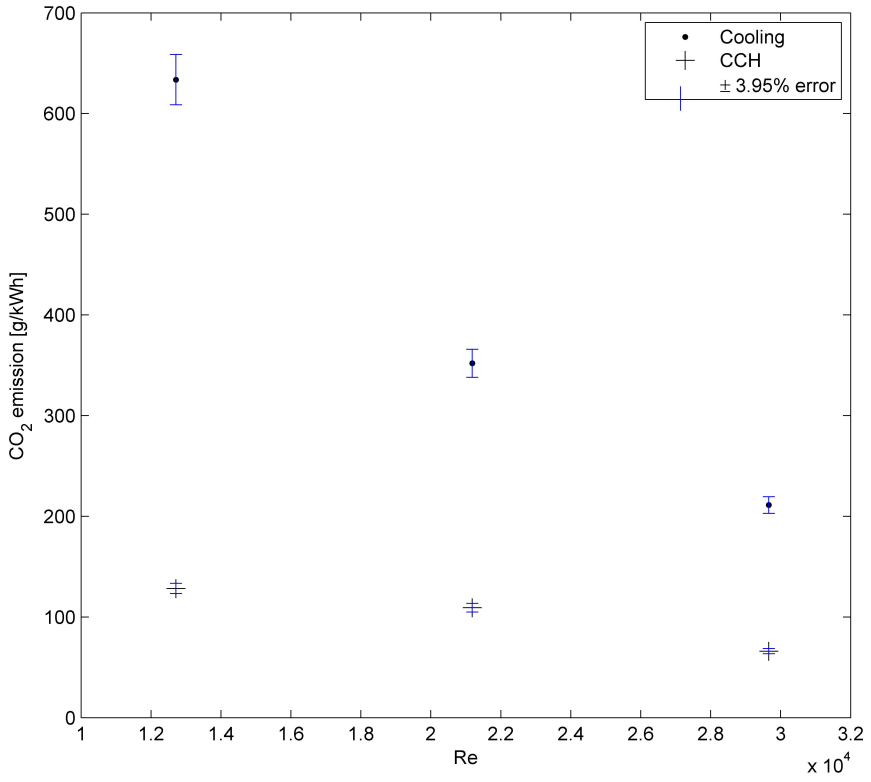

Figure 6.47: Emissions of CO_2 for cooling only and CCH

only. Figure 6.50 shows the emission of hexane for Miscanthus pellets for single generation of cooling only and CCH. The emissions decrease with increased net energy output similar to the other pollutants and are considerably lower for the combined cooling and heating compared to the single generation of cooling or heating. Figure 6.51 shows the particulate emissions for Miscanthus logs for single generation of cooling and CCH. As for the other pollutants the emissions decrease with increased energy output. The limits shown on the graph are taken from Caserini *et al.* (2010) who compiled average emissions of PM_{10} particulates for various burning units. The emissions for both generation schemes are lower than the average reported values. Obviously the boiler used in this study is different in its layout from conventional pellet burners and there is a considerable

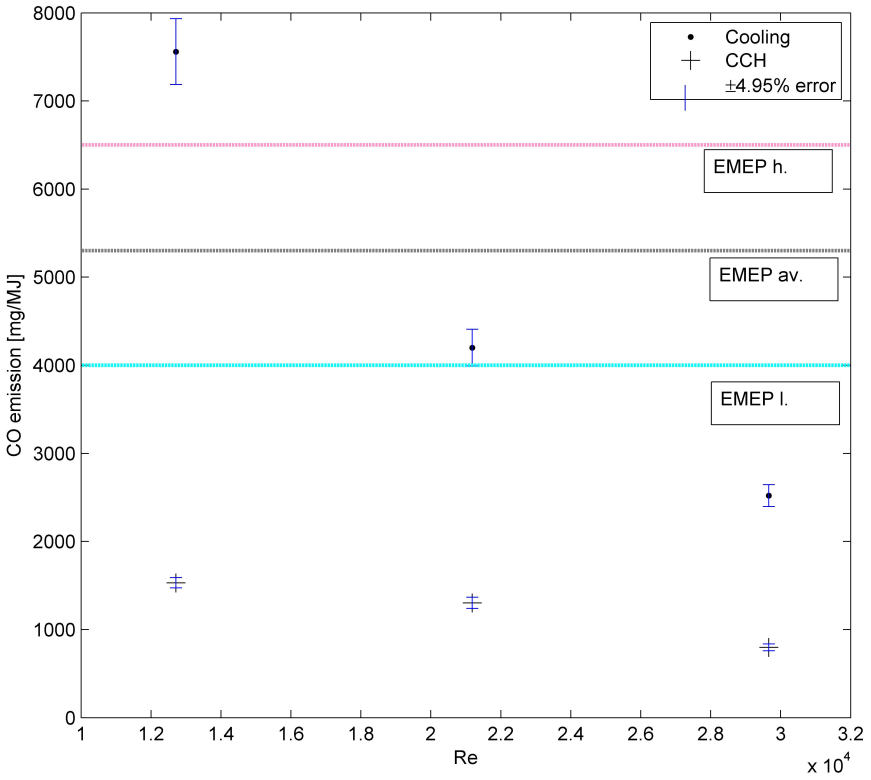

Figure 6.48: Emissions of CO for cooling only and CCH

flight path through the unit before the installation of the measuring device, which will cause a decrease in fly-ash and smoke.

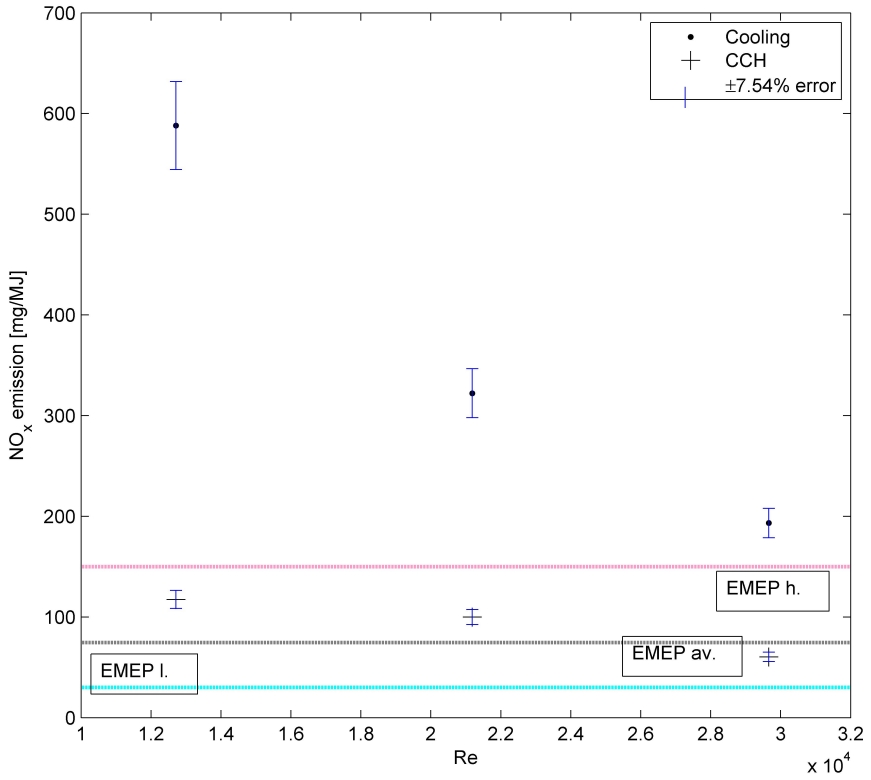

Figure 6.49: Emissions of NO_x for cooling only and CCH

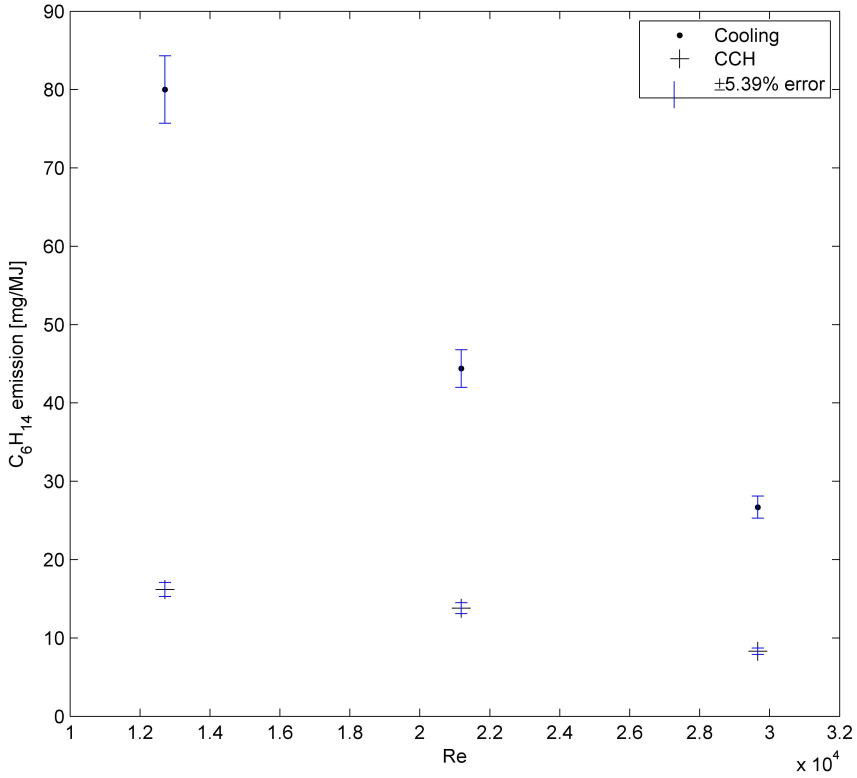

Figure 6.50: Emissions of C_6H_{14} for cooling only and CCH

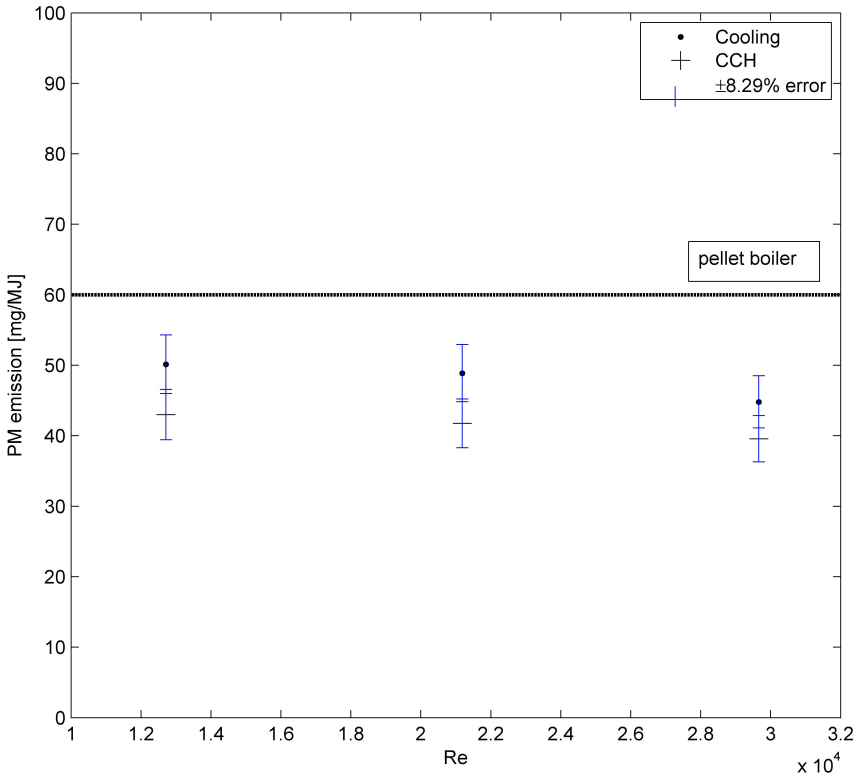

Figure 6.51: Emissions of particulate matter for cooling only and CCH

6.5 Comparative Savings for Combined and Single Generation

This section compares the different schemes discussed previously with combined generation and conventional stand-alone generation. Figure 6.52 shows a comparison of the different utilisation factors for the three schemes investigated during the course of this study. Here, the net useful energy output is compared to the total energy input to the system. The difference between unity is considered a net loss to the system in form of exhaust heat (±4%), unaccounted losses through the walls of the combustion chamber, pipework and others. Although the utilisation factors are almost identical when comparing heating to cooling only, there is a considerable increase when combining the two modes. The drop in energy utilisation for the combined mode at higher Reynolds number, compared to an almost stable situation for cooling only, is due to an increased power input being lost to the surroundings. This is also reflected in a drop in cooling COP for the same Reynolds number. Figure 6.53 shows a comparison of relative CO_2 emission for electricity, natural gas, heating oil, and Miscanthus. The emissions are shown for the combined modes of CHP, CCH and tri-generation as well as the total comparative emissions from the stand-alone emissions (indicated by sg). As expected there is a considerable decrease of emissions when combining systems as compared to the stand-alone generation. The emissions from electricity production and the burning of natural gas and oil are based on published data by DEFRA (2011a) and BIS (2011) and the utilisation and power outputs are based on the measured values in the tests. From the graph, natural gas is the lesser emitting one, however it is assumed that the Miscanthus pellets used in this study are carbon neutral. Since the emitted CO_2 will be used during the growth stages of the future Miscanthus plants for energy purposes. An extensive LCA of the fuels is beyond the scope of this study. Figure 6.54 shows a comparison of savings of energy input for the combined system and its equivalent stand-alone system. As expected there is a considerable decrease for the combined systems. Additionally, the graph shows the increase in utilisation for the combined systems to be as much as 45% for combined cooling and heating and tri-generation and in excess of 20% for combined heat and power. The savings are as much as 70 kW

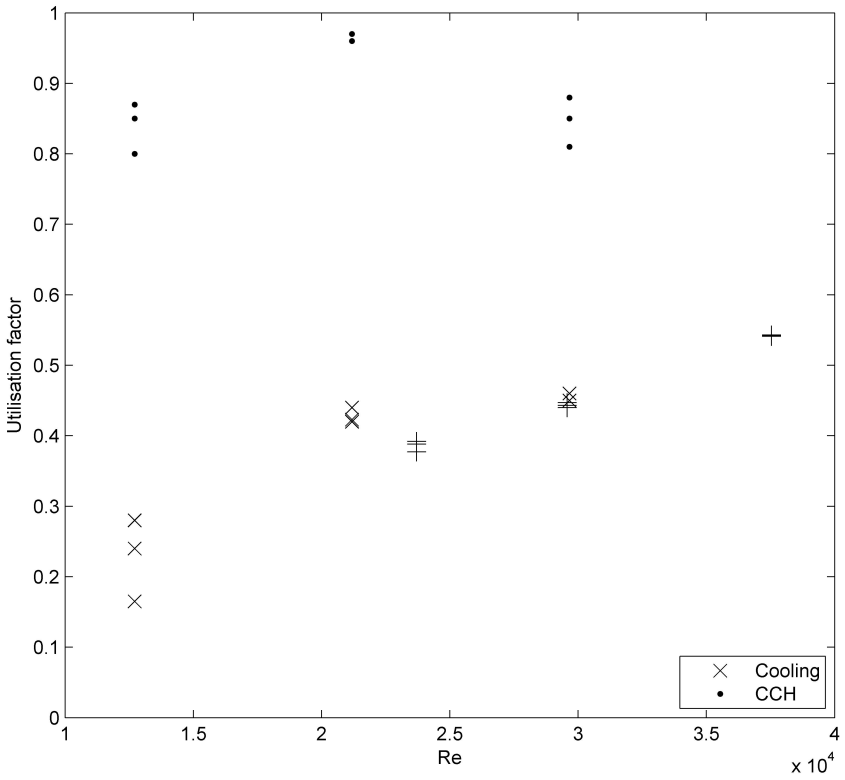

Figure 6.52: Performance utilisation for cooling, heating and combined cooling and heating

when comparing CHP and its equivalent single generation and approximately 50 kW when comparing the other two combined schemes to their equivalent single generation system.

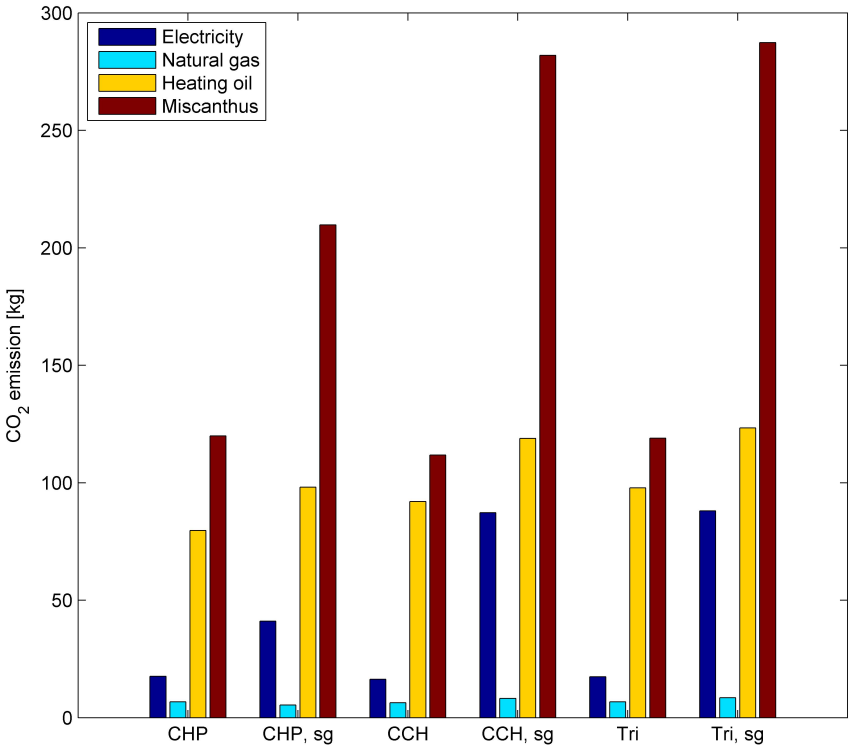

Figure 6.53: Comparison of CO_2 emission for combined and single generation schemes

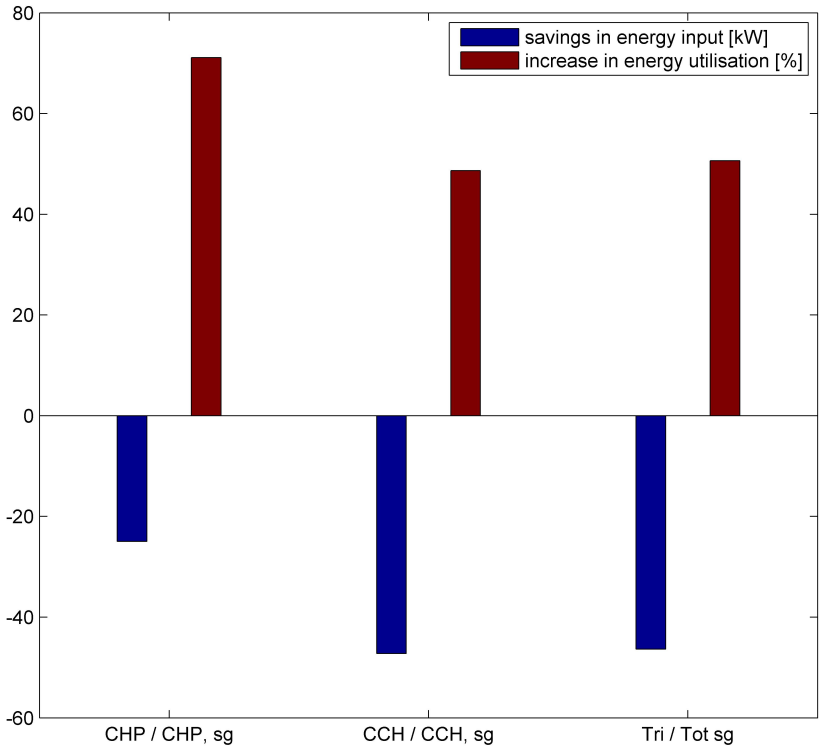

Figure 6.54: Comparative difference in energy utilisation

6.6 General Discussion

In general, the discussion of the results of this study can be summarised in the following points.

- The biomass boiler was run as a stand-alone water heater and as the heat source for the absorption unit. The fuel consumption (kg/hr) was constant for all tests, yet the net useful power output changed with different Reynolds numbers. This resulted in increased performances when comparing the utilisation factors for heating or cooling alone compared to combined cooling and heating.

- The emissions of CO_2, CO, C_6H_{14}, NO_x and particulates decreased with increased energy output as expected. Generally, the emissions were lower than the observed data in other studies and the computer model proved well in giving average prediction for emission from solid biomass combustion.

- The model and the experimental results show that it is feasible to utilise biomass heat to drive an absorption unit as long as the utilisation of the heat sink is well structured. The overall cooling COP measured was between 0.35 and 0.60 which is close to the unit being run on solar power and corresponds well with the simulated results. The results also show that the flow of the different circuits can be used to increase or decrease the cooling or heating output, which could prove useful for different applications.

- The utilisation factor of combined cooling and heating is much higher (as expected) than that of single generation. The results showed that the factor for CCH and tri-generation is approximately 40% higher than that of single generation and 25% for CHP compared to single generation.

- Comparing the different combined schemes with the total output of CO_2 under single generation, shows differences of as much as 100 kg for Miscanthus and even 30 kg for heating oil.

- The model of the Stirling engine did show a feasible output and efficiency for the engine. The tests show a temperature of almost 30 K for 2.5 bar

pressure charge. Unfortunately, it was not possible to run the engine at higher pressures due to too much vibration which caused the piston to jam in the cylinder.

Chapter 7

Conclusions and Recommendations

This chapter gives the answers to the questions raised in the introductory chapter, in the light of experimental and theoretical findings of the investigation. It also proposes some recommendations for future studies in combined generation of biomass applications.

7.1 Conclusions

From the present study, the following conclusions can be drawn:

Experiments were designed and carried out to investigate the performance of single generation of cooling/heating and the combined cooling and heating mode. The results show that the energy output from combined generation are much higher than that of single generation. The fuel consumption is more or less the same for tests with similar parameters, which results in an increased energy utilisation with increased energy output. Reynolds numbers in the region of 30,000 for heating only (45%) and 21,000 for cooling only (45%) as well as CCH (95%) showed the best energy utilisation factors for the system investigated in this study. The test results show that a good energy utilisation can be achieved by carefully adjusting the flows in the different circuits. There is a potential for regulating the required output of heating and cooling with the heat source flow rate according to the demand. Additionally, there is a potential of enough

excess heat for this particular biomass boiler to be used for further heating uses. The analytical model of the biomass combustion proves adequate to predict the emissions from biomass combustion, as compared to measured and published data. The emissions tests show that there is a considerable decrease in harmful emissions with increased energy utilisation. This is especially the case for the combined systems of generation in comparison with the total emissions from the individual single generation schemes. The fuel properties analysis gave a useful insight into the composition of the fuels and its effect: the energy content is indirectly proportional to ash and moisture content and directly proportional to the sum of volatile matter and fixed carbon content.

The computational fluid dynamics investigations of the heat exchangers and the Stirling engine showed a good tool to gain further insight into the flow and heat transfer. This is in general not possible to determine in real-life tests and thus prove a resourceful tool during the design stages of the different components. In particular the CFD analysis of the Stirling engine allowed to verify the changes made to the cooler, compared to the original design, and show that they were adequate without impeding the performance of the engine.

The analytical tool developed to determine the performance of the Stirling engine was used to simulate the effect of changing the gas and the pressure in the engine. As expected, the use of a lighter gas than air will result in a higher thermal efficiency of the engine as less work is required to overcome flow friction. This flow friction has a negative impact on the work output of the engine. There is a higher pressure drop for a heavier working fluid than for a lighter one. The actual work output could be increased by 10% by swapping the working gas from air to Helium. Above 7.5 *bar* the increase in efficiency with increased pressure becomes less significant and the amount of heat required to drive the engine becomes more important with higher pressure. The laboratory tests show that the engine can be used as a cooler with temperature drops to just above freezing for pressures as low as 2.5 *bar*.

The analytical model of the absorption refrigeration unit shows good results and operating conditions compared to similar studies. The simulation was run for a variety of temperature ranges for the cooling, heat sink and heat source.

As expected, the results show an increase in COP for increased heat source temperature as well as for decreased heat sink temperature while keeping all other variables unchanged. The major conclusion from all the results is that hot water from biomass combustion provides a suitable source for the absorption system. The tests showed a cooling COP in the regions of 0.30 – 0.60, whereas the model predicted an operating region of 0.30 – 0.50 depending on the heat sink temperatures.

The tests showed that the combustion of biomass is a viable energy source for combined cooling and heating. The comparison between the different generation schemes shows comparative energy savings of up to 40% in comparison to single generation and an increase in energy utilisation of approximately 50% depending on operating conditions. In comparison to standard fossil fuel sources, this could provide potential savings of CO_2 between 10 kg (natural gas) and 100 kg (heating oil) depending on the chosen scheme for equivalent energy output.

The literature review and the testing has proved biomass combined generation systems to be an adequate option for the energy sector in Luxembourg. Not only, is the high fuel dependency on fossil fuel addressed but the high investment costs of the unit can be partially covered by grants and public funding. Biomass has gained a rise in public interest over the last couple of years and this thesis has partially contributed towards this by disseminating the results to local and private forest owners by means of presentations. Additionally, the newly introduced legislation regarding the increased energy utilisation in buildings (EU directive 2002/91/CE) can be addressed with the installation of combined biomass applications.

7.2 Recommendations

At this stage both theoretical and experimental work has achieved its objectives and the following recommendations can be considered:

Either a smaller biomass boiler can be used, or a larger buffer tank for the excess heat is required. Although the tests worked as expected and the results obtained are satisfactory, the fuel feed rate was reduced to the lowest setting

to prevent a boiling of the water. Due to the laboratory availability and the university's plans to convert the room used for testing as a Centre of excellence for Biomass; there is a potential to fully utilise the proposed system for space heating by means of an underground floor heating system and/or cooling depending on the requirements.

The Stirling engine could not be driven of waste heat from the combustion of biomass unit, as the unit was on loan and thus could not be modified. Additionally the heating could not be used in the test bay area due to an issue with connecting water next to a three phase electricity connection. This is certainly something that will be resolved in the near future, as parts of this project will be included in an INTERREG IVB project entitled 'ARBOR' to commence in spring 2011.

The results have shown that the return heat source temperature of the absorption unit still has a temperature of around 75°. This could be used for additional heating use depending on demand. Although the biomass boiler used in these tests proves to be too large for single family housing, a smaller unit could be used to conduct the same tests, and thus show a better energy utilisation even at higher operating conditions of the boiler.

A combination of solar and biomass heat should show potential in less sunny climates. In this case the down-times of the system could be compensated by using heat from a biomass combustion unit and thus find a fine balance between solar and biomass energy.

Appendix A

Chemical Properties of Substances

Table A.1: Chemical specifications of the substances used in this study

Substance	**Molar mass [g/mol]**	**Enthalpy of formation [kJ/mol]**
O	16	249.190
O_2	32	0
CO	28	-110.530
CO_2	44	-393.520
H_2	2	0
OH	17	39.460
H_2O	18	-241.820
N_2	28	0
NO	30	90.297
NO_2	46	33.098

Table A.2: K_p equilibrium values of the substances used in this study

Temp [K]	$H_2 \rightleftharpoons 2H$	$O_2 \rightleftharpoons 2O$	$N_2 \rightleftharpoons 2N$	$H_2O \rightleftharpoons \frac{1}{2}H_2 + \frac{1}{2}O_2$	$H_2O \rightleftharpoons \frac{1}{2}H_2 + OH$	$CO_2 \rightleftharpoons CO + \frac{1}{2}O_2$	$\frac{1}{2}N_2 + \frac{1}{2}O_2 \rightleftharpoons NO$
298	-164.005	-186.975	-667.480	-92.208	-106.208	-103.762	-35.052
500	-92.827	-105.630	-213.372	-52.691	-60.281	-57.616	-20.295
1000	-39.803	-45.150	-99.372	-23.163	-26.034	-23.529	-9.388
1200	-30.874	-35.005	-80.011	-18.182	-20.283	-17.871	-7.569
1400	-24.462	-27.742	-66.329	-14.609	-16.099	-13.842	-6.270
1600	-19.637	-22.285	-56.055	-11.921	-13.066	-10.830	-5.294
1800	-15.866	-18.030	-48.051	-9.826	-10.657	-8.497	-4.536
2000	-12.840	-14.622	-41.645	-8.145	-8.728	-6.635	-3.931
2200	-10.353	-11.827	-39.391	-6.768	-7.148	-5.120	-3.422
2400	-8.276	-9.497	-32.011	-5.619	-5.832	-3.860	- 3.019
2600	-6.517	-7.521	-28.304	-4.648	-4.719	-2.801	-2.671
2800	-5.002	-5.826	-25.117	-3.812	-3.763	-1.894	-2.372
3000	-3.685	-4.357	-22.359	-3.086	-2.937	-1.111	-2.114
3200	-2.534	-3.072	-19.937	-2.451	-2.212	-0.429	-1.888
3400	-1.516	-1.935	-17.800	-1.891	-1.576	0.169	-1.690
3600	-0.609	-0.926	-15.898	-1.392	-1.088	0.701	-1.513
3800	0.202	-0.019	-14.199	-0.945	-0.501	1.176	1.356
4000	0.934	0.796	-12.660	-0.542	-0.044	1.599	-1.216
4500	2.486	2.513	-9.414	0.312	0.920	2.490	-0.921
5000	3.725	3.895	-6.807	0.996	1.689	3.197	-0.686
5500	4.743	5.023	-4.666	1.560	2.318	3.771	-0.497
6000	5.590	5.963	-2.865	2.032	2.843	4.245	-0.341

Appendix B

Specifications of Apparatuses and Instruments

Table B.1: Carborobot boiler specifications

Manufacturer	**Specifications**	
	Model	Farmer F40
	Heat output (kW/h)	5-40
	Consumption of (kg/h)	
Carborobot	coal (18 MJ/kg)	9
1211 Budapest Varrogepgyar	pellet (14 MJ/kg)	12
u.4	max. log use	13
Hungary	Fuel hopper size (m^3)	0.32
`www.carborobot.com`	Boiler size (lit)	430
	CO max (mg/m^3)	250
	NO_x max (mg/m^3)	400
	Flue temperature ($^\circ$)	130-160

Table B.2: Generator specifications

Manufacturer	**Specifications**	
Leroy-Somer Motors, Gears & Drives Southern Office 8 The Square, Stockley Park Uxbridge, Middlesex UB11 1FW `www.leroy-somer.co.uk`	Model	LSRPM90SC
	Prime power output (kW)	1.8
	3 phase	
	50 Hz	
	900 rpm (max)	
	Power factor	0.82
	Voltage output (V)	360
	Current output (A)	3.8

Table B.3: Heat exchanger specifications

Manufacturer	**Specifications**	
	Model	Elecro Multi Tubular
	Rating (kW)	25
Elecro Engineering Ltd.	Tube side	
Unit 11	connection (mm)	50
Gunnelswood Park	flow rate (m^3/h)	0.7
Stevenage	pressure drop (kPa)	1.4
Hertfordshire	Shell side	
SG1 2BH	connection (mm)	26/34
`www.elecro.co.uk`	flow rate (m^3/h)	6.0
	pressure drop (kPa)	3.8
	Flow regime	counter-current

Table B.4: ClimateWell TCA absorption unit specifications

Manufacturer	**Specifications**		
ClimateWell Corporate HQ Instrumentvaegen 20 SE-126 53 Haegersten Sweden `www.climatewell.com`	Nominal Power	cooling (kW)	5-10
	Prime consumption	electrical (W)	18
	COP	thermal	0.68
	Max. inlet temp.	heat source ($°C$)	120
	Max. pressure	heat source (bar)	10
	Pressure drop (kPa)	heat source ($25\,l/min$)	30
		heat sink ($50\,l/min$)	38
		cooling ($25\,l/min$)	45
	Energy storage (kWh)	cooling	56
	Salt solution	Lithium Chloride	$LiCl$
	Heat source circuit	Flow (l/min)	25-30
		Power range (kW)	15-20
		Temperature ($°C$)	out: 75-100 in: 85-100
	Distribution circuit	Flow (l/min)	25-30
		Power range (kW)	5-10
		Temperature ($°C$)	out: 10-16 in: 15-21
	Heat sink circuit	Flow (l/min)	50-60
		Power range (kW)	20-30
		Temperature ($°C$)	out: 30-45 in: < 30

Table B.5: Mercury barometer specification

Manufacturer	**Specifications**	
	Model	62/248-3
Short & Mason	Range ($mmHg$)	680-830
London	Accuracy ($mmHg$)	$\pm$ 0.3
	Resolution ($mmHg$)	0.05

Table B.6: Manometer specifications

Manufacturer	**Specifications**	
Airflow Development Ltd.	Model	na
High Wycombe	Range (mmH_2O)	0-100
`www.airflow.co.uk`	Accuracy (mmH_2O)	0.05
	Resolution (mmH_2O)	0.01

Table B.7: Magneto-dynamic oxygen analyser specifications

Manufacturer	**Specifications**	
Servomex ltd.	Model	570 Oxygen
Crownborough	Range	0.0 - 100.0 % O_2
`www.servomex.com`	Accuracy	$\pm$ 0.05%
	Resolution ($mmHg$)	0.1 %

Table B.8: Gas analysers specifications for CO, CO_2, Hexane and NO_x

Manufacturer	**Specifications**	
A.D.C. Ltd.	Model	Infra-red gas analysers
Industrial Centre	Range	CO: 0.0-0.5%
Pinar Road		CO_2: 0.0-20%
Hoddesdon		C_6H_{14}: 0-5000 ppm
EN11 0FF		NO_x: 0-10000 ppm
`www.adc-service.co.uk`	Accuracy	± 1-2%

Table B.9: Double pass particulate monitor specifications

Manufacturer	**Specifications**	
Dynoptic Systems Ltd.	Model	DSL-330
Furlong House	Measuring principle	Light transmission
Crowfield	Wavelength (nm)	510-540 (green LED)
Brackley	Range (mg/m^3)	0-1000
NN13 5TW	Accuracy	± 2%
`www.dynoptic.co.uk`	Resolution (mg/m^3)	0.1
	Operating humidity	5-100 %
	max. temp. ($°C$)	600
	amb.temp. ($°C$)	-20 + 50

Table B.10: Oxygen bomb calorimeter thermometer specifications

Manufacturer	**Specifications**	
PARR Instruments	Model	PARR 6775
211 53^{rd} Street	Probe type	Thermistor
Moline, Illinois	Range ($^{\circ}C$)	10-40
61265 USA	Resolution ($^{\circ}C$)	0.001
`www.parrinst.com`	Accuracy ($^{\circ}C$)	$\pm$ 0.1%

B11. Air pressure uncertainty The air pressure was measured by a mercury barometer. From the technical specifications issued by the manufacturer, the accuracy of the barometer is (BS 2520:1983) as shown in Table B.5, and the relative systematic uncertainty is given as $\pm 0.3\, mmHg$.

$$\Delta e_s = \frac{\pm 0.3}{830} = \pm 0.04\%$$

The random uncertainty for the barometer is based on a typical value (706 $mmHg$) taken during the experiments and the random uncertainty determined as 3.61 $mmHg$.

$$\Delta e_r = \frac{3.61}{830} = 0.51\%$$

Combining the systematic and random uncertainty by linear additive (ADD) and root-sum-square (RSS) methods yields:

$$U_{ADD} = 0.0004 + 0.0051 = \pm 0.55\%$$

$$U_{RSS} = \sqrt{0.0004^2 + 0.0051^2} = \pm 0.51\%$$

B12. Fuel flow rate uncertainty The fuel flow rate is determined by the total mass of fuel consumed during the tests. The systematic uncertainty is

introduced by the manufacturing process of the scale, the reading of the calibrated scale and the reading of the timer. The same weighing technique as for the bulk density is used (EN15103). It is assumed that this will render the systematic uncertainty of the density of the fuel negligible. Based on this, the following systematic uncertainties are estimated.

- For the scale:
  - Maximum weight of the scale: $m_{fuel} = 34000.0\,g$
  - Possible uncertainty of the scale: $\Delta m_{fuel} = \pm 0.1\,g$
  - Systematic uncertainty of the scale: $\frac{\Delta m_{fuel}}{m_{fuel}} = \frac{0.1}{34000} = 2.94 \times 10^{-6}$
- For the timer:
  - The length of time: $t = 24\,hours$
  - Possible uncertainty of the timer: $\Delta t = \pm 0.5\,s$
  - Systematic uncertainty: $\frac{\Delta t}{t} = \frac{0.5}{24 \times 3600} = 5.78 \times 10^{-6}$

It is safe to assume that the systematic uncertainty of the scale and the timer is negligible. The uncertainty for the fuel flow rate then gives:

$$\frac{\Delta \dot{m}_{fuel}}{\dot{m}_{fuel}} = 2.94 \times 10^{-6} + 5.78 \times 10^{-6} = 8.72 \times 10^{-6}$$

The systematic uncertainty for the fuel flow rate is negligible. The random uncertainty of the fuel flow rate is mainly introduced by the reading of the scale and the timer. For an average value of $m_{fuel} = 8.445\,kg$, and a random uncertainty of $\pm 0.212\,kg$, the relative random uncertainty becomes:

$$\Delta e_{r(m)} = \frac{0.212}{8.445} = \pm 2.51\%$$

For an average time interval of $t = 4635s$ and the random uncertainty of $\pm 122.36s$, the relative random uncertainty becomes:

$$\Delta e_{r(t)} = \frac{122.36}{4635} = \pm 2.64\%$$

The maximum random uncertainty for the fuel flow is then:

$$\Delta e_{r\dot{m}} = 0.0251 + 0.0264 = 5.15\%$$

Combining the systematic and random uncertainty by linear additive (ADD) and root-sum-square (RSS) methods yields:

$$\begin{aligned} U_{ADD} &= 0 + 0.0774 = \pm 7.74\% \\ U_{RSS} &= \sqrt{0^2 + 0.0774^2} = \pm 7.74\% \end{aligned}$$

B13. Exhaust gas flow rate uncertainty The exhaust gas flow rate is measured with a pitot static tube and a manometer. The systematic uncertainty is introduced by the manometer, the reading of the calibrated manometer, and the systematic uncertainty of the density of the exhaust gas.

- For the manometer:
  - Range: $h = 0 - 100\, mmH_2O$
  - Possible uncertainty: $\Delta h = \pm 0.05\, mmH_2O$
  - Systematic uncertainty of the manometer: $\frac{\Delta h}{h} = \frac{0.05}{100} = 0.05\%$

For the density of the exhaust gas (0.93%), the same principle as outlined for the air inlet flow rate uncertainty is used. The systematic uncertainties are due to the air density and the conversion of the manometer reading in mmH_2O to Pa. It is assumed that reported value for the density of water of $997.1 kg/m^3$ $\pm\, 0.5\%$ at atmospheric conditions is valid. The systematic uncertainty for the gravitational force 'g' is estimated at $9.81 m/s^2$ $\pm\, 0.5\%$. The following systematic uncertainty is then determined:

$$\begin{aligned} \Delta e_{s_{\Delta P}} &= \sqrt{\left(e_{s_{\rho w}} \frac{1}{\rho_w}\right)^2 + \left(e_{s_g} \frac{1}{g}\right)^2 + \left(e_{s_h} \frac{1}{h}\right)^2} \\ &= \sqrt{0.005^2 + 0.005^2 + 0.0005^2} = 0.71\% \end{aligned}$$

Now, the relative systematic uncertainty for the exhaust gas flow rate becomes:

$$\Delta e_s = 0.0056 + 0.0071 = 1.27\%$$

The random uncertainty for the conversion of the reading is only dependent on the reading of the manometer and the density of air. For an average reading value of 1.477 mmH_2O, and a random uncertainty of $\pm 0.0422\ mmH_2O$, the relative random uncertainty becomes:

$$\Delta e_{r_h} = \frac{0.0422}{1.477} = 2.86\%$$

The total random uncertainty for the exhaust gas measurement is then determiend as follows:

$$\Delta e_r = 0.0286 + 0.0092 = 3.78\%$$

Combining the systematic and random uncertainty by linear additive (ADD) and root-sum-square (RSS) methods yields:

$$\begin{aligned} U_{ADD} &= 0.0127 + 0.0378 = \pm 5.05\% \\ U_{RSS} &= \sqrt{0.0127^2 + 0.0378^2} = \pm 3.99\% \end{aligned}$$

B14. Water flow rate uncertainty The water flow rates are measured at five different locations with four different devices. The uncertainties are determined for each flow rate independently. The systematic uncertainty is introduced by the flow meter, the reading of the flow meter, and the systematic uncertainty of the density of water.

- For the digital flow meter (MW1):
  - Systematic uncertainty of the flow meter: $\pm = 0.01\%$

It is assumed that the systematic uncertainty for the timer is negligible. For the density of the water flow (0.50%), the same principle as outlined for the air inlet

flow rate uncertainty is used. The systematic uncertainty of the water flow rate is then:

$$\Delta e_s = 0.0001 + 0.005 = 0.51\%$$

- For the spring flow meter (MW3 - MW5):
  - Maximum reading: $\dot{V} = 50\, lit/min$
  - Possible uncertainty: $\Delta\dot{V} = \pm 2\, lit/min$
  - Systematic uncertainty: $\frac{\Delta\dot{V}}{\dot{V}} = \frac{2}{50} = 4\%$

For the density of the water flow (0.50%), the same principle as outlined for the air inlet flow rate uncertainty is used. The systematic uncertainty of the water flow rate (MW3-MW5) is then:

$$\Delta e_s = 0.04 + 0.005 = 4.50\%$$

The flow rate (MW6) is measured with an orifice plate, the uncertainty is introduced by the orifice diameter, the coefficient of discharge, the reading of the manometer and the conversion of the manometer reading.

- For the coefficient of discharge of the installed orifice plate:
  - Average: $Cd = 0.6117$
  - Possible error: $\Delta Cd = 0.005$
  - Systematic error: $\Delta e_{s_{Cd}} = \frac{0.005}{0.6117} = 0.82\%$
- For the free flow area through the orifice (the diameter will be considered)
  - Diameter of orifice: $d = 33\, mm$
  - Possible error $\Delta d = 0.01\, mm$
  - Systematic error: $\Delta e_{s_d} = \frac{0.01}{33} = 0.03\%$
- For the reading of the manometer
  - Range of the manometer: $0 - 1\, bar$

– Possible reading error: 1 $mbar$

– Systematic error: $\Delta e_{s_h} = \frac{0.001}{1} = 0.1\%$

For the density of the water flow (0.50%), the same principle as outlined for the air inlet flow rate uncertainty is used. The systematic uncertainty of the water flow rate is then:

$$e_s = \sqrt{0.0082^2 + (2 \times 0.0003)^2 + (0.5 \times 0.005)^2 + (0.5 \times 0.001)^2} = 0.86\%$$

Now the relative random uncertainties are determined for each flow meter and presented in Table B.11. The relative random uncertainty for the timer of 0.11%,

Table B.11: Relative random uncertainties for the flow meters

MW	**Random unc.**	**Average read.**	**Relative random unc.**
1	5.384	315.567	1.71%
2	not used		
3	0.050	11.933	0.42%
4	0.133	31.467	0.42%
5	0.195	14.123	1.38%
6	0.622	326.667	0.19%

is based on the random uncertainty of 0.774 and an average reading of 721 s. All other random uncertainties are negligible or are not taken into account for reasons mentioned before. Combining the systematic and random uncertainty by linear additive (ADD) and root-sum-square (RSS) methods yields for MW1:

$$\begin{aligned} U_{ADD} &= 0.0051 + 0.0171 = \pm 2.22\% \\ U_{RSS} &= \sqrt{0.0051^2 + 0.0171^2} = \pm 1.78\% \end{aligned}$$

Combining the systematic and random uncertainty by linear additive (ADD) and

root-sum-square (RSS) methods yields for MW3 and MW4:

$$\begin{aligned} U_{ADD} &= 0.0450 + 0.0042 = \pm 4.92\% \\ U_{RSS} &= \sqrt{0.0450^2 + 0.0042^2} = \pm 4.52\% \end{aligned}$$

Combining the systematic and random uncertainty by linear additive (ADD) and root-sum-square (RSS) methods yields for MW5:

$$\begin{aligned} U_{ADD} &= 0.0450 + 0.0138 = \pm 5.88\% \\ U_{RSS} &= \sqrt{0.0450^2 + 0.0138^2} = \pm 4.71\% \end{aligned}$$

Combining the systematic and random uncertainty by linear additive (ADD) and root-sum-square (RSS) methods yields for MW6:

$$\begin{aligned} U_{ADD} &= 0.0086 + 0.0019 = \pm 1.05\% \\ U_{RSS} &= \sqrt{0.0086^2 + 0.0019^2} = \pm 0.88\% \end{aligned}$$

B15. Electrical input uncertainty The electrical input is measured with a FLUKE 1735 power meter. Additionally, the values are verified by an oscilloscope. The systematic uncertainty is introduced by measurement of the current ($\pm 0.50\%$), the voltage ($\pm 1.00\%$) and the power factor ($\pm 1.00\%$), taken from the manual of the equipment. The total systematic uncertainty for the power is calculated by adding the errors of voltage and current. The error due to the power factor is obtained by multiplying the specified error by unity minus the value for the corresponding power factor. The random error for the voltage is based on an average reading of $211.91\,V$ with a random uncertainty of ± 1.715, for the current an average reading of $0.624\,A$ with a random uncertainty of ± 0.028, for the power factor an average reading of 0.673 with a random uncertainty of ± 0.032. This gives the following random errors:

- $\Delta e_{rV} = \frac{1.715}{211.91} = 0.81\%$
- $\Delta e_{rI} = \frac{0.028}{0.624} = 4.49\%$

- $\Delta e_{rPF} = \frac{0.032}{0.673} = 4.75\%$

Combining the systematic and random uncertainty by linear additive (ADD) and root-sum-square (RSS) methods yields for the voltage:

$$\begin{aligned} U_{ADD} &= 0.005 + 0.0081 = \pm 1.31\% \\ U_{RSS} &= \sqrt{0.005^2 + 0.0081^2} = \pm 0.95\% \end{aligned}$$

Combining the systematic and random uncertainty by linear additive (ADD) and root-sum-square (RSS) methods yields for the current:

$$\begin{aligned} U_{ADD} &= 0.01 + 0.0449 = \pm 5.49\% \\ U_{RSS} &= \sqrt{0.01^2 + 0.0449^2} = \pm 4.60\% \end{aligned}$$

Combining the systematic and random uncertainty by linear additive (ADD) and root-sum-square (RSS) methods yields for the power factor:

$$\begin{aligned} U_{ADD} &= 0.01 + 0.0475 = \pm 5.75\% \\ U_{RSS} &= \sqrt{0.01^2 + 0.0475^2} = \pm 4.85\% \end{aligned}$$

B16. Oxygen content The remaining content of the oxygen in the exhaust gas was measured by the oxygen gas analyser. The systematic error for the oxygen analyser is ±0.05%, according to the manufacturer. A typical value of the reading for the oxygen analyser is 19.35% with an uncertainty of 0.342, thus the random uncertainty is:

$$\Delta e_{rO_2} = \frac{0.342}{19.35} = 1.77\%$$

Combining the systematic and random uncertainty by linear additive (ADD) and root-sum-square (RSS) methods yields for the oxygen analyser:

$$\begin{aligned} U_{ADD} &= 0.0005 + 0.0177 = \pm 1.82\% \\ U_{RSS} &= \sqrt{0.0005^2 + 0.0177^2} = \pm 1.77\% \end{aligned}$$

B17. Exhaust emission uncertainty The exhaust emissions are measured by the A.D.C. infra-red gas analysers. Their respective systematic errors are 2.00% according to the manufacturer. The random errors are based on average readings and their uncertainties as follows: For the CO analyser a typical reading is 0.01% with an uncertainty of 0.00046:

$$\Delta e_{rCO} = \frac{0.00046}{0.01} = 4.60\%$$

For the CO_2 analyser a typical reading is 1.471% with an uncertainty of 0.066:

$$\Delta e_{rCO_2} = \frac{0.066}{1.471} = 4.53\%$$

For the NO_x analyser a typical reading is 22.857 ppm with an uncertainty of 1.662:

$$\Delta e_{rNO_x} = \frac{1.662}{22.857} = 7.27\%$$

For the C_6H_{14} analyser a typical reading is 8.571ppm with an uncertainty of 0.43:

$$\Delta e_{rC_6H_{14}} = \frac{0.43}{8.571} = 5.02\%$$

Combining the systematic and random uncertainty by linear additive (ADD) and root-sum-square (RSS) methods yields for the CO analyser:

$$\begin{aligned} U_{ADD} &= 0.02 + 0.046 = \pm 6.60\% \\ U_{RSS} &= \sqrt{0.02^2 + 0.046^2} = \pm 5.02\% \end{aligned}$$

Combining the systematic and random uncertainty by linear additive (ADD) and root-sum-square (RSS) methods yields for the CO_2 analyser:

$$\begin{aligned} U_{ADD} &= 0.02 + 0.0453 = \pm 6.53\% \\ U_{RSS} &= \sqrt{0.02^2 + 0.0453^2} = \pm 4.95\% \end{aligned}$$

Combining the systematic and random uncertainty by linear additive (ADD) and root-sum-square (RSS) methods yields for the NO_x analyser:

$$\begin{aligned} U_{ADD} &= 0.02 + 0.0502 = \pm 7.02\% \\ U_{RSS} &= \sqrt{0.02^2 + 0.0502^2} = \pm 5.40\% \end{aligned}$$

B18. Particulate matter uncertainty The particulate matter in the exhaust gas was measured by a dynoptic opacity meter. The systematic error for the particulate matter is ±2.00%, according to the manufacturer. A typical value of the reading for the oxygen analyser is 134.28 mg/m^3 with an uncertainty of 10.79, thus the random uncertainty is:

$$\Delta e_{rPM} = \frac{10.79}{134.28} = 8.04\%$$

Combining the systematic and random uncertainty by linear additive (ADD) and root-sum-square (RSS) methods yields for the opacity meter:

$$\begin{aligned} U_{ADD} &= 0.02 + 0.0804 = \pm 10.04\% \\ U_{RSS} &= \sqrt{0.02^2 + 0.0804^2} = \pm 8.29\% \end{aligned}$$

B19. Heat input (Q_{in}) uncertainty The systematic and random uncertainty of the heat input is derived from the added errors of the fuel flow rate and the energy content of the fuel as follows:

$$\begin{aligned} \Delta e_{sQ_{in}} &= 0 + 0.0073 = 0.73\% \\ \Delta e_{rQ_{in}} &= 0.0365 + 0 = 3.65\% \end{aligned} \tag{B.1}$$

Combining the systematic and random uncertainty by linear additive (ADD) and

root-sum-square (RSS) methods yields for the heat input:

$$\begin{aligned} U_{ADD} &= 0.0073 + 0.0365 = \pm 4.38\% \\ U_{RSS} &= \sqrt{0.0073^2 + 0.0365^2} = \pm 3.72\% \end{aligned}$$

B20. Heat output (Q_s) uncertainty The systematic and random uncertainty of the heat output of the heat source is derived from the added errors of water flow meter ($MW1$), the specific heat capacity, thermocouples ($T8$) and ($T9$) as follows:

$$\begin{aligned} \Delta e_{sQ_s} &= 0.005 + 4 \times 10^{-5} + 0.004 + 0.004 = 1.30\% \\ \Delta e_{rQ_s} &= 0.0171 + 0.0044 + 0.0025 = 2.40\% \end{aligned} \tag{B.2}$$

Combining the systematic and random uncertainty by linear additive (ADD) and root-sum-square (RSS) methods yields for the heat output:

$$\begin{aligned} U_{ADD} &= 0.013 + 0.024 = \pm 3.70\% \\ U_{RSS} &= \sqrt{0.013^2 + 0.024^2} = \pm 2.73\% \end{aligned}$$

B21. Cooling output (Q_{ac}) uncertainty The systematic and random uncertainty of the cooling output of the heat source is derived from the added errors of water flow meter ($MW3$), the specific heat capacity, thermocouples ($T10$) and ($T11$) as follows:

$$\begin{aligned} \Delta e_{sQ_{ac}} &= 0.0403 + 1.90 \times 10^{-6} + 0.004 + 0.004 = 4.83\% \\ \Delta e_{rQ_{ac}} &= 0.0042 + 0.0019 + 0.0077 = 1.38\% \end{aligned} \tag{B.3}$$

Combining the systematic and random uncertainty by linear additive (ADD) and

root-sum-square (RSS) methods yields for the cooling output:

$$\begin{aligned} U_{ADD} &= 0.0483 + 0.0138 = \pm 6.21\% \\ U_{RSS} &= \sqrt{0.0483^2 + 0.0138^2} = \pm 5.02\% \end{aligned}$$

B22. Heat output (Q_{hs}) uncertainty The systematic and random uncertainty of the heat output of the heat sink is derived from the added errors of water flow meter ($MW6$), the specific heat capacity, thermocouples ($T14$) and ($T15$) as follows:

$$\begin{aligned} \Delta e_{sQ_{hs}} &= 0.0086 + 5.72 \times 10^{-6} + 0.004 + 0.004 = 1.66\% \\ \Delta e_{rQ_{hs}} &= 0.0019 + 0.0097 + 0.0119 = 2.35\% \end{aligned} \tag{B.4}$$

Combining the systematic and random uncertainty by linear additive (ADD) and root-sum-square (RSS) methods yields for the heat sink output:

$$\begin{aligned} U_{ADD} &= 0.0166 + 0.0235 = \pm 4.01\% \\ U_{RSS} &= \sqrt{0.0166^2 + 0.0235^2} = \pm 2.88\% \end{aligned}$$

B23. Exhaust output (Q_{ex}) uncertainty The systematic and random uncertainty of the exhaust output of the heat sink is derived from the added errors of the gas flow, the specific heat capacity, thermocouples ($T1$) and ($T3$) as follows:

$$\begin{aligned} \Delta e_{sQ_{ex}} &= 0.0045 + 2.24 \times 10^{-5} + 0.004 + 0.004 = 1.25\% \\ \Delta e_{rQ_{ex}} &= 0.015 + 0.01 + 0.007 = 3.20\% \end{aligned} \tag{B.5}$$

Combining the systematic and random uncertainty by linear additive (ADD) and

root-sum-square (RSS) methods yields for the exhaust output:

$$\begin{aligned} U_{ADD} &= 0.0125 + 0.032 = \pm 4.45\% \\ U_{RSS} &= \sqrt{0.0125^2 + 0.032^2} = \pm 3.44\% \end{aligned}$$

References

Al-Shemmeri, T.T. 1993. *Combustion Lecture Notes.* Staffordshire University.

Alanne, K., & Saari, A. 2004. Sustainable small-scale CHP technologies for buildings: the basis for multi-perspective decision making. *Renewable and Sustainable Energy Reviews*, **8**(5), 401–431.

Alstom. 2004 (JA147). *CFD guides design of biomass retrofit to increase capacity by* 25% *and decrease ash.* Articels by FLUENT software users, Alstom Powers Inc.

Althouse, D.A., Turnquist, C.H., & Bracciano, A.F. 2000. *Modern Refrigeration and Air-Contioning.* 18^{th} edn. Illinois (USA): Goodheart-Wilcox Company ltd.

Anon. 2011a. *Biohousing - Sustainable, comfortable and competitive biomass based heating of private houses.* online, `http://www.biohousing.eu.com` [accessed 31/01/2011].

Anon. 2011b. *Cool Pack v.1.46.* Software, Department of Engineering University of Denmark, `www.et.dtu.dk/coolpack` [accessed 31/01/2011].

Anon. 2011c. *The Government of Luxembourg online.* online, `http://www.luxembourg.public.lu` [accessed 31/01/2011].

Anon. 2011d. *A Woodfuel Strategy for England.* online, `http://www.forestry.gov.uk/england` [accessed 31/01/2011].

Anthal, M.J. 1978. Energy from Biomass and Wastes. *Institute of Gas Technology.*

Aphornratana, S. 1995. Research on absorption refrigerators and heat pumps. *International Energy Journal*, **17**(1), 1–19.

Aphornratana, S., & Eames, I.W. 1998. Experimental investigation of a combined ejector-absorption refrigerator. *International Journal of Energy Research*, **22**, 195–207.

Aristov, Y. 2007. New family of solid sorbents for adsorptive cooling material scientist approach. *Journal of Engineering Thermophysics*, **16**(2), 63–72.

ASHRAE. 2009. *Fundamentals*. American Society of Heating, Refrigeration and Air-Conditioning Engineers, Altanta (USA).

Backström, M., & Emblik, E. 1965. *Kältetechnik*. 3^{rd} edn. Verlag G. Braun.

Badin, J., & Kirschner, J. 1998. Biomass greens US power production. *Renewable Energy World*, **1**.

Bales, C., & Nordlander, S. 2005. *TCA Evaluation: Lab measurements, modelling and system simulations*. Solar Energy Research Center Högskolan Dalarna (Sweden).

Bales, C., Ganterbein, P., Jähnig, D., & Versker, H. 2008 (7-10 October, Lisbon (Portugal)). *031 Chemical and sorption storage - Results from IEA-SHC Task 32*. EuroSun 2008.

Baxi. 2011. *Baxi website*. online, `http://www.baxi.co.uk` [accessed 31/01/2011].

Beale, W., & Chen, G. 1992 (Ohio (USA)). *Small Stirling free-piston engines for cogeneration*. Tech. rept. Sunpower Inc.

Best, R., & Holland, F.A. 1990. A study of the operating characterisics of an experimental absorption cooler using ternary systems. *International Journal of Energy Research*, **14**, 553–561.

Bhaduri, S.C., & Verma, H.K. 1986a. Heat of mixing R22 absorbent mixture. *International Journal of Refrigeration*, **11**, 92–95.

Bhaduri, S.C., & Verma, H.K. 1986b. P-T-X behaviour of R22 wiht five different absorbers. *International Journal of Refrigeration*, **9**, 262–266.

Biomass. 2011. *Biomass Energy Centre website*. online, `http://www.biomassenergycentre.co.uk` [accessed 31/01/2011].

BIOS. 2011. *Austrian Biomass Association*. online, `http://www.bios-bioenergy.at` [accessed 31/01/2011].

BIS. 2011. *BIS website*. online, Department for Business, Innovation & Skills (fomer BERR), `www.bis.gov.uk` [accessed 31/01/2011].

Bowman, R.A., Mueller, A.C., & Nagle, W.M. 1940. Mean Temperature Difference in Design. *Transactions of ASME*, **62**, 283–294.

Bretsznajder. 1971. Prediction of the transport and other physical properties of fluids. *International Series of Monographs in Chemical Engineering*, **2**.

CarbonTrust. 2011. *Biomass heating: a practical guide for potential users (CTG012)*. online, `http://www.carbontrust.gov.uk/publications` [accessed 31/01/2011].

Caserini, S., Livio, S., Giugliano, M., Grosso, M., & Rigamonti, L. 2010. LCA of domestic and centralized biomass combustion: The case of Lombardy (Italy). *Biomass and Bioenergy*, **34**, 474–482.

Cengel, Y.A., & Boles, M.A. 1997. *Thermodynamics - An Engineering Approach.* 2^{nd} edn. McGraw-Hill.

Chen, J., Kim, K.J., & Herold, K.E. 1996. Performance enhancement of a diffusion-absorption refrigerator. *International Journal of Refrigeration*, **19**(3), 208–218.

Chen, L.T. 1988. A new ejector-absorber cycle to improve the COP of an absorption refrigerator. *Applied Energy*, **30**, 37–51.

Cheng, C., & Yu, Y. 2010. Numerical model for predicting thermodynamic cycle and thermal efficiency of a beta-type Stirling engine with a rhombic-drive mechanism. *Renewable Energy*, **35**, 2590–2601.

Chung, H., Huor, M.H., Prevost, M., & Bugarel, R. 1984 (19-24 September). *Domestic heating application of an absorption heat pump.* Proceedings International Conference, University of Bristol (UK).

Cleveland, C.J. 2009. *Concise Encyclopedia of the history of energy.* Academic Press.

Climatwell. 2011. *ClimateWell website.* online, `http://www.climatewell.com` [accessed 31/01/2011].

Cogen. 2011. *Cogen Europe - Agenda to cogeneration.* online, `http://www.cogen.org` [accessed 31/01/2011].

Conde, M.R. 2004. Properties of aqueous solutions of lithium and calcium chlorides: formulations for use in air-conditioning equipment design. *International Journal of Thermal Science*, **43**(367-382).

Cooper, S., & Coronella, C. J. 2005. CFD simulations of particle mixing in a binary fluidised bed. *Powder Technology*, **151**, 27–36.

da Costa, E. C. M., dos Santos, C.A.C., & Ribeiro, C.M.U. 2005. Study of a diffusion-absorption refrigeration cycle using NH_3 water-helium as working fluids. 18^{th} *International Congress of Mechanical Engineering, ABCM, Ouro Preto (Brazil)*, 6-11 November.

Darlington, R., & Strong, K. 2005. *Stirling and Hot Air Engines: An Insight into Building and Designing Experimental Model Stirling Engines.* The Crowood Press Ltd.

de Paepe, M., d'Herdt, P., & Mertens, D. 2006. Micro CHP systems for residential applications. *Energy Conversion and Management*, **47**, 3435–3446.

DEFRA. 2011a. *defra website*. online, Department for Environment Foord and Rural Affairs, `www.defra.gov.uk` [accessed 31/01/2011].

DEFRA. 2011b. *Waste Wood as a Biomass Fuel - Market Information Report*. online, `http://www.defra.gov.uk` [accessed 31.01.2011].

Donaldon, K., Brown, D., Clouter, A., Duffin, R., & MacWee, W. 2002. The pulmonary toxicology of ultrafine particles. *Journal of Aerosol Medicine*, **15**(2), 213–230.

Dong, L., Liu, H., & Riflat, S. 2009. Development of small-scale and micro-scale biomass fuelled CHP systems - A literature review. *Applied Thermal Engineering*, **29**, 2119–2126.

Dornburg, V., & Faaij, A.P.C. 2001. Efficiency and economy of wood-fired biomass energy systems in relation to scale regarding heat and power generation using combustion and gasification technologies. *Biomass and Bioenergy*, **21**, 91–108.

Dossat, R.J., & Horan, J.T. 2001. *Principles of Refrigeration*. 5^{th} edn. New Jersey (USA): Prentice-Hall.

Douglas, J.F., Gasiorek, J.M., & Swaffield, J.A. 2005. *Fluid Mechanics*. 4^{th} edn. Prentice-Hall.

Emwelt.lu. 2006. *Changement climatique - Agir pour un défi majeur,* 1^{er} *plan d'action en vue de la réduction des émissions* CO_2 *(Climate change - First national action plan).*

Emwelt.lu. 2007. *Bestimmung der Potenziale und Ausarbeitung von Strategien zur verstärkten Nutzung von erneuerbaren Energien in Luxemburg (Potential and strategies for the increased utilisation of renewable energies in Luxembourg).* Tech. rept. Frauenhofer Institut für System- und Innovationsforschung, Energy Economics Group TU Wien, Ministère de l'environment & Ministère de l'économie et du commerce extérieur.

Enatec. 2011. *Enatec Micro-cogen website*. online, `http://www.enatec.com` [accessed 31/01/2011].

EPA. 2007 (September). *Biomass combined heat and power catalogue of technologies*. US Environmental Proetection Agency.

EPA. 2011a. *Technology characterisation: gas turbines*. online, `http://www.epa.gov` [accessed 31/01/2011].

EPA. 2011b. *Technology characterisation: steam turbines*. online, `http://www.epa.gov` [accessed 31/01/2011].

EPA. 2011c. *What is PM?* online, `http://www.epa.gov` [accessed 31/01/2011].

ETSU. 1976. *The fast pyrolysis of oilseed rape B/M5/00533/18/Rep.* Tech. rept. Aston University and ETSU.

Fiedler, F. 2004. The state of the art of small-scale pellet based heating systems and relevant regulations in Sweden, Austria and Germany. *Renewable and Sustainable Energy Reviews*, **8**, 201–221.

Finkelstein, T. 1994. *Insights into the thermodynamics of Stirling cycle machines.* pp. 1829-1834 A/AA94-3951-CP.

Fisher, T.F., Kasbohm, M.L., & Rivero, J.R. 1976. Clean Fuels from Biomass, Sewage, Urbran Refuse, Agricultural Wastes. *Institute of Gas Technology.*

Formosa, F., & Despesse, G. 2010. Analytical model for Stirling cycle machine design. *Energy Conversion and Management*, **51**, 1855–1863.

Frenzi, A., Russo, F., Vasta, S., Tokarev, M., & Yu, I. 2007. An advanced solid sorption chiller using SWS-1L. *Applied Thermal Engineering*, **27**(13), 2200–2204.

Geelen, L.M.J., Huigbregts, M.A.J., den Hollander, H., & Rogas, A.M.J. 2009. Confronting environmental pressure, environmental quality and human health impact indicators of priority air emissions. *Atmospheric Environment*, **43**, 1613–1621.

Gerber, S., Behrendt, F., & Oeverman, M. 2010. An Euleian modelling approach of wood gasification in a bubbling fluidised bed reactor using char as material. *Fuel*, **89**(10), 2903–2917.

Gomez-Barea, A., & Lechner, B. 2010. Modelling of biomass gasification in fluidised bed. *Progress in Energy and Combustion Science*, 444–509.

Gommed, K., & Grossman, G. 2007. Experimental investigation of a liquid dessicant system for solar cooling and dehumidification. *Solar Energy*, **81**, 131–138.

Goor, F., Jossart, J-M., & Ledent, J.F. 2000. ECOP: an economic model to assess the willow short rotation coppice global profitability in a case of small scale gasification pathway in Belgium. *Environmental Modelling and Software*, **15**, 279–292.

Griselin, N., & Bai, X.S. 2000. Particle dynamics in a biomass fired furnace - predictions of solid residence changes with operations. *IFRF Combustion Journal*, **9**, 30.

Groll, E.A. 1997. Current status of absorption/compression cycle technology. *ASHRAE*, **193**(1).

Grossman, G., & Michelson, E. 1986. *Absorption heat pump simulation and studies, a modular computer simulation of absorption systems.* Tech. rept. Technion Israel Institute of Technology & Department of Energy US.

Grossman, G., Zaltash, A., Adcock, P.W., & Devault, R.C. 1995. Simulating a 4-effect absorption chiller. *ASHRAE*, June, 45–53.

Gupta, Y., Metchop, L., Frantzis, A., & Phelan, P.E. 1997. Comparative analysis of thermally activated environmentally friendly-cooling systems. *Solar Energy*, **40**(1), 49–54.

Hadjsophocleus. n.D.. Guidelines for the use of CFD simulations for fire and smoke modelling. *American Society of Heating, Refrigeration and Air-Conditioning Engineers*, 583–594.

Haiber, E., Lubich, C., & Roche, M. 1989. *The numerical solution of differential algebraic systems by Runge-Kutta methods.* Springer Verlag.

Hanna, W.T., Wilkinson, W.H., & Ball, D.A. 1984 (19-24 September). *The Battelle dual cycle absorption heat pump.* Proceedings International Conference, University of Bristol (UK).

Hawkes, A.D., & Leach, M.A. 2007. Cost-effective operating strategy for residential micro-combined heat and power. *Energy*, **32**, 711–723.

Hermansson, S., Olausson, C., Thurnman, H., Ronnback, M., & Leckner, B. 2006 (April 18-21). *Combustion disturbance in the fuel bed of grate furnaces.* Proceedings of the 7^th European conference on industrial furnaces and boilers (Porto, Portugal).

Herold, K.E., Radermacher, R., & Klein, S.A. 1996. *Absorption chillers and heat pumps.* 1^{st} edn. CRC Press.

Higman, C., & van der Burgt, M. 2003. Gasification Processes. *Gasification*, 85–170.

Hinds, W. 1999. *Aerosol Technology.* 2^{nd} edn. John Wiley & Sons.

Hobson, M., & Thistlethwaite, G. 2003. Emission factor programme Task 7 - Review of residential and small scale commercial combustion sources. *UK NAEI*, **1**(AEAT/ENV/R/1407).

Huang, L.Y., Wen, J.X., Karayiannis, T.G., & Matthews, R.D. 1996. *CFD modelling of fluid flow and heat transfer in a shell and tube heat exchanger.* School of Engineering Systems and Design, South Bank University.

Hughes, I., & Hase, T. 2010. *Measurements and their Uncertainties: A pratical guide to modern error analysis.* Oxford.

IEA. 2009. *450 Scenario Copenhagen 2009.* press release.

IEA. 2011. *IEA publications.* online, `http://www.iea.org/publications` [accessed 31/01/2011].

IEA, & OECD. 2004. *Energy Policies of IEA countries - Luxembourg 2004 review.*

IEA, & OECD. 2008. *Energy Policies of IEA countries - Luxembourg 2008 review.*

IIR. 2007. *A brief history of refrigeration.* International Institute of Refrigeration.

ISO. 1999. *EN303-5:1999 Heating boilers - Heating boilers with forced draught burners, heating boilers for solid fuels, hand and automatically fired, nominal heat output of up to* $300kW$*. Terminology, requirements, testing and marking.*

ISO. 2009a. *EN14774-(1-3):2009 Solid biofuels - Determination of moisture content.*

ISO. 2009b. *EN15103:2009 Solid biofuels - Determination of bulk density.*

ISO. 2009c. *prEN15400:2009 Solid recovered fuels - Determination of calorific value.*

ISO. 2010. *EN14961:2010 Solid biofuels - Fuel specifications and classes.*

Jacob, U., & Eicker, U. 2006 (21-25 August). *Simulation and performance of diffusion cooling machines for solar cooling.* Proceedings of the 9^{th} World Renewable Energy Congress, Florence (Italy).

Jacob, U., Eicker, U., Taki, A.H., & Cook, M.J. 2003 (16-19 June). *Development of an optimised solar driven diffusion-absorption cooling machine.* Proceedings of ISES, Göteburg (Sweden).

Jacob, U., Eicker, U., Schneider, D., & Teuber, A. 2007 (18-20 April). *Heat transfer in Components and Systems for Sustainable Energy Technologies.* HEAT Set Conference, Chambéry (France).

Jacob, U., Spiegel, K., & Pink, W. 2008 (20-22 May). *Development and experimental investigation of a novel 10kW ammonia/water absorption chiller - CHILLI PSC - for air-conditioning and refrigeration systems.* 9^{th} International IEA Heat Pump Conference, Zurich (Switzerland).

Jurado, F., Cano, A., & Corpio, J. 2004. Biomass based micro-turbine plant and distribution network stability. *Energy Conversion and Management*, **45**, 2713–2727.

Kaer. 2006. Towards a CFD based mechanistic deposit formation model for straw-fired boilers. *Fuel*, **85**, 833–848.

Kaltschmitt, M., & Bridgwater, A.V. 1997 (April 09-11). Research development and demonstration needs for biomass gasification and pyrolysis. *In: Conference on Gasification Networks / Pyrolysis Networks.*

Karle, S.C., & Shaligram, A.D. 2009. Feasibility study on rapid thermal processing. *Solid state Electronics*, **53**, 1046–1049.

Kaushik, S.C., & Kumar, R. 1987. A comparative study of an absorber heat recovery cycle for solar refrigeration using NH_3-refrigerant with liquid adsorbents. *Energy Res.*, **11**, 123–132.

Kays, W.M., & London, A.L. 1984. *Compact Heat Exchangers.* 3^{rd} edn. Krieger Publishing.

Keating, E.L. 2007. *Applied Combustion.* 2^{nd} edn. CRL Press Taylor Francis Group.

Kongtragool, B., & Wongwises, S. 2003. A review of solar powered Stirling engines and low temperature differential Stirling engines. *Renewable and Sustainable Energy Reviews*, **7**, 131–154.

Kongtragool, B., & Wongwises, S. 2006. Thermodynamic analysis of the Stirling engine including dead volume of hot space, cold space and regenerator. *Renewable Energy*, **31**(3), 345–359.

Koornneef, J., Junginger, M., & Faaij, A.P.C. 2007. Development of fluidized bed combustion - An overview of trends, performances and cost. *Progress in Energy and Combustion Science*, **33**, 19–55.

Kruse, A. 2009. Hydrothermal biomass gasification. *Journal of Suprecritical Fluids*, **47**, 391–399.

Lane, N.W., & Beale, W.T. 1982. *A biomass fired* $1kW_e$ *Stirling engine generator and its applications in South Africa.* Tech. rept. Sunpower Inc., Ohio (USA).

Lin, I., Wang, Y., Al-Shemmeri, T.T., Ruxton, T., & Turner, S. 1996. An experimental investigation of a household size trigeneration. *Applied Thermal Engineering*, **16**(2), 163–173.

Lora, E.S., & Andrade, R.V. 2009. Biomass as energy source in Brazil. *Renewable and Sustainable Energy Reviews*, **13**, 777–788.

Mahkomov, K. 2006. Design improvements to a Biomass Stirling engine using mathematical analysis and 3D CFD modelling. *Journal of Energy Resources Technology, ASME*, **128**, 203–215.

Martini, W.R. 1983. *Stirling Engine Design Manual.* University Press of Pacific, Hawaii.

Mayia, M.P. 2003. *Studies on gas circuit of diffusion absorption refrigerator.* 21^{st} IIR International Congress of Refrigeration, Washington (USA).

Mémorial. 2005 (November). *Règlement grand-ducal du 14 octobre 2005 1) concernant la fourniture d'énergie électrique basée sur les énergies renouvelables et 2) modifiant le règlement grand-ducal du 30 mai 1994 concernant la production d'énergie électrique basée sur les énergies renouvelables ou sur la cogénération ainsi que le règlement grand-ducal du 22 mai 2001 concernant l'introduction d'un fonds de compensation dans le cadre de l'organisation du marché de l'électricité (Luxmbourgish law regarding electricity production based on renewable energies or combined heat and power systems).* A N:181/2005.

Mémorial. 2009 (Avril). *Règlement grand-ducal du 20 avril 2009 instituant un régime d'aides pour la promotion de l'utilisation rationelle de l'énergie et la mise en valeur des énergies renouvelables (Lumbourgish law governing subsidies and feed-in tariffs in respect to the use of renewable energies).* A N:083/2009.

Messerer, A., Schmatloch, V., Poeschl, U., & Niessner, R. 2007. Combined particle emission reduction in industry. *Biomass and Bioenergy*, **31**, 512–521.

Minchener, A., Cross, P., Smith, T., & Fisher, A.M. 2000. *Fluidised bed combustion systems for power generation and other industrial applications.* CRE Group Limite.

Misirlioglu, Z., Canel, M., & Smag, A. 2007. Hydrogasification of chars under high pressures. *Energy Conversion and Management*, **48**(52-58).

Misra, R.D., Sahoo, P.K., & Gupta, A. 2006. Thermoeconomic evaluation and optimization of an aqua-ammonia vapour-absorption refrigeration system. *International Journal of Refrigeration*, **29**(1), 47–59.

Moaveni, S. 2003. *Finite Element Analysis - Theory and Applications with Ansys.* 2^{nd} edn. Prentice-Hall.

Munson, B. R., Young, D. F., Okiishi, T. H., & Huebsch, W. H. 2009. *Fundamentals of Fluid Mechanics: SI Version.* John Wiley & Sons.

Murakami, T., Xu, G., Suda, T., Matsuzawa, Y., Tani, H., & Fujimori, T. 2007. Some process fundamentals of biomass gasification in a dual fluidized bed. *Fuel*, **86**, 244–255.

Mursito, A.T., Hirahima, T., & Sasaki, K. 2010. Upgrading and dewatering of raw tropical peat by hydrothermal treatment. *Fuel*, **89**, 635–641.

Najjar, Y.H.S. 1996. Enhancement of performance of a gas turbine engines by inlet air cooling and cogeneration systems. *Applied Thermal Engineering*, **16**(2), 163–173.

Nigam, P.S., & Singh, A. 2010. Production of liquid biofuels from renewable resources. *Progress in Energy and Combustion Science*, **37**(1), 52–68.

Nikoo, M.B., & Mahinpey, N. 2008. Simulations of biomass gasification in fluidisesd bed reactor using Aspen Plus. *Biomass and Bioenergy*, **32**, 1245–1254.

Nussbaumer, T. 2005 (October 17-21). *Overview on particles from biomass combustion*. 14^{th} European Biomass conference in Paris.

Nussbaumer, T., Czesch, C., Klippel, N., Johannsson, L., & Claes, T. n.D. (Swiss Federal Office of Energy). *Particulate emission from Biomass Combustion in IEA countries*. IEA Bioenergy Task 32.

Oberweis, S. 2010 (November). *The potential of biomass in the energy sector of Luxembourg*. Symposium organsied by "Privatbësch Besetzer Lëtzebuerg".

Oberweis, S., & Al-Shemmeri, T.T. 2010 (Granada (Spain), March 23-25,). *Effect of Biodiesel blending on emissions and performance in a stationary diesel engine*. International Conference on Renewable Energies and Power Quality (ICREPQ'10).

Onowwioma, H.I., & Ugursal, V.I. 2006. Residential cogeneration systems: A review of the current technology. *Renewable and Sustainable Energy Reviews*, **10**, 389–431.

Organ, A., & Finkelstein, T. 2010. *Thermodynamics and gas dynamics of the Stirling cycle machine*. Cambridge University Press.

Organ, A.J. 1997. *The Regenerator and the Stirling Engine*. Willey Blackwell.

Parikh, J., Channiwala, S.A., & Ghosal, G.K. 2005. A correlation for calculating HHV from proximate analysis of solid fuels. *Fuel*, **84**, 487–494.

Pericleous, K.A. 2008. Computer modelling for the analysis of fluid flow, heat transfer and combustion in industry (CHAM). *Energy World*, **161**, 9–11.

Prasad, B.G., & Shiva. 2004. Benchmarking in CFD. *Proceedings of the ASME Heat Transfer/Fluids Engineering Summer Conference*, **23**, 1221–1227.

Pritchard, D. 2005. *Biomass fuelled indirect fired micro-turbine*. Tech. rept. B/T1/00790/00/00/REP. Talbott's Heating Ltd., dti.

Puech, P., & Tishkova, V. 2011. Thermodynamic analysis of a Stirling engine including regenerator dead volume. *Renewable Energy*, **36**, 872–878.

Quadrelli, R., & Petersen, S. 2007. The energy climate challenge: Recent trends in CO_2 emissions from fuel combustion. *Energy Policy*, **35**(11), 5939–3953.

Rane, M.V., Amrane, K., & Radermacher, R. 1993. Performance enhancement of a two-stage vapour compression heat pump with solution circuits by eliminating the rectifier. *International Journal of Refrigeration*, **16**(4), 247–257.

Ratte, J. 2003. Comparison of contact and radiant ablative pyrolysis of biomass. *Analytical and Applied Pyrolysis*, **70**(2), 601–618.

Ratte, J., Marias, F., Vaxelaire, J., & Bernada, P. 2009. Mathematical modelling of slow pyrolysis of a particle of treated wood waste. *Journal of Hazardous Materials*, **170**, 1023–1040.

Rostami, A.A., Hajalibol, M.R., & Wrenn, S.E. 2004. A biomass pyrolysis sub-model for CFD application. *Fuel*, **83**, 1519–1525.

RUBIN. 2008. *Regionale Strategie zur nachahltigen Umsetzung der Biomasse Nutzung (Regional strategies for the sustainable utilisation of biomass.* Tech. rept. INTERREG III(A).

Sanjuan, C., Soutullo, S., & Heras, M.R. 2010. Optimisation of a solar cooling system with interior energy storage. *Solar Energy*, **84**(7), 1244–1254.

Scollo, L., Valdez, P., & Baron, J. 2008. Design and construction of a Stirling engine prototype. *International Journal of Hydrogen Energy*, **33**(13), 3506–3510.

Scott, S.A, Davey, M.P., Dennis, J.S., Horst, I., Howe, C.J., Lea-Smith, D.J., & Smith, A.G. 2010. Biodiesel from algae: challenges and prospects. *Current Opinion in Biotechnology*, **21**, 277–286.

Senertec. 2011. *Senertec website.* online, `http://www.senertec.de` [accessed 31/01/2011].

Seyboth, K., Beurskens, L., Langniss, O., & Sims, R.E.H. 2008. Recognising the potential for renewable energy heating and cooling. *Energy Policy*, **36**(7), 2460–2463.

Shen, D.K., & Gu, S. 2009. The mechanism for thermal decomposition of cellulose and its main products. *Bioresource Technology*, **100**, 6496–6504.

Sideros. 2011. *Sideros website.* online, `http://www.sideros.com` [accessed 31/01/2011].

Soltes, E.J., Wiley, A.T., & Lin, S.C.K. 1981. Biomass Pyrolysis - Towards an understanding of its versatility and potentials. *Biotechnology and Bioengineering*, 125–136.

Splinthoff, H. 2000. Verbrennung und Vergasung in Wirbelschichtanlagen - Stand, Entwicklung und Forschungsbedarf (Combustion and Gasification - State of the art literature review).

Srikhirin, P., Aphornratana, S., & Chungpaibulpatana, S. 2001. A review of absorption refrigeration technologies. *Renewable and Sustainable Energy Reviews*, **5**, 343–372.

Stahl, M., Granstrom, K., Berghel, J., & Renstrom, R. 2004. Industrial processes for biomass drying and their effects on the quality of wood pellets. *Biomass and Bioenergy*, **27**, 621–628.

Steimle, F., Lamprichs, J., & Beck, P. 2007. *Stirling Maschinen-Technik - Grundlagen, Konzepte, Entwicklung, Anwendungen*. 2^{nd} edn. Heidelberg (Germany): CF Muller Verlag.

Stierlin, H., Wassermann, U., Doerfler, W., & Boessel, J. 1992 (BEW 92-019). *Messungen an Diffusions-Absorptions- Wärmepumpen*. Bundesamt für Energiewirtschaften Schweiz (Switzerland).

StirlingAG. 2011. *Stirling Systems AG website*. online, `http://stirling-systems.ch` [accessed 31/01/2011].

Stopford, P.J. 2002. Recent applications of CFD modelling in the power generation and combustion industries. *Applied Mathematical Modelling*, **26**, 351–374.

Subramaniam, A.K., & Marwaha, Y. 2006. Use of bagasse and other fuels in high pressure travelling grate boilers. *International Sugar Journal*, **108**, 6–9.

Sun, Z.G. 2008. Experimental investigation of integrated refrigeration systems (IRS) with gas engine, compression chiller and absorption chiller. *Energy*, **33**, 431–436.

Teresa, M.M., Martins, A.A., & Caetano, N.S. 2010. Microalgae for biodiesel production and other applications: A review. *Renewable and Sustainable Energy Reviews*, **14**, 217–232.

Thiers, S., Aoun, B., & Peuportier, B. 2010. Experimental characterization, modelling and simulation of a wood pellet micro-combined heat and power unit as a heat source for a residential building. *Energy & Building*, **42**(6), 896–903.

Thomas, B. 2008. Benchmark testing of a micro CHP unit. *Applied Thermal Engineering*, **28**, 2049–2054.

Tobiasen, L., Skytte, R., Pedersen, L.S., Pedersen, S.T., & Lindberg, M.A. 2007. Deposit characteristic after injection of additives to a Danish straw-fired suspension boiler. *Fuel Processing Technology*, **88**, 1108–1117.

Umweltbundesamt. 2005. *Hintergrundpapier zum Thema Staub/Feinstaub (Department of Environment, Paper on particulates)*. Berlin (Germany).

UN. 1999. *Protocol to abate acidification, eutrophication and ground level ozone.* United Nations Economic Commission for Europe, Gothenburg.

UN. 2008. *Kyoto Protocol - Reference Manual.* United Nations Framework Convention on Climate Change, Germany.

UN. 2009a. *Copenhagen Accord FCCC/CP/2009/11/Add.1.* United Nations Framework Convention on Climate Change.

UN. 2009b. *Handbook for the Vienna convention for the protection of the ozone layer.* Ozone Secretariat UN Environment Programme.

Urieli, I., & Berchowitz, D.M. 1984. *Stirling Cycle Engine Analysis.* Institute of Physics Publishing.

van der Woude, R., tan Haaken, E., Zutt, S., Vriesma, B., & Beckers, G. 2004 (5-7 May). *Intermediate results of the enatec micro cogeneration system field trials.* International Stirling Forum, Osnabrück (Germany).

Viesmann. 2011. *Viesmann website.* online, `http://www.viesmann.de` [accessed 31/01/2011].

Vinterbäck, J. 2004. Pellets 2002: the first world conference on pellets. *Biomass and Bioenergy*, **27**, 513–520.

Vliet, G.C., Lawson, M.B., & Lithglow, R.A. 1982. Water-lithium bromide double-effect absorption cooling cycle analysis. *ASHRAE*, **88**, 811–822.

Wahlund, B., Yan, J., & Westermark, M. 2002. A total energy system for fuel upgrading by drying biomass feedstock for cogeneration: a case study of Skelleftea bioenergy combine. *Biomass and Bioenergy*, **23**, 271–281.

Walker, G. 1980. *Stirling engines.* Oxford: Clarendon Press.

Wang, Y., Namioka, T., & Yoshikawa, K. 2009. Effect of the reforming reagents and fuel species on tar reforming reaction. *Bioresource Technology*, **100**, 6610–6614.

Wardeneier, K., & van de Bulck, E. 1997. Steady-state waste combustion and air flow optimisation in a field scale rotary kiln. *Environmental Engineering Science*, **14**, 43–54.

Watts, F.G., & Gulland, C.K. 1985. Triple-fluid vapour-absorption refrigerators. *Journal of Refrigeration*, July, 107–115.

Way, R.J.B. 1976. Methods for determination of composition and thermodynamic properties of combustion products for internal combustion engine calculations. *Proceedings of the Institution of Mechanical Engineers*, 687–697.

Weintraub, Steven H. 2009. *Galois Theory*. 2^{nd} edn. Springer Verlag.

Welfring, J., & Weidenhaupt, A. 2003. *Ganzheitliche Betrachtung der energetischen Holznutzung (State of the art review on the use of wood for the energy sector)*. Tech. rept. AEL / CRTE.

West, C.D. 1981 (August). Theoretical basis for the Beale number. *In: Intersociety Energy Conversion Engineering Conference*.

Whispergen. 2011. *Whispergen website*. online, `http://www.whispergen.com` [accessed 31/01/2011].

WHO. 2006. *Air quality guidelines for particulate matter, ozone, nitrogen, dioxide and sulphur dioxide - Global update*. World Health Organization.

Wiesenthal, T., & Mourelatou, A. 2006. *How much bioenergy can Europe produce without harming the environment*. Tech. rept. EEA and OPOCE.

Wiggers, V.R., Meier, H.F., Wisniewski., A., Barros, A.A.C., & Michel, M.R.W. 2009. Biofuels from continuous fast pyrolysis of soybean oil: A pilot plant study. *Bioresource Technology*, **100**, 6570–6577.

Wu, D.W., & Wang, R.Z. 2006. Combined cooling, heating and power: A review. *Progress in Energy and Combustion Science*, **32**, 459–495.

Yang, Y.B., Newman, R., Sharifi, V., Swithenbank, J., & Ariss, J. 2007. Mathematical modelling of straw combustion in a $38MW_e$ power plant furnace and effect of operating conditions. *Fuel*, **86**, 129–142.

Yin, C., Rosendahl, L.A., & Kaer, S.K. 2008. Grate-firing of biomass for heat and power generation. *Progress in Energy and Combustion Science*, **34**, 725–754.

Yuan, S. W. K., & Spradley, J. E. 1992. A third order computer model for Stirling refrigerators. *Advances in Cryogenic Engineering*, **37**(B), 1055–1062.

Zeiler, K.G., Heacox, D.A., Toon, S.T., Kadam, K.L., & Brown, L.M. 1995. Use of microalgae for assimilation and utilisation of carbon dioxide from fossil fuel-fired power plant flue gas. *Energy Conversion and Management*, **36**(6-9), 707–712.

Zhou, H., Jensen, A.D., Glarborg, P., Jensen, P.A., & Kavaliauskas, A. 2005. Numerical modelling of straw combustion in a fixed bed. *Fuel*, **84**, 389–403.

Zohar, A., Jelink, M., Levy, A., & Borde, I. 2005. Numerical investigation of a diffusion-absorption refrigeration cycle. *International Journal of Refrigeration*, **28**(4), 515–525.